Numerical Modelling Investigation of Rock Mass Behaviour under Gravity Dams

by

Younis Mustafa Ali Alshkane

B.Sc., M.Sc.

Thesis submitted to the University of Nottingham for
the degree of Doctor of Philosophy

July 2015

DECLARATION OF ORIGINALITY

Title of Thesis: Numerical Modelling Investigation of Rock Mass Behaviour under Gravity Dams

This is to declare that I am the sole author of this thesis, that the original work is my own, unless otherwise referenced and indicated, and that this thesis has not been submitted for a higher degree to any other institution or university.

Author's Name: **YOUNIS MUSTAFA ALI ALSHKANE**

Signature:

Date: 27-5-2015

Supervised by

DR. ROD STACE   **DR. ALEC MARSHALL**

Signature: Signature:

Date: 27-5-2015   Date: 27-5-2015

DEDICATION

To the memory of the Kurdish people martyred by chemical weapons and in the processes of 'Anfal Genocide' in Iraqi Kurdistan during the 1980s, and those who sacrificed their souls for the sake of freedom in Iraq.

To my parents whom I owe my life.

ABSTRACT

The study of rock mass behaviour is a broad subject in the rock mechanics field which still needs more research and investigation, especially for geotechnical issues associated with dam construction. Since it is difficult to study rock mass behaviour at a large scale in the laboratory, the numerical modelling technique is an alternative method which can be used efficiently in this field. In this thesis two codes have been selected for this purpose. The first code was a continuum code FLAC (Fast Lagrangian Analysis of Continua), which was used to study the effect of a weak rock joint on the stability of a concrete gravity dam as well as to model the gravity dam with its foundation as a continuum. The second code was the Distinct Element Method (DEM) software package UDEC (Universal Distinct Element Code), which was used to study the fully jointed rock mass behaviour under the gravity dam. The equivalent strength and deformability parameters of jointed rock masses were also studied using UDEC. Furthermore, the cause of strain hardening behaviour in jointed rock samples was studied using UDEC and experimental methods.

Based on UDEC models, it was concluded that only the low dip angle of the joints on downstream side, dipping upstream had a significant effect on the evaluated deformation of the dam. This was confirmed by using FLAC to model a single weak joint (using interfaces), which may exist in the upstream or downstream direction, on the stability of the dam. Furthermore, to obtain a better understanding of the rock mass behaviour, the equivalent strength parameters as well as the deformation modulus of a rock mass were determined using UDEC. A novel FISH (imbedded language in UDEC) function was developed for this purpose. A range of numerical simulations of uniaxial compressive strength (UCS) and triaxial tests were conducted on the numerical rock mass samples for these purposes. To validate this, the defor-

mation modulus of the rock mass predicted by an analytical equation, quoted from literature, was compared with the numerical results that were given by UDEC. It was found that UDEC can efficiently be used to determine the strength and deformability parameters of rock masses and that at certain specific joint configurations, the rock mass behaviour was similar to granular material.

In addition, it was concluded, for the first time, that the non-uniform distribution of axial loading on the jointed rock sample was the main cause of strain hardening especially for a joint that has a dip angle of 60 degree. To overcome this problem, a new loading configuration was developed for applying a uniform distribution of axial stress on the jointed rock samples in order to reduce the effect of platen-rock interaction on the axial stress-strain relationship, using UDEC and laboratory tests.

Finally, the study of rock mass strength and deformability parameters of Surqawshan dam's foundation in Iraq were determined using UDEC and the results were compared with rock classification systems: RMR and GSI. According to the UDEC results all methods give a similar evaluation of friction angle; however, GSI overestimates the cohesion. The UDEC and GSI gave reasonable estimations of deformation modulus, whereas RMR overestimated it. Generally, for rapid estimation of deformability and strength parameters, especially for weak sedimentary rock, the deformation modulus can be predicted from the GSI system, whereas the strength parameters can be estimated using RMR.

LIST OF PUBLICATION

Based upon aspects of the research presented in this thesis, the following papers have been produced.

a) Published conference papers:

- Y. M. ALSHKANE, A. M. MARSHALL and L. R. STACE, 2014. Continuum and discontinuum modelling of gravity dams on jointed rock foundations: in Rock Engineering and Rock Mechanics: Structures in and on Rock Masses. CRC Press. In: ISRM European Rock Mechanics Symposium (EUROCK 2014). 745-750

- Y. M. ALSHKANE, A. M. MARSHALL and L. R. STACE, 2014. The effect of a weak foundation rock joint on the stability of a concrete gravity dam. In: International Discrete Fracture Engineering Conference, DFNE 2014, Vancouver, BC, Canada. Paper no. 207.

- Y. M. ALSHKANE, A. M. MARSHALL and L. R. STACE, 2015. Obtaining foundation rock mass properties of the Surqawshan earth dam using UDEC. Abstract accepted for Eurock 2015 conference that will be held in Austria in 7 October 2015.

b) Prepared journal papers:

- Y. M. ALSHKANE, A. M. MARSHALL and L. R. STACE, 2015. The strength and deformability predictions of an interlocked blocky rock mass using UDEC.

- Y. M. ALSHKANE, A. M. MARSHALL and L. R. STACE, 2015. The strain hardening behaviour of jointed rocks - an experimental and numerical investigation.

- Y. M. ALSHKANE, A. J. BUTTRESS, A. M. MARSHALL, L. R. STACE, and M. K. MOHAMMED 2015. Geotechnical - Microstructural Characterization and Swelling Behaviour of the Gercus formation at Surgawshan Dam foundation in Northern Iraq.

ACKNOWLEDGEMENT

First of all, I am very thankful to my supervisors Dr. Rod Stace and Dr. Alec Marshall, for their academic guidance, kind continuous encouragement and generous support during my studies.

I wish to gratefully acknowledge the facilitation of the Ministry of Higher Education and Scientific Research in Iraq for providing a full scholarship. I am also thankful to the Iraqi Cultural Attaché in London for their continuous encouragements and support during my PhD studies.

I wish to record my sincere appreciation for Mr. Mark Dale, Dr. Nigel Neate, Mr. Thomas Buss, Mr. Andrew Maddison, Mr. James Meakin and Mr. Balbir Loyla in the University of Nottingham for their assistance with the experimental work; and Dr. Ghafor A. Hamasur and Dr. Fuad M. Qadir in the University of Sulaimani in Iraq for their help during the field study of Surqawshan Dam in the Kurdistan Region of Iraq.

I would like to acknowledge the General Directorate of Dams and Reservoirs in the Kurdistan Region of Iraq for providing the rock cores of Surqawshan Dam's foundation, and thanks to Mr. Aram Hussain Ali, the geologist who provided the facilities to arrive at the site and collect samples. Also, I would like to acknowledge the funds provided by the Nottingham Centre for Geomechanics and Graduate School Travel Prize at Nottingham University to attend the symposium of EUROCK2014.

Acknowledgements are also given to all my friends, especially Mr. Twana Kamal Haji at the Nottingham Centre for Geomechanics, with whom I have had a wonderful time during my PhD study, and my friend Dr. Serwan Al-Zahawi, the Head of the Civil Engineering Department in Engineering Faculty of Sulaimani University in Iraq, for his help and encouragement.

Finally, and most importantly, I thank my parents, my sisters, my brothers and my wife, without whose generous encouragement and help I would have not been able to conduct my PhD. Also, I would like to acknowledge my children, Heshoo, Nali and Naz (HNN), for their patience and understanding of the situation during my studies.

LIST OF CONTENTS

CHAPTER 3 METHODOLOGY

CHAPTER 6 STRENGTH PREDICTION OF ROCK MASS STUDY BY UDEC

CHAPTER 9 CONCLUSIONS AND RECOMMENDATIONS

LIST OF TABLES

LIST OF FIGURES

NOTATION

F_o Factor of safety against overturning

F_s Sliding factor

F_{SF} Shear friction factor

F_{LE} Factor of safety against sliding

RQD   the rock quality designation

RMR   Rock Mass Rating

UCS   Uniaxial compression stress strength

E_{rm} The deformation modulus of rock masses

σ_1' Effective major principal stress

σ_1 Major principal stress

σ_3' Effective minor principal stress

σ_3 Minor principal stress

m_b Hoek brown failure criterion constant

s Hoek brown failure criterion constant

a Hoek brown failure criterion constant

σ_t Tensile strength

c Cohesion

$\emptyset$ Angle of internal friction

GSI   Geological Strength Index

D   Disturbance factor for GSI system

$\overline{\sigma}_h$ Effective horizontal stress

$\overline{\sigma}_v$ Effective vertical stress

v Poisson's ratio

K Bulk modulus

G Shear modulus

σ_{max}^t The maximum tensile strength

c_j Cohesion of the interface

$\emptyset_j$ Friction angle of interface surfaces

τ_s Shear stress

σ_n Normal stress

p_w Fluid density

ρ Block mass density

ρ_d Dry density

q Flow rate

θ_r The degree of rotation

g The acceleration of gravity

a_o The joint aperture at zero normal stress

u_n The joint normal displacement

a_{res} The minimum joint aperture

a_{zero} The joint aperture at zero normal stress

a_{max} The maximum joint aperture

p The domain pressures

K_w Bulk modulus of the fluid

k_n Normal stiffness of the interface or joint

$k_s.$ Shear stiffness of the interface or joint

$\bar{v}$ Lateral strain ratio

$\bar{E}$ The plane-strain deformation modulus

σ_y Vertical stress

d   Distance

t   Time

v   Velocity

E_r The modulus of elasticity of intact rock

R The stiffness ratio (k_s/k_n)

R_{pp} Stiffness ratio of platen-platen contact

R_{pr} Stiffness ratio of platen-rock contact

R_{rr} Stiffness ratio of rock-rock contact

$\bar{v}$ Lateral strain ratio,

NLC   New loading configuration

XRD   X-Ray Diffraction

EDX   Energy Dispersive X-ray

SEM   Scanning Electron Microscope

PLT   Point Load Test

Chapter 1 Introduction

1.1 Introduction

Since the dawn of civilization, complex human communities have been dependent on sophisticated physical infrastructure and engineering to meet their basic needs. Industrialisation and urbanisation since the 18th century have intensified the demands of human societies for large-scale civil engineering. One of the most ancient engineering forms that continue to be fundamentally important to human life is the dam. The main purpose of building dams is to ensure a reliable water supply for drinking and irrigation. In the modern age the function of dams has been expanded to include hydropower and flood management.

Since it is impossible to build a dam on a homogeneous foundation, it is built on the rock masses, so there is possibility of sliding failure along one of the discontinuity in the rock mass or sliding along the rock-foundation interface. According to Douglas (2002), dams built on jointed rock mass foundation are susceptible to fail due to sliding. Examples of geological conditions in which sliding may be possible are shown in Figure 1.1; therefore the study of every aspect related with geology of foundation would contribute to design a dam perfectly in terms of safety and economy.

Although usually characterised by sophisticated and skilled engineering from their inception, there are cases of dams failing throughout history, often with catastrophic results such as Malpasset dam in France (Wittke and Leonards, 1987). There has thus been a great amount of research into the causes of such incidents, in order to improve dam technology and to build dams safely and economically. Numerous techniques have been applied to study the stability of dams, such as limit equilibrium method, physical modelling, photoelastic technique and numerical methods. The latter were the most popular and powerful among researchers because of their capability to capture the failures accurately and economically. Many numerical methods have been developed to analyse different types of structures, such as the finite elements method (FEM), the boundary elements method (BEM), the discrete element method (DEM) and the finite difference method (FDM).

Generally, most incidents have occurred due to events in dam foundations such as sliding, tensile cracks and piping (Boyer, 2006; Douglas, 2002). However, due to their complex structure and locale, there are many issues that must be considered regarding the stability of concrete dams, such as the rock mass behaviour under dams and the effect of a weak joint in the foundation on dam stability (Figure 1.2), which might be in the upstream or in downstream direction of the dam. This weak joint can be developed according to the geological

conditions in the foundations of dams (Figure 1.1). These issues are explored in this research using conceptual gravity dams. Also, it was found that the information on how to assess the strength of the dam's foundation or rock masses was limited. Figure 1.3 shows the typical loads included in a 2D stability analysis of a gravity concrete dam and the common terminology that has been used in the study. Gravity dams depend upon their weight for stability against sliding and overturning (Novák et al., 2007).

This research is based on the numerical modelling technique to study the effect of a joint configuration of a rock mass in the rock foundation of a gravity dam on its stability using continuum and discontinuum models, as well as the effect of a weak single joint on the dam's stability using continuum model. Dynamic seismic loading from earthquakes or explosives are not considered; the stress analysis is essentially static in its nature.
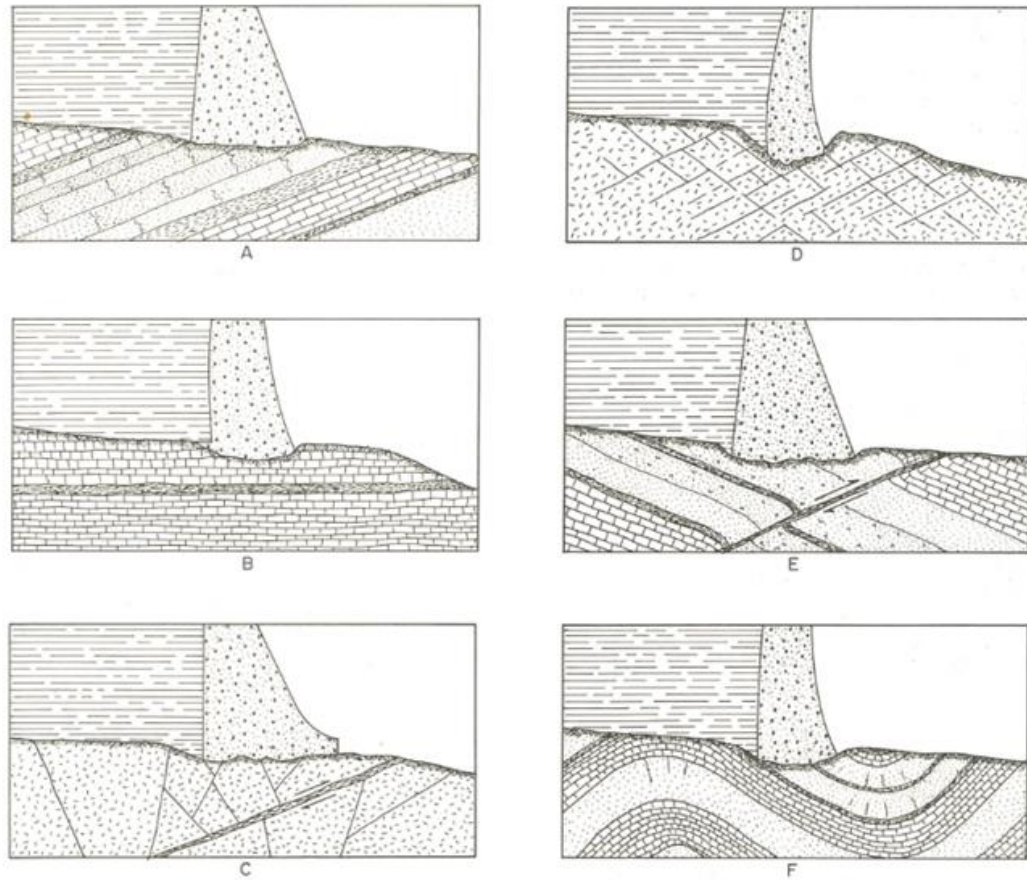
Figure 1.1 Geological conditions promoting failure of foundation of dams (Wyllie, 2003)
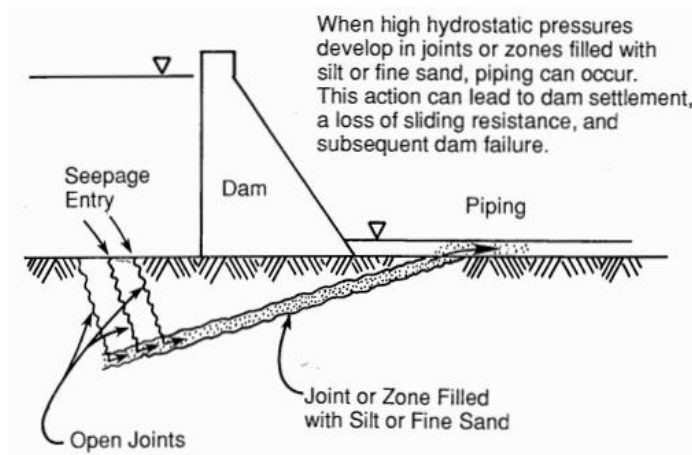
Figure 1.2 Weak layer under Gravity Dam(USBR, 1988)
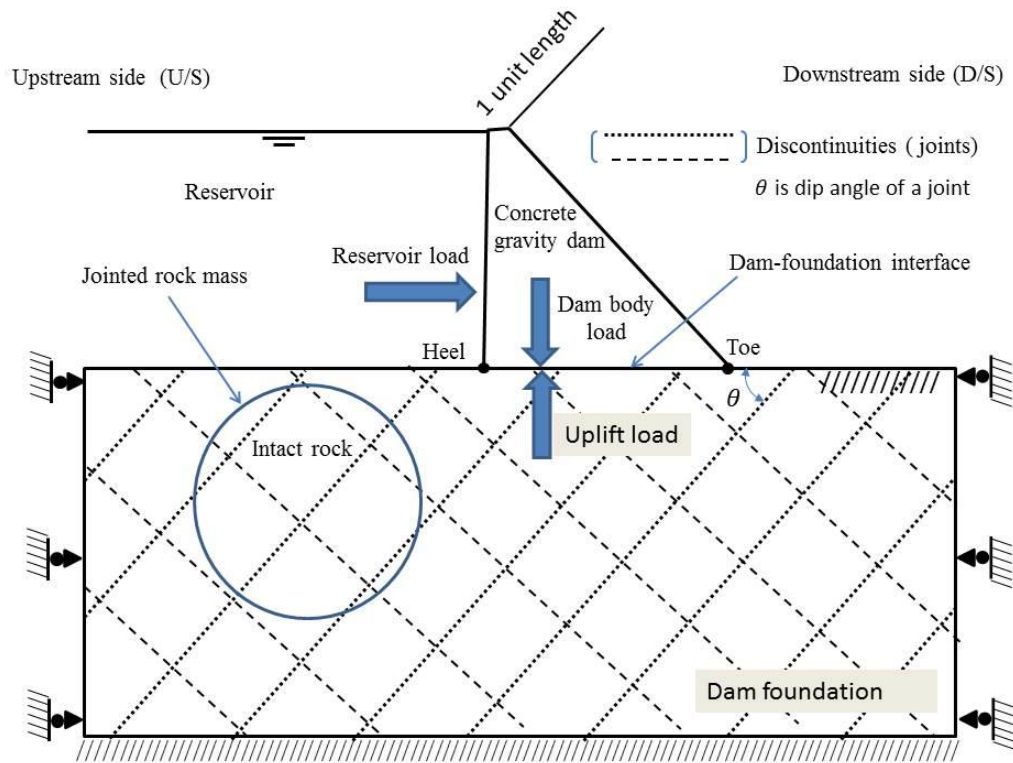
Figure 1.3 Cross section of a typical gravity dam with jointed rock mass foundation

1.2 Aims

The aims of this project are twofold. The first is the application of the numerical modelling method to analyse the stability of a concrete gravity dam resting on a rock mass containing joints using a continuum model (using FLAC^{2D}) and a discontinuum model (using UDEC^{2D}) in a plane strain state. The second aim is to predict the equivalent strength and deformability parameters of rock masses as well as the cause of strain hardening behaviour in jointed rock samples using UDEC.

1.3 Objectives

The objectives of this study can be summarized into the following points:

1. To simulate numerically a concrete gravity dam and its foundation using the two numerical codes.

2. Verification of modelling by comparing results with classical methods to determine stress distribution using combined triangular and rectangular strip loadings on an elastic medium.

3. To find the effect of a joint interbedded with rock foundation on the stability of the concrete gravity dam and to find the most dangerous location of that joint in the upstream or downstream directions.

4. To study the effect of a joint dip angle on dam stability.

5. To compare between continuum and discontinuum modelling of rock mass foundation under gravity dam.

6. To find the equivalent strength and deformability parameters of a rock mass using the discontinuum model.

7. To investigate the cause of strain-hardening in a jointed rock sample with a joint that dips at around 60 degrees.

1.4 Limitations of Study

In every research especially numerical modeling there should be some limitations. In this study the main limitation was using 2D simplification of 3D model. The simple Mohr-Coulomb criterion with linear elastic-perfectly plastic also was used for both intact and jointed rock masses. It should be mentioned that these assumption would not affect the overall goal of the study. However, 3D modeling could be the topic of a future study. Furthermore, a nonlinear model such as the Barton-Bandis could be used for the joints and the Hoek-Brown nonlinear failure envelope could be used for intact rock in a future study.

1.5 Thesis outline

The thesis consists of nine chapters (Figure 1.4), as described below:

Chapter One introduces the background of the research area and justifies this research. It also presents the research aim and objectives. An overview of the thesis is given in this chapter.

Chapter Two is the general literature review. This presents historical dam failures, previous work on dam stability, and the available rock classification system that can be used to analyse the rock mass behaviour for the foundation of dams.

Chapter Three describes the research methodology. In this chapter the numerical methodology using two numerical continuum and

discontinuum codes is described as well as the experimental methodology adopted.

Chapter Four details a conceptual model designed as a theoretical model. The theoretical model was assumed to be a gravity concrete dam, for simplicity. Results are compared between a continuum model (FLAC) and a discontinuum model (UDEC) and the codes are evaluated to determine which gives the most realistic prediction compared to the conventional stress distribution at the contact between the dam and the foundation.

Chapter Five presents and analyses the effect of a weak joint in the dam's foundation on its stability using a continuum model (FLAC).

Chapter Six describes a rock mass study by UDEC and presents a validation of the numerical model by comparing the deformation modulus for a blocky rock mass predicted by UDEC with analytical predictions. Also, the equivalent mechanical properties predicted by UDEC are presented. The equivalent properties are used in a case study analysis considering the behaviour of a rock mass under a concrete gravity dam as a continuum using the finite difference software FLAC, and results are compared with those obtained using UDEC.

Chapter Seven presents the reliability of the numerical modelling by comparing the experimental axial stress-axial strain of small-scale

intact and jointed sandstone rock samples which were collected from Birchover Quarry in the UK with a discontinuum model using UDEC.

Chapter Eight presents the equivalent rock mass properties of a real dam foundation in Iraq by UDEC. The samples from the foundation of the real dam were collected and the equivalent properties of the rock mass were determined using UDEC. The results were compared with the two popular rock mass classification systems, RMR and GSI. Also, the new loading configuration is presented in this chapter.

Chapter Nine presents the main conclusions and recommendations for future work.
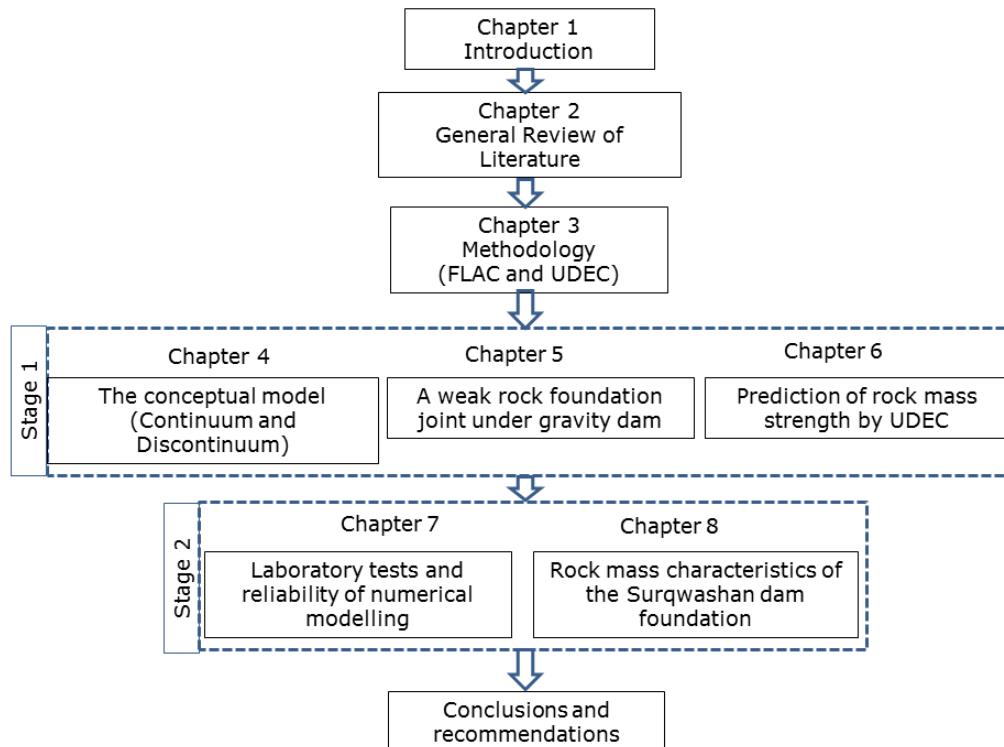
Figure 1.4 Layout of chapters of the research

Chapter 2 General Review of Literature

2.1 Introduction

A rock mass generally can be defined as an assemblage of intact rock blocks connected by discontinuities (Figure 2.1) that make the rock mass to behave like anisotropic materials under loading. One of the main aims of rock mechanics is to understand the interaction of intact rock blocks with their inherited discontinuities and to be able to predict how they will behave in response to loads acting on them, which in turn depends on their material properties (de Vallejo and Ferrer, 2011).

In the field of rock mechanics the term 'discontinuities' is used to represent all planes of weakness along which the intact rock coherence is interrupted. In recent publications this term is usually replaced by the term 'fracture' (Wittke, 2014). 'Discontinuities' classification can be based on the magnitude of shear displacement along the discontinuities. The term 'joints' is used for discontinuities if the past shear displacement along discontinuities is zero. Discontinuities, on which larger shear displacement have taken place are called 'faults' (Wittke, 2014). Figure 1.1 shows typical discontinuities of a jointed limestone rock. In this study the term 'joints' is usually used for describing all discontinuities.

The study of rock masses behaviour under dams is one of the most challenging issues in the rock mechanics field since the size of a representative model is too large for laboratory study. Attempts to model rock mass behaviour under a gravity dam in the laboratory are seldom undertaken due to the high cost, the difficulty of dealing with large models in the laboratory, the difficulty of coupling flow of water with stresses under gravity dams, and the time required.

In this study the rock mass behaviour under gravity dam was investigated taking into account different aspects. The first aspect was modelling the rock mass behaviour under gravity dam using both continuum and discontinuum models. The second aspect was simulating a large triaxial test of a jointed rock mass using UDEC so as to study rock mass behaviour under loading direction as well as to predict the equivalent strength and deformability parameters of the rock mass. Thirdly, the reliability of numerical modelling of a jointed rock mass was studied by comparing the results of an experimental work on small scale jointed rock samples with UDEC and finally, the equivalent strength and deformability parameters of a real rock mass was predicted using UDEC and rock mass classification systems. In the following sections the general literature review that relates with these aspects is provided.
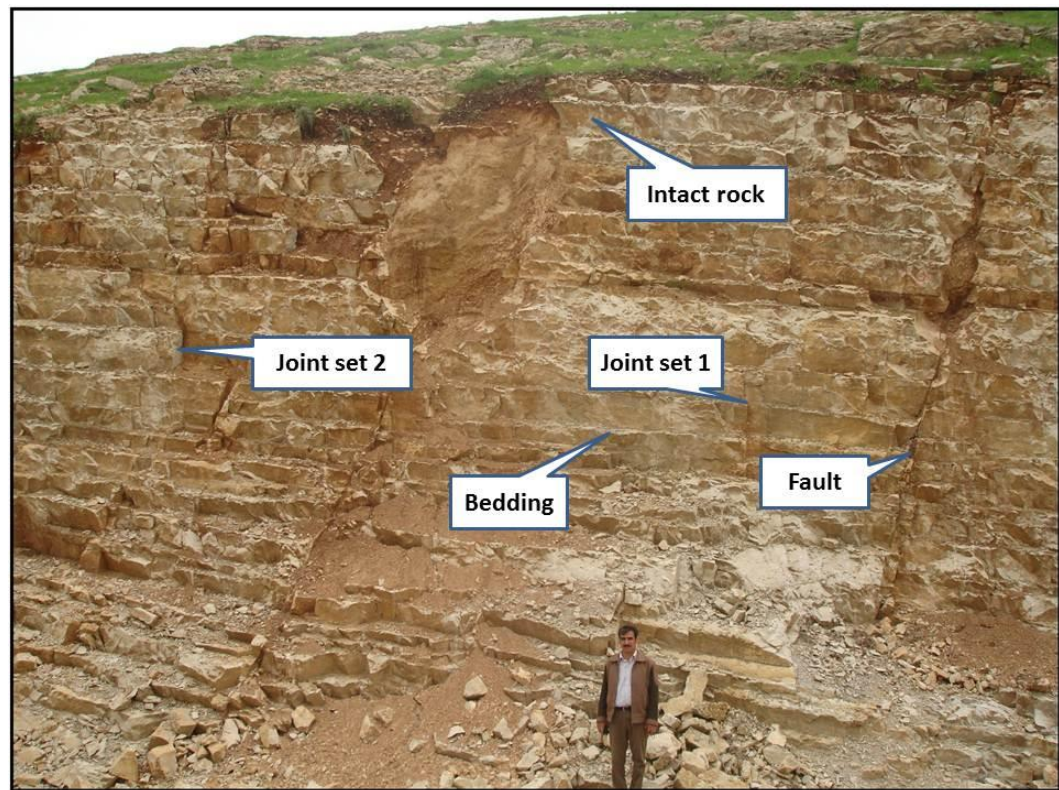
Figure 2.1 Rock mass. Blocks of limestone separated by discontinuities (Kurdistan of Iraq)

2.2   Conventional Design Method

Current dam design methods typically rely heavily on the conventional limit equilibrium analysis method. Generally, a concrete gravity dam is constructed in three stages: preparation of foundation, construction of the dam's body, and filling of the reservoir with water. After the reservoir has been filled, the water induces a lateral pressure on the upstream face of the dam that should be resisted by the shear strength of the rock in the foundation along the joint or weak layer to inhibit sliding failure (Wyllie, 1999).

The basic stability requirements for a gravity dam for all conditions of loading are (Varshney, 1982):

1 that it be safe against overturning at any horizontal plane within the structure, at the base, or at a plane below the base;

2 that it be safe against sliding on any horizontal or near-horizontal plane within the structure, at the base, or in any rock in the foundation; and

3 that the allowable unit stresses in the concrete or in the foundation material is not exceeded.

2.2.1 Overturning safety factor

The factor of safety against overturning is the first criterion used for the stability analysis of gravity dams. This method was developed during the last century, and was the only requirement to guarantee that the resultant forces due to reservoir and dam body should fall in the middle third of the dam base (Nicholson, 1983). This requirement is still in use for assessing overturning stability.

The stability of dams against overturning (F_o) can be computed as a ratio of resistant moment ($\sum M_r$) to disturbing moment ($\sum M_d$) about the toe of the dam. This ratio is known as the factor of safety against overturning, and its value must be greater than one (Equation 2.1). The overturning stability is calculated by applying all the vertical forces ($\sum N$) and lateral forces for each loading condition to the dam, then summing moments ($\sum M$) caused by the consequent forces about the

downstream toe. The resultant location along the base is shown in Equation 2.2. The vertical stress distribution can be calculated using Equations 2.3 and 2.4. The resultant locations should be within the middle third of the dam base, as shown in Figure 2.2 (USACE, 1995).

$$F_o = \frac{\sum Mr}{\sum Md)} \qquad\qquad 2.1$$

Resultant force $(R) = \frac{\sum M}{\sum N}$ \qquad\qquad 2.2
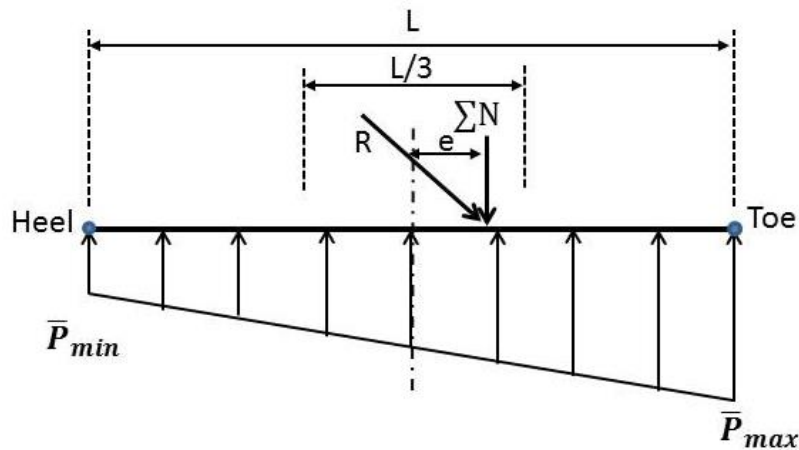
Figure 2.2 Location of resultant force within the middle third of base (e=L/6) (USACE, 1995)

$$\overline{P}_{min} = \frac{\sum N}{L}\left(1 - \frac{6e}{L}\right) \qquad\qquad 2.3$$

$$\overline{P}_{max} = \frac{\sum N}{L}\left(1 + \frac{6e}{L}\right) \qquad\qquad 2.4$$

2.2.2 Sliding stability assessment

The assessment of a dam's stability is a challenging task in engineering, rendered more complex where the dam structure is built

on blocky, weak-jointed rock, because the plane of failure is not clearly defined. The only stability criterion to assess the stability of dams was that the resultant forces due to the reservoir and dam body must be within the middle third of the dam's base. At the end of the 19th century it was noticed that dam failures often occurred by sliding along the dam foundation contact or along a weak layer within the dam's foundation. Also, it was discovered that the uplift pressure has an important effect on the stability. As a result, stability analyses that accounted for these factors began to emerge. Subsequently, different methods have been developed to assess dams' stability against sliding, specifically the sliding factor, shear friction factor and limit equilibrium methods.

2.2.2.1   Sliding factor

The sliding factor (F_s) can be calculated by dividing the sum of the horizontal forces due to reservoir load (H) by the sum of the vertical forces (N), as illustrated in Equation 2.5 (Jansen, 1988). The value of F_s should be smaller than 0.75 for usual loading condition.

$$F_s = \frac{\sum H}{\sum N - \sum U} \hspace{4cm} 2.5$$

where, $\sum N$=sum of normal forces, $\sum U$=sum of uplift forces, $\emptyset$=angle of internal friction, $\sum H$=sum of horizontal forces.

This method calculates a mobilized coefficient of friction, which should be smaller than the allowable coefficient of friction. This method was

used until the 1930s to assess the sliding stability of gravity dam. Figure 2.3 shows the assumed horizontal sliding plane with parameters used for calculating F_s.
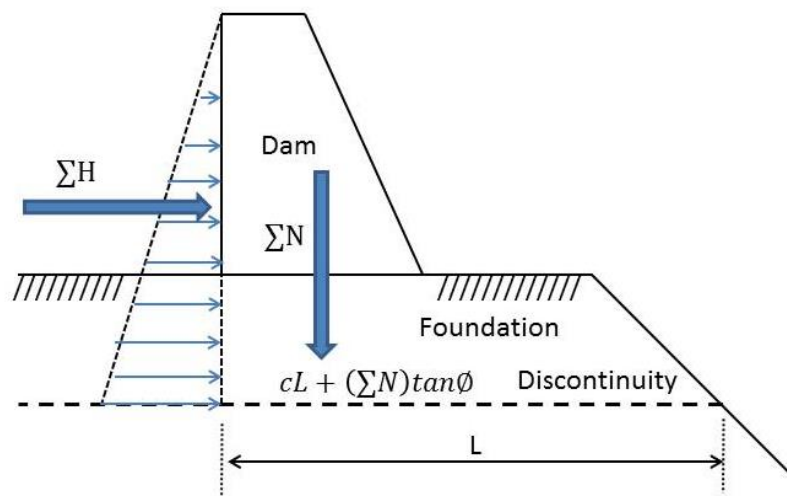
Figure 2.3 A sliding plane in the dam's foundation (Underwood and Dixon, 1977)

2.2.2.2   The shear friction factor

The shear friction factor was introduced by Henny (1933, cited in Nicholson (1983)) based on the Coulomb equation. Henny's basic equation for calculating the factor of safety was:

$$Q = \frac{S}{P} \hspace{6cm} 2.6$$

In which Q was the factor of safety of shear; S the total shear strength resistance along the sliding plane; P the water pressure acting parallel to sliding plane.

The total resistance shear strength, S, was defined by the following equation:

$$S = S_1 + k(W - U)$$ 2.7

In which S_1 was the total shear strength at zero normal stress; k was the factor of shear strength increase; W was the weight of the structure above an assumed sliding plane; and U is uplift force under sliding plane.

An updated version of Equation 2.7 can be written thus:

Shear resistance force (S)$= cA + (\sum N - \sum U)\tan\emptyset$ 2.8

Where c is cohesion of the sliding plane, A is the contact area of the sliding plane, $\sum N$ is the summation of normal forces, $\sum U$ is the summation of uplift forces and $\emptyset$ is the angle of friction of sliding plane.

Now shear friction factor (F_{SF}) can be defined as the ratio between total resistance to shear (S) and sliding to the horizontal load $(\sum H)$, as shown in Equation 2.9:

$$F_{SF} = \frac{cA + (\sum N - \sum U)\tan\emptyset + P_p}{\sum H}$$ 2.9

Where P_p is the maximum passive resistance force of the rock wedge at toe in the downstream direction.

The Corps of Engineers in the USA expanded the shear friction factor of safety to include sloped sliding planes and embedment toe

resistance. The expanded factor of safety for sliding plane dipping upstream (Figure 2.4) at an angle α can be as in Equation 2.10:

$$F_{SF} = \frac{\frac{cA_S}{\cos \alpha_S (1 - \tan \alpha_S \tan \emptyset)} + \sum N \tan(\emptyset + \alpha_S) + P_p}{\sum H} \qquad 2.10$$

where $A_S = L_S * 1$ for plane strain condition.
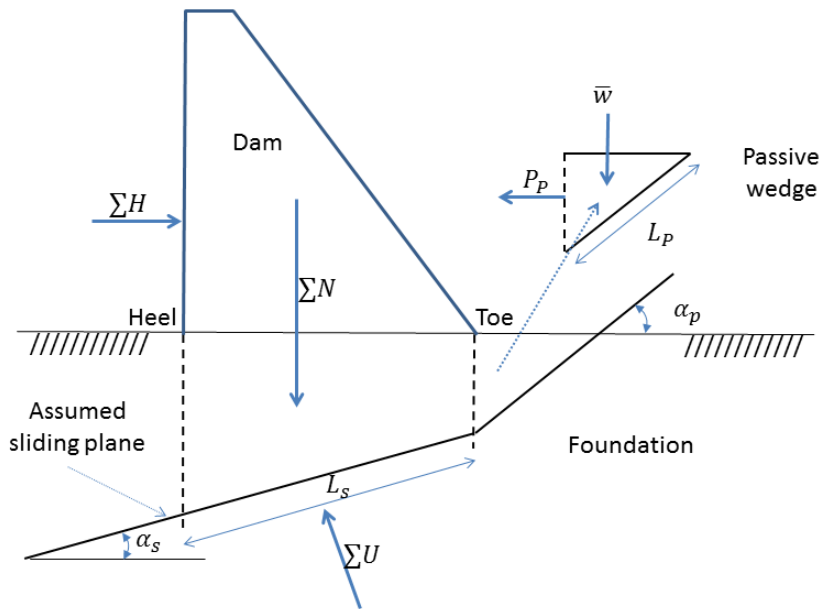
Figure 2.4 Forces acting on a hypothetical dam with inclined sliding planes according to the shear friction method (Nicholson, 1983)

If the sliding plane is dipping downstream, the shear friction factor can be written as:

$$F_{SF} = \frac{\frac{cA_S}{\cos \alpha_S (1 + \tan \alpha_S \tan \emptyset)} + \sum N \tan(\emptyset - \alpha_S) + P_p}{\sum H} \qquad 2.11$$

where $A_S = L_S * 1$ for plane strain condition.

The equation for P_p can be calculated as:

$$P_p = \frac{cA_p}{\cos \alpha_p (1 - \tan \alpha_p \tan \emptyset)} + \sum N \tan(\emptyset + \alpha_p) \qquad 2.12$$

where $A_p = L_P * 1$ for plane strain condition

2.2.2.3 Limit equilibrium method

The shear friction concept was replaced by limit equilibrium method in a Department of the Army Engineering Technical Letter (ETL) 1110-2-256 (Department of the Army office, Chief of Engineer 1981) (U.S. Army Corps of Engineers, 1981). However, the shear friction factor is still in use by other agencies.

Based on the limit equilibrium, the stability of a concrete gravity dam along the rock foundation interfaces between the rock foundation and the dam or along a weak joint in the foundation rock mass can be calculated by dividing the resistance shear strength by the driving shear stress along the surface plane as presented in Equation 2.13. This ratio has been defined as a factor of safety against sliding:

$$\boldsymbol{F_{LE}} = \frac{\tau_f}{\tau} = \frac{cA + (\sum N - \sum U)\boldsymbol{tan\emptyset}}{\sum H} \qquad 2.13$$

where τ_f is the available maximum shear strength, τ is the applied shear stress, c=cohesion, A=contact area between the dam and the foundation, $\sum N$=summation of normal forces, $\sum U$=summation of uplift forces, $\emptyset$=Angle of internal friction, and $\sum H$=summation of shear forces.

According to Nicholson (1983), the basic assumptions required to develop the stability equations for the limit equilibrium method are as follows:

1. The factor of safety is defined according to Equation 2.13.

2. Impending failure occurs according to the requirements imposed by perfectly-plastic failure theory.

3. The maximum shear strength that can be mobilized is adequately defined by the Mohr-Coulomb failure criteria.

4. Failure modes can be represented by two-dimensional, kinematically possible planes.

5. The factor of safety computed from the stability equations is the average factor of safety for the total potential failure surface.

6. The vertical forces between wedges are assumed to be negligible.

7. The structural wedge must be defined by one wedge.

The limit equilibrium factor can also be used for calculating the safety factor against sliding of dipped sliding planes. For sliding plane dipping upstream the following equation can be used:

$$F_{LE} = \frac{CA_S + (\Sigma V \cos \alpha_S + \Sigma H \sin \alpha_S) \tan \varphi}{\Sigma H \cos \alpha_S - \Sigma V \sin \alpha_S} \qquad \text{2.14}$$

When a sliding plane is dipping downstream the factor can be calculated by:

$$F_{LE} = \frac{CA_S + (\Sigma V \cos\alpha_S - \Sigma H \sin\alpha_S)\tan\varphi}{\Sigma H \cos\alpha_S + \Sigma V \sin\alpha_S}$$

2.15

Snell and Knight (1991) used a generalized theoretical model to study the influence of faults dipping upstream within ranges from 0-25 degrees of dip under two types of dams: rockfill and a typical concrete gravity dam. They used the limit equilibrium method to calculate the factor of safety against sliding along the stratum or weak layer. They showed that the possibility of failure due to sliding along these strata should not be ignored.

2.3 Equivalent Mechanical Parameters.

For the safe and economical design of dams constructed on jointed rock, a reliable estimation of the strength and deformation properties of the foundation rock is required. In recent years, the use of numerical modelling tools, such as the continuum-based Finite Element (FE) and Finite Difference (FD) methods, and the discontinuum Discrete Element Method (DEM), have become increasingly popular for the analysis and design of dams.

For these models, the required deformation modulus of the rock mass is generally based on rock mass classification systems which were developed mainly for tunnelling and mining purposes. These include the Rock Quality Designation (RQD) (Deere and Deere, 1989), the Rock Mass Rating (RMR) (Bieniawski and Orr, 1976) the Tunnelling Quality Index (Q) (Barton et al., 1974), the Geological Strength Index (GSI)

(Hoek, 1994), or from empirical equations which were developed based on Uniaxial Compressive Strength (UCS) tests (Ramamurthy and Arora, 1992; Ramamurthy et al., 1993; Zhang and Einstein, 2004). These researchers developed empirical equations to find the deformation modulus and unconfined strength of a rock mass. However, for cohesionless jointed rock, at specific joint orientations, the rock mass behaves like a granular material and, therefore, an unconfined test of rock masses may not be a good choice. Many researchers have attempted to compute the unconfined compressive strength based on empirical equations mentioned above such as Edelbro et al. (2007) and Zhang (2010). Also some researchers have used the Hoek cell to study jointed rock behaviour under varying confining pressures, such as Asef and Reddish (2002). However the Hoek cell may not give reasonable results for jointed rock samples especially when the failure mode is slippage along joints since the Hoek cell was designed to study intact rock sample behaviour under compression. This will be shown in chapter 7.

The direct in-situ measurement of the mechanical properties of rock mass is very expensive and time consuming (Zhang, 2005; Zhang and Einstein, 2004). Attempts to characterise large-scale rock mass properties in the laboratory are seldom undertaken due to the high cost, the difficulty of dealing with large samples in the laboratory, and the time required (Hoek, 1983). The maximum size of tested samples

quoted in the literature is 60cm × 60cm × 130cm (Reik and Zacas, 1978). Other physical models developed to simulate rock mass in the laboratory have been smaller: [e.g. 30cm × 12.5 cm × 8.6cm (Kulatilake et al., 2001a) and 15cm × 15cm × 8cm (Singh and Singh, 2008b)]. These physical models might not represent reality accurately since the block sizes have an effect on the rock matrix stiffness and strength (Bhasin and Høeg, 1998; Edelbro et al., 2007). The mechanical properties of intact rock and discontinuities can be determined in the laboratory by triaxial and direct shear methods. However, the in-situ interaction between intact rock blocks with discontinuities is very complex and it is generally not adequate to simply use un-modified laboratory-based measurements of rock properties within models which try to capture the global rock mass behaviour.

Numerical modelling provides a method that can help understand how laboratory-based measurements of rock properties relate to full-scale predictions of rock mass behaviour. Recently, Noorian Bidgoli et al. (2013) used UDEC to predict the strength parameter of a rock mass model. However, they did not validate their finding with an analytical solution and they did not fully discuss the post failure behaviour. Noorian Bidgoli and Jing (2014a) extended the study of (Noorian Bidgoli et al., 2013) by changing the direction of loading on a rock mass so as to study the anisotropy of strength. Again, they did not

validate their findings and they did not discuss the post failure behaviour with modes of failures.

Up to the present time, numerical modelling is the best method to study the rock mass behaviour. But, it should be mentioned that the input to the numerical modelling is very important and element of rock mass testing (UCS, triaxial, direct shear) provides this input. Incorrect element testing can lead to misleading numerical modelling results as will be presented in this study.

2.4 Available Rock Mass Classification System

The rock mass is made up of intact rock blocks with various geological discontinuities among them, and so the mechanical properties of both intact substance and the discontinuities must be taken into account in any rock classification system. Rock classification systems are used in order to predict the equivalent strength and deformability parameters of rock masses.

There are many rock mass classification systems developed mainly for tunnelling and mining purposes. These include the Rock Quality Designation index (RQD) (Deere and Deere, 1989), the Rock Mass Rating (RMR) (Bieniawski and Orr, 1976), the Tunnelling Quality Index (Q) (Barton et al., 1974) and the Geological Strength Index (GSI) (Hoek, 1994; Hoek and Brown, 1997; Hoek et al., 1995; Marinos and Hoek, 2001). The only classification system that gives information for

gravity dams is RMR by Bieniawski and Orr (1976), which was later modified by Romana et al. (2003) for assessing the safety of old dams. However, there is still scope for developing a more efficient rock classification system for dam design.

2.4.1 Rock Quality Designation (RQD)

In 1964 Deere (Deere and Deere, 1989) introduced the RQD as an index for assessing the quality of borehole rock core. This index can be defined as the ratio (in percent) between sums of solid pieces of core of 100mm or longer to the total length of the core run.

$$RQD = \frac{\text{Sum of cores} \geq 100mm}{\text{total drill run}} * 100\% \qquad\qquad 2.16$$

Table 2.1 shows the relationship between RQD and engineering quality of rock mass. Figure 2.5 shows the procedure for calculating RQD

This index is one of the simplest methods that has extensively been used by geologists for core logging, however, it is not sufficient on its own to provide an adequate description of rock (Bieniawski and Orr, 1976).

Table 2.1 Correlation between RQD and rock quality (Deere and Deere, 1989)

RQD (%)	Rock quality
<25	Very poor
25-50	Poor
50-75	Fair
75-90	Good
90-100	Excellent
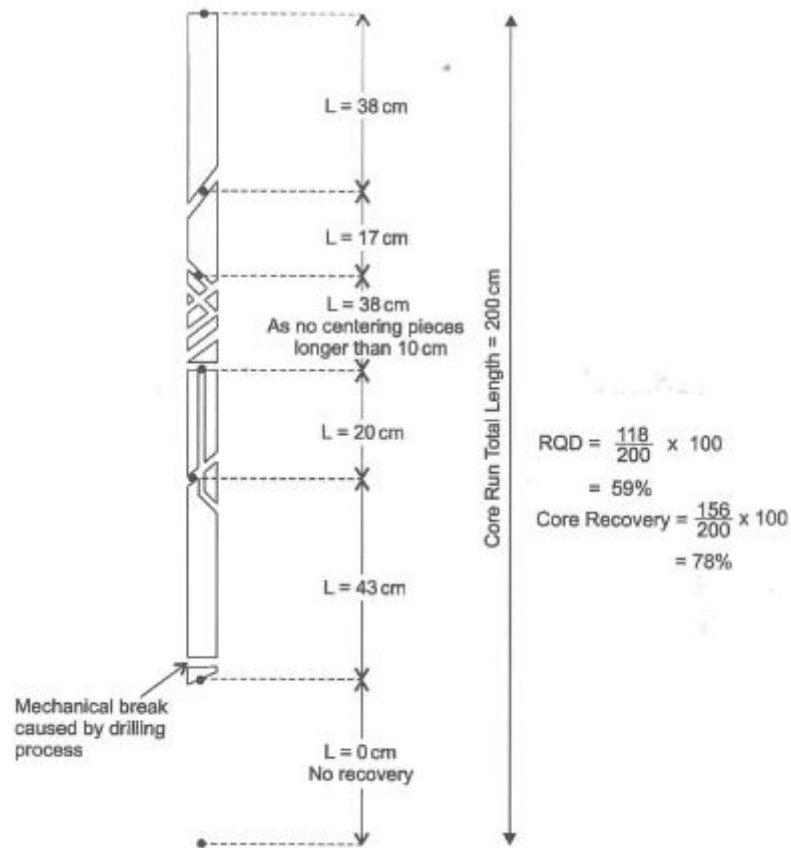
Figure 2.5 Computation of rock quality designation (RQD)
(Deere and Deere, 1989)

2.4.2 Rock Mass Rating (RMR)

RMR was initially developed by Bieniawski (1973) when he was working at the South African Council of Scientific and Industrial Research (CSIR) on his experience in shallow tunnels in sedimentary rocks (Kaiser et al., 1986). Over the years this classification has been modified: in 1974, the classification parameters were reduced from eight to six; in 1975, the ratings were adjusted; in 1976 the assessment of stability of dam was added to the system according to

the dip angle of the main joint set; and in 1979 ISRM (1978) rock mass description was adopted. Hence it is important to state which version is used when RMR values are estimated. This classification combines several factors, as listed below:

1. Uniaxial compression strength of intact rock (UCS).

2. The rock quality designation index (RQD).

3. Spacing of discontinuities.

4. Condition of discontinuities.

5. Ground water conditions.

6. Orientation of discontinuities.

The above parameters can be measured in the field, including the UCS, which can be predicted by the point load test on drill core. The RMR system or the Geomechanics Classification for rock masses is presented in Table 2.2. Different ratings are assigned to each parameter according to its degree of importance. The sum of ratings of the first five parameters in part A in Table 2.2 is called basic RMR. This basic RMR is adjusted in order to predict the final RMR value according to the joints' orientation by using part B of Table 2.2. The quality of rock mass can be determined from part C of Table 2.2. Finally, the equivalent strength parameters can be predicted using the final RMR in part D in Table 2.2. It should be noted that this classification system is most relevant to tunnel and slope stability problems.

Table 2.2 The input parameters used in RMR_1989 classification system (Palmström, 2009)

A. Classification parameters and their ratings in the RMR system

	PARAMETER		Range of values // RATINGS						
1	Strength of intact rock material	Point-load strength index	> 10 MPa	4 - 10 MPa	2 - 4 MPa	1 - 2 MPa	For this low range, uniaxial compr. strength is preferred		
		Uniaxial compressive strength	> 250 MPa	100 - 250 MPa	50 - 100 MPa	25 - 50 MPa	5 - 25 MPa	1 - 5 MPa	< 1 MPa
		RATING	15	12	7	4	2	1	0
2	Drill core quality RQD		90 - 100%	75 - 90%	50 - 75%	25 - 50%	< 25%		
	RATING		20	17	13	8	5		
3	Spacing of discontinuities		> 2 m	0.6 - 2 m	200 - 600 mm	60 - 200 mm	< 60 mm		
	RATING		20	15	10	8	5		
4	Condition of discontinuities	a. Length, persistence	< 1 m	1 - 3 m	3 - 10 m	10 - 20 m	> 20 m		
		Rating	6	4	2	1	0		
		b. Separation	none	< 0.1 mm	0.1 - 1 mm	1 - 5 mm	> 5 mm		
		Rating	6	5	4	1	0		
		c. Roughness	very rough	rough	slightly rough	smooth	slickensided		
		Rating	6	5	3	1	0		
		d. Infilling (gouge)	none	Hard filling		Soft filling			
			–	< 5 mm	> 5 mm	< 5 mm	> 5 mm		
		Rating	6	4	2	2	0		
		e. Weathering	unweathered	slightly w.	moderately w.	highly w.	decomposed		
		Rating	6	5	3	1	0		
5	Ground water	Inflow per 10 m tunnel length	none	< 10 litres/min	10 - 25 litres/min	25 - 125 litres/min	> 125 litres /min		
		$p_w / \sigma 1$	0	0 - 0.1	0.1 - 0.2	0.2 - 0.5	> 0.5		
		General conditions	completely dry	damp	wet	dripping	flowing		
	RATING		15	10	7	4	0		

p_w = joint water pressure; $\sigma 1$ = major principal stress

B. RMR rating adjustment for discontinuity orientations

		Very favourable	Favourable	Fair	Unfavourable	Very unfavourable
RATINGS	Tunnels	0	-2	-5	-10	-12
	Foundations	0	-2	-7	-15	-25
	Slopes	0	-5	-25	-50	-60

C. Rock mass classes determined from total RMR ratings

Rating	100 - 81	80 - 61	60 - 41	40 - 21	< 20
Class No.	I	II	III	IV	V
Description	VERY GOOD	GOOD	FAIR	POOR	VERY POOR

D. Meaning of ground classes

Class No.	I	II	III	IV	V
Average stand-up time	10 years for 15 m span	6 months for 8 m span	1 week for 5 m span	10 hours for 2.5 m span	30 minutes for 1 m span
Cohesion of the rock mass	> 400 kPa	300 - 400 kPa	200 - 300 kPa	100 - 200 kPa	< 100 kPa
Friction angle of the rock mass	< 45°	35 - 45°	25 - 35°	15 - 25°	< 15°

For adjusting the basic RMR for dam foundations, Bieniawski and Orr (1976) proposed Table 2.3 to assess the stability of dams according to the dip angle of the main joint set. Table 2.3 was based on experience and on the stress distribution in foundation rock masses (Gaziev and

Erlikham, 1971) as well as on an assumption that both the arch and the gravity effects were present in a dam structure. This table should be used with caution, as indicated within the original text (Bieniawski and Orr, 1976): "*this table is tentative only and represents a simplification of a problem which is justified for rock mass classification purposes only*." Since publication of this paper in 1976, there has been very little work published to prove the reliability of the factors presented in Table 2.3. Also, this table is not reproduced in the RMR system version published in 1989 (Bieniawski, 1989).

Table 2.3 Adjusting factors for dam foundation and stability assessment (Bieniawski and Orr, 1976)

Joint Information	Dip 0-10	Dip 10 - 30		Dip 30 - 60	Dip 60-90
		Dip Direction			
		Upstream	Downstream		
Assessment	**VF**	**U**	**FA**	**F**	**VU**
Rating	0	-15	-7	-2	-25

Note: VF is Very favourable, U is Unfavourable, FA is fair, F is favourable and VU is Very Unfavourable.

Snell and Knight (1991) systematically studied the problem of dam stability, taking into account all of the forces and stresses acting on the dam by using the limit equilibrium method. Based on their study, Romana (2003) proposed a new set of adjusting factors, as shown in Table 2.4.

Table 2.4 Adjusting factors for the dam stability (RSTA)
(Romana, 2003)

Type of Dam	VF	F	FA	U	VU
Fill	Others	10-30 DS	0-10 A	-	-
Gravity	10-60 DS	30-60 US 60-90 A	10-30 US	0-10 A	-
Arch	30-60 DS	10-30 DS	30-60 US 60-90 A	10-30 US	0-10 A
R_{STA}	0	-2	-7	-15	-25

Note: DS is Dip Downstream, US is Dip Upstream, and A is any direction.
Other notation as in Table 2.3.

The deformation modulus (E_{rm}) of rock masses can be obtained by using the following correlation developed by Bieniawski (1978) for RMR greater than 50:

$$E_{rm} = 2\,RMR - 100 \quad \text{(in GPa)} \qquad 2.17$$

Serafim and Pereira (1983) developed the above equation so that it can be generally used for estimating the deformation modulus of rock masses as in the following equation:

$$E_{rm} = 10^{\frac{(RMR-10)}{40}} \qquad \text{(in GPa)} \qquad 2.18$$

2.4.3 Geological Strength Index (GSI)

Since publication of the RMR in 1974, it has gained popularity within the rock mechanics field because the system is simple to use, and classification parameters can easily be obtained from the field (Bieniawski, 1989). However, by 1995 it was recognized by researchers that the Bieniawski RMR was difficult to apply to very weak rock masses (Hoek and Marinos, 2007). Also, it was felt a system based more deeply on fundamental geological observations

and less on 'numbers' was needed. This resulted in the development of the GSI (Hoek and Marinos, 2007).

The GSI was introduced by Hoek (1994) and Hoek et al. (1995) as a replacement for Bieniawski's RMR so that it can be used as an input data for the Hoek-Brown criterion (see Eq. 2.19). It provides a system that can be used for estimating the reduction in rock mass strength for different geological conditions. Table 2.5 and Table 2.6 present this system. Table 2.5 provides the deformability and strength parameters for each rock mass category by using field observation data. Table 2.6 shows the estimation of GSI that was used in a software program called 'RocLab' that was downloaded (free) from http://www.rocscience.com (Hoek et al., 2002).

$$\sigma_1' = \sigma_3' + \sigma_{ci}\left(m_b\frac{\sigma_3'}{\sigma_{ci}} + s\right)^a \qquad\qquad 2.19$$

where m_b ,s, and a are constants for the rock mass.

Table 2.5 Characterisation of undisturbed rock masses (Hoek et al., 1995)

GENERALISED HOEK-BROWN CRITERION

$$\sigma_1' = \sigma_3' + \sigma_c \left(m_b \frac{\sigma_3'}{\sigma_c} + s \right)^a$$

σ_1' = major principal effective stress at failure

σ_3' = minor principal effective stress at failure

σ_c = uniaxial compressive strength of *intact* pieces of rock

m_b , s and a are constants which depend on the composition, structure and surface conditions of the rock mass

STRUCTURE	SURFACE CONDITION	VERY GOOD — Very rough, unweathered surfaces	GOOD — Rough, slightly weathered, iron stained surfaces	FAIR — Smooth, moderately weathered or altered surfaces	POOR — Slickensided, highly weathered surfaces with compact coatings or fillings containing angular rock fragments	VERY POOR — Slickensided, highly weathered surfaces with soft clay coatings or fillings
BLOCKY - very well interlocked undisturbed rock mass consisting of cubical blocks formed by three orthogonal discontinuity sets	m_b/m_i s a E_m ν GSI	0.60 0.190 0.5 75,000 0.2 85	0.40 0.062 0.5 40,000 0.2 75	0.26 0.015 0.5 20,000 0.25 62	0.16 0.003 0.5 9,000 0.25 48	0.08 0.0004 0.5 3,000 0.25 34
VERY BLOCKY - interlocked, par-tially disturbed rock mass with multifaceted angular blocks formed by four or more discontinuity sets	m_b/m_i s a E_m ν GSI	0.40 0.062 0.5 40,000 0.2 75	0.29 0.021 0.5 24,000 0.25 65	0.16 0.003 0.5 9,000 0.25 48	0.11 0.001 0.5 5,000 0.25 38	0.07 0 0.53 2,500 0.3 25
BLOCKY/SEAMY - folded and faulted with many intersecting discontinuities forming angular blocks	m_b/m_i s a E_m ν GSI	0.24 0.012 0.5 18,000 0.25 60	0.17 0.004 0.5 10,000 0.25 50	0.12 0.001 0.5 6,000 0.25 40	0.08 0 0.5 3,000 0.3 30	0.06 0 0.55 2,000 0.3 20
CRUSHED - poorly interlocked, heavily broken rock mass with a mixture of angular and rounded blocks	m_b/m_i s a E_m ν GSI	0.17 0.004 0.5 10,000 0.25 50	0.12 0.001 0.5 6,000 0.25 40	0.08 0 0.5 3,000 0.3 30	0.06 0 0.55 2,000 0.3 20	0.04 0 0.60 1,000 0.3 10

Table 2.6 Estimate of GSI based on geological descriptions from program 'RocLab' (Hoek et al., 2002).

	SURFACE CONDITIONS				
	VERY GOOD	GOOD	FAIR	POOR	VERY POOR
STRUCTURE	DECREASING SURFACE QUALITY ⟹				
INTACT OR MASSIVE - intact rock specimens or massive in situ rock with few widely spaced discontinuities	90			N/A	N/A
BLOCKY - well interlocked un-disturbed rock mass consisting of cubical blocks formed by three intersecting discontinuity sets		70			
VERY BLOCKY- interlocked, partially disturbed mass with multi-faceted angular blocks formed by 4 or more joint sets			50		
BLOCKY/DISTURBED/SEAMY - folded with angular blocks formed by many intersecting discontinuity sets. Persistence of bedding planes or schistosity					
DISINTEGRATED - poorly inter-locked, heavily broken rock mass with mixture of angular and rounded rock pieces				20	
LAMINATED/SHEARED - Lack of blockiness due to close spacing of weak schistosity or shear planes	N/A	N/A			10

DECREASING INTERLOCKING OF ROCK PIECES — values shown in grid: 80, 60, 40, 30

Once the GSI has been predicted, the strength parameter for generalised Hoek-Brown criterion (Hoek et al., 1992) can be calculated as follows:

$$m_b = m_i \, exp\left(\frac{GSI-100}{28-14D}\right) \qquad\qquad\qquad 2.20$$

$$s = exp\left(\frac{GSI-100}{9-3D}\right) \qquad\qquad\qquad\qquad 2.21$$

$$a = 0.5 + \frac{1}{6}\left(e^{\frac{-GSI}{15}} - e^{\frac{-20}{3}}\right) \qquad\qquad\qquad 2.22$$

in which D is the factor of disturbance and can be estimated from Table 2.7.

For the rock masses of good to reasonable quality, the GSI should be greater than 25 and in this case 'a' in Eq. 2.22 approaches 0.5.

For rock masses of very poor quality, the GSI should be smaller than 25 and the value of 's' in Eq.2.21 set to zero.

The equivalent deformation modulus of a rock mass can be calculated by:

$$E_{rm}(GPa) = \left(1 - \frac{D}{2}\right)\sqrt{\frac{\sigma_{ci}}{100}} \cdot 10^{\frac{(GSI-10)}{40}} \qquad\qquad 2.23$$

$$E_{rm}(GPa) = \left(1 - \frac{D}{2}\right) \cdot 10^{\frac{(GSI-10)}{40}} \qquad\qquad 2.24$$

Eq.2.23 applies for $\sigma_{ci} \leq 100$ MPa otherwise Equation 2.24 is used.

Hoek and Diederichs (2006) proposed two new relations (Eq. 2.25a and Eq.2.25b) using a sigmoid function to estimate the deformation modulus of a rock mass, based on several empirical equations proposed by other researchers. These equations were developed after an analysis of in-situ deformation moduli for a wide range of rock masses from China and Taiwan. Equation 2.25a can be used where only GSI data are available, whereas Equation 2.25b can be used where reliable value of the intact rock modulus and GSI data are available. It should be noted that these equations are universally applicable for isotropic rock masses.

$$E_{rm}(MPa) = 100,000 \left(\frac{1-\frac{D}{2}}{1+e^{((75+25D-GSI)/11)}} \right)$$ 2.25a

$$E_{rm} = E_i \left(0.02 + \frac{1-\frac{D}{2}}{1+e^{((60+15D-GSI)/11)}} \right)$$ 2.25b

Because the Mohr-Coulomb criterion is still widely used by researchers in the rock mechanics field, and most geotechnical software is written in terms of Mohr-Coulomb criterion, the equivalent angles of friction and cohesive strength for each rock mass and stress range can be predicted by fitting an average linear relationship to the curve produced by Eq. 2.19 for a range of minor principal stress values defined by $\sigma_1 < \sigma_3 < \sigma_{3\,max}$ (Hoek et al., 2002), as shown in Figure 2.6. For general failure envelope range, $\sigma_{3\,max}$ is equal to quarter of uniaxial compression strength (UCS).

The tensile strength is calculated by:

$$\sigma_t = -\frac{s\,\sigma_{ci}}{m_b}$$ 2.26

The Hoek-Brown criterion and the equivalent Mohr-Coulomb criterion have been implemented in the software program 'RocLab'. This code includes charts and tables for estimating the Hoek-Brown parameters as well as the equivalent Mohr-Coulomb parameters, and the GSI value.
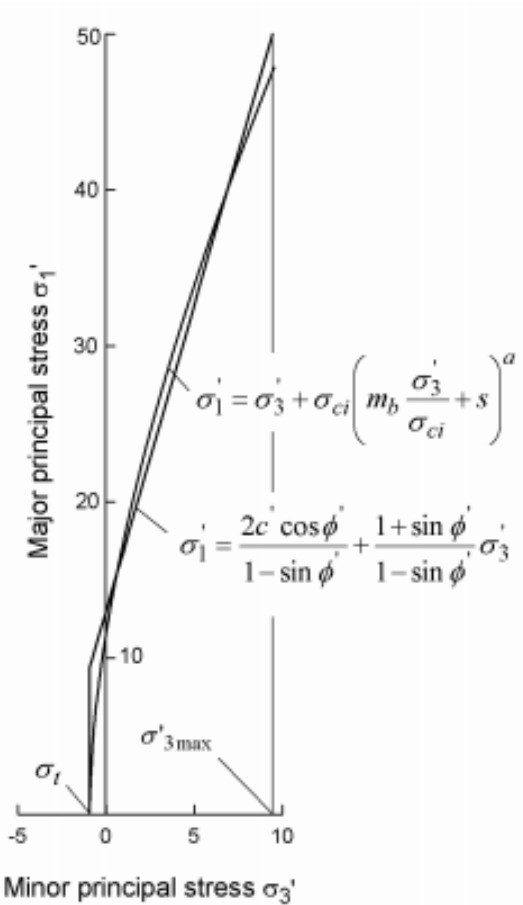
Figure 2.6 Relationships between major and minor principal stresses for Hoek-Brown and equivalent Mohr-Coulomb criteria (Hoek et al., 2002).

Table 2.7 Guidelines for estimating disturbance factor D (Hoek et al., 2002)

Appearance of rock mass	Description of rock mass	Suggested value of D
	Excellent quality controlled blasting or excavation by Tunnel Boring Machine results in minimal disturbance to the confined rock mass surrounding a tunnel.	$D = 0$
	Mechanical or hand excavation in poor quality rock masses (no blasting) results in minimal disturbance to the surrounding rock mass. Where squeezing problems result in significant floor heave, disturbance can be severe unless a temporary invert, as shown in the photograph, is placed.	$D = 0$ $D = 0.5$ No invert
	Very poor quality blasting in a hard rock tunnel results in severe local damage, extending 2 or 3 m, in the surrounding rock mass.	$D = 0.8$
	Small scale blasting in civil engineering slopes results in modest rock mass damage, particularly if controlled blasting is used as shown on the left hand side of the photograph. However, stress relief results in some disturbance.	$D = 0.7$ Good blasting $D = 1.0$ Poor blasting
	Very large open pit mine slopes suffer significant disturbance due to heavy production blasting and also due to stress relief from overburden removal. In some softer rocks excavation can be carried out by ripping and dozing and the degree of damage to the slopes is less.	$D = 1.0$ Production blasting $D = 0.7$ Mechanical excavation

2.5 Previous Work of Gravity Dams on a Jointed Rock Mass

In this section previous research related to gravity dams on a jointed rock mass is given. In the present time there are two main methods that can be used to study the behaviour of a dam: physical and numerical modelling.

2.5.1 Physical modelling

Zhu et al. (2010) studied sliding in the foundation of a gravity dam using a physical model (Figure 2.7). It was found that the horizontal displacement at the heel and toe indicate dam stability condition. Also, it was concluded that if there is enough bonding between the dam and the foundation, the sliding failure develops within the rock mass. Figure 2.8 shows the development of a tension crack due to reservoir load. However they could not couple the stresses with the flow of water. This is one of the disadvantages of this example of physical modelling of gravity dams on rock mass. Also, the effect of joint orientation was not considered.
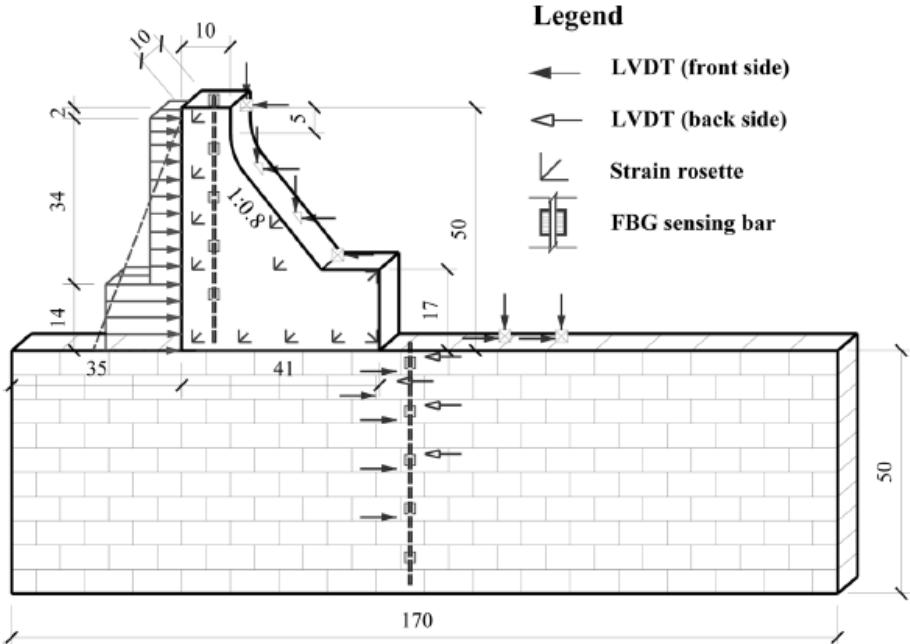
Figure 2.7 Model dimensions and instrumentation set-up (all dimensions in cm) (Zhu et al., 2010).
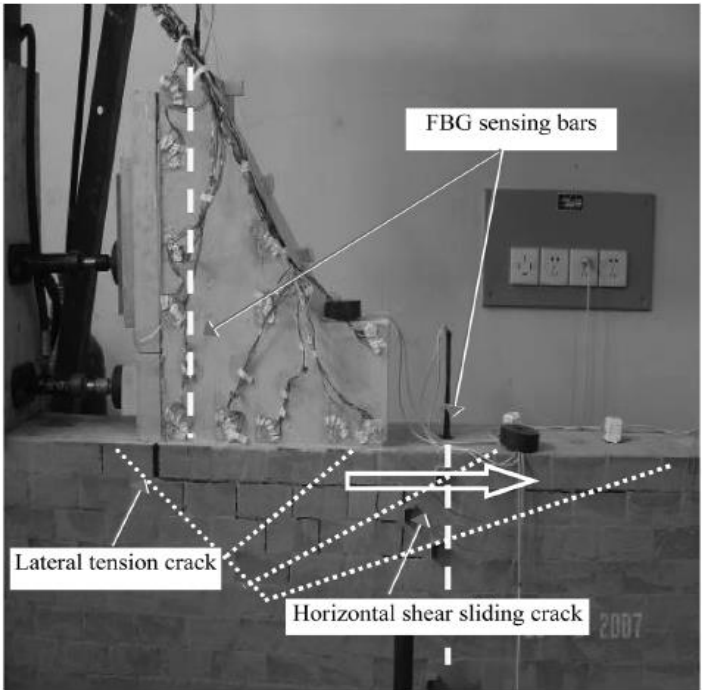
Figure 2.8 Photograph of sliding failure of the model dam (Zhu et al., 2010)

Fishman (2009) discussed the stability factor in terms of sliding, overturning and limit turning; he concluded that sliding is only possible in specific cases where weakened joints appear near the interface between the structure and the foundation. Also, the results of classical overturning analysis are unrealistic, and this failure is not possible. The limit turning mode proposed by him involves partial turning of the structure, and is accompanied by downstream crushing and upstream rupture of the foundation. The failure mechanism is shown in Figure 2.9.
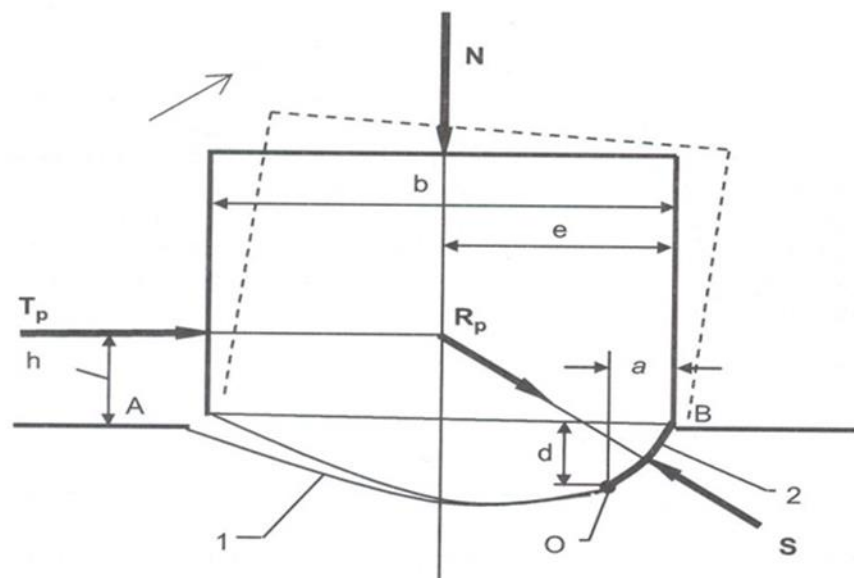
Figure 2.9 Failure of block- foundation model (Fishman, 2009).

Rp is resultant force at limit state; S is force of crushing resistance; O is turn axis ; '1' is tensile cracks; '2' is compressive crack. Displacement scale is 10:1 in relation to block scale.

Jian Liu (2003b) Part I observed that there are many unavoidable limitations in physical and numerical modelling approaches, and there is no universally acceptable approach to analyse the problem perfectly. This is why physical models are still integral to dam studies, as in the stability assessment of the Three Gorges Dam foundations in China (Figure 2.10). Based on the geological investigation and mechanical tests, various physical models were built in 2D and 3D for some critical dam sections. Special materials were used to simulate the dam foundation system. The overloading technique was used to bring the model to failure. In this method the factor of safety can be defined as 'the ratio between the maximum external load inducing the part of sliding of the dam foundation and the upstream hydrostatic load' (Jian Liu, 2003b). The results showed that the foundation of no. 3 (Figure 2.10) powerhouse-dam section is the most critical with regard to stability against sliding failure. Again, the effect of rock joints on dam stability was not addressed; it is difficult to model the jointed rock foundation under dams using physical modelling. Hence, the alternative method of numerical modelling was adopted in this research study.
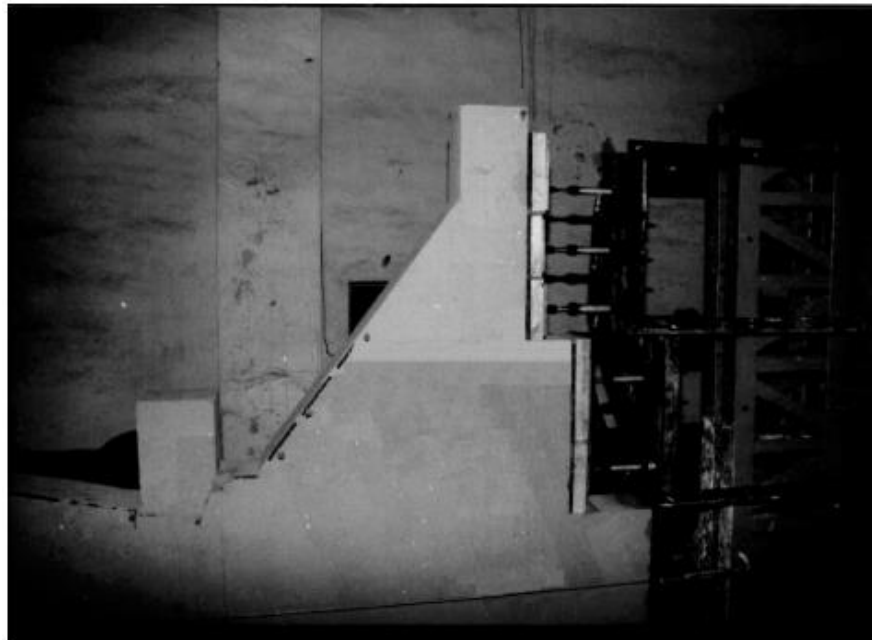
**Figure 2.10 Loading apparatus for the physical model tests
(Jian Liu, 2003b)**

2.5.2 Numerical modelling

Varshney (1972) studied the effect of seams of weaker rock and faults
on the stress distribution in a concrete gravity dam using FEM (Table
2.8). He utilized a vertical fault at the heel, toe, and the centre of the
dam base. He showed that the location and orientation of the weak
layer affects the stress arrangement in a dam to a great extent.
However, the effect of variations in the dip angle and fault location
(both upstream and downstream from the dam) were not considered
in his paper. Singh and Varshney (1974) utilized the finite element
method to study the influence of faults with dip angles of 0, 45, and -
45 degrees on the behaviour of a concrete gravity dam. In addition,

they used a fault at the heel, mid-base, and at toe to determine which

joint location and dip angle have the greatest effect on the dam

behaviour. They concluded that faults located at the toe should be

avoided especially when dipping upstream at a 45 degree angle.

However, only one fault inclination with a dip angle of 45 degrees was

studied in both upstream and downstream directions

Table 2.8 Effect of fault location and orientation on stress distribution in semi-infinite plane (Varshney, 1972)

Fault location and orientation	Effect on the distribution of			
	σ_x	σ_y	σ_{xy}	σ_1
1. Vertical fault at u.s. heel	Tensile zone u.s. of dam and compressive zone d.s. of dam	De-stressing u.s. of fault, stresses increase d.s.	Not much change than in normal foundation	De-stressing u.s. of fault; stresses increase d.s.
2. Central fault inclined upstream at an angle of 45°	,,	,,	,,	,,
3. Centrally located vertical fault	,,	,,	,,	,,
4. Central fault inclined d.s. at an angle of 45°	Tensile zone u.s. of dam and compressive zone d.s. of dam. Substantial increase in stress values	Stresses decrease d.s. of dam, heavy compressive stresses u.s. of fault	,,	Stresses decrease d.s. of dam, heavy compressive stresses u.s. of fault
5. Vertical fault at downstream toe	,,	,,	,,	,,

Jian Liu (2003a) used both the limit equilibrium method and finite

element method to study the influence of step by step reduction of

shear strength of non-persistent joints on the dam foundation system

stability of the Three Gorges Dam (Figure 2.11) in China. The results

were compared with the physical model, which was part I of the paper

described in the previous section. The comparison showed that the physical and numerical modelling results supported each other. The results indicated that the gently dipping joints are the most crucial factor that controls the stability of foundation. The results for safety factor against sliding along critical joint surface are shown in Table 2.9. It can be seen that the results from two-dimensional analyses are lower than those from three-dimensional for both physical and numerical modelling. However, they did not make a parametric study to show whether this comparison would change or not.
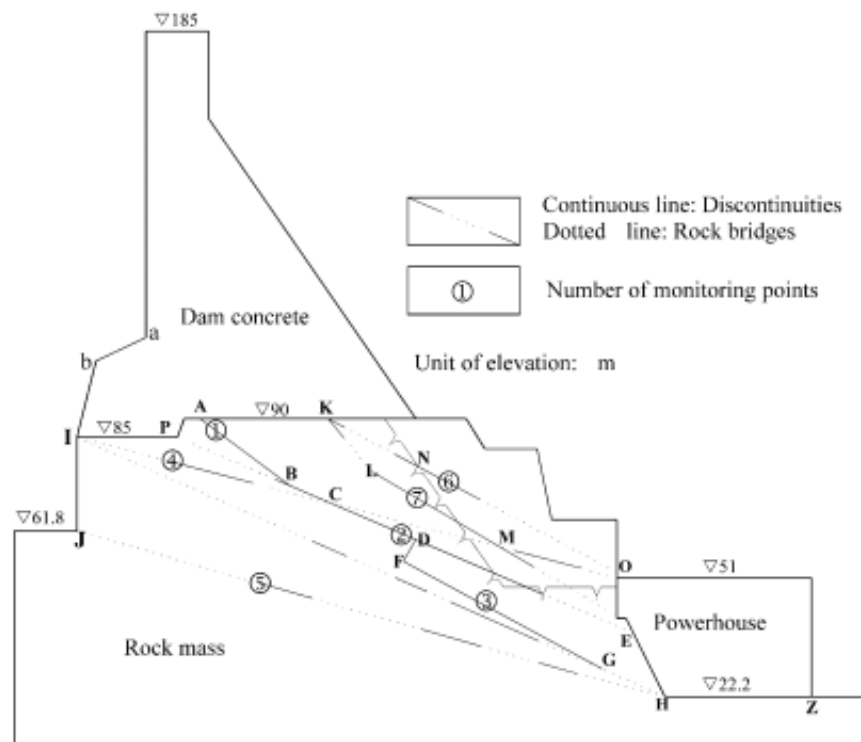
Figure 2.11 Geological model of no.3 left power-dam section of the three-gorge dam (Jian Liu, 2003a)

Table 2.9 Comparison between physical and numerical for safety factor (Jian Liu, 2003a)

Method	2-D FEM	3-D FEM	Limit equilibrium	2-D physical modelling	3-D physical modelling
Safety factors	3.85	4.37	4.17	3.5	4.0

Dolezalova (2004) studied the stability and seepage conditions of an old masonry dam named Bysticks (Figure 2.12), situated in northern Moravia, using the Universal Distinct Element Code (UDEC). A reduction factor on shear strength was used to bring the dam foundation system to limit equilibrium, in order to find the factor of slip safety along the contacts between the dam and the rock. However the effect of joints orientation on dam stability was not studied because the model represented an actual case study of a gravity dam on jointed rock foundation.
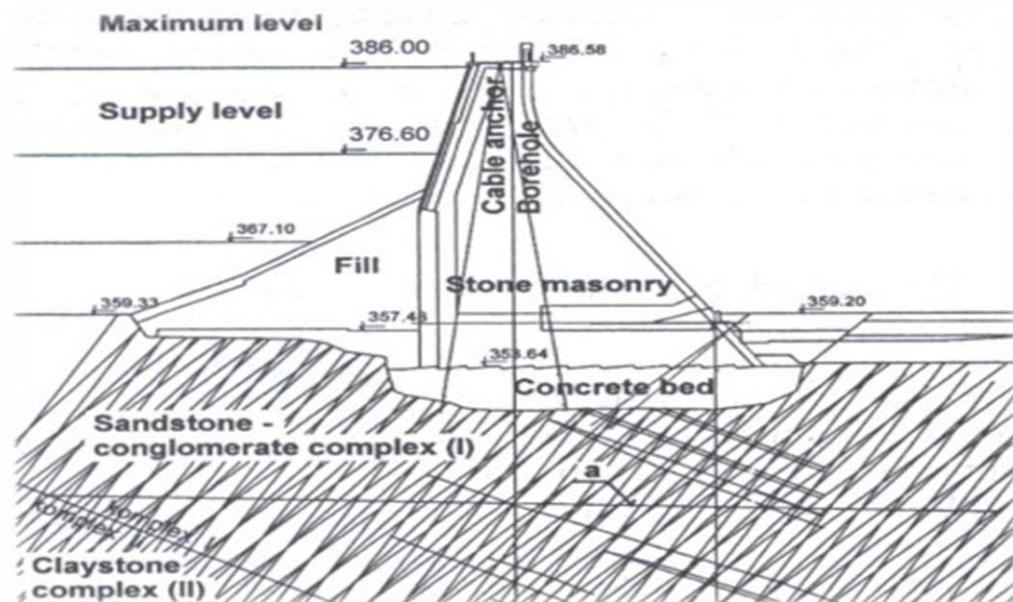
Figure 2.12 Cross-section of Bystricks stone station masonry dam (Dolezalova, 2004)

Barla et al. (2004) used the numerical modelling technique in plane strain condition to assess the stability of a 73m high concrete gravity dam founded on a jointed granitic rock mass in Italy. They compared UDEC and FLAC codes to analyse the concrete gravity dam on a rock mass. The results showed that the factor of safety against sliding computed by UDEC is much lower than that produced by the continuum model (FLAC). However, it will be shown in this thesis that both approaches may give similar results under most conditions and differences only occur for a few cases of joint set angles and low joint strength. Also it was concluded that the joint upstream, especially that near to the heel, was opened during hydrostatic loading, since the dam underwent a rotation toward the downstream direction (Figure 2.13). However, the effect of joint dipping angle was not studied.
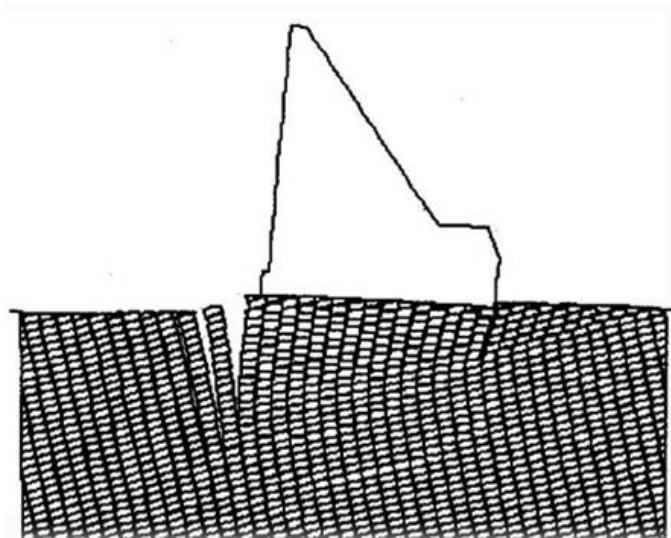
Figure 2.13 Deformed configurations with the deterministic joint pattern model (Barla et al., 2004)

Gimenes and Fernández (2006) used a distinct element method (DEM) numerical model to simulate the rock mass behaviour under Albigna Dam in Switzerland. This dam is founded on jointed granitic rock; the numerical code was used to evaluate the potential for sliding surfaces in the dam's foundation. UDEC was used to assess the nature of flow regime in the rock foundation. The opening and closing of joints were monitored before the reservoir filling and after reservoir filling, so as to compute the changes in joint apertures. These changes are computed as a percentage, as shown in Figure 2.14. It can be seen that a tension crack develops in the region near the heel as a result of the tension stress after reservoir filling.
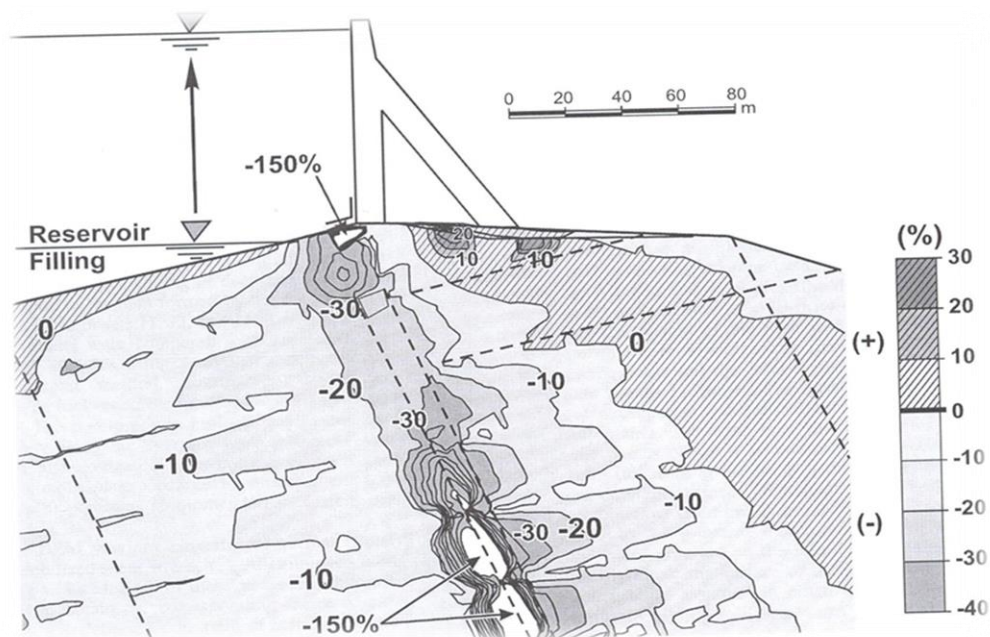
Figure 2.14 Albigna dam hydro mechanical model results. Percent changes of hydraulic apertures in jointed rock foundation at maximum operating level. (+) for joint closure and (-) for joint opening (Gimenes and Fernández, 2006).

Wei et al. (2008) conducted a numerical study to analyse the stability of the Xiangjiaba concrete gravity dam in China using three-dimensional finite element methods. The strength reserve factor method was used to simulate progressive failure and possible unstable modes of the dam's foundation. In this method the strength of weak layers under the dam was reduced until plastic failure appeared under the dam, indicating failure of the dam. The results pointed out that the maximum bearing strength was controlled by the strength of silt-laden layers (Figure 2.15) under the dam.
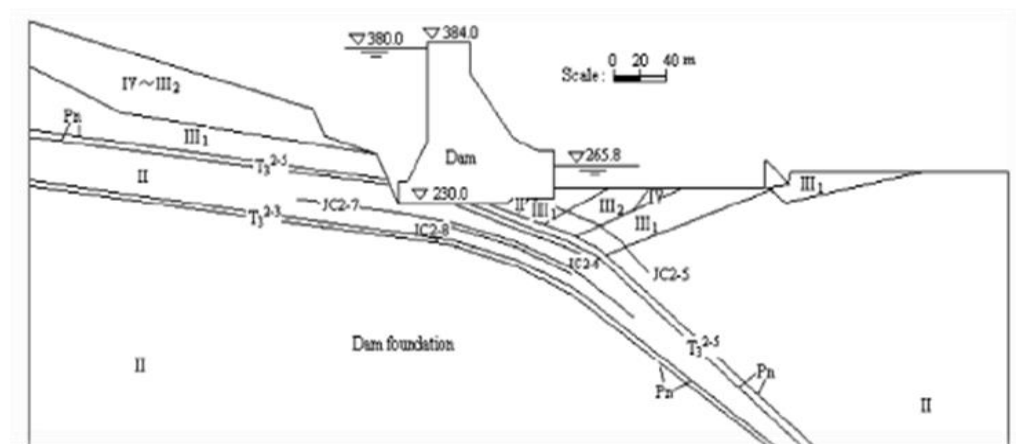
Figure 2.15 The geological structure of Xiangjiaba Hydropower Station (Wei et al., 2008)

Zhang et al. (2008) studied the stability of gravity dams on a sloping layered rock foundation. They used the commercial finite element software ADINA. The strength reduction method was adopted to evaluate the stability of gravity dams. The displacement at the heel, crest and toe of the dam (Figure 2.16) was recorded step by step

during strength reduction and used as a criterion to indicate the failure. Also, the plastic zone was used as a criterion to indicate failure of dam foundation system.
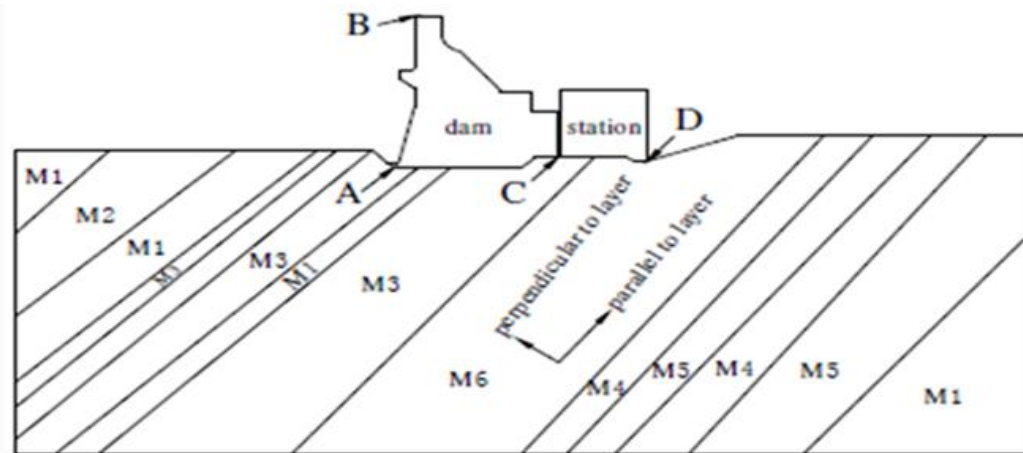
Figure 2.16 the dam and sloped layered rock foundation (Zhang et al., 2008)

2.6 Historical Dam Incidents

There is no doubt that dams should be constructed on a strong foundation in an area with geological and seismological stability. Although the most competent foundations have been chosen to construct dams, some of them have failed. There are various publications relating to dam incidents, such as Douglas (2002); ICOLD (1974); ICOLD (1983); ICOLD (1995). According to these, about thirty percent of incidents occurred due to some deficiency of the rock foundations, therefore some important dam incidents related to foundation rock defects (which have changed the approaches of dam

design) are presented in this section. According to ICOLD (1995), in page 13, a failure is defined as:

> "Collapse or movement of part of a dam or its foundations, so that the dam cannot retain water. In general, a failure results in the release of large quantities of water, imposing risks on the people or property downstream".

Terzaghi (1929), cited in Boyer (2006) wrote:

> "To avoid the shortcomings associated with present practice requires first of all expert translation of the findings of the geologist into physical and mechanical terms. Next it requires the evaluation of the most unfavourable mechanical possibilities which would be expected under the existing geologic conditions; and finally to assume for the design of the structure the most unfavourable possibilities. These mental operations represent by far the most important, most difficult, and most neglected tasks in the field of dam foundations."

Boyer (2006) commented on the above as:

> "Unfortunately, the shortcomings referred to by Dr. Terzaghi are still evident in today's practice more than 70 years after his statement was first penned! Dam incidents and failures continue to occur, albeit at a lower frequency of occurrence. Many of these failures are directly attributed to a lack of

knowledge and understanding of site geologic conditions and neglect of a critical assessment of potential dam foundation failure modes".

2.6.1 The Austain Dam (1909-1911)

The Austain Dam site is located in Pennsylvania, USA. The structure was a concrete gravity dam constructed on interbedded sedimentary rock (sandstone and shale) (Figure 2.17). Martt et al. (2005) presented stability analyses based on shear strength tests of different interfaces of the foundation (Concrete/Sandstone, Sandstone/Sandstone, Sandstone/Shale, Shale/Shale) in order to define the cause of failure. They concluded that the dam was safe against bearing capacity failure, but it was not safe against sliding, especially between sandstone and shale, since its sliding safety factor was 0.6. This is why the sliding took place in its foundation.
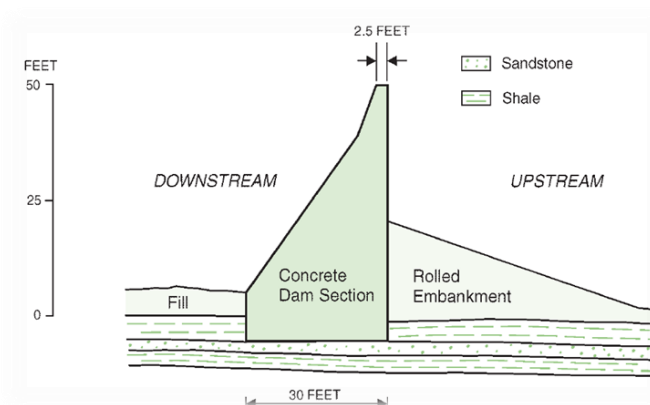
Figure 2.17 Austain Dam before failure (Greene and Christ, 1998)

2.6.2 The St. Francis Dam (1926-1928)

The St. Francis Dam was an arched concrete gravity dam located in the USA. The dam was constructed on two kinds of rock; the canyon floor and the left abutment consist of mica schist, while the right abutment is a red conglomerate. A fault separates these two formations; this fault has a strike mostly parallel with the direction of water flow in the canyon, and it crosses the dam site on the right side. The materials under the dam would be softened when immersed in water. Theories of the possible reasons for the failure of this dam focus on softening and sliding (Figure 2.18).
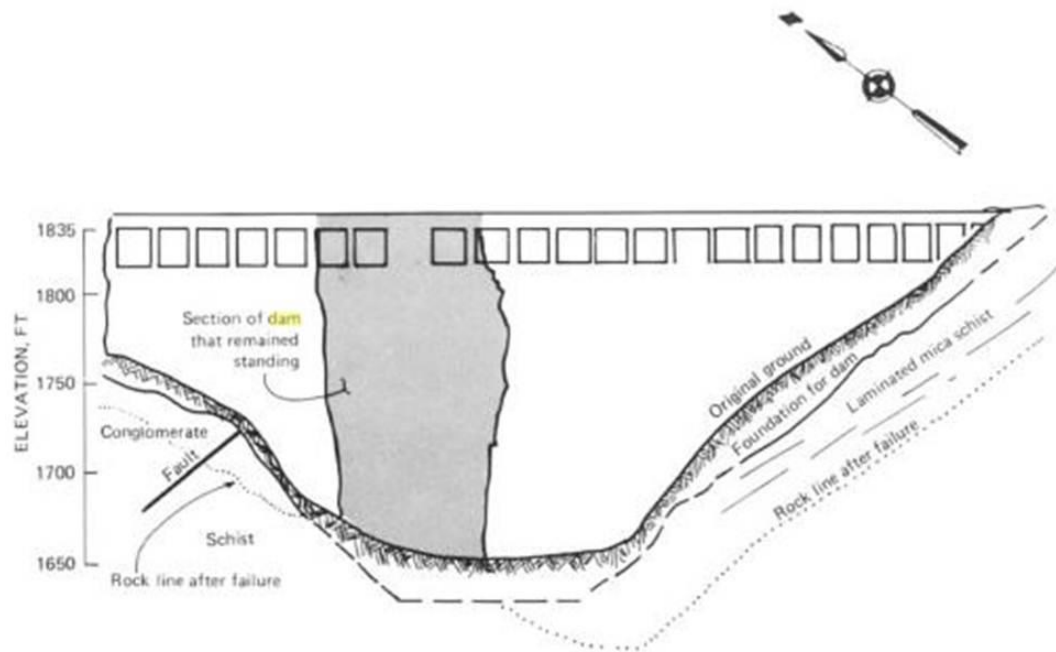
Schist - in many places strongly sheared, commonly along planes roughly parallel with the schistosity

Conglomerate - composed chiefly of detritus derived from the schist and granite. Hard when dry, disintegrates in water.

Figure 2.18 St. Francis Dam cross-section showing foundation conditions and rock surface after failure (Jansen, 1988)

2.6.3 Malpasset Dam (1954-1959)

The Malpasset Dam was a high (60m) double arched concrete dam located in Tanneron Massif, France (Figure 2.19). The dam was founded on a foliated rock mass. The left abutment rock is fresh schistose foliation, while the right abutment rock is massive gneiss foliation. There are many noticeable discontinuities in the dam's foundation, such as the denser mesh of 2 to 3 cm and the bigger mesh of 20 to 50 cm. Also, there are numerous joints and faults that mostly dip in the downstream direction (Figure 2.19). The dam failed in 1959 mainly because of heavy rainfall cause flooding and then rapid filling of the reservoir, and secondly due to sliding of the foundation along an inactive fault. As a result, uplift pressure increased along the inactive fault in the foundation of the dam, which dislodged a wedge of rock located directly downstream between the toe and the fault. The cause of failure was studied by many researchers, and the outcome of these studies is two hypotheses proposed by Bellier and Londe (Wittke, 1990) (Figure 2.20) and Wittke and Leonards (1987) (Figure 2.21), the latter of which is a modified version of the former. Both hypotheses concur that the sliding occurred along a fault, which was dipping upstream due to open joints upstream, which led to increase water pressure on the rock wedge in the left abutment.
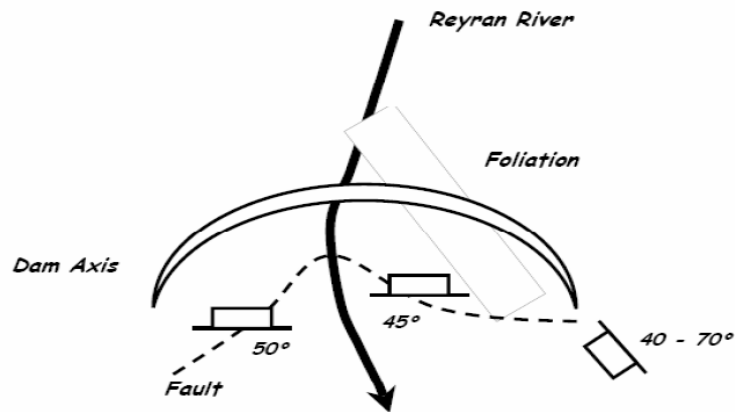
Figure 2.19 Geology of the Malpasset dam (Londe, 1987)
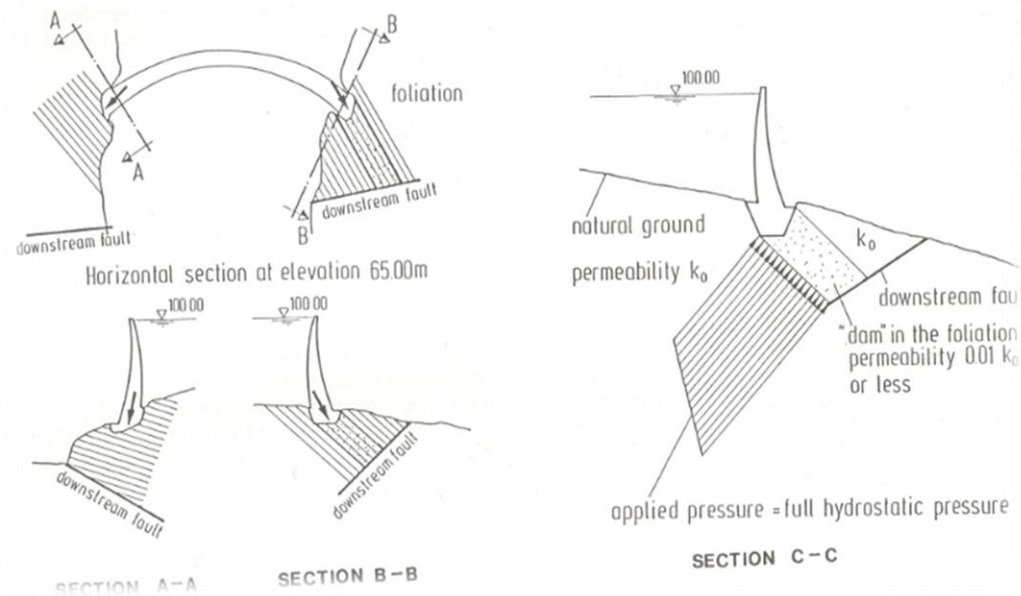
Figure 2.20 Hypothesis of failure proposed by Bellier and Londe (Wittke, 1990)
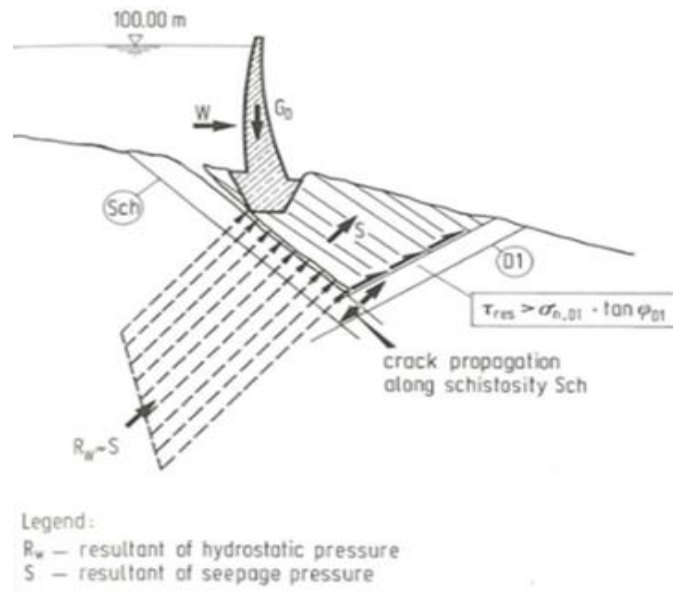
Figure 2.21 Hypothesis of failure proposed by Wittke and Leonards (1987)

2.7   Summary and Conclusions

Most historical dam failures have been a result of some sort of deficiency in the dam foundation. These deficiencies are often related to the jointed condition of the bedrock, and perhaps some uncertainty as to the orientations of these joints and how they control rock mass behaviour. A relatively small number of studies involving rock mass behaviour under gravity dam are available.

From the general literature review, it is obvious that there are many gaps in the understanding of rock mass behaviour under a concrete gravity dam that need to be investigated. One of these gaps is the effect of a dominant joint on the stability of concrete dams, as well as rock mass behaviour under dams. It might be very expensive to study

this behaviour by using physical models, because several models would be needed. A process of simulating the joint also makes the modelling impractical, so one can conclude that the only possible method that could be used economically and practically is the numerical method. This is the rationale for adopting numerical modelling in this study. However, laboratory tests are required in order to obtain representative input parameters for the numerical models. Incorrect input parameters can result in misleading numerical results. The next chapter presents the numerical methodology used as well as the required laboratory tests to determine the input parameters for the methodology as well as studying the reliability of numerical models.

Chapter 3 Methodology

3.1 Introduction

This chapter introduces the methodology that has been adopted in this study. Two methodologies were chosen: the numerical methodology and the experimental methodology. The numerical methodology was used to study the effect of a rock mass fabric as well as the effect of a weak joint on a dam's stability using both continuum and discontinuum models.

Experimental methods are required in order to obtain representative input parameters for the numerical models using small scale rock samples. Incorrect prediction of input parameters can result in misleading numerical results. Therefore in this study experimental methodology is used to obtain input parameters for the numerical modelling and studying the reliability of numerical study of jointed rock samples in chapters 7 and 8.

3.2 Numerical Methodology

This section provides a brief description of the numerical modelling codes (FLAC2D and UDEC) used for this research. The FLAC code is used for continuum modelling and also to investigate the effect of a single foundation rock joint dipping downstream or upstream on the stability of a gravity dam. Different locations and angles are checked in order to determine which one is critical to the stability of the dam. The

UDEC code is used for discontinuum modelling of the rock mass under a gravity dam. UDEC is used in this study because it is capable of modelling the many joints that exist within rock as well as the intact rock blocks within the rock mass. In this method, the domain of interest is represented as an assemblage of rigid or deformable blocks and the contacts between them are identified and updated continuously during the entire deformation process. UDEC is a common and powerful DEM package used for the numerical study of rock mass behaviour (Cundall, 1980; Itasca, 2011). UDEC has the ability to model the discontinuities within the rock mass as well as the intact rock blocks using appropriate constitutive relationships.

3.2.1 FLAC2D

The Fast Lagrangian Analysis of Continua (FLAC) is a 2-D explicit finite difference program that can be used to simulate the stress-strain behaviour of rock in response to gravitational loads such as those that occur as a result of dam construction. This code has been specially developed for geotechnical and mining engineering mechanics computation. The formulation is based on the treatment of the problem domain as a continuum that responds in accordance to one or more constitutive relationships that have been selected. Version 6.0 was used in this study. FLAC2D can be used to solve complex problems in rock mechanics, especially dam construction in stages. Three fundamental components of a project should be specified so as

to set up a model to run a simulation: a finite difference grid; boundary conditions and initial stress conditions; and constitutive model and material properties. When these components are described in the model the initial equilibrium state is computed. The general solution procedure described in Figure 3.1, suggested by the Itasca Consulting Group Inc. (Itasca, 2008), is convenient since it represents the sequence of processes that occurs in the physical environment. It should be noted that FLAC is a powerful numerical modelling technique that has been used by many researchers in geomechanics, so verification of the code is not necessary.
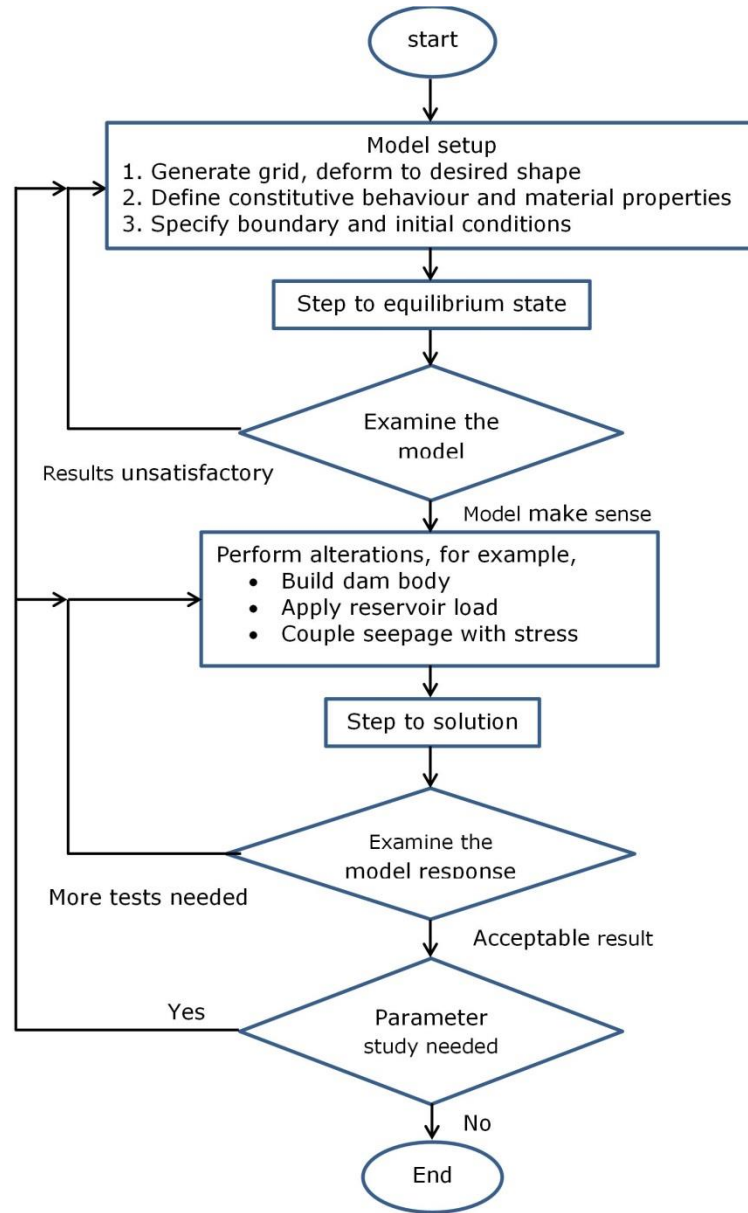
Figure 3.1 General solution procedure for static analysis (modified from Itasca, 2008)

3.2.1.1   Finite difference grid

The grid in FLAC is similar to mesh to that in a FEM code. In FLAC the

continua, which may possibly consist of different materials, are divided

into small elements called zones that together form a grid. Initially the

zones are square, but they can be later distorted so that the boundaries fit an irregular given shape. The zones can also vary in size across the grid.

As a general rule, finer zones produce more accurate output, especially when yielding and localization are crucial components of the model. Also, the shape of the zones has an effect on accuracy. Reasonable accuracy is achieved for zones with uniform dimensions.

The aspect ratio of zone dimensions should be around unity; any ratio above 5:1 may give inaccurate results, but a high aspect ratio of zones is quite acceptable in regions of low strain gradient, such as remote boundary regions.

3.2.1.2 Boundary conditions and initial stress conditions

After the grid is generated, boundary and initial conditions are applied. The in-situ state (i.e., the boundary and stress conditions before any loading) is defined by boundary and initial stresses of the geotechnical project. Boundaries can be divided into two categories: real boundaries such as the ground surface and dam boundary etc.; and the artificial boundary, which does not exist in reality, but which must be introduced so as to enclose the number of zones chosen to represent a region of infinite extent. The latter is selected on condition that it does not affect the stress state in the problem. The artificial boundaries are

chosen as far as possible from the dam. In this research, the vertical boundary was located at a distance roughly four times the height of the dam from the toe and the heel. The horizontal boundary was located at a depth of almost three times the height of the dam from the base of the ground surface.

The initial stresses should be assigned before any alteration (i.e., adding layer of embankment, excavations, and loading). These stresses can be obtained from field measurements. However when these are not available, they are calculated by using the theory of elasticity, as shown in Equation 3.1 (Hudson and Harrison, 1997):

$$\bar{\sigma}_h = \frac{v}{1-v}\bar{\sigma}_v \qquad\qquad 3.1$$

Where: $\bar{\sigma}_h$=effective horizontal stress, $\bar{\sigma}_v$=effective vertical stress and v=Poisson's ratio

3.2.1.3 Constitutive models

Constitutive models are distributed into three groups: elastic, plastic, and time-dependent. Twelve constitutive models have been implemented in FLAC, of which the following three were chosen for this study:

1. Null;

2. Elastic, isotropic; and

3. Mohr-Coulomb plasticity.

Every model has been developed to represent a specific type of constitutive behaviour commonly associated with geologic materials. In this research the null model was utilized, since construction is done in stages; the whole geometry of the dam and its foundation should be initialized firstly and then removed using this model. The behaviour of the dam is considered to be elastic material; therefore elastic isotropic technique is selected to model it. To represent the rock foundations and the explicit joint (interfaces), the Mohr-Coulomb criteria with elastic perfectly plastic were chosen. The Mohr-Coulomb model is applicable for most general engineering problems. Also, Mohr-Coulomb parameters for cohesion and friction angle are usually more readily available than other properties for geo-engineering materials. More details about the Mohr-Coulomb criterion and how it is used in FLAC Code can be found in the Code's user manual (Itasca, 2008).

The above models along with examples of representative materials and possible applications of the models are provided in Table 3.1.

Table 3.1 FLAC constitutive models (Itasca, 2008)

Model	Representative Material	Example Application
null	void	holes, excavations, regions in which material will be added at later stage
elastic	homogeneous, isotropic continuum; linear stress-strain behavior	manufactured materials (e.g., steel) loaded below strength limit; factor-of-safety calculation
transversely isotropic elastic	thinly laminated material exhibiting elastic anisotropy (e.g., slate)	laminated materials loaded below strength limit
Drucker-Prager plasticity	limited application; soft clays with low friction	common model for comparison to implicit finite-element programs
Mohr-Coulomb plasticity	loose and cemented granular materials; soils, rock, concrete	general soil or rock mechanics (e.g., slope stability and underground excavation)
strain-hardening / softening Mohr-Coulomb	granular materials that exhibit nonlinear material hardening or softening	studies in post-failure (e.g., progressive collapse, yielding pillar, caving)
ubiquitous-joint	thinly laminated material exhibiting strength anisotropy (e.g., slate)	excavation in closely bedded strata
bilinear strain-hardening/softening ubiquitous-joint	laminated materials that exhibit nonlinear material hardening or softening	studies in post-failure of laminated materials
double-yield	lightly cemented granular material in which pressure causes permanent volume decrease	hydraulically placed backfill
modified Cam-clay	materials for which deformability and shear strength are a function of volume change	geotechnical construction on clay
Hoek-Brown plasticity	isotropic rock material	geotechnical construction in rock
Cysoil (cap-yield)	soils that exhibit decreasing stiffness as plastic strains develop	geotechnical construction in soft soils

3.2.1.4   Material properties

The material properties implemented in the FLAC Code are generally sorted in one of two groups: elastic deformability properties and strength properties. Furthermore, there are special considerations such as the definition of post-failure properties, the extrapolation of

laboratory-measured properties to the field scale, the spatial variation of properties and randomness of the property distribution, and the dependence of properties on confinement and strain.

One of the most difficult elements in the generation of a model is properties selection, due to the high uncertainty in the property database. When conducting an analysis, especially in geotechnical engineering, the field data may never be known perfectly. However, with the appropriate selection of properties based upon the available database, important insights into the physical problem can still be gained. Material properties are conventionally derived from laboratory testing programs.

3.2.1.4.1   Deformability properties

The properties required for the isotropic elastic model are bulk modulus and shear modulus. These two moduli are used in FLAC rather than Young's modulus and Poisson's ratio because it is thought that both moduli correspond to more fundamental aspects of material behaviour. These moduli can be computed from the following equations:

$$K = \frac{E}{3(1-2v)}$$
3.2

$$G = \frac{E}{2(1+v)}$$
3.3

where: K, G are Bulk and Shear Modulus respectively, E = Young's Modulus, and $v =$ Poisson's ratio

The above equations should be used with caution when v is near 0.5 for undrained cases, since the computed value of K will be unrealistically high and convergence to the solution will be very slow. It is better to fix the value of K at its known physical value (estimated from an isotropic compaction test) and then compute G from K and v.

Models that include groundwater flow require the bulk modulus of the water, K_w. The physical value of K_w is 2 GPa for pure water at room temperature, but the value selected should depend on the purpose of the analysis (Itasca, 2008).

3.2.1.4.2   Strength properties

The required shear strength properties in Mohr-Coulomb with elastic-perfectly plastic material are the cohesion and the angle of internal friction. These parameters can be obtained by performing a series of tri-axial tests in the laboratory or from field tests. These parameters are used in a failure criteria equation to check whether the material is failed or not. The basic criterion for material failure in FLAC is the Mohr-Coulomb relation, which is a linear failure surface corresponding to shear failure:

$$f^S = \sigma_1 - \sigma_3 N_\varphi + 2c\sqrt{N_\emptyset} \qquad\qquad 3.4$$

where: $N_\emptyset = (1 + \sin\emptyset)/(1 - \sin\emptyset)$;

σ_1=the major principal stress (compressive is negative)

σ_3=the minor principal stress (compressive is negative)

$\emptyset$=friction angle; and c=cohesion

Shear failure is detected if $f^s < 0$

The Mohr-Coulomb criterion loses its physical validity when the normal stress becomes tensile. However, for simplicity, the failure envelope is spread into tensile region to the point at which minor principal stress (σ_3) equals the uniaxial tensile strength (σ^t):

$$f^t = \sigma_3 - \sigma^t \qquad\qquad 3.5$$

Tensile yield is detected if tensile strength is exceeded and $f^t > 0$.

The maximum tensile strength (σ_{max}^t) can be obtained using the following equation:

$$\sigma_{max}^t = \frac{c}{\tan \emptyset} \qquad\qquad 3.6$$

Usually the actual measurement of tensile strength (σ^t) results a lower value than those estimated using Eq. 3.6; therefore, a tension cut off should be used as shown in Figure 3.2.
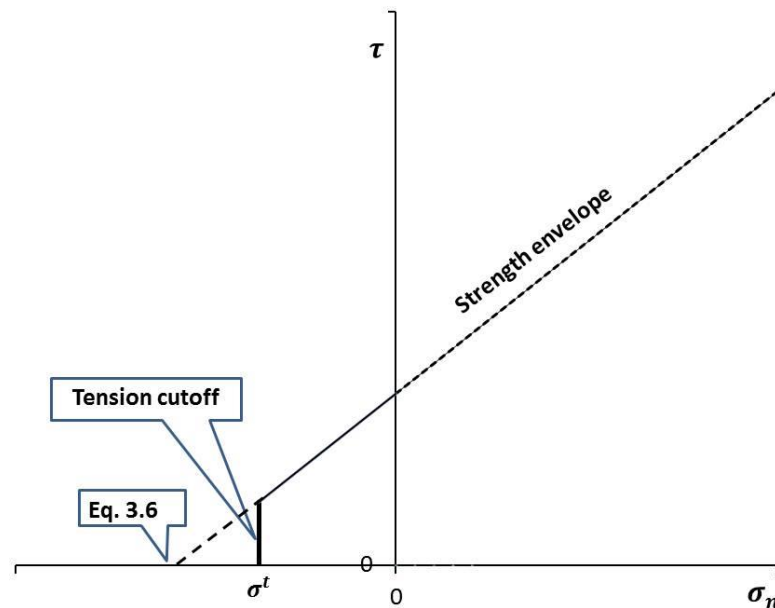
Figure 3.2 Mohr-Coulomb strength envelope with a tension cut-off

3.2.1.5   The interfaces

The following are some examples of interfaces (discontinuities) encountered in geotechnical engineering, especially in rock foundations:

1. Joint, fault or bedding planes in a geologic medium;

2. An interface between a foundation and the soil or dam;

3. A contact plane between a bin or chute and the material that it contains; and

4. A contact between two colliding objects.

Sliding or separation may occur along the mentioned planes. In order to study their effect on a problem, FLAC Code provides interfaces that are characterized by Coulomb sliding and/or tensile separation. Interfaces have the properties of friction, cohesion, dilation, normal and shear stiffness and tensile strength. Although there is no restriction on the number of interfaces or the complexity of their intersections, it is generally not reasonable to model more than a few simple interfaces with FLAC, because it is awkward to specify complicated interface geometry.

The program UDEC (Itasca, 2011) is specifically designed to model many interacting bodies; it should be used instead of FLAC for the more complicated interface problems (i.e., many joint sets). In FLAC, an interface is represented as normal and shear stiffness between two planes which may contact each other (Figure 3.3).
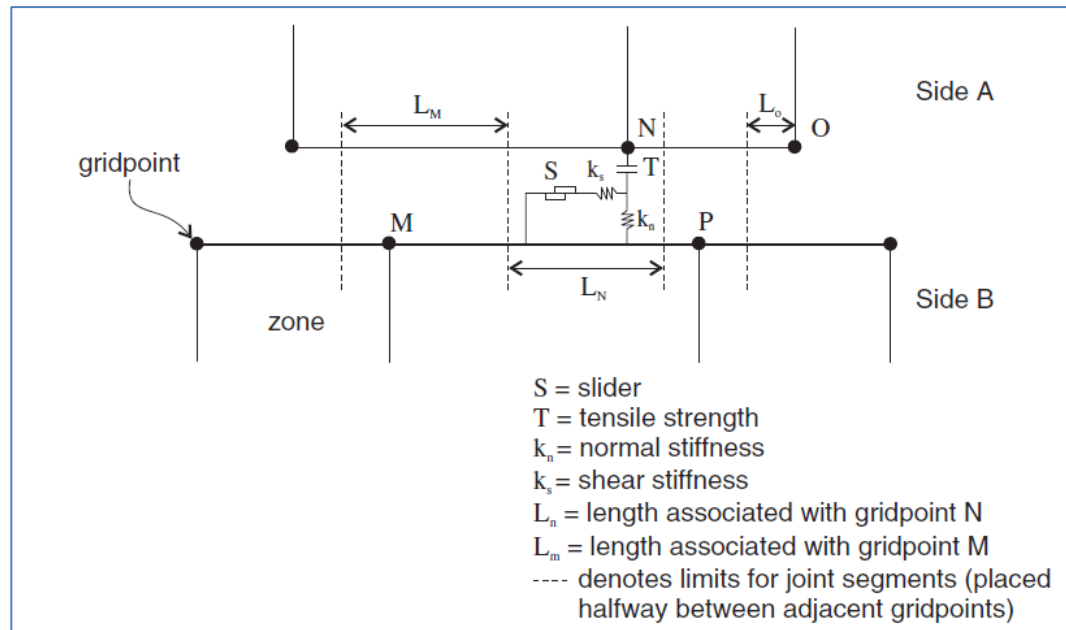
Figure 3.3 An interface represented by sides a and b, connected by shear (ks) and normal (kn) stiffness springs (Itasca, 2008)

The Coulomb shear-strength criterion limits the shear force by the following relation:

$$F_{smax} = c_j\, L + \tan \emptyset_j\, F_n \qquad\qquad 3.7$$

Where c_j=cohesion (in stress units) along the interface, L=effective contact length (Figure 3.3), and $\emptyset_j$=friction angle of interface surfaces.

More details about the interface and how it is applied in FLAC can be found in the program's user manual (Itasca, 2008). The dilation angle was taken as zero for all analyses.

3.2.2 UDEC

UDEC code is a distinct element program produced by Itasca Company (Itasca, 2011) especially to analyse a discontinuous medium. A

discontinuous medium can be distinguished from a continuum medium by the existence of joints or faults between blocks of the medium, such as intact rock in the rock mass. UDEC uses an explicit time-marching scheme to solve the equations of motion directly. Figure 3.4 shows an example of a UDEC model with the terminologies that are used.
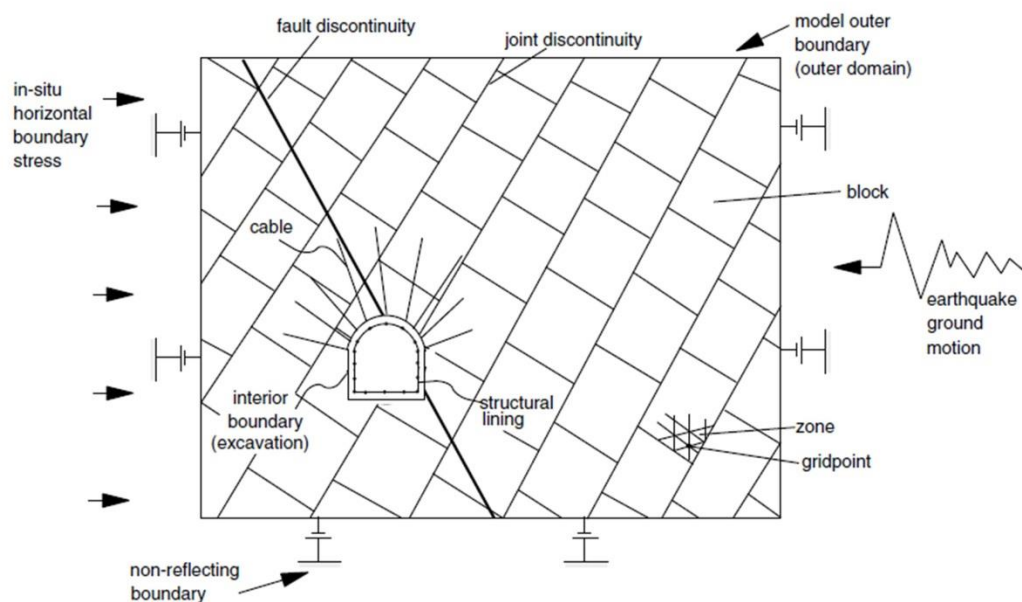
Figure 3.4 Example of a UDEC model (not to scale)(Itasca, 2011)

The UDEC developed by Cundall (1980) is a 2D explicit finite difference program for discontinuum modelling that simulates the stress-strain behaviour of rock mass in response to gravitational loads, such as the those resulting from dam construction. It can also simulate the flow of water through rock mass fractures and fully couple this with stresses

(hydromechanical response). UDEC simulates a rock mass as a gathering of discrete blocks separated by joints that are represented by interfaces. The contact forces and displacements at the interfaces of a stressed assembly of blocks are determined by means of a series of computations that trace the motions of the blocks. These motions are caused by the propagation of disturbances through the block system caused by body forces or applied loads, such as dam body forces and reservoir load. This is a dynamic process in which the physical properties affect the speed of propagation (Itasca, 2011)

A time-stepping algorithm numerically represents the dynamic behaviour in which the velocities and accelerations are kept constant within the time step. The solution scheme is identical to that used by the FLAC 2D code for continua.

The computations achieved in the UDEC alternate between application of Newton's second law at all blocks and a force displacement law at all contacts. The force-displacement law is used to find contact forces from known (and fixed) displacements. Newton's second law gives the motion of the blocks resulting from the known (and fixed) forces acting on them. If the blocks are deformable, motion is calculated at the grid points of the triangular finite-strain elements within the blocks. The application of the block material constitutive relations then gives new stresses within the elements. Figure 3.5 shows the computation cycle

for the distinct element method. The details about the motion

equations in this figure can be found it Itasca manual (Itasca, 2011).
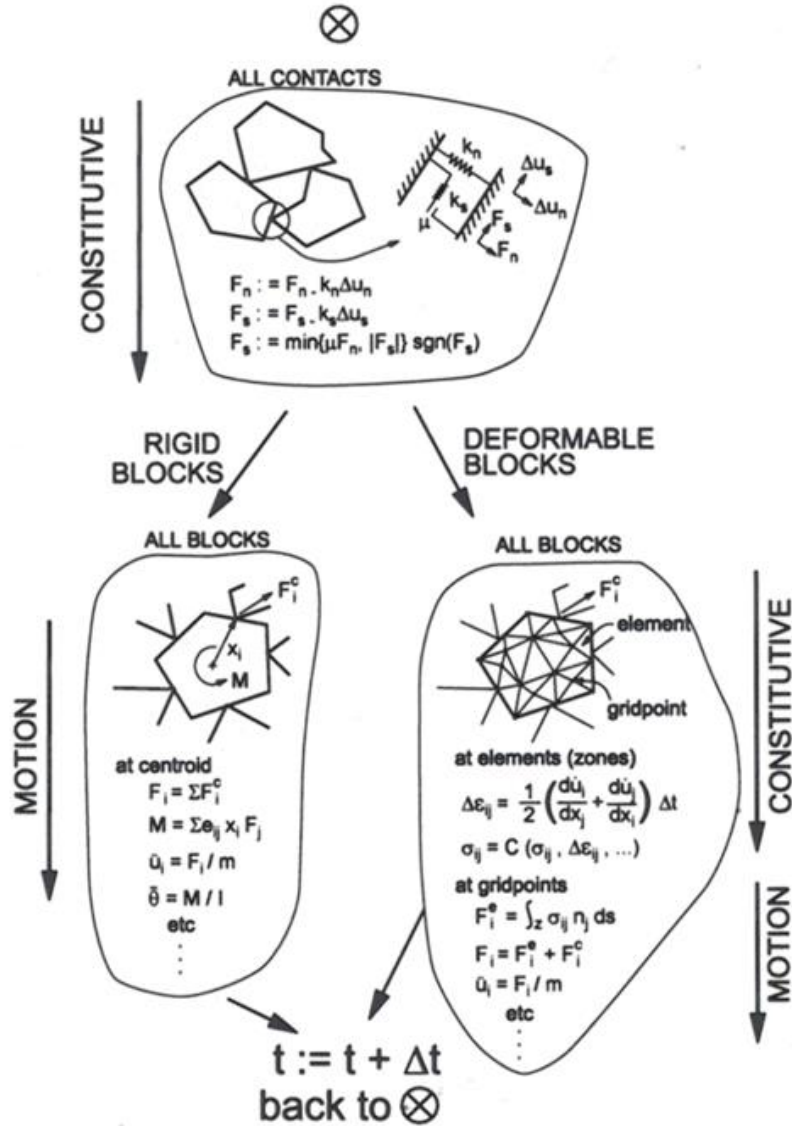
Figure 3.5 Computation cycle for the UDEC (Itasca, 2011)

Three fundamental components of a problem must be specified in

order to set up a model to run a model with UDEC: a distinct-element

model block with cuts to create problem geometry, boundary and

initial conditions, and constitutive behaviour and material properties.
The general solution procedure for an explicit static analysis is
presented in Figure 3.6, developed by Itasca Consulting Group. This
procedure is convenient because it represents the sequence of
processes that occur in the physical environment.
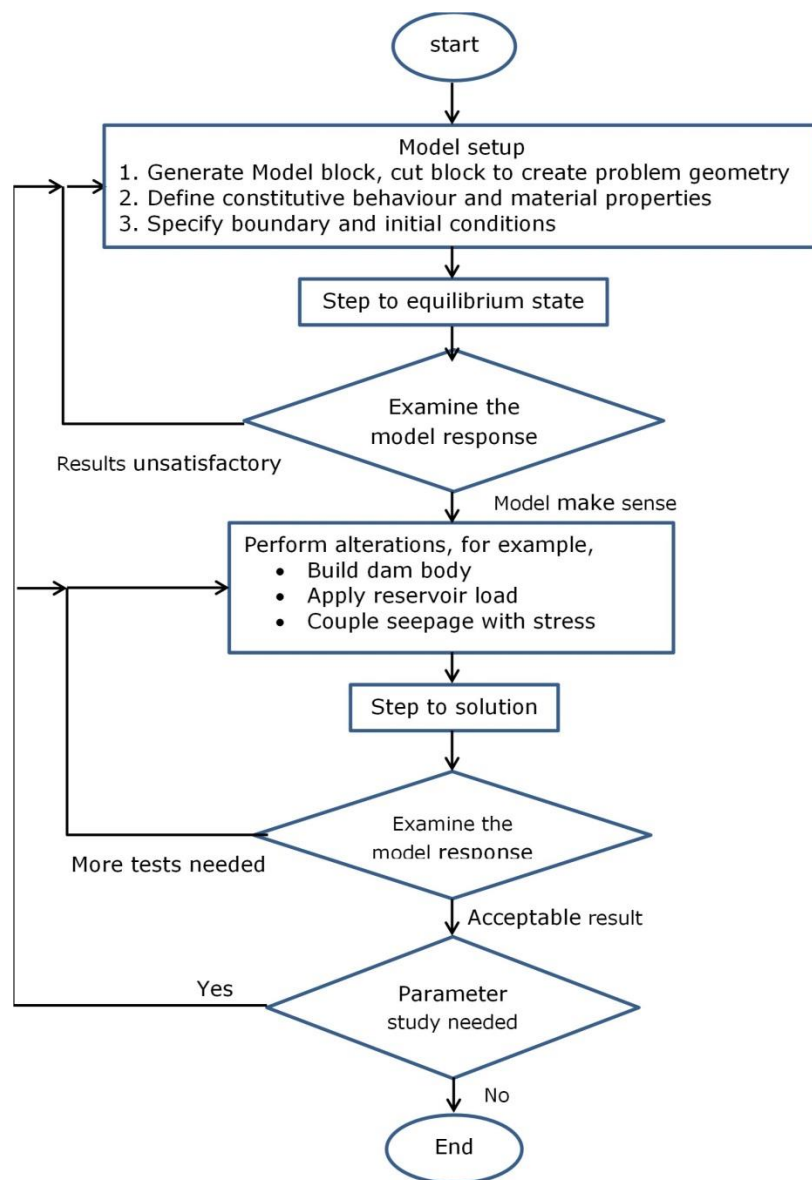
**Figure 3.6 General solution procedures for static analysis
(modified from Itasca, 2011)**

3.2.2.1   Blocks and blocks constitutive models

In the distinct element method, blocks may be rigid or deformable. Cundall et al. (1978) has given the basic formulation for rigid blocks. This formulation represents the rock medium as a set of distinct blocks that do not change their geometry as a result of applied loading. This formulation is most applicable to problems in which the behaviour of the system is dominated by discontinuities, and for which the material elastic properties may be ignored.

In this research the blocks are considered to be deformable. These blocks are internally divided into finite-difference triangular elements called zones. The complexity of deformation of the blocks depends on the number of zones into which the blocks are discretized. The aspect ratio of zone dimensions (triangle base to height ratio) should be as near unity as possible and anything greater than 5:1 is possibly inaccurate.

The constitutive models given in UDEC Version 5.0 are distributed into null, elastic and plastic. The following models are used in this research.

Null model group (null model): a null material model is used to represent material that is removed or excavated. In this research it is used since the construction of gravity dam is achieved in stages; the whole geometry of the concrete dam and its foundation should be initialized firstly and then the dam body is removed using null model then the dam body is applied in stages.

Elastic model group: since the behaviour of the concrete dam is considered to be elastic (due to its materials), the elastic isotropic is selected to model it. For this model, the required properties are: density (ρ_d); bulk modulus (k); and shear modulus (G).

Plastic model group: the Mohr-Coulomb model is used to model the deformable blocks with elastic perfectly plastic. This is a conventional model used to represent shear failure in soils and rocks. Vermeer (1984) reported laboratory test results for sand and concrete that match well with the Mohr-Coulomb criterion. This model is applicable for most engineering problems. Also, the parameters for the model are usually easily determined. For this model, the required properties are: dry density (ρ_d); bulk modulus (k); shear modulus (G); friction angle ($\emptyset$); cohesion (c); dilation angle (ψ); and tensile strength (σ^t). If any of these properties are not assigned, their values are set to zero by default.

3.2.2.2   Boundary conditions in UDEC

After the deformable blocks are generated and the blocks divided into triangular-shaped finite-difference zones, boundary and initial conditions are applied. The in-situ state (such as the boundary and stress conditions before any loading) is defined by boundary and initial stresses of the geotechnical project.

Similar boundary conditions that were used in FLAC model were used in UDEC model of gravity dam as well. In addition, two mechanical boundaries were used in UDEC to simulate UCS and triaxial tests. These boundaries are prescribed stress and prescribed displacement. The prescribed stress was used to simulate stress control test and prescribed displacement was used to simulate the strain control test.

3.2.2.3   Contact behaviour model

The following joint constitutive models are available to define the behaviour of joints in UDEC: point contact - Coulomb slip; joint area contact - Coulomb slip; joint area contact - Coulomb slip with residual strength; continuously yielding; and Barton–Bandis joint model. Table 3.2 presents these model and examples of representative materials and possible applications. According to this table and the results of direct shear on planer smooth jointed rock which showed elastic plastic behaviour, the conventional Mohr–Coulomb joint area contact model has been selected.

Table 3.2 Joint constitutive models in UDEC (Itasca, 2011)

Model	Representative Material	Example Application
point contact	limited application; particulate material; loosely compacted blocks of irregular shape	slope stability in highly disturbed, broken and fractured rock
area contact	joints, faults, bedding planes in rock	general rock mechanics (e.g., underground excavation)
area contact with displacement weakening	rock joints displaying distinct peak/residual strengths	general rock mechanics
continuously yielding	rock joints displaying progressive damage and hysteretic behavior	cyclic loading and load reversal with predominant hysteretic loop; dynamic analysis
Barton-Bandis	rock joints defined by Barton-Bandis index properties	estimation of changes in hydraulic apertures

Material properties must be assigned to all discontinuities (i.e., contacts) in the simulated model. Joint models are assigned with the JOINT model command. There are four built-in constitutive models for discontinuities and one optional model which is Barton-Bandis-model. The model sufficient for most analyses is the (elastic-perfectly plastic) area-contact Coulomb slip model, which is assigned to discontinuities with the command joint model area.

Material properties for the joint models are also assigned with the JOINT model command, following the model name. For the Coulomb slip model, the required properties are: normal stiffness (k_n); shear stiffness (k_s); joint friction angle ($\emptyset_j$); cohesion (c_j); dilation angle (ψ_j); and tensile strength ($\sigma^t{}_j$). If any of these properties are not assigned, their values are set to zero by default.

The stress-displacement relation is assumed to be linear for normal direction as shown in the following equation:

$$\Delta\sigma_n = -k_n.\Delta u_n \qquad\qquad 3.8$$

If tensile strength (σ_t) is exceeded, then the normal stress is $\sigma_n = 0$

where: $\Delta\sigma_n$ is the effective normal stress increment; and

Δu_n is the normal displacement.

The shear-horizontal displacement relation is controlled by constant shear stiffness, k_s.

The shear stress, τ_s, is bounded by a combination of cohesive and frictional strength.

Thus, if $\qquad |\tau_s| \leq c + \sigma_n.\tan\varphi = \tau_{max}$

then $\qquad\qquad \Delta\tau_s = k_s.\Delta\tau_s^e$

If shear strength is exceeded then, $|\tau_s| \geq \tau_{max}$

then

$$\tau_s = sign(\Delta u_s).\tau_{max} \qquad\qquad 3.9$$

where Δu_s^e is the elastic component of the incremental shear displacement; and

Δu_s is the total incremental shear displacement.

The contact forces can be calculated by multiplying the stresses by the joint contact area (Ac):

$F_s = \tau_s * Ac$ and $F_n = \sigma_n * Ac$

In this study, because the smooth planar joint is used, the dilation angle is assumed to be zero.

3.2.2.4   Fluid flow in joints

Fluid flow through rock joints has been implemented in the UDEC code, thereby achieving a fully coupled mechanical-hydraulic analysis, in which the mechanical deformation has an effect on joint permeability and in contrary fracture fluid pressures affect the mechanical properties. Figure 3.7 shows the effects that are modelled in UDEC.
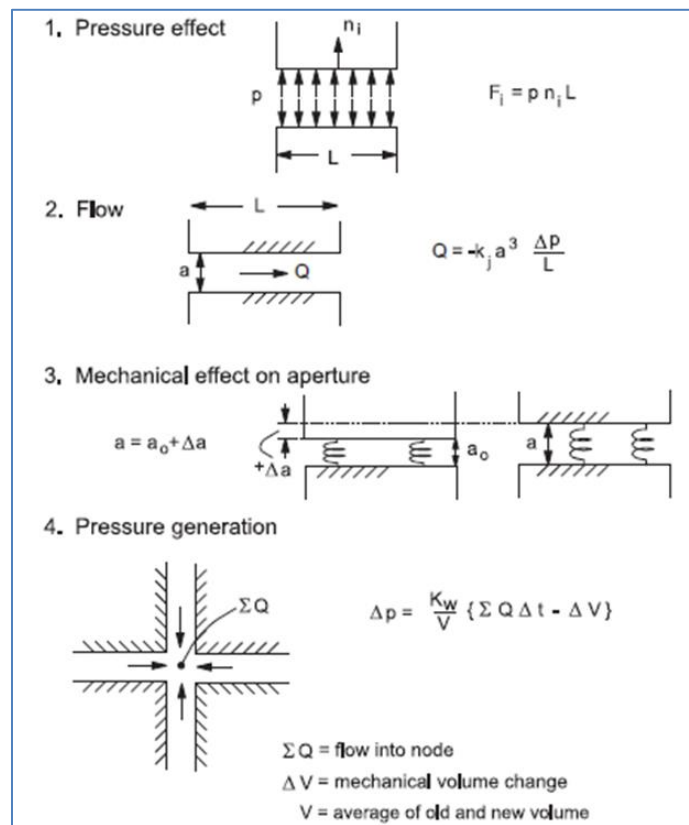
Figure 3.7 Fluid-solid interactions in discontinua (Itasca, 2011)

There are five modes of fluid flow implemented in UDEC:

1. Basic algorithm – transient flow of a compressible fluid

2. Steady-state flow algorithm

3. Transient flow of an incompressible fluid

4. Transient flow of a compressible gas

5. Two-phase flow in joints

In this study the second algorithm is used, because the final steady state is of interest. This mode is similar to the first mode. The algorithm is based on the scaling of the fluid bulk modulus and of the domain volumes, which are unimportant in the steady-state regime. When this option is used, the fluid flow time-step is arbitrarily set equal to the mechanical time-step, and the fluid bulk modulus is automatically defined. Full details about other modes of flow can be found in Itasca manual (Itasca, 2011).

The UDEC domains are used to model fluid flow through joints. The domains are the contact area between blocks. In case of flow these joints are filled with water under pressure. Figure 3.8 shows domains that are formed between blocks; each domain has a number through which it can be known. Considering the figure, domain 2 is found at the intersection of two joints, whereas domain 5 is a void space. Letters A to F represent the contact point that separates the contact

area to domains. The external and internal forces are exerted on blocks through these points.
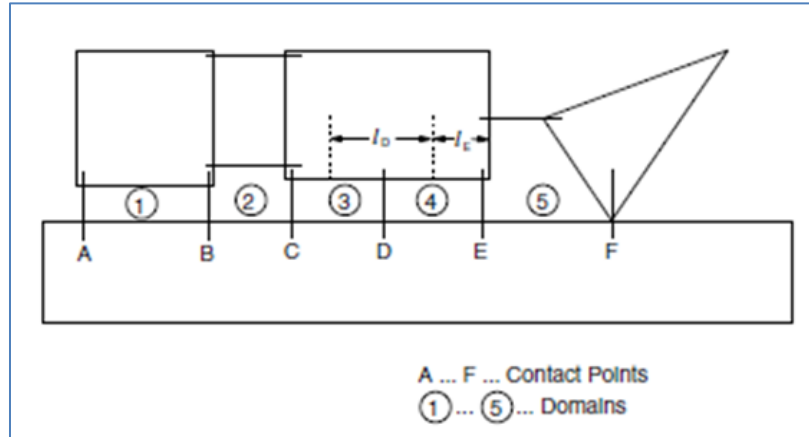
Figure 3.8 Flow in joints modelled as flow between domains (Itasca, 2011)

The pressure differential between adjacent domains governs the flow. Two different ways are used to calculate the flow rate, depending on the type of contact. For a point contact (i.e., corner-edge, as contact F in Figure 3.8, or corner-corner), the flow rate from a domain with pressure p1 to a domain with pressure p2 is given by:

$$q = -k_c \Delta p \hspace{4cm} 3.10$$

where: k_c=a point contact permeability factor, and

$$\Delta p = p_2 - p_1 + p_w g(y_2 - y_1) \hspace{3cm} 3.11$$

where p_w is the fluid density; g is the acceleration of gravity (assumed to act in the negative y-direction); and y_1, y_2 are the y-coordinates of the domain centres.

In the case of an edge-to-edge contact, a contact length can be defined (e.g., in Figure 3.8, l_D and l_E denote the lengths of contacts D and E, respectively). The length is defined as half the distance to the nearest contact to the left plus half the distance to the nearest contact to the right. In this case, the cubic law for flow in a planar fracture (Witherspoon, 1980) can be used. The flow rate is then given by:

$$q = -k_j a^3 \frac{\Delta p}{l} \qquad\qquad 3.12$$

where: k_j is a joint permeability factor (whose theoretical value is 1/12µ);

µ is the dynamic viscosity of the fluid;

a is the contact hydraulic aperture; and

l is the length assigned to the contact between the domains

The hydraulic aperture is given, in general, by

$$a = a_o + u_n \qquad\qquad 3.13$$

where: a_o is the joint aperture at zero normal stress; and

u_n is the joint normal displacement (positive denoting opening).

A minimum value, a_{res}, is assumed for the aperture, below which mechanical closure does not affect the contact permeability. A maximum value, a_{max}, is also assumed, for efficiency, in the explicit calculation (arbitrarily set to five times a_{res}, but it can be changed by the user). The variation of aperture with normal stress on the joint is

depicted in Figure 3.9. The above expression is a very simple relation between joint mechanical and hydraulic apertures; more elaborate relations, such as the empirical law proposed by Barton et al. (1985), might also be used.
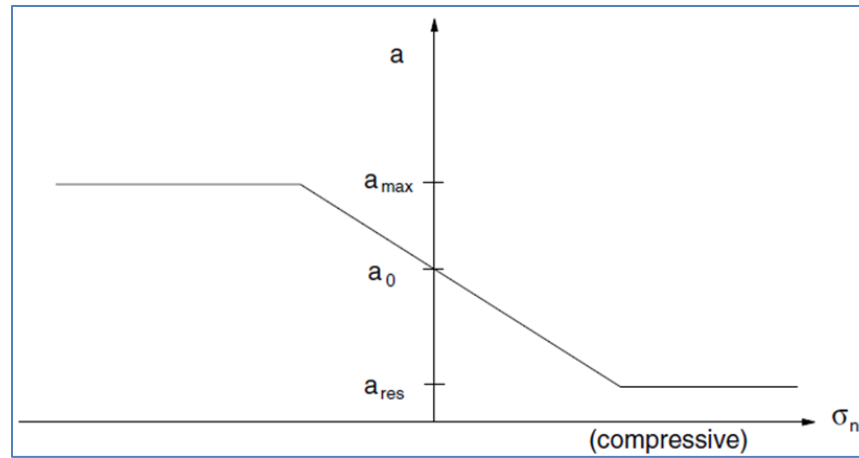
Figure 3.9 Relation between hydraulic aperture, and joint normal stress (Itasca, 2011)

The domain pressures are calculated by the following formula:

$$p = p_o + K_w Q \frac{\Delta t}{V} - K_w \frac{\Delta V}{V_m} \qquad\qquad 3.14$$

Where p_o is the domain pressure in the preceding timestep;

Q is the sum of flow rates into the domain from all surrounding contacts;

K_w is the bulk modulus of the fluid;

$V = V - V_o$; and

$V_m = (V + V_o)/2$,

Where V and V_o are the new and old domain areas, respectively.

The loads exerted by the water on the edges of the surrounding blocks can be calculated. These forces are then added to the other forces to be applied to the block contact points, such as the mechanical contact forces and external loads. As a consequence of this procedure, total stresses will result inside the impermeable blocks, and effective normal stresses will be obtained for the mechanical contacts.

3.3 Experimental Methodology

Whether using FLAC or UDEC, the input parameters for these codes should be predicted by testing the elements of the rock mass, such as intact rock blocks and joints based on small-scale samples in the laboratory. Also, to understand and get a sense about the numerical results, the experimental work is very essential. Therefore, in this research, the author decided to do some experimental work on rock mass elements.

Samples from two sites were selected by the author to do experimental work. One of these sites is the Birchover Quarry in Derbyshire (Post Code: DE4 2BN) in the UK. Birchover Gritstone is from the Millstone Grit of Carboniferous age. The rock type of this quarry is pink to buff fine grained sandstone, which was selected for comparison of the numerical results of jointed rock samples with triaxial test results using a Hoek and soil cells so as to study the

reliability of using UDEC to study jointed rock mass, as presented in chapter 7. The second site is in Iraq, concerning the foundation of an earth dam, which was selected so as to study the equivalent strength and deformability parameters of its rock mass by UDEC, as presented in Chapter 8.

The laboratory test programme was designed and carried out by the author. The author was also in charge of the analysis and interpretation of the test data. It should be noted that the processes of coring and preparation of rock samples and the operation of compression machine for UCS and triaxial tests were conducted by the responsible technician in the rock mechanics laboratory in the University of Nottingham, under the supervision of the author.

For both sites the rock mass's elements such as intact rock blocks and joints were tested so as to find the physical and mechanical parameters to use them as input to the numerical code UDEC.

The following sections present the apparatus and testing machines that have been used in this study at the University of Nottingham laboratories in the experimental work:

3.3.1 Sample preparation

The samples preparation were performed according to ISRM (1981). Cylindrical samples of 84mm length and 40mm diameter were drilled out using core drill (Figure 3.10a) from each of the 75mm diameter

cores and 300mm length of the Surqawshan site rock material where-as samples were drilled out from rock blocks (Figure 3.10b) of Birchover Quarry. In addition, Jointed sandstone samples (120 mm long by 50 mm diameter) were prepared from Birchover Quarry by creating a single smooth planar joint at a dip angle (θ) measured from horizontal using the saw cut shown in Figure 3.10c. The samples ends were grounded using the Rock Grinder shown in Figure 3.10d. Fur-thermore, cylindrical samples of 20 mm length and 40mm diameter were prepared to conduct tensile strength and point load tests.
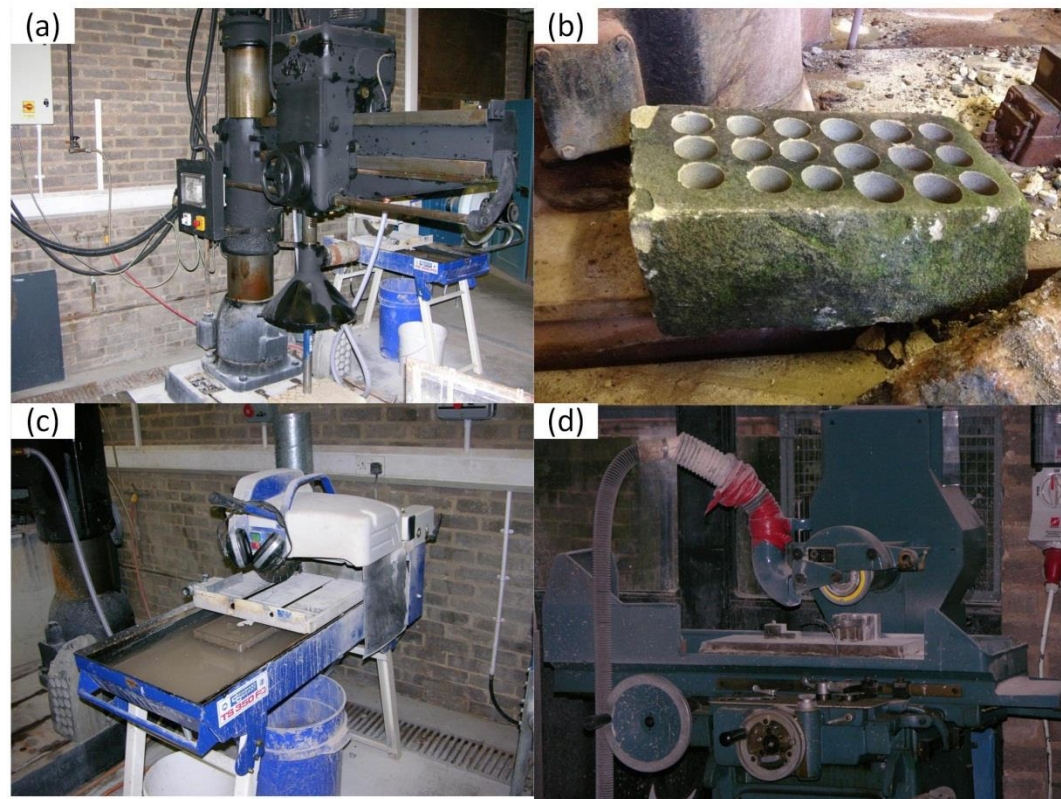
Figure 3.10 Samples preparation apparatus, (a)Core Drill, (b) cored rock block, (c) Saw cut, (d) Rock Grinder

3.3.2 Compression tests

The UCS and triaxial tests were conducted for both Birchover Quarry and the Surgawshan dam site using the RDP Howden 1000 kN servo-controlled hydraulic stiff press. Axial load was applied at a displacement rate of 0.002 mm/sec. The axial displacement was measured by a pair of linear variable differential transformers (LVDTs) with a precision of $\pm$ 0.005mm mounted on both sides of the samples between the platens as shown in Figure 3.11. For triaxial tests, Hoek cell was used.
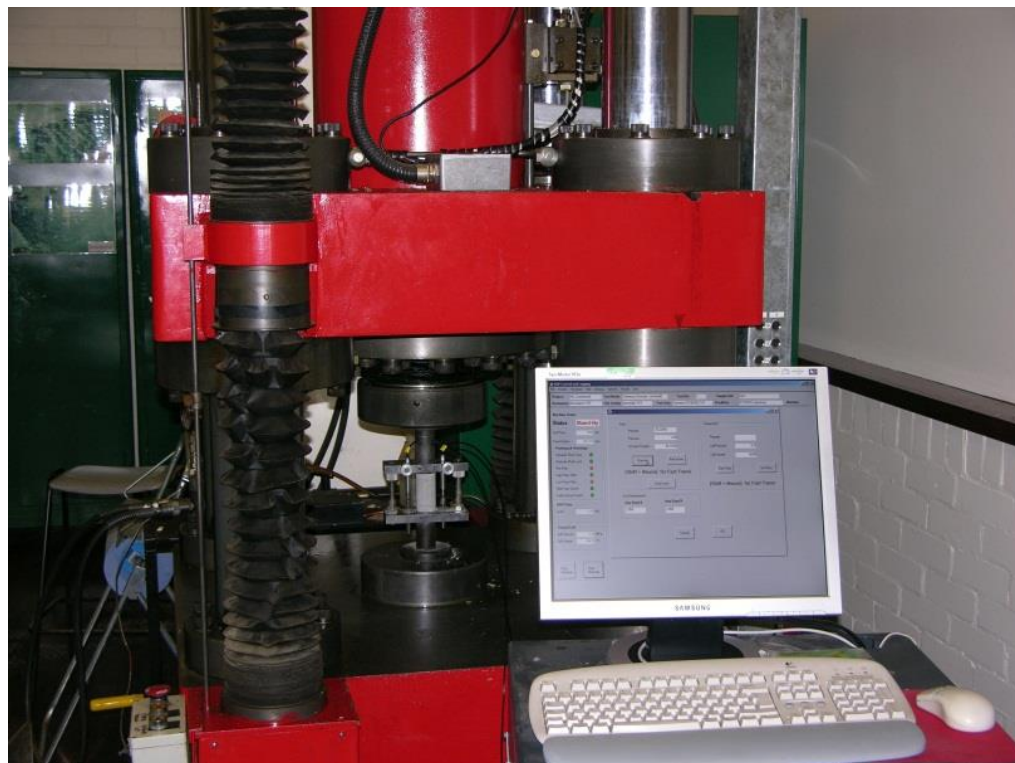
Figure 3.11 The RDP Howden 1000 kN servo-controlled hydraulic stiff press

3.3.3 Direct shear test

The direct shear box apparatus (Wykeham Farrance model 27-WF2160) shown in Figure 3.12 is normally used for soil samples testing. In this work it was used to determine the interface properties of a smooth planar rock joint. The test equipment consists of a metal box which is split into an upper and lower half and in which two samples (upper and lower) are placed. Normal stress is applied to the upper surface of the upper sample using a dead load and hanger. Shear stress is applied along the joint between the samples by moving the bottom half of the box with a displacement rate of 0.5 mm/min relative to the top.
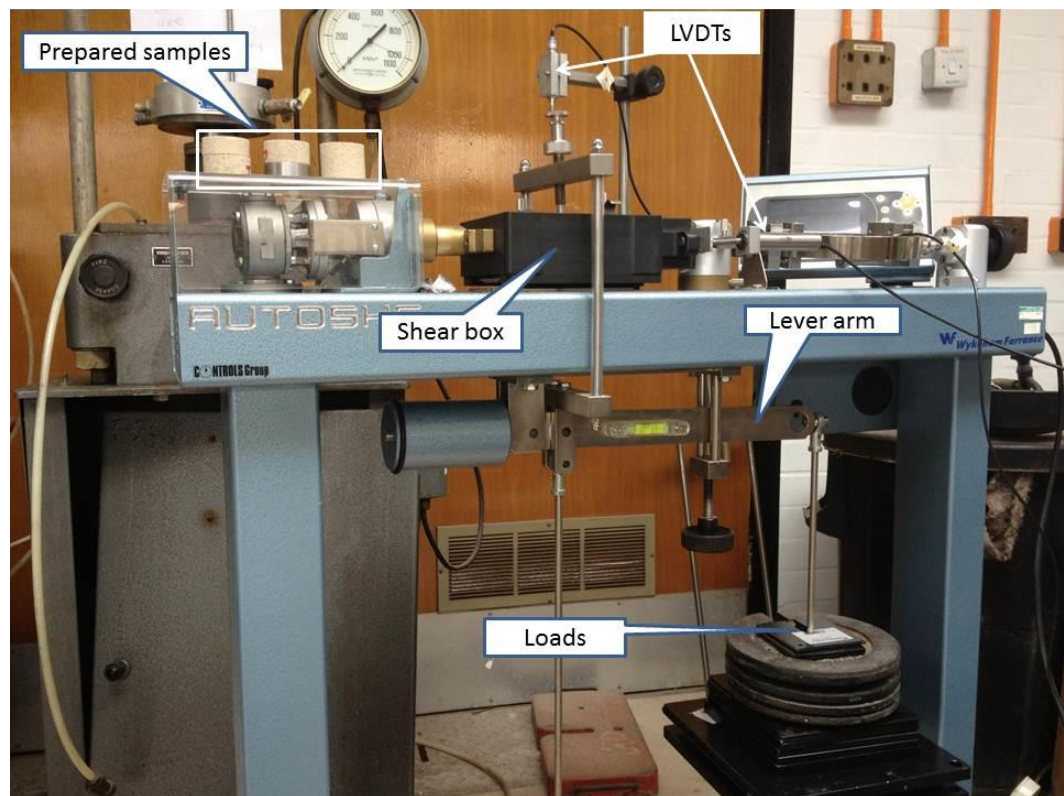
Figure 3.12 Direct shear box apparatus

3.3.4 Brazilian Test

The Brazilian test, also referred to as the 'indirect tensile strength' (ISRM, 1981) was used to estimate the uniaxial tensile strength of prepared intact rock samples. A disc-shaped rock sample was loaded diametrical as a strip load by two steel loading jaws shown in Figure 3.13a using Denison testing machine shown in Figure 3.13b. The rate of loading should be about 200 N/sec so that the failure in the rock samples occurs within 15-30 sec (ISRM, 1981).

(a)   (b)   (c)
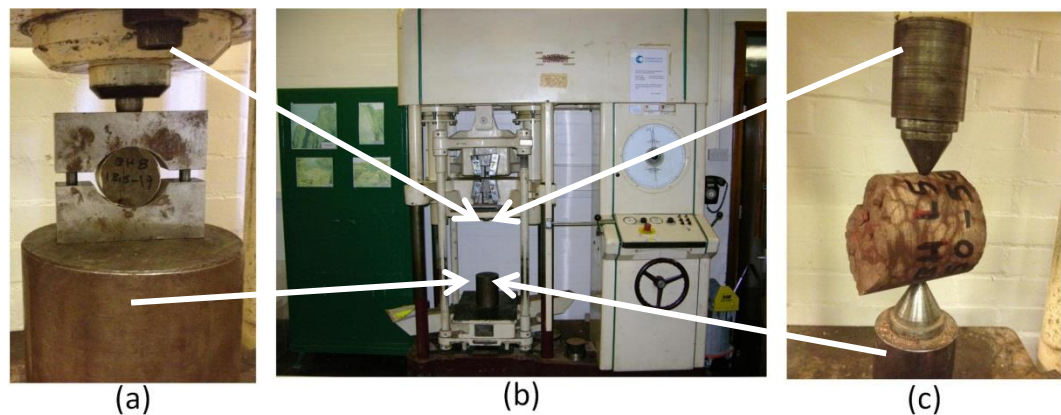
Figure 3.13 Testing apparatus, (a) Brazilian test apparatus, (b) Denison testing machine, (c) spherically truncated conical plat-ens

3.3.5 Point load test

The point load test is an index that can be used to predict UCS of intact rock. The International Society of Rock Mechanics (Franklin, 1985) has suggested a procedures for testing and results calculation. This can be done on three types of samples: diametrical core, axial

core, and lump or block particle. In this research the diametrical test is selected to perform the test on selected samples from the Surqawshan dam site. In this study, the testing machine shown in Figure 3.13b was used to load a cylindrical sample by a pair of spherically truncated conical platens (Figure 3.13c) that have an opening angle of 60°.

3.3.6 Mineralogical analysis XRD and SEM-EDX

A combination of X-ray diffraction (XRD) (Figure 3.14a) and Scanning Electron Microscope combined with Energy Dispersive X-ray (SEM-EDX) (Figure 3.14b) were used to determine the average mineralogical composition of the Surqawshan rock samples. The rock samples from different boreholes and depths were ground into a powder and passed through a 75µm sieve for XRD examination. These samples were positioned and flattened carefully in the sample holder of the XRD machine. A scanning speed of 2° per minute and a step of 0.05° (step times = 4 Sec.) were used in the range of 10 and 70° using a Bruker – AXS D8 Advance XRD equipment with a CuKα radiation at an accelerating voltage of 40 kV.

SEM-EDX analysis was undertaken using a Philips XL 30 ESEM-FEG fitted with an Oxford Instruments INCA model spectrometer for energy-dispersive X-ray (EDX) analysis. This was done to characterise both the microstructural features and the elemental composition of the

samples using BSE mode with a spot size of as little as 2-3 µm and 20 kV accelerating voltage.

The chemical composition was determined by EDX point analysis on powdered samples as well as EDX- map analysis on polished intact rock samples. The two types of SEM samples were coated with approximately 15nm layer thick of carbon. First, a cube of 10mm cut from a core cylindrical sample with a dimension of 75mm diameter and 300mm length. The surfaces of the specimens (intact rock samples) were exposed to an initial polishing using a fine emery paper to ensure a smooth and plane surface. After that, the specimens surface were mechanically ground with 200, 400, 800 and 1200 grit abrasive papers before the coating process. The samples were finally coated using an automatic sputter coater device before acquiring the SEM images. The powder samples were prepared by pressing to flatten their surface and subsequently fixed on small SEM stubs before the coating.

(a)   (b)

**Figure 3.14 (a) X-ray diffractometer type Siemens D500, (b)
SEM-EDX apparatus type Philips XL 30 ESEM-FEG**

3.4   Summary and Conclusions

In this chapter the methodology adopted has been explained and
justified. In numerical methodology, the continuum and discontinuum
codes have been presented as modelling tools. In the continuum code
(FLAC), the foundation is considered as a continuum that contains a
joint. This joint is introduced in the FLAC as an interface. Also the
interface is used in the contacted area between the concrete dam and
the rock foundation; this will be used in the next chapter, which is
about the conceptual model. Simulating more than one of the
discontinuities in the rock mass is very complex and time-consuming.

This makes study of a rock mass by UDEC more practical than FLAC, as presented in this study.

In this thesis, the discontinuum code UDEC is used to study the rock mass behaviour under gravity dams using conceptual and realistic models whereas the continuum model FLAC is used to study the effect of a weak joint on dam's stability

In the experimental methodology, the brief description of selected sites from which the rock samples were taken for the required laboratory tests are presented in chapters 7 and 8. In addition, the apparatus and testing machines used in this study were presented.

Chapter 4 The Conceptual Model

4.1 Introduction

'*A model is an aid to thought, rather than a substitute for thinking*' (Starfield and Cundall, 1988).

In this chapter a conceptual model was developed so as to study the rock mass behaviour under a gravity dam. The model is a concrete gravity dam on a rock mass which was designed using the limit equilibrium method with a sufficient factor of safety against sliding. The dam with its foundation system is analysed using both FLAC and UDEC in a plane strain condition for simplicity. In both codes the seepage is coupled with stresses in order to obtain a realistic analysis. The behaviour of the intact material is treated as elastic perfectly-plastic (Mohr-Coulomb) and the area contact Coulomb slip model (elastic perfectly plastic) is used for joints.

4.2 Design of the Gravity Dam

In this thesis, the concrete dam was designed using the criteria for dams' stability mentioned in chapter 2. The dam was assumed to have a height of 50m and a base length of 45m (see Figure 4.1). The height of the water in the reservoir was set equal to the dam height. The dimensions of the dam have been estimated so that the resultant of all forces across the base lies within its middle third (Thomas, 1976). Dams should be designed to be safe against overturning and sliding.
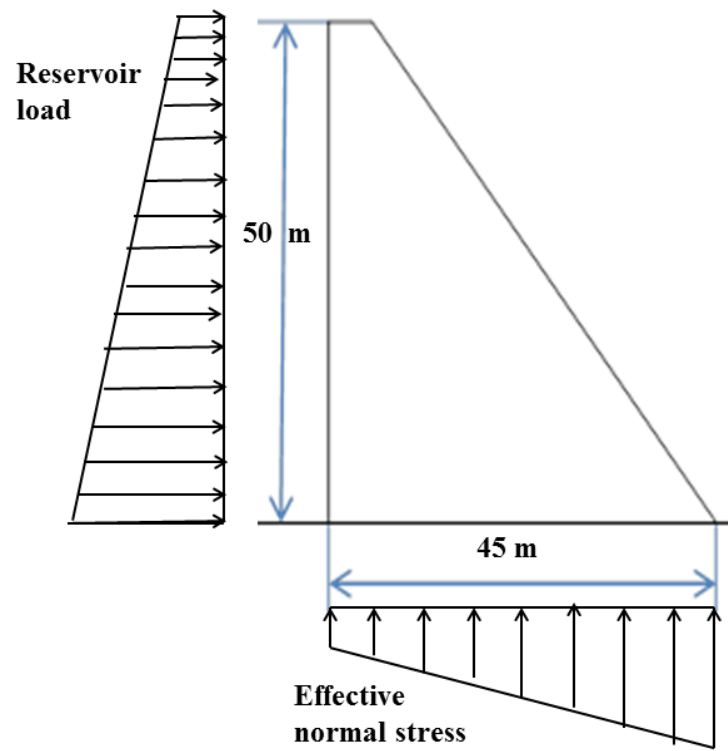
Figure 4.1 Dimensions of the concrete gravity dam

4.2.1 Loads

In reality, there are potentially many loads acting on a dam. For the conceptual model used here, only the dead load and reservoir load are taken into account. For real design of dams, all types of loads should be considered. Full details about the potential loads that can affect dams can be found in a variety of texts, for example Novák et al. (2007).

4.2.2 Stability Analysis

There are two types of assessment of the sliding factor. The first method is given by Equation 2.9, which gives the shear friction factor (F_{SF}) at the contact between the dam and the foundation. The F_{SF} should be greater than 3 according to the American Engineering Army Corps design criteria (USACE, 1995). The second method for determining a sliding factor (F_s) can be calculated by dividing the sum of the horizontal forces due to reservoir load ($\sum H$) by the sum of the vertical forces (N), as illustrated in Equation 2.5 (Jansen, 1988). The value of F_s should be smaller than 0.75 for usual loading. Also, induced stresses in the concrete and foundations must not exceed the allowable stresses in both materials (Varshney, 1982).

The stability of the dam was computed using Equations 2.5 and 2.9, the results of which are shown in Table 4.1. The uplift pressure was assumed to be distributed linearly from heel to toe of the dam

Table 4.1 Stability assessment results

Stability Type	Ratio
The shear friction factor, F_{SF} (Eq. 2.9)	3.410
Effective sliding factor, F_s (Eq. 2.5)	0.625

The resultant force was computed and it was found to be within the middle third of the dam's base (eccentricity of resultant force from the centreline of the dam base, e=3.177m). The induced distribution of stresses due to the dam weight and reservoir load was calculated according to USACE (1995). The minimum effective vertical stress at the heel was found to be 0.256 MPa; the maximum value at the toe of the

dam was 0.633 MPa. Also, the stability of the dam against overturning

(F_o.) (computed as a ratio of resistant moment to the disturbing mo-

ment about the toe of the dam) was found to be 1.7

4.3 Geometry and Properties

Figure 4.2 shows the UDEC model geometry which was used in this re-

search.
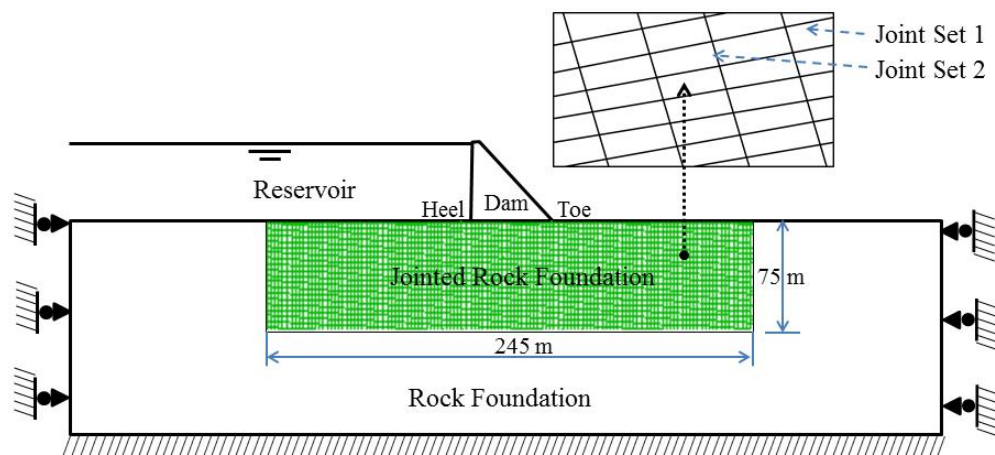
Figure 4.2 Model geometry (joint details apply to UDEC model)

For the continuum model the extent of the foundation rock was 500m

in width and 150m in depth. For the discontinuum model, the dam

foundation was divided into two regions; the first region (75m ×

245m) under the dam was considered as a blocky rock mass of two

sets of joints (see magnified area in Figure 4.2); the second region

(with outer dimensions equivalent to the continuum model) was con-

sidered as an intact rock. The size of the individual blocks in the joint-

ed foundation was 2m by 4m. The boundary conditions were as follows; the sides were restrained in the horizontal direction and the base was restrained in the vertical and horizontal directions. Tables 4.2 and 4.3 show the properties for the model components. These properties are as follow: bulk modulus (K), shear modulus (G), joint normal stiffness (k_n), joint shear stiffness (k_s), cohesion (c), and tensile strength (σ^t), coefficient of friction ($\emptyset$). The hydraulic properties of joints such as joint permeability factor (kj), minimum joint aperture (a_{res}) and maximum joint aperture (a_{zero}) are shown in Table 4.4

For the UDEC model since the medium was considered as a jointed rock mass, the stiffness of fictitious joints was calculated using Equation 4.1 which was developed by Itasca (2011) so that the stiffness of the discontinuum model is equivalent to the continuum model:

$$k_n = factor \; x \; max \left[\frac{\left(K + \frac{4}{3}G \right)}{\Delta z_{min}} \right] \qquad 4.1$$

Shear stiffness was assumed as $k_s = 0.5 \, k_n$, because as recommended by Itasca (2011) the best ratio between k_n and k_s is from 2 to 10.

The $factor$ is a multiplication factor (usually set to 10). In this study it was set to 5.

K and G are the bulk and shear moduli, respectively; and Δz_{min} is the smallest width of an adjoining zone in the normal direction as shown in Figure 4.3.
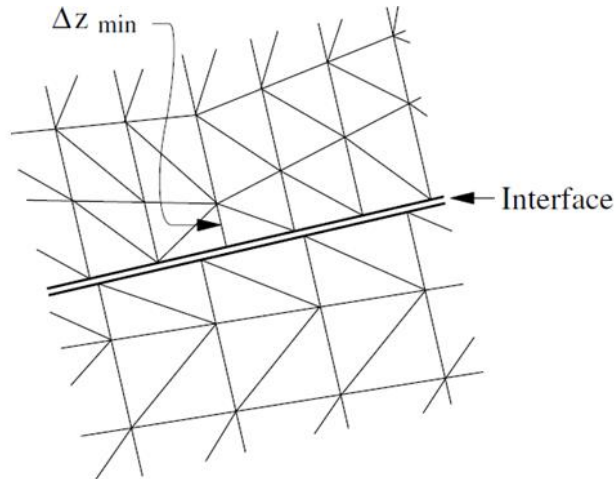
Figure 4.3 Zone dimension used in stiffness calculation (Eq.4.1)

Table 4.2 Material properties

Material	Density (ρ) kg/m^3	K GPa	G GPa	c MPa	$\emptyset$ Degree	σ^t MPa
concrete	2400	12.2	10.3	-	-	-
intact rock	2415	26.8	7.0	0.6	35	0.3

Table 4.3 Material properties of joints

	K_n GPa/m	K_s GPa/m	c_j MPa	$\emptyset_j$ degrees	σ^t_j MPa
rock-dam contact	3	1	0.6	40	0.3
Joints					
Case 1(intact)	54	27	0.4	32	0.2
Case 2(reduced)	54	27	0	32	0

Table 4.4 Hydraulic properties of joints

discontinuities	k_j Pa^{-1}S^{-1}	a_{zero} mm$\times10^{-4}$	a_{res} mm$\times10^{-4}$
joints (rock-rock contacts)	300	2	1
dam-rock contact	300	2	1

4.4 Simulation of the Models

The construction simulation of the gravity concrete dam is achieved in three stages. Firstly, the foundation rock is constructed; in this stage the in-situ stresses are initialized and the displacements (after reaching equilibrium) are reset to zero. Secondly, the concrete dam is installed; in this stage the stresses and displacements under the dam are recorded. Also the displacement of the dam crest is calculated. Thirdly, the water load due to the reservoir is applied and the same recordings from stage two are made again.

For the discontinuum model, several joint configurations were prepared to study the effect of joint dip on the stability of dams. The whole rock mass was rotated counter-clockwise, as shown in Table 4.5. The models generated were named according to the rotation (dip angle) of joint set 1 as follows: J0, J5, J15, J30, J37, J45, J60, J75, and J90. Each case was modelled in two conditions; case 1 considered the 'intact' joint strengths in Table 4.3 whilst case 2 used the 'reduced' strengths (setting joint cohesion and tensile strength to zero while keeping the joint friction angle as 32 degrees).

Table 4.5 Joint set geometry

Joint Set	Joint Dip	Spacing (m)
Set 1	$0 + \theta_r$*	2
Set 2**	$86 + \theta_r$	4

*θ_r is degree of rotation, from 0 to 90.
** See Figure 4.2

4.5 Results

4.5.1 Stresses under the dam

Normal and shear stresses were calculated under the dam for the FLAC model and for both joint strength cases in the UDEC model (intact and reduced – see Table 4.3). Figure 4.4 shows the stress distribution at the contact between the dam and the foundation for model J0 (only intact joint strength considered, case 1). The values before (R Empty) and after (R Full) reservoir filling are shown. It can be seen that there is excellent agreement between the FLAC and UDEC results for the model and the conventional limit equilibrium analysis method. One can conclude that both codes might give the same results when joints strength is high. However, for case 2 (reduced joint strengths), the results are different, as can be seen in Figure 4.5 for case J0. In this case, the stresses under the dam fluctuate and high stress concentrations caused by block rotations are predicted by UDEC and as a result the normal and shear stresses are reduced to zero at some points under the dam. This finding is very important to calculate the safety factor against sliding because the contact area between the foundation and the concrete dam will reduce due to the loss of normal stress. In addition, the normal stress increases (point loads) under the dam may lead to the development of new cracks in the rock blocks and shear failure in intact rock, which depends on the tensile strength of the blocks and the intact shear strength of the rock, respectively.
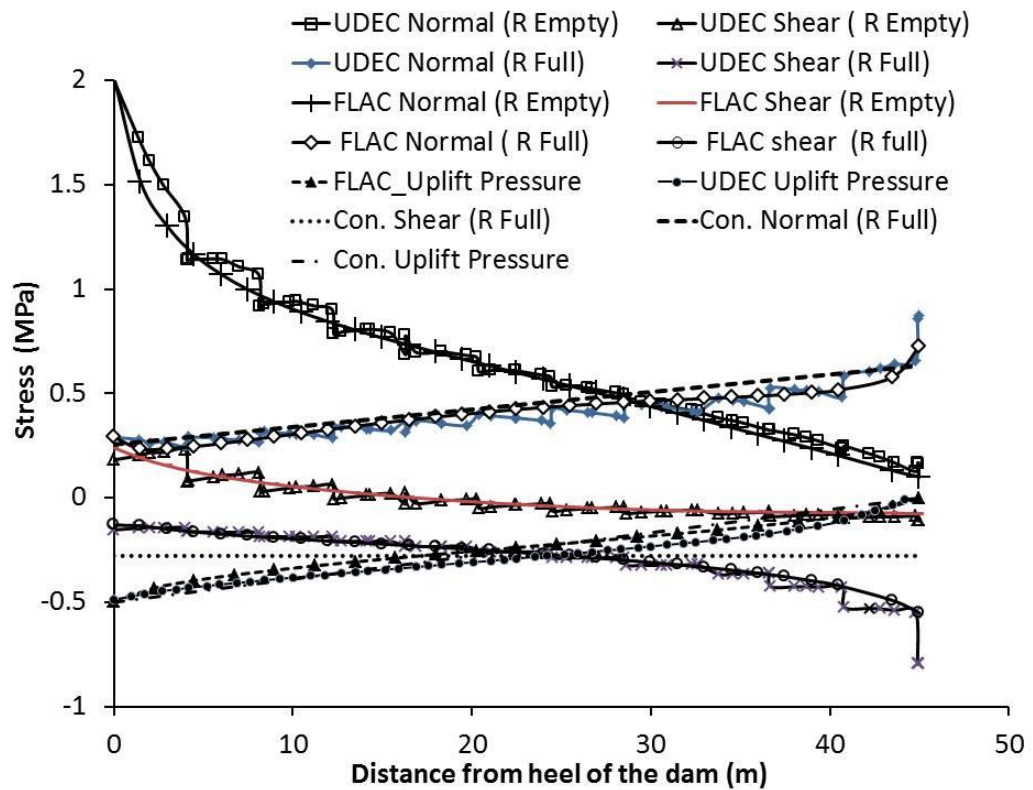
Figure 4.4 Stresses in contact area between the dam and the foundation (for UDEC: Model J0, case 1)
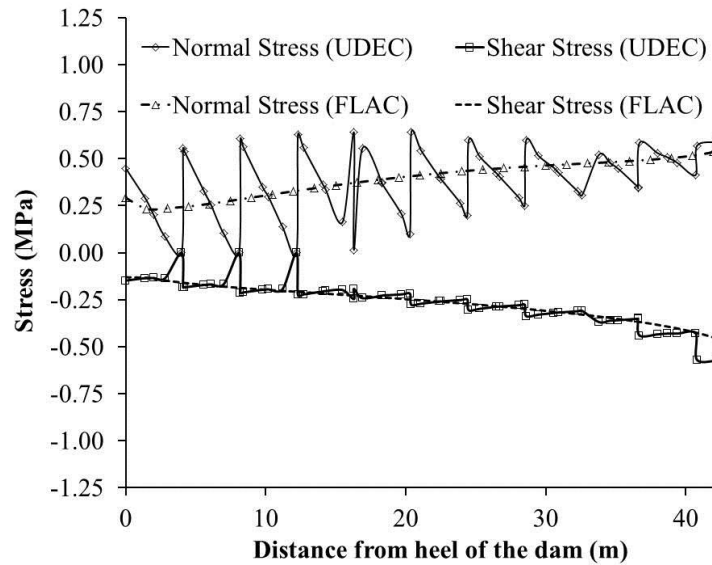
Figure 4.5 Stress distributions under the dam (for UDEC: Model J0, case 2).

4.5.2 Displacements under the dam

The horizontal displacement of the dam at the toe and heel are presented in Figure 4.6. It can be seen that the joint configuration has an important effect on the dam's stability. The results indicate that both models J5 and J15 (joint set 1 dip angle = 5 and 15 degrees) are affected by joint strength reduction. The other joint rotation results are not significantly affected by joint strength reduction. To confirm this observation, the vertical displacement at the dam-foundation contact was computed for both the full joint strength and joint strength reduction cases, as shown Figure 4.7. This figure again shows that the critical cases are J5 and J15. The results from the FLAC model are also shown in Figure 4.7 from which it can be concluded that the deformation calculated by FLAC is lower than in UDEC because of joint deformation.
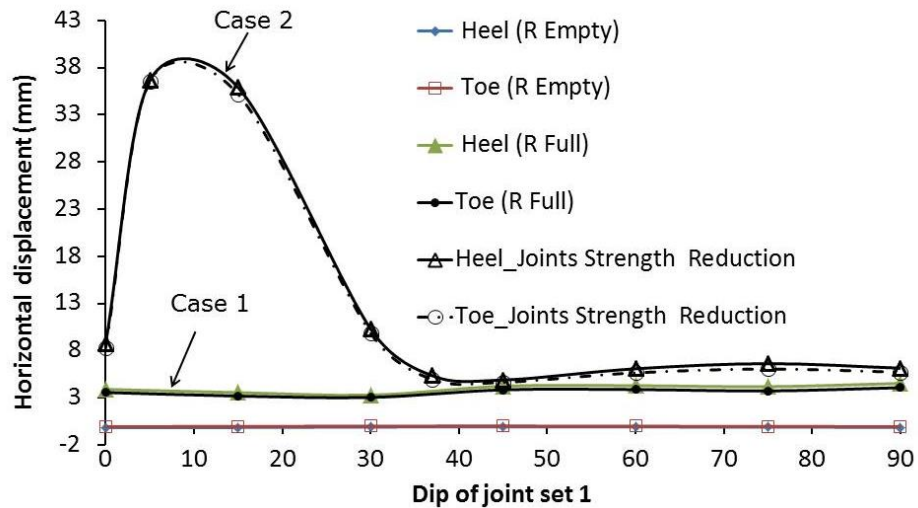
Figure 4.6 Horizontal displacement at toe and heel with dip angle of set 1 (UDEC)
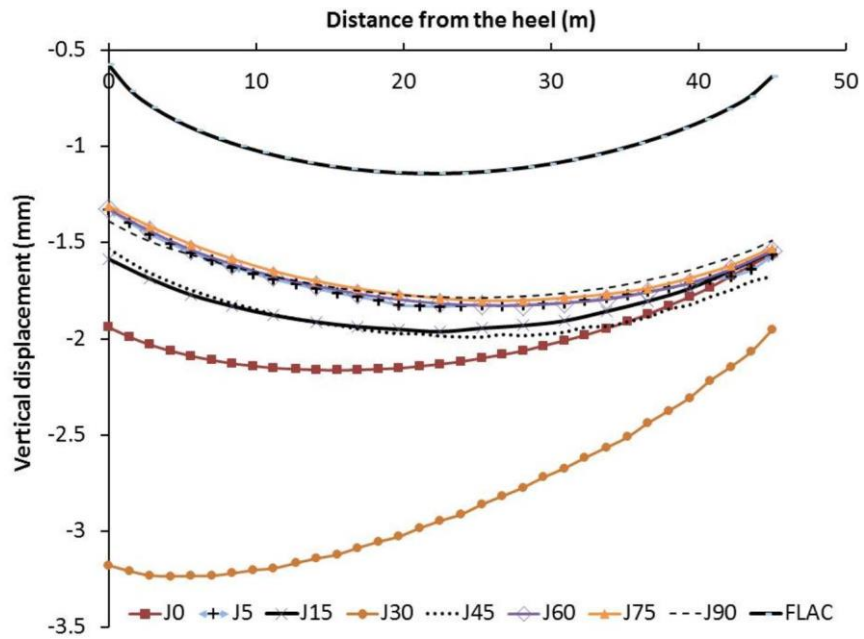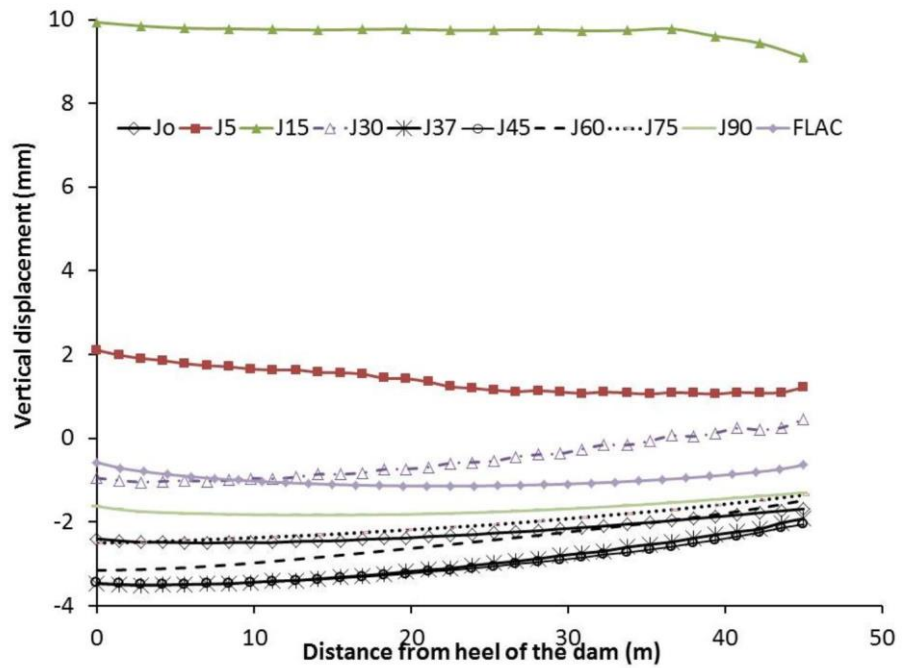
Figure 4.7 Vertical displacements for all models, (a) before joint strength reduction (case 1), (b) after joint strength reduction (case 2)

4.5.3 Stability assessment

The assessment of a dam's stability is not an easy task in Engineering. This task is possibly more difficult where the dam structure is built on blocky weak jointed rock because the plane of failure is not clearly defined. In case of reduced joint strength the system may not fail along a plane directly beneath the dam. In this study different techniques have been used to assess the stability of the model. In the first technique, Equations 2.5 and 2.9 were used to check the stability against sliding, see Figures 4.8 and 4.9. The second technique measured displacements at selected points under the dam in both vertical and horizontal direction, as shown in Figures 4.6 and 4.7. A third method, applicable only to the numerical models, considers if a state of numerical equilibrium can be reached whereby nodal velocities go to zero. In the UDEC simulations J5 and J15, the models did not reach a state of equilibrium. Figure 4.10 shows the velocity vectors in the model at an arbitrary stage after significant movements had occurred which illustrate the failure mechanism of the dam (sliding within the underlying foundation). The first technique indicated the dam was stable against sliding whereas the second and third technique indicated that both cases J5 and J15 failed. These analyses were applied on the model which was analysed by Barla et al. (2004) for deterministic joints (similar to the joint configuration used in this study). For the material and geometric details described it was found that the UDEC simulation did not reach a state of equilibrium, indicating that the structure was not sta-

ble and failed by sliding along the joints under the base of the dam. This suggests that the discontinuum results presented in Barla et al. (2004) may not represent a fair representation of equilibrium conditions after reservoir filling.

Figure 4.8 shows the sliding factor method results calculated by Equation 2.5. It can be seen that UDEC gives a higher sliding factor than FLAC and the conventional method. According to the UDEC results, if the cohesion between the dam and the foundation deteriorated, the dam might fail by sliding because the mobilized friction angle is almost equal to the available friction angle. This can be seen in Figure 4.9, which shows the shear friction factor (F_{SF}) predicted using Equation 2.9. Here UDEC (for intact joint strength) gives an F_{SF} value lower than the other methods, however the difference between results is less than 7%. This minor difference might be due to the method of predicting the effective normal stresses in the dam-foundation contact. In FLAC, the flow of water in the interface between the dam and foundation cannot be modelled and as a result the pore water pressure was predicted from the nearest grid points. In UDEC the flow can be modelled in the interface. Also in Figure 4.8 are the F_S results for reduced joint strength, and once again UDEC gives higher values except for case J15.
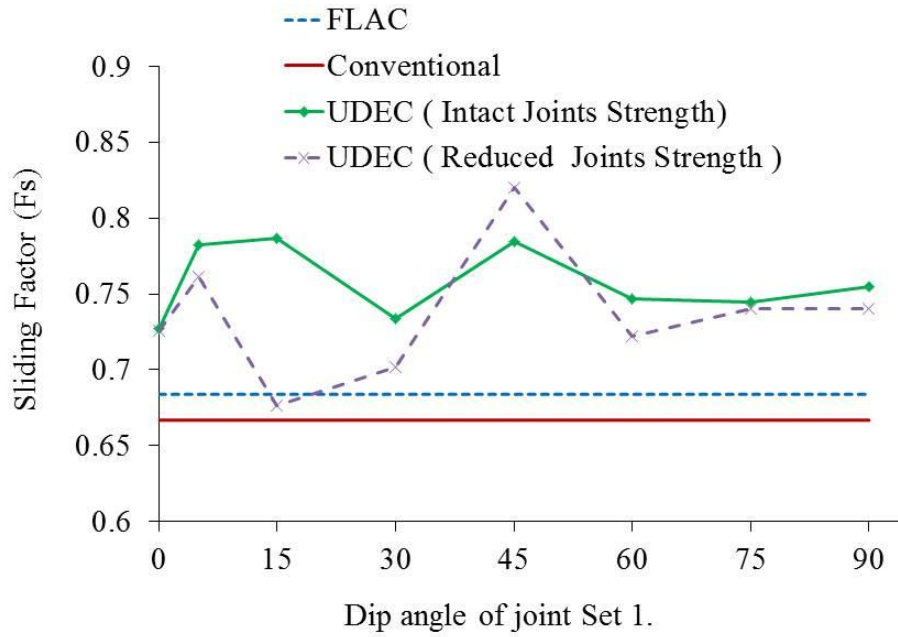
**Figure 4.8 Sliding factor (Equation 2.5) along the dam-rock in-
ter-face (should be less than 0.75 for stability)**
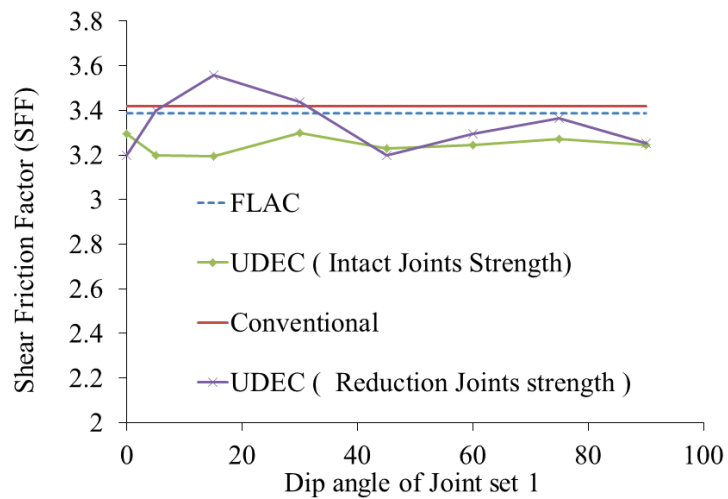
**Figure 4.9 Shear Friction Factor (Equation 2.9) along the dam-
rock interface (should be greater than 3 for stability)**
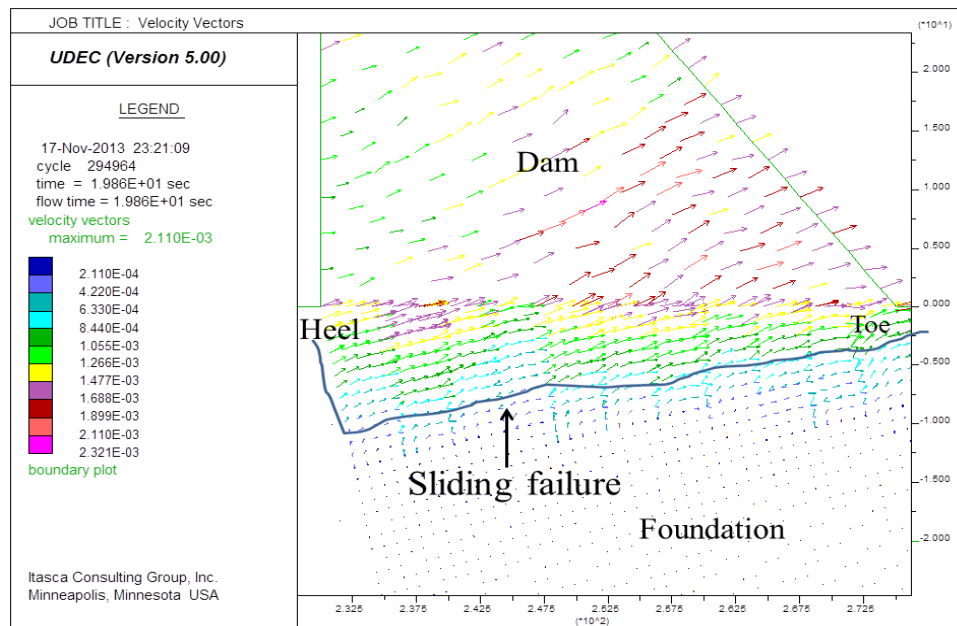
Figure 4.10 Velocity vectors for case J15 at sliding along foundation.

4.6 Summary and conclusions

In this chapter a hypothetical concrete gravity dam was designed using the conventional analytical methodology which is based on limit equilibrium theory with a reasonable factor of safety. The continuum and discontinuum approaches were used to analyse the dam. It was found that the codes give similar results to the conventional theoretical approach when the rock foundation blocks are not rotated by the stress regime created by the dam and reservoir. However, this similarity was found to depend on the joint strength and joint configuration. As the joint strength is reduced, UDEC was found to provide a seemingly more realistic representation of the behaviour of a jointed system and arguably a more realistic prediction of the stress distribution under

the dam. These results are valuable for engineers involved in future

dam design. Also, this study may be a guide to develop a new classifi-

cation system for dams on rock mass. This can be done by extending

the analysis from 2D to 3D using 3DEC and developing a conceptual

3D model.

In the next chapter the theoretical model that was developed will be

used to study the effect of a weak joint in upstream or downstream on

the dam stability using continuum code (FLAC).

Chapter 5 FLAC Analysis of a Weak Joint in the Dams Foundation

5.1   Introduction

There are many issues that affect the stability of concrete dams. One of these issues is the effect of weak layers in the foundation rock. Rock masses under dams often contain weak elements such as bedding planes, fractures, joints, faults and seams of weaker materials. They may be weathered by the flow of water which can lead to a reduction of strength, and in turn, may affect the stability of the dam. Generally, most of the incidents of instability have occurred in the foundations of dams (Boyer, 2006; Douglas, 2002). An example of such an incident is the failure of the Malpasset dam in France (Figure 2.21). Although the Malpasset dam is an arch dam, the failure mechanism of the foundation is directly relevant to this study.

A review of the literature shows that there are few studies of the effect of a weak joint in the foundation rock on the stability of a dam. Snell and Knight (1991) used a generalized theoretical model to study the influence of faults dipping upstream within ranges from 0-25 degree of dip under two types of dams: rockfill and a typical concrete gravity dam. They used the limit equilibrium method to calculate the factor of safety against sliding along the stratum or weak layer. They showed

that the possibility of failure due to sliding along these strata should not be ignored.

In previous chapter, both a continuum model (FLAC) and a discontinuum model (UDEC) were applied to evaluate which code gives the most realistic prediction on the stability of a concrete dam on a rock mass foundation. It was concluded that both codes can give similar results and this similarity was found to depend on joint strength and configuration. As the joint strength was reduced, UDEC was found to provide a better representation of the behavior of a jointed system and arguably a more realistic prediction of the stress distribution under the dam. Also the author showed that the failure mechanism for a discontinuum model is sliding along a joint dipped 15 degree in the upstream direction. As a result of this previous work this study investigated the influence of only one joint within a dam's foundation, on its stability.

5.2 Geometry and Properties

Figure 5.1 shows the base model geometry which was used previously in chapter 4. The foundation rock dimensions were 500m in width and 150m in depth. The boundary conditions were as follows; the sides were restrained in the horizontal direction and the base was fixed in both directions. The material properties for intact rock and the dam were obtained from Table 4.2. It should be mentioned that the property of the weak joint (rock/rock contact) used in this chapter is different from that used in chapter 4 because a weak joint used to represent a

weak layer that may exist in the foundation of dams. Table 5.1 shows

the properties for the contact properties.
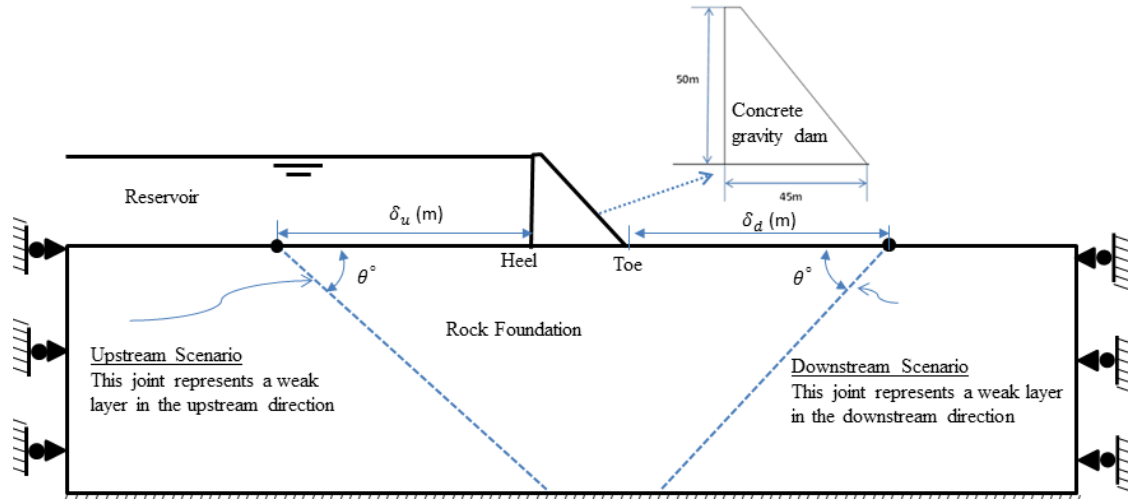
Figure 5.1 Model geometry

Table 5.1 Material properties of joints

	k_n GPa/m	k_s GPa/m	c_j MPa	$\varnothing_j$ degrees	$\sigma^t{}_j$ MPa
Rock-dam contact	3	1	0.6	40	0.3
Joint					
Case1	2.7	0.9	0.2	25	0.2
Case2	2.7	0.9	0	15	0

5.3   Simulation of the foundation with weak layer

To simulate the effect of a weak joint within the foundation on the sta-

bility of the gravity dam, several joint locations selected in the up-

stream and downstream directions with different dip angles were pre-

pared, as shown in Figure 5.1. The models generated were named ac-

cording to the location and dip angle of the joint, for example a joint

located in downstream direction at δ_d=5m from the toe of the dam with a dip angle of 30 degrees was named as DJ30at5 and a joint located at upstream direction at δ_u=4.5m from the heel with a dip angle of 60 was named as UJ60at4.5. Each case was modelled in two conditions; Case 1 considered the 'intact' joint strengths whilst Case 2 used the 'reduced' strengths (setting joint cohesion and tensile strength to zero while reducing the joint friction angle to 15 degrees).

For a weak layer located in the upstream direction, three joint locations were chosen as follows: at the heel of the dam, at 4.5m from the heel, and at 35m from the heel. For each location, six dip angles were checked: 15, 30, 45, 60, 75, and 90 degrees. Eighteen models in all were generated for the upstream side. For a weak layer located in the downstream direction, four locations were chosen: at the toe of the dam and at 5, 20, and 50 m from the toe, respectively. For each location the same six dip angles used in the upstream cases were checked, with the exception that for joints located at the toe, only dip angles of 15, 30 and 90 degrees were checked. Twenty one models were generated for the downstream side.

5.4 Results

5.4.1 Displacements

To illustrate the effect of a weak layer on the stability of dams, the vertical displacements were measured along the contact between the

rock and foundation. Also the horizontal displacements were measured at the top (crest) of the dam on the upstream face.

5.4.1.1   Downstream scenario

The horizontal displacement at the crest of the dam versus the dip angle of the joint modelled is presented in Figure 5.2. The horizontal displacement for the base model is shown for comparison. It can be seen that the joint location and its dip angle have an important effect on the dam's stability. The results indicate that the dam is not stable when the dip angle of the weak layer (Case 2) is 15 degrees and is located at a distance of δ_d/H of 0.1 and 0.4 (the circled 'Failed model' results in Figure 5.2 represent models that did not reach numerical equilibrium, indicating dam instability).

To confirm this observation, the vertical displacement at the dam-foundation contact was computed for the models that have a joint dipping upstream in the downstream direction, as shown in Figures 5.3-5.7. These figures again show that the critical cases (where the model failed to reach numerical equilibrium) are where dip angle is 15 degrees and the location of the joint is between 0.4 and 0.6 times the height of the dam measured from the toe (a $\delta_d/H = 0.6$ model was also run (Figure 5.7) for a joint dip of 15 degrees which did reach a stable state similar to the $\delta_d/H = 1.0$ model). It can be seen that when the distance between the toe and the joint location is more than half the

dam's height, the effect of reducing the shear strength (Case 2) on the dam deformation is not serious.

Generally, when the strength of the joint is reduced (Case 2), the horizontal displacement at the crest of the dam decreases with an increase in dip angle up to 45 degrees and then the displacement increases when the dip of the joint becomes larger than 45 degrees
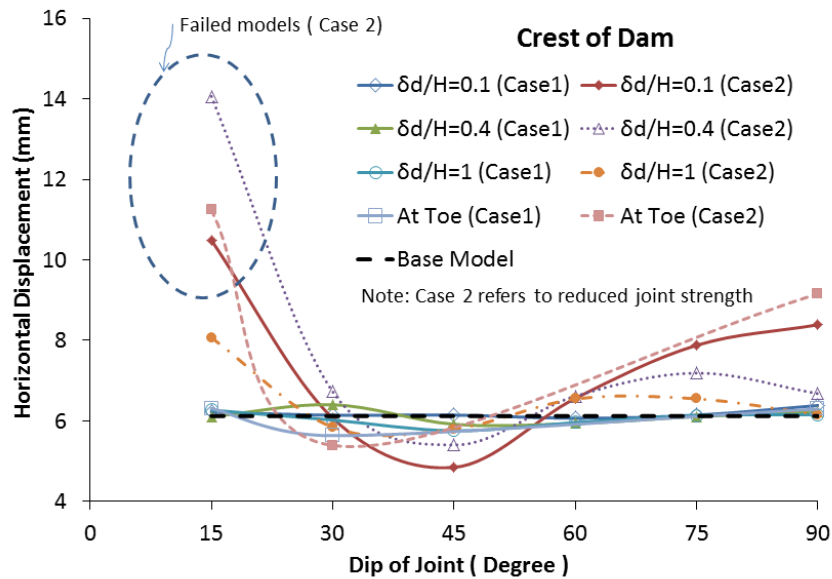
Figure 5.2 Horizontal displacements at the crest of the dam with variation of joint angle - downstream scenario
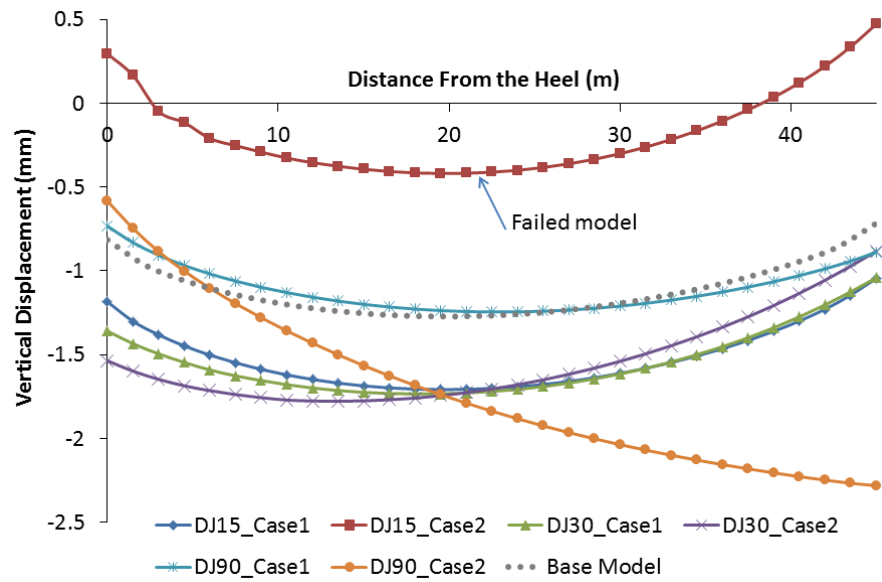
Figure 5.3 Joints located at toe ($\delta_d/H = 0$) of the dam – down-stream scenario
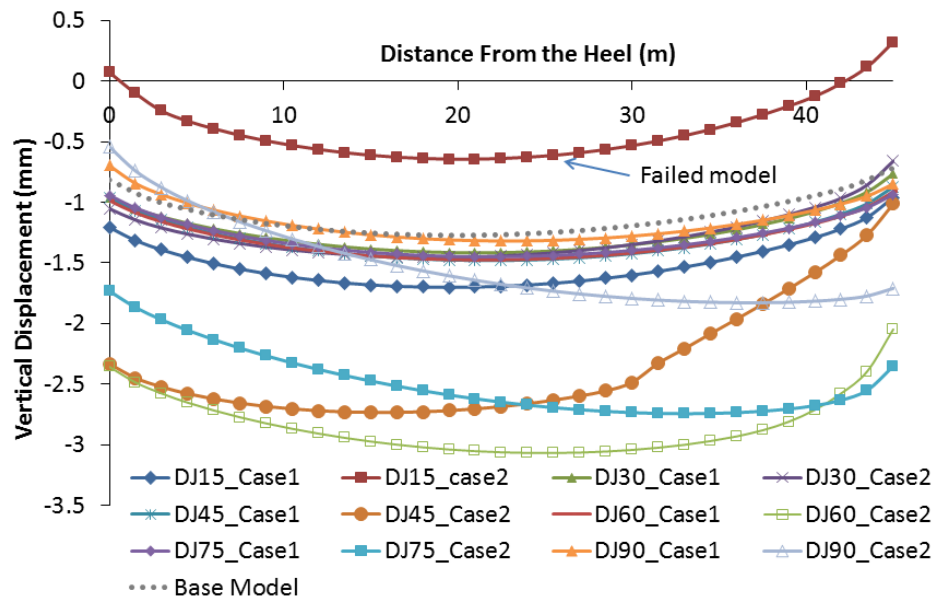
Figure 5.4 Vertical displacement for joint located at 5m ($\delta_d/H = 0.1$) from the toe of the dam – downstream scenario
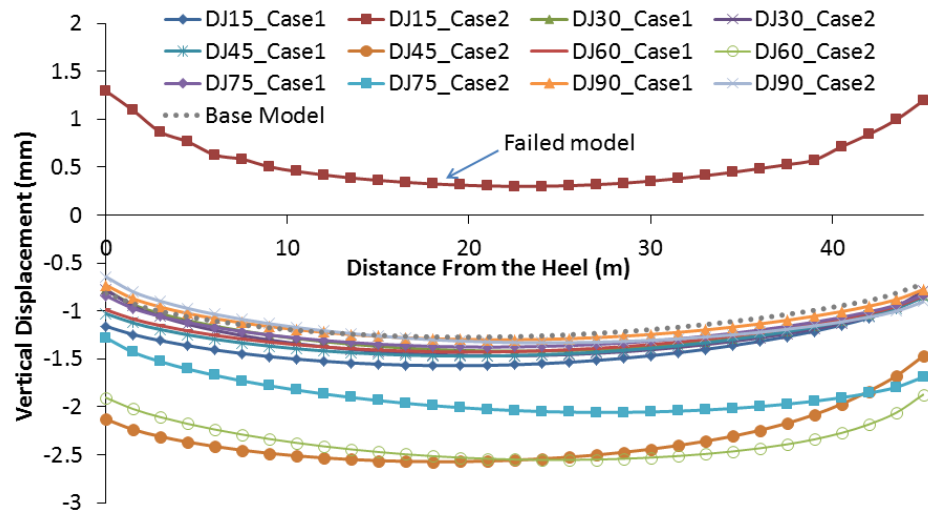
Figure 5.5 Vertical displacement for joint located at 20m($\delta_d/H = 0.4$) from the toe of the dam – downstream scenario
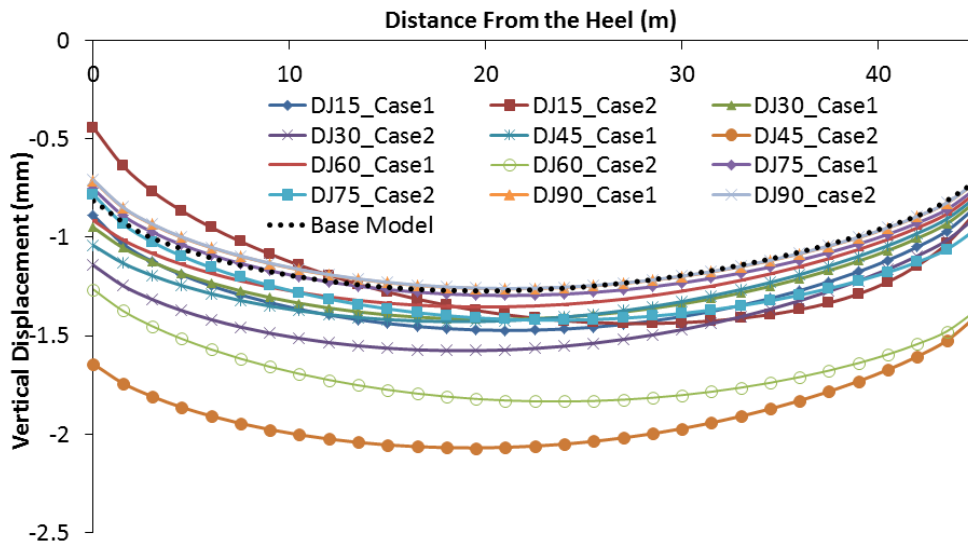
Figure 5.6 Vertical displacement for joint located at 50m ($\delta_d/H = 1$) from the toe of the dam – downstream scenario
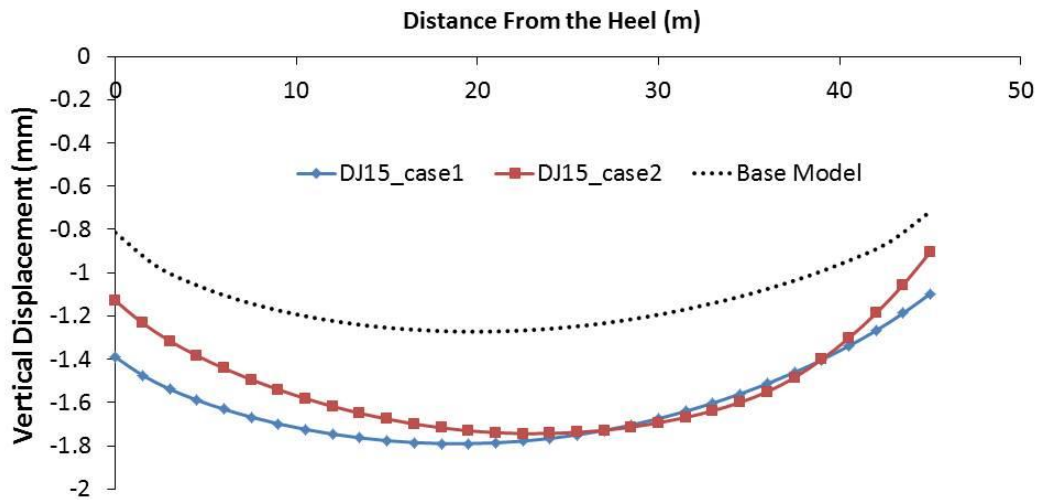
Figure 5.7 Vertical displacement for joint located at 30m ($\delta_d/H = 0.6$) from the toe of the dam – downstream scenario

5.4.1.2   Upstream scenario

Figure 5.8 shows the results for crest horizontal displacements versus the joint dip angle for the joint positions considered. Generally the horizontal displacement tends to reduce with increasing joint dip angle up to an angle of about 60 degrees. It can be seen that the case where joint dip angle is 15 degrees gives the maximum displacement, especially when the shear strength of the joint is reduced (Case 2) whereas a joint with a dip angle of 60 has the minimum displacement when the joint's strength is reduced.
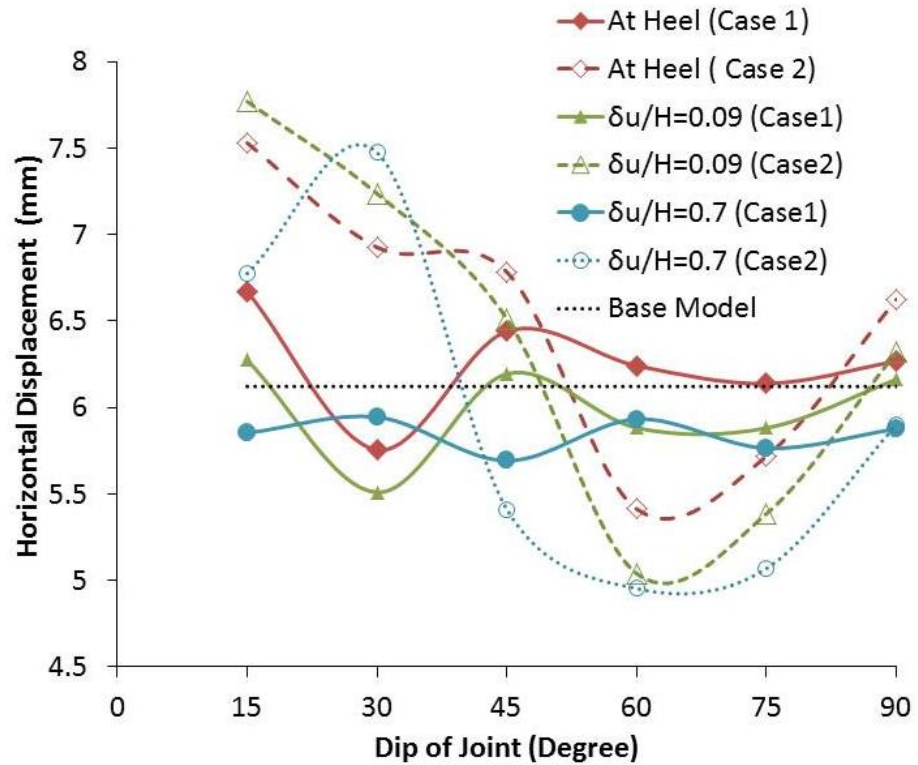
Figure 5.8 Horizontal displacements at crest of dam with joint angle – upstream scenario

Figures 5.9-5.11 show vertical displacements beneath the dam for the joints located upstream of the dam. Overall, the models have similar trends to the downstream scenario and the maximum displacement occurs when the joint dip angle is between 30° and 60° for the reduced joint strength (Case 2). It can be seen that the joint dip has a similar effect on vertical displacement irrespective of joint location in the upstream direction. This is due to the fact that the resultant force induced by the reservoir and dam loading acts on the downstream side of the joint and causes slipping along the joint, without causing a

global instability Furthermore, the location of the maximum vertical displacement for Case 2 is approximately at one-quarter of the dam base measured from the heel, whereas the maximum vertical displacement is at the mid-base of the dam for Case 1 and the shape of deflection line is similar to that of the base model.
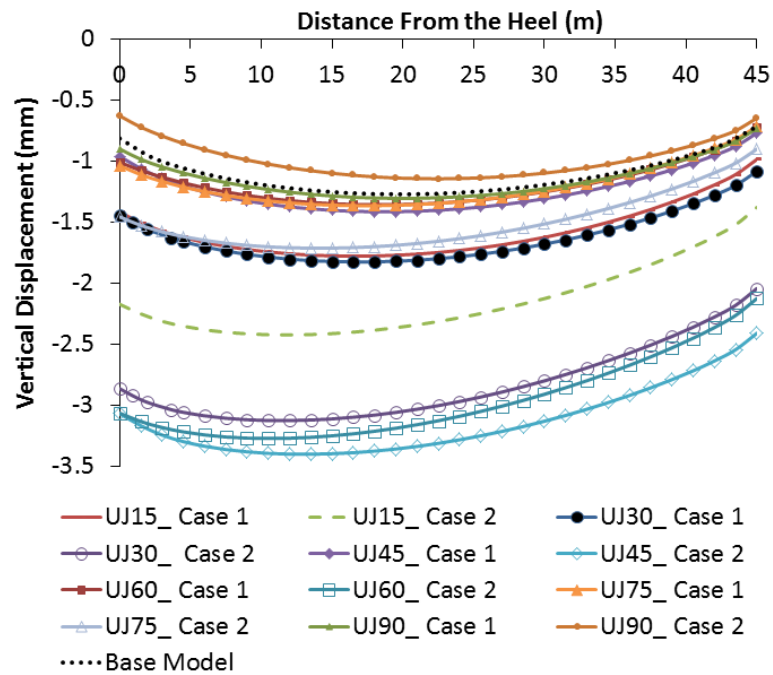
Figure 5.9 Vertical displacements for joint at the heel ($\delta_u/H = 0$) – upstream scenario
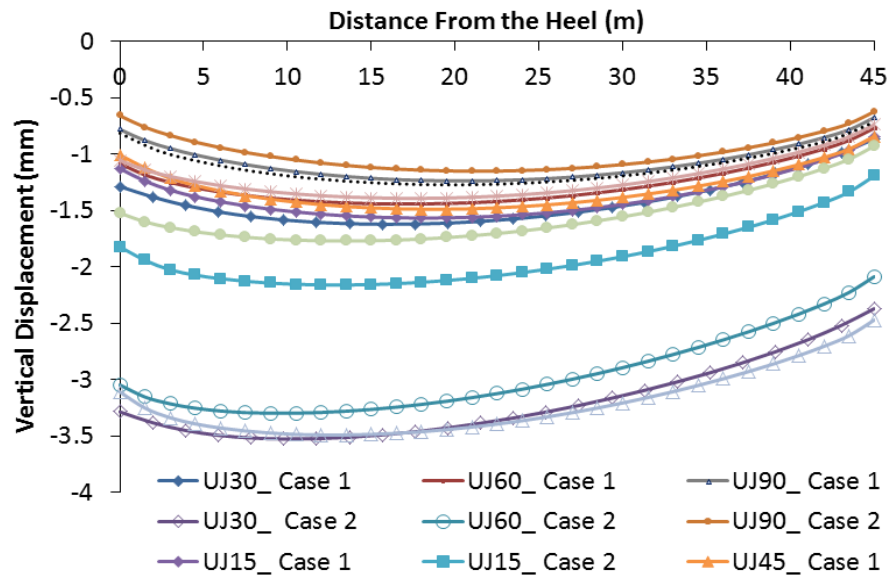
Figure 5.10 Vertical displacement for joint at 4.5m ($\delta_u/H = 0.09$) from the heel of dam – upstream scenario
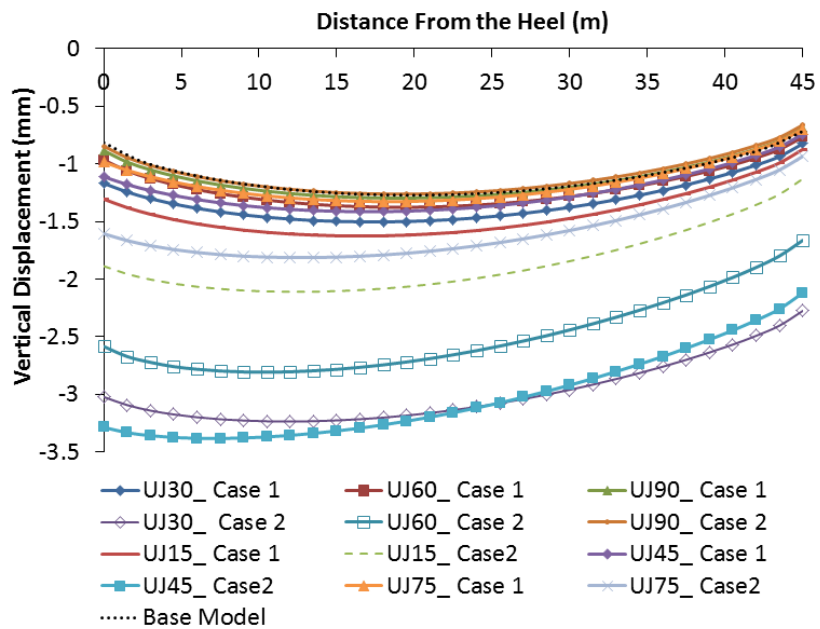
Figure 5.11 Vertical displacements for joint at 35m ($\delta_u/H = 0.7$) from the heel of dam – upstream scenario

5.5 Stability assessment and Discussion

Bieniawski and Orr (1976) proposed Table 2.3 to assess the stability of dams according to the dip angle of the main joint set. In addition, they used this to classify rock masses under dams according to the Rock Mass Rating (RMR) system, which is a geomechanical classification system proposed originally by Bieniawski (1973). Table 2.3 was based on experience and on the stress distribution in foundation rock masses (Gaziev and Erlikham, 1971) as well as on an assumption that both the arch and the gravity effects were present in a dam structure. This table should be used with caution, as indicated within the original text (Bieniawski and Orr, 1976): *"this table is tentative only and represents a simplification of a problem which is justified for rock mass classification purposes only."* Since publication of this paper in 1976, there has been very little work published to prove the reliability of the factors presented in Table 2.3. Also this table is not reproduced in the RMR system version published in 1989 (Bieniawski, 1989)

In this study, displacements have been measured at selected points under the dam in the vertical direction and at the crest of the dam in the horizontal direction, as shown in Figures 5.2-5.11. Also, a state of numerical equilibrium was checked in order to identify whether the model was stable or not. It was shown that the models DJ15 did not reach a state of equilibrium where the distance between the joint location (δ) and the toe of dam was less than half of dam's height.

Figure 5.12 shows the velocity vectors for model DJ15at5 at an arbitrary stage of the numerical simulation (the model did not reach equilibrium, indicating instability) and after significant horizontal movement of the dam had occurred. The vectors illustrate the failure mechanism of the dam (sliding along the weak layer). According to Table 2.4, the assessment of model DJ15at5 is fair whereas according to Table 2.3 and the numerical models presented in this thesis, it is unfavorable. Therefore, this study suggests that Table 2.4 should also be used with caution and should be checked by using numerical modelling or other appropriate means. These results illustrate the need for a more rigorous rock mass classification system for dam construction.

Figure 5.13 shows the shear friction factor (F_{SF}) predicted using Equation 2.9 for model DJ15at5 versus maximum displacement vector. The F_{SF} was increased by increasing the density of concrete in the dam. As can be seen, increasing the factor of safety against sliding will stabilize the weak layer within the foundation of the dam. According to these results, the F_{SF} factor should be at least 4 or greater for concrete gravity dams on jointed rock so as to stabilize a weak layer that may exist under the dam. According to this result, one may conclude that the Malpasset dam, which was described in chapter 2, would not fail if there was enough stabilizing force resulting from the dam's body on the discontinuities in the foundation of the Malpasset dam. It should be noted that in arch dams, the effective vertical stress at the dam-

foundation contact may reduce because of the arching effect after ap-

plying the reservoir load. This should be taken into account in the de-

sign of arch dams on a jointed rock mass. It would be interesting to

study this arching effect using a 3D discontinuum model such as 3DEC.

It should be noted that the maximum displacement vector for $F_{SF}=3.41$

was calculated at an arbitrary step after significant movement of the

dam along the joint (case 2) indicating failure of the model.
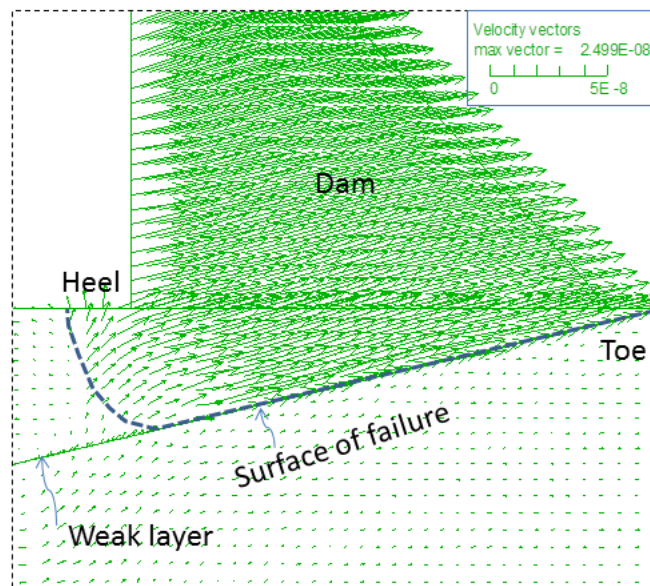
Figure 5.12 Velocity vectors (m/sec) for model DJ15at5
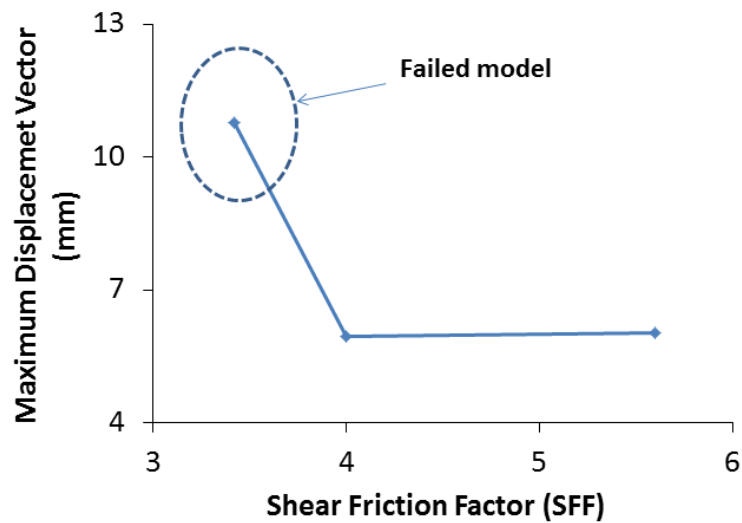
Figure 5.13 Shear friction factor along the dam-foundation contact for model DJ15at5 from heel

5.6   Summary and Conclusion

In this chapter the effect of a weak joint in the foundation of dam in both the upstream and downstream direction on the stability of a concrete gravity dam has been studied using numerical continuum modelling. Only one joint was selected from the rock mass in order to demonstrate the mechanisms involved within a simple model format. The author has attempted to demonstrate that both the location and orientation of the weak joint have an important effect on the stability of a dam. The modelling described suggests that a joint located on the downstream side of the dam dipping upstream at 15 degrees is a critical case for the dam's stability, especially where the distance between the toe and the joint location is less than half of the dam's height. This

study suggests that the shear friction factor for the dam foundation contact should have a value of at least 4. These results have implications for engineers involved in future dam design. Additionally this study concludes that further development of a rock mass classification system specifically for dam construction would be beneficial.

Using continuum model such as FLAC to study the effect of a weak joint of weak layer within a rock mass on dams' stability requires reliable prediction of the equivalent strength and deformability parameters of the rock mass. In the next chapter these parameters will be evaluated using UDEC.

Chapter 6 Strength Prediction of Rock Mass Study by UDEC

6.1   Introduction

According to the literature review there is a few number of researches have studied the determination of the equivalent mechanical parameters of jointed rock masses especially using UDEC. Therefore, to fully understand the behaviour of a jointed rock mass under a dam, a numerical modelling exercise has been undertaken which includes discontinuum simulations of both triaxial tests on jointed rock and the dam foundation rock mass. In the study, the behaviour of the intact material is treated as elastic perfectly-plastic (Mohr-Coulomb) and for joints the Area Contact Coulomb Slip model (elastic perfectly plastic) is used. A range of numerical simulations of UCS and Triaxial tests were conducted on rock mass samples in order to predict the equivalent mechanical properties for the rock mass. To validate this, the deformation modulus of the rock mass predicted by analytical equations, quoted from literature, was compared with the numerical results given by UDEC The blocky rock masses that have two joint sets were classified into two types: the first type was named as blocky rock mass (Figure 6.1a) whereas the second type was named as an interlocked block rock mass (Figure 6.1b). The rock mass under Pedrógão gravity dam was taken as a case study. The equivalent mechanical properties pre-

dicted by UDEC were used to model the foundation rock under the Pedrógão gravity dam using the continuum analysis code FLAC.
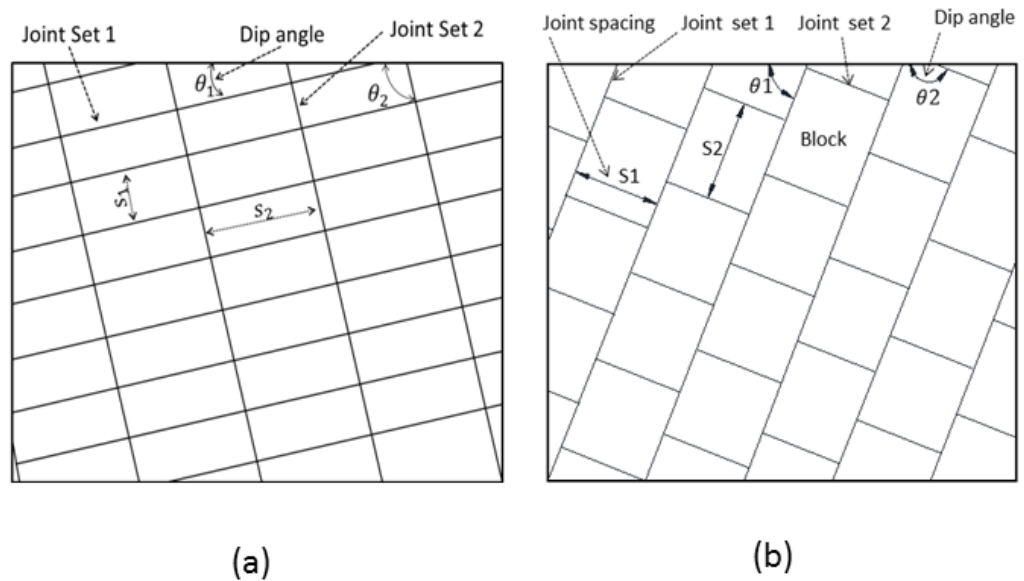
Figure 6.1 Rock mass: (a) blocky rock mass and (b) interlocked blocky rock mass

6.2 Validation

Numerical studies should, where possible, be validated against other available predictive methods. Therefore, in this study the equivalent deformation modulus for a blocky rock mass, whose configuration is similar to that in Figure 6.1(a), under a gravity dam described by Barla et al. (2004) is calculated using UDEC. The size of the individual blocks in the jointed rock was 2m × 4m. The material properties for the blocky rock mass (validation model) are shown in Tables 6.1 and 6.2 which were taken from Barla et al. (2004). These properties are as follows: for rock blocks, Young's modulus (E_i), Poisson's ratio (v), cohe-

sion (c), tensile strength (σ^t) and angle of friction ($\emptyset_j$); for joints, joint

normal stiffness (k_n), joint shear stiffness (k_s), cohesion (c_j), and coef-

ficient of friction ($\emptyset$).

Table 6.1 Material properties for blocky rock mass (Barla et al., 2004)

Material	Density(ρ)	E_i	v	c	$\emptyset$	σ^t
	kg/m^3	GPa		MPa	Degree	MPa
Intact Rock	2650	20	0.3	7.5	58	3.3

Table 6.2 The joints properties for blocky rock mass (Barla et al., 2004)

Joints	k_n GPa/m	k_s GPa/m	c_j MPa	$\emptyset_j$ Degree	σ^t MPa
Rock / Rock contact	50	0.5	0	30	0

The rock mass was analysed numerically using UDEC by conducting

large scale UCS tests (30m × 60m) but under a range of different di-

rections of loading on the rock mass. The rotation of loading was

achieved by rotating two sets of joints together in steps ($\theta = 15^o$ /

step) counter clockwise. For each step the deformation modulus was

calculated according to ISRM (1981) and the results are presented in

Figure 6.2. This figure shows that the deformation modulus highly depends on loading direction on the jointed rock masses. Barla el al. (2004) reported that the deformation modulus of this rock mass was taken as 10 GPa and they used this value as an equivalent deformation modulus of rock mass under a gravity dam whereas in this study the range of deformation modulus predicted by UDEC is between 2.2-18.1 GPa.
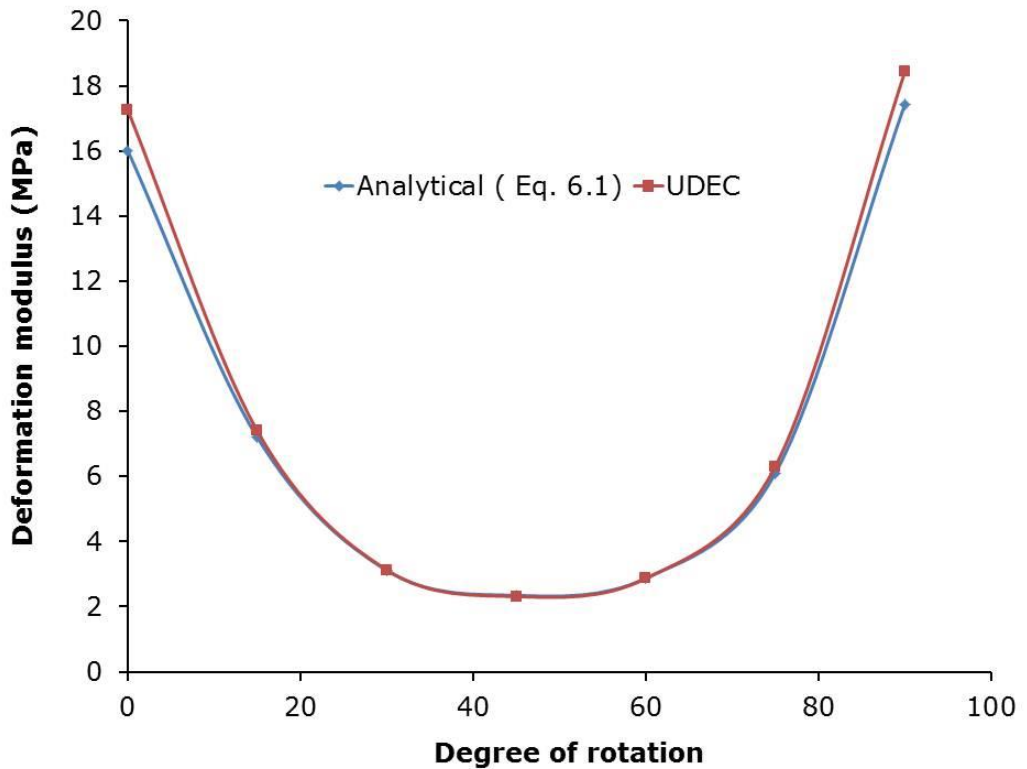
Figure 6.2 Deformation modulus versus degree of rotation of block rock mass

Figure 6.2 compares UDEC results against predictions based on Yoshinaka and Yamabe (1986), who proposed Equation 6.1 for the de-

termination of equivalent deformation modulus (E_e) of a rock mass that consists of two continuous joint sets, see Figure 6.1(a).

The amount of deformation of the rock mass is related to the deformation of the intact rock and the joints. Equation 6.1 shows that the rock mass modulus depends on the joint orientation and spacing as well as the joint and rock stiffness. Figure 6.2 shows that the UDEC results agree well with the predictions obtained using Equation 6.1.

$$E_{rm} = \left[\frac{1}{E_i} + \frac{cos^2\theta_1}{S_1}\left(\frac{sin^2\theta_1}{k_{s1}} + \frac{cos^2\theta_1}{k_{n1}}\right) + \frac{cos^2\theta_2}{S_2}\left(\frac{sin^2\theta_2}{k_{s2}} + \frac{cos^2\theta_2}{k_{n2}}\right)\right]^{-1} \qquad 6.1$$

where: k_s , k_n are shear and normal stiffness of the joint set, S is joint spacing, θ is dip angle , E_i is the Young's modulus of the intact rock , and subscripts 1 and 2 relate to the joint set number (see Figure 6.1).

6.3 Strength and Deformability of Rock Mass using UDEC

This section presents results from a series of compression tests simulations conducted on intact rock and interlocked blocky rock mass samples using UDEC. Two test cases were considered: an unconfined compressive strength test and a confined compression test. Since the models were performed under plane strain conditions, the out-of-plane strain is required to be zero. Therefore, the equivalent modulus of deformation and Poisson's ratio obtained from the tests were modified according to Equations 6.2 and 6.3 (Potyondy and Cundall, 2004) in order to obtain conventional elastic parameter values.

$$v = \frac{\bar{v}}{1+\bar{v}}$$

6.2

$$E = \bar{E}(1 - v^2)$$

6.3

where v is Poisson's ratio, $\bar{v}$ is lateral strain ratio, $\bar{E}$ is the plane-strain modulus of deformation, and E is the modulus of deformation.

Because the philosophy of this study is to show how to predict the equivalent strength and deformability parameters of jointed rock mass under a gravity dam, a theoretical model can be developed for this purpose. However, the author selected from literature the Pedrógão dam built on a jointed rock mass (Farinha et al., 2012) to do the study with more interesting. Pedrógão gravity dam, based on information from Farinha et al. (2012), is a roller compacted concrete dam (RCC) constructed on the Guadiana river in Portogal. The construction of the dam was started in April 2004 and finished in February 2006. The maximum height of the dam is 43m and the total length is 448 m. Because the dam axis is straight, it is viable to be analysed in the plane strain condition. The maximum height of retained water during the dam's service is 33.8 m. The rock foundation consists of jointed granite. Figure 6.3 shows the Pedrógão gravity dam and joint sets. There are five sets of joints as illustrated in Figure 6.3b. Because a plane strain was used in this study, only two joint sets were taken into account. The first one is **set g** which is a sub horizontal continuous joint with joint set spacing of 5 m; the other is **set b** which is an almost staggered vertical discontinuous joint (subsequent of 5m of joint and

gap of 5m) with joint set spacing of 5m $\pm$2m. In this study the spacing

of **set b** was taken as 5m for simplicity. The resulting rock was named

as interlocked block rock mass.

(a) Downstream view from the right side
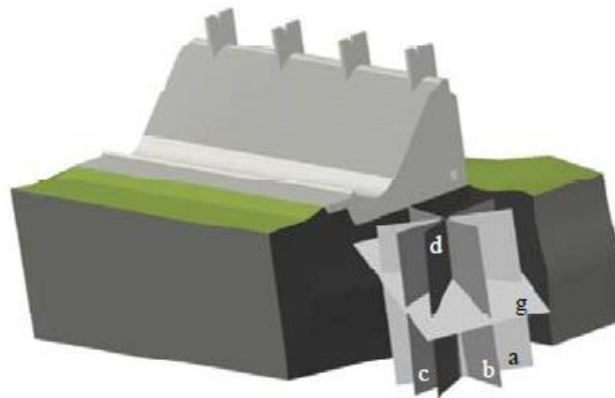
(b) The main sets of rock joints in relation to the dam

Figure 6.3 Pedrógão dam. (a) Downstream view from the right side; (b) The main sets of rock joints in relation to the dam (after Farinha et al. (Farinha et al., 2012))

The behaviour of the rock mass was analysed numerically and the equivalent Mohr-Coulomb strength and deformability parameters were obtained. The parameters were then used for a numerical model simulation of the Pedrogao dam. Also, the behaviour of this type of rock mass is not well understood because of the complex interactions between the interlocking blocks. Figure 6.1 (b) shows the interlocked blocky rock mass considered. It should be noted that this analysis differs to that presented in Farinha et al. (2012), where a randomly distributed non-persistent joint set was considered. The same properties mentioned by Farinha et al. (2012) were used in this study except for the intact rock, which required additional Mohr-Coulomb parameters (Table 6.3). Also, for the joints the normal stiffness is fixed at 10 GPa/m and shear stiffness is 5 GPa/m (Table 6.4) because the aim is to study the effect of loading direction on the rock mass behaviour. Table 6.4 shows the properties of the joints that have been used in this research.

Table 6.3 Material properties for UDEC analysis of Pedrogao dam (Farinha et al., 2012)

Material	ρ	E_i	v	c	$\emptyset$	σ^t
	kg/m^3	GPa		MPa	Degrees	MPa
Concrete	2400	30	0.2	-	-	-
Intact Rock	2650	10	0.2	2[*]	45[*]	1[*]

Note*: Assumed in this study.

Table 6.4 Joint properties for UDEC analysis of Pedrogao dam (Farinha et al., 2012)

Joints	k_n	k_s	c_j	$\emptyset_j$	σ^t_j
	GPa/m	GPa/m	MPa	Degree	MPa
Rock / Dam Interface	10	0.5 K_n	2	30	2
Rock / Rock contact	10	0.5 K_n	0	30	0

6.3.1 The UDEC Analysis

Broadly speaking, there are two types of loading on the foundation of a dam: dam body loads and reservoir loads. These will develop two resultant forces in the foundation rock mass (Figure 6.4): one of them can be assumed to be vertical in the area beneath the reservoir (F2) whereas the other will be affected by the reservoir and dam and its direction depends on the magnitude of the respective loads (F1). To simulate these loading conditions, the rock mass was tested using UDEC under unconfined and confined conditions at 10 intervals of rotation (anticlockwise from 0 to 90 degrees). The ten UDEC models were named according to the dip angle of joint set 1 as follows: J0, J10, J20…J90. Joint set 2 was always perpendicular to joint set 1.

For the confined tests, the UDEC model was tested under a range of confining stress from 0 to 8 MPa. The equivalent Mohr-Coulomb strength and stiffness (ISRM, 1981) parameters were determined based on the obtained results.
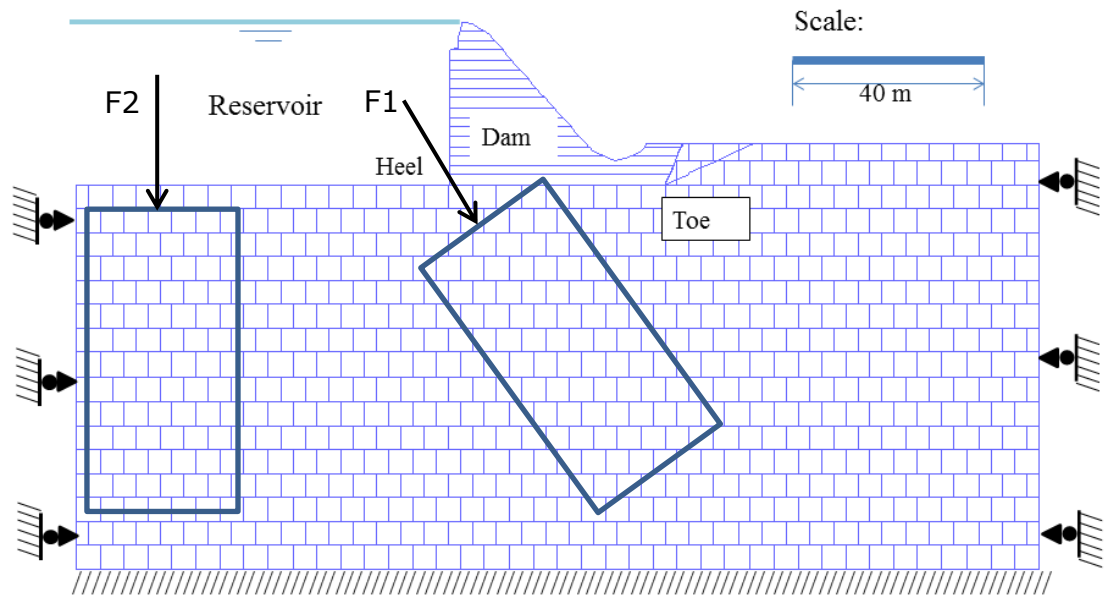
Figure 6.4 UDEC model showing resultant forces on the dam foundation

6.3.2 Selection of loading type

Practically there are two ways in which loads can be applied on intact rock or jointed rock masses samples. These are either strain-controlled or stress-controlled tests (Figure 6.5). In order to predict a failure load, it is often better to use strain controlled rather than stress controlled boundary conditions. Strain control can be simulated in UDEC by applying a constant velocity and measuring the boundary reactions forces rather than applying forces and measuring displacements in a stress-controlled test. In the stress controlled method, as the applied force approaches the collapse load, the system becomes difficult to control (Itasca, 2011).

In UDEC displacement cannot be applied directly for simulating the real strain-controlled test. In order to apply a given displacement to a

boundary, it is necessary to fix the boundary and prescribe the boundary's velocity for a given number of steps by using the boundary command. For instance, if the required displacement is (d), a velocity (v) is applied for a time increment (t) as shown in Eq.6.4 below:

$$\mathrm{d} = \mathrm{v} * t \hspace{5cm} 6.4$$

where $t = \Delta t * N$ in which Δt is the time step and N is number of steps.

In order to minimize any shocks to the system being modelled v should be kept small and N large. Applying small velocity is time consuming. Therefore, Itasca developed a FISH function named Servo-control which can be used to minimize the influence of inertia effects on the response of the model. In this FISH function the applied velocities can be adjusted as a function of the maximum unbalanced force in the model. This servo-control function requires the user to estimate the lower and upper limits of unbalance forced. Baghbanan (2008) estimated these limits when confining the numerical samples when he used this FISH function to determine the equivalent strength properties of a fractured rock mass. Recently, Noorian Bidgoli et al. (2013) used this FISH function to determine the strength parameters of the same model that was used in Baghbanan (2008). However, this function may overestimate the axial stress after yield stress because after yield the sample is numerically unstable, and therefore, the author applied another methodology in which after each 50 steps, the platen

movement was stopped and the model was stepped to equilibrium as illustrated in Figure 6.6 for the strain-controlled part of a test.

Noorian Bidgoli and Jing (2014b) and Noorian Bidgoli et al. (2013) compared the results of strain controlled method with those of the stress controlled method using UDEC. They showed that stress-strain behaviour was changed by loading conditions with higher average axial stress under the strain-controlled test condition than that under the stress-controlled condition. However, numerically both methods should have given similar results under similar boundary conditions. They compared two models with different boundary condition and this is why the strain-controlled method gave higher stress and deformation modulus than the stress-controlled method. It should be noted that in the strain controlled method using UDEC, the upper boundary is only moved downwards with an assigned velocity as a rigid platen whereas in the stress-control method the upper boundary is free to move in any direction during loading. In the former, blocks just under the boundary are restricted from rotating freely. As a result strain hardening oc-curred, whereas in the latter method, the blocks just under the bound-ary are free to rotate and to move. As a result part of model slides and a sudden failure occurs. In order to illustrate these phenomena, the author used both methods to study the axial stress- axial strain rela-tionship for a regular jointed rock mass. A special FISH function was written and implemented in UDEC (see appendix A). In this code both

strain-controlled and stress-controlled methods can be achieved. For

the strain controlled test the reactions (R1 and R2), see Figure 6.5a,

on both upper and lower boundaries were calculated during the down-

wards movement of the upper platen at a velocity of 10 mm/sec. In

the stress-control test, only the reaction force (R2) can be calculated

because there is only a lower boundary (Figure 6.5b). The flow chart

of this code is shown in Figure 6.6 and the written code is presented in

Appendix A. Also, the average vertical stresses (σ_Y) in the zones of

blocks were calculated for both methods for checking the equilibrium

of the models. The axial stress was computed by dividing the average

values of reaction forces on the platens by the sample cross section

width and the axial strain was computed using the displacement of the

top platen.
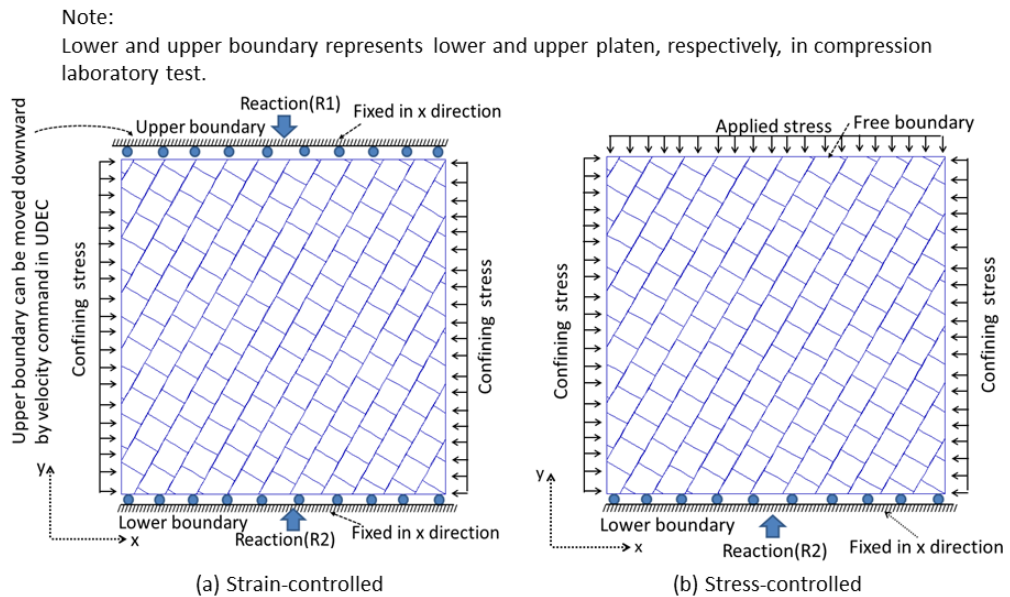
Figure 6.5 Numerical simulation of the compression test on the rock masses
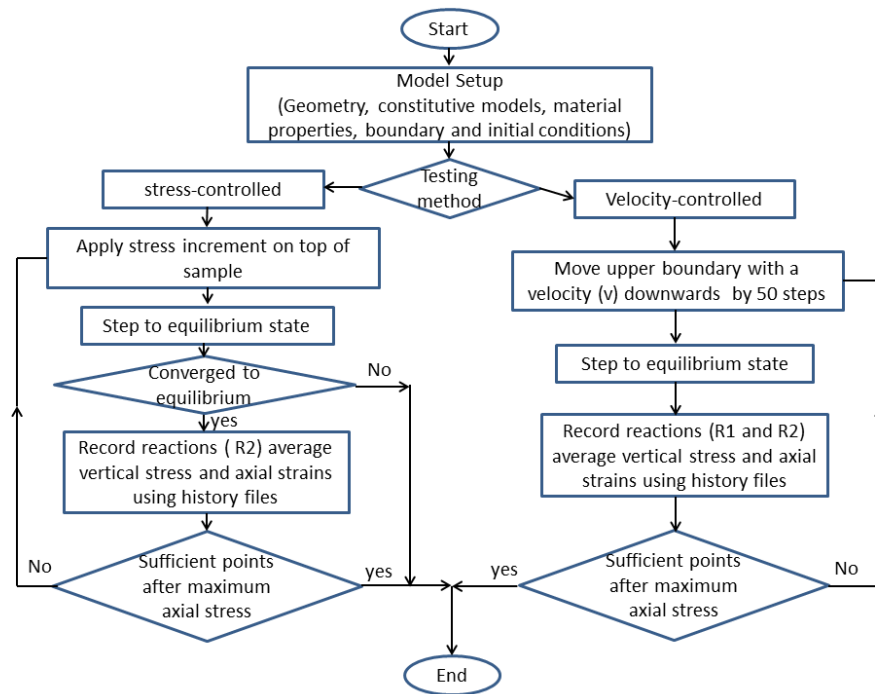
Figure 6.6 Flow chart for the developed code RMSPUDEC

In modelling a laboratory triaxial test, the platens were treated as a rigid boundary because the stiffness of the platens is much more than the stiffness of the rock samples. Also, modelling platens within the loading system are time consuming. The rock mass described in section 6.3 was used here. This type of rock mass consists of two smooth joint sets. The first joint is continuous whereas the second joint set is staggered and perpendicular to joint set 1. The size of sample was selected to be 60m x 60 m so as to make a fair comparison with the study presented by Noorian Bidgoli and Jing (2014b) with regard to sample shape. Figure 6.7 shows the axial stress-axial strain plot for numerical samples tested under a confining stress of 1 MPa. In this

study three methods were used to construct the axial stress-axial strain graph. These methods are: strain-control using the methodology proposed in this study, strain-control using a servo control FISH function provided by Itasca (2011), and the stress-control methodology. As can be seen, the strain-controlled methods display strain-hardening behaviour after yield stress. Here, the yield stress can be defined as the required axial stress to fully develop slip along joint set 1. Because most of the joints in set 1 intersect the lower boundary of the sample, which is fixed in the vertical direction the blocks were rotated (Figure 6.8). As a result strain-hardening occurred. However, the axial stress produced by servo-control is higher than that in the methodology proposed above.

This is because after yield stress, the system becomes numerically unstable. This can be shown from the unbalanced force history (Figure 6.9b). Unlike the strain-controlled test, the stress-controlled test did not show any strain hardening behaviour because part of model failed suddenly without converging to equilibrium. At yield stress the system failed suddenly and the model did not converge as shown in Figure 6.9a. This is because, in UDEC the loading is applied through the flexible boundary and any point on the boundary can move freely in any direction; therefore, the failure occurred along a joint of set 1 as shown in Figure 6.8c. All of the methods gave identical results of yield stress and deformation modulus. However, after yield stress the

strain-controlled method using the servo-control function gave higher axial stress than the strain-controlled method using the proposed method. It seems that the proposed method in this study can accurately predict the axial stress-axial strain curve as the model is numerically stable before and after yield stress.

This can be seen from the history of the unbalanced force in Figure 6.10. It should be mentioned that the simulation time in the servo-controlled method is faster than the proposed method since the velocity is varied in the servo-control during simulation whereas in the proposed method the velocity is constant during the simulation time. This can be overcome in the proposed method by increasing the strain velocity without significant effect on the results. Different velocities (10 mm/sec to 160 mm/sec) were applied to check the effect of strain velocity on the axial stress-axial strain and the results are presented in Figure 6.11. From this one can conclude that the strain velocity in the proposed method did not significant effect on the results. However, the strain velocity should be less than 40 mm/sec so as to capture the yield stress accurately.
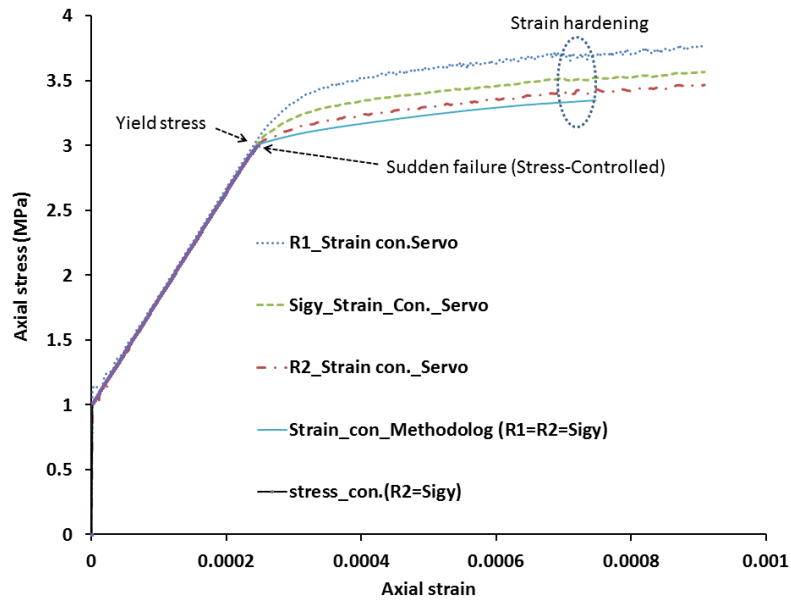
Figure 6.7 Axial stress-axial strain resulting from different method of testing a rock mass under confining stress of 1 MPa. Note: Sigy=σ_y is an average vertical stresses in the sample
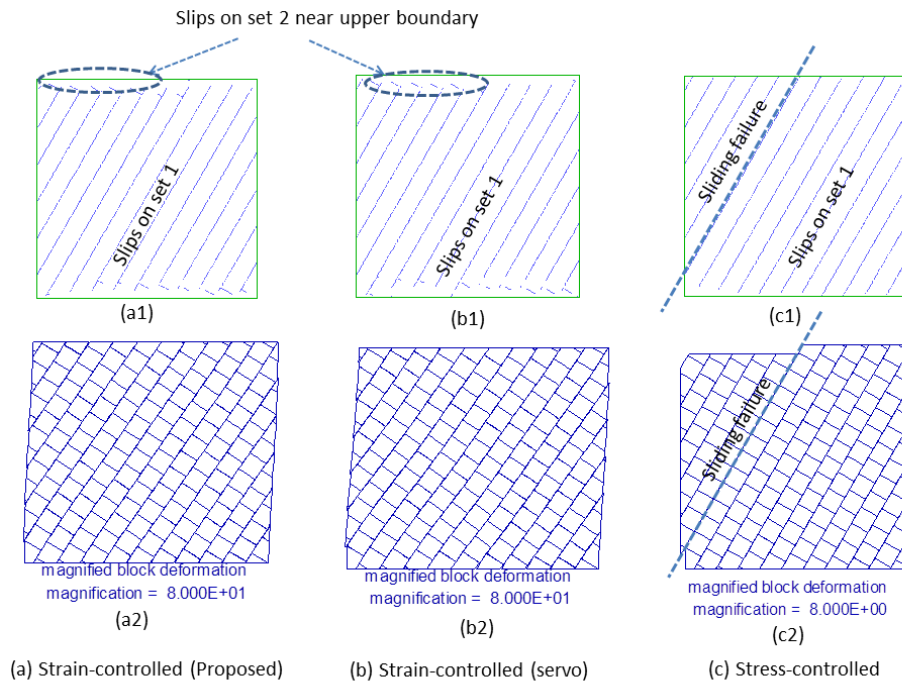
Figure 6.8 Block deformations with slip along joints for different methods of testing rock mass sample

(a) Stress-controlled   (b) Strain-controlled (Servo-Control)
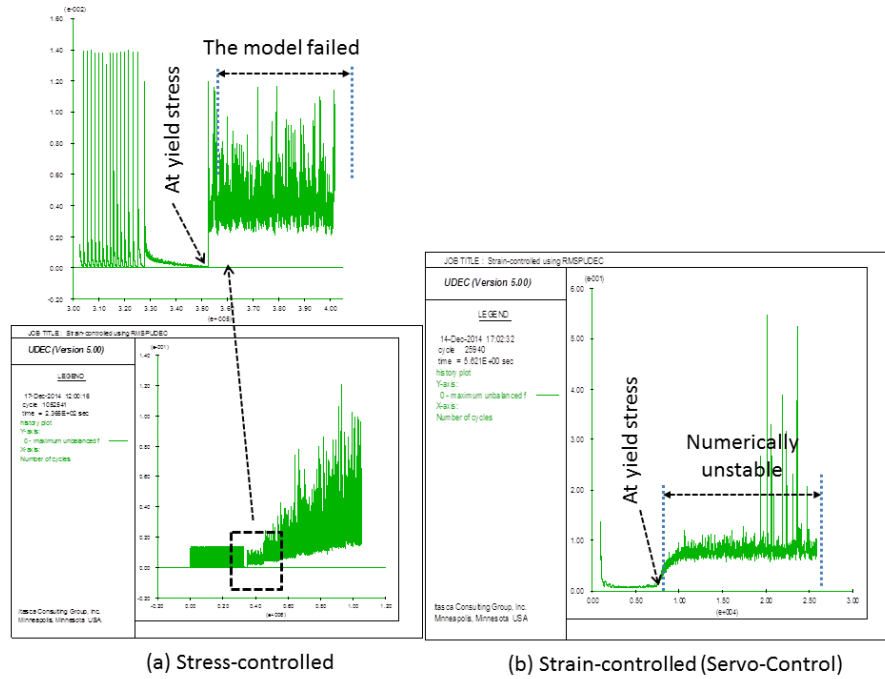
Figure 6.9 Unbalanced force history for a stress-controlled and strain-controlled confined compression tests (Servo-Control).
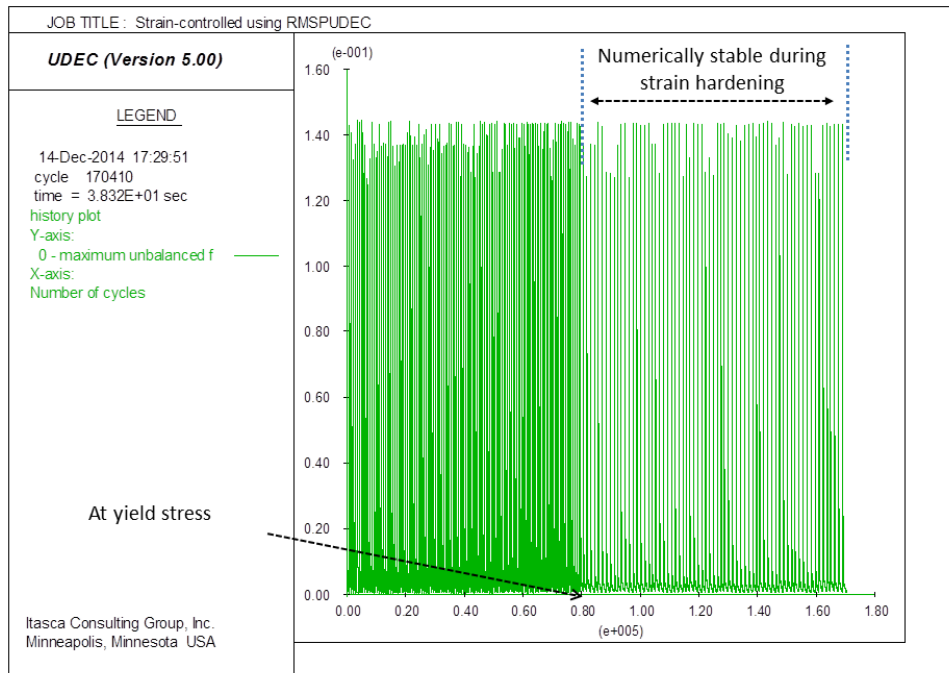
Figure 6.10 Unbalanced force history for a confined compression test for strain-controlled (proposed method)
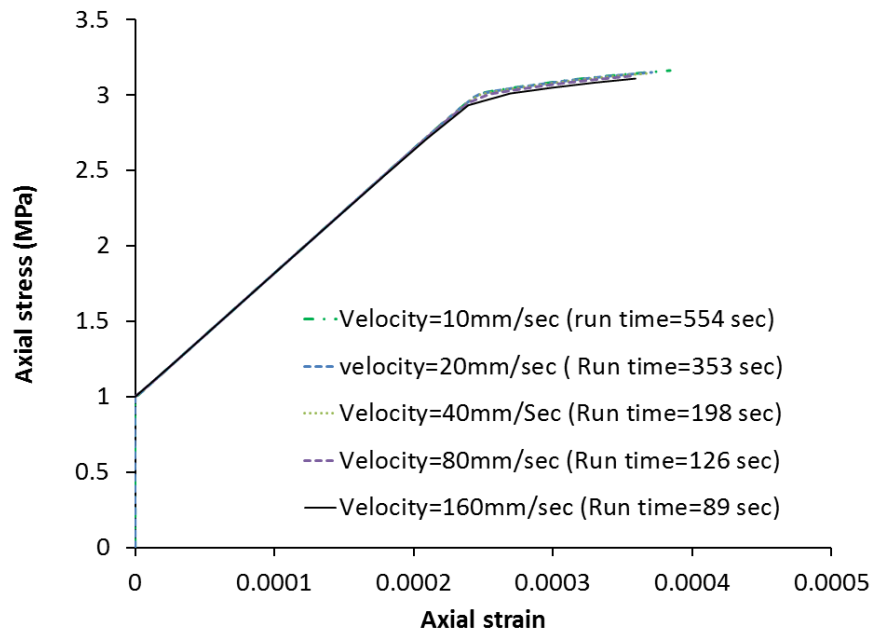
Figure 6.11 The effect of applied strain velocity on axial stress-strain curve

As was explained in the introduction, both strain-controlled and stress-controlled methods can give identical results under the same boundary conditions. To show this the author loaded the numerical sample by applying the axial stress through a platen and not directly on the boundary. Figure 6.12 shows the sample with an upper steel platen. The properties of the steel platen was taken from literature (Singh and Singh, 2008a). These properties are as follow: density=7800 kg/m³, shear modulus=110 GPa, and bulk modulus is 185 GPa. Fig. 6.13 shows the results produced by stress-controlled using the set up shown in Fig.6.12. It can be seen that both methods gave identical results under the same boundary conditions.
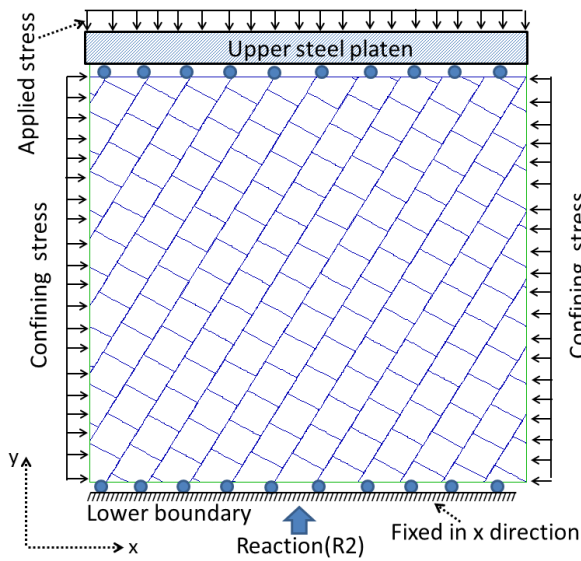
Figure 6.12 Numerical sample with upper platen for stress controlled method
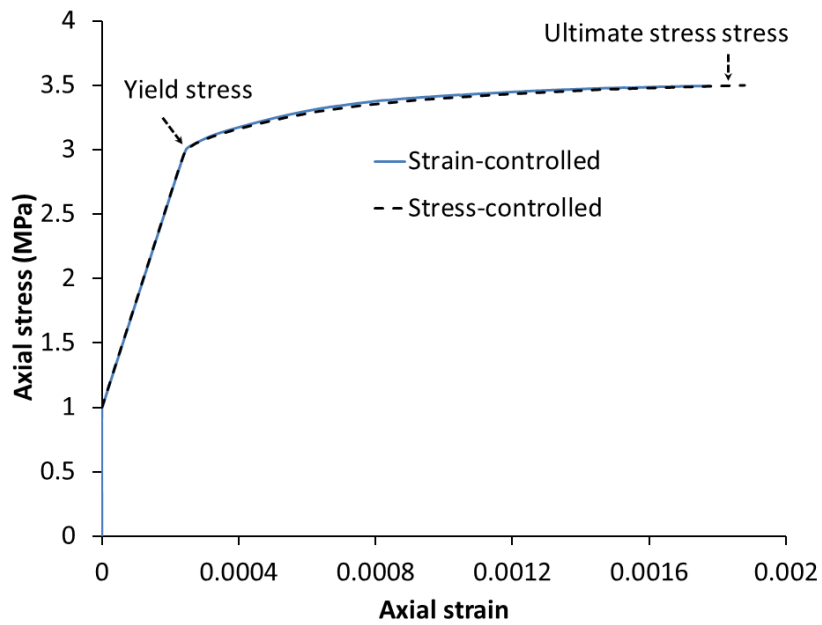
Figure 6.13 Stress-strain curve by proposed method and stress-controlled method

6.3.3 Selection of sample size

In randomly distributed joints the sample size has a significant effect on the stress distribution inside the sample when numerical modelling of a large scale samples is used, and hence the predicted strength and deformability parameters may be affected (Mas Ivars et al., 2011). In systematically distributed joints in rock masses the sample size has a minor or negligible effect; however, a sample's shape may affect the post yield failure if the sample is failed by sliding.

To study the effect of sample scale on the mechanical parameters of a rock mass, two different joint configurations were selected based on the failure mode for the interlocked blocky rock mass shown in Figure 6.1b. For each configuration different sizes of numerical sample were generated as shown in Figures 6.14 and 6.15. The dip angle of joint set 1 was 30 degree for configuration 1 and 60 degree for configuration 2. The results are presented in Figures 6.14 and 6.15, respectively, which show that the deformation modulus was not affected by sample size and shape. However, in configuration 2 the post failure behaviour was affected by size and shape especially for the square shaped sample, in which the axial stress-axial strain displayed strain hardening behaviour. This hardening behaviour is due to the fact that the joints in set 1 did not cross the sample through both sides: only one of the joint ends crossed the upper or lower platen boundary. As a result, the joint was restricted from sliding and strain hardening oc-

curred until it reached the ultimate stress as illustrated in Figure 6.16. This strain hardening resulted from the interlocking and rotations of the blocks. All models in Figure 6.15 failed by slip and block rotations, except the sample size of 120x120 which was failed by double kink band as shown in Figure 6.17. It would be interesting to study these kink bands in detail by doing a parametric study about the effect of joint friction angle, blocks size, and joint spacing; however, because the kink band is not in the scope of this study, it will not be studied in detail but it should be noted that the block size in the rock mass model has an important effect on producing kink bands.

It can be concluded that for a systematic jointed rock mass the sample size has no great effect on the axial stress- axial strain relationship, and therefore it was decided to use the size 30x60m, which is most appropriate for the dam's base width as shown in Figure 6.4.
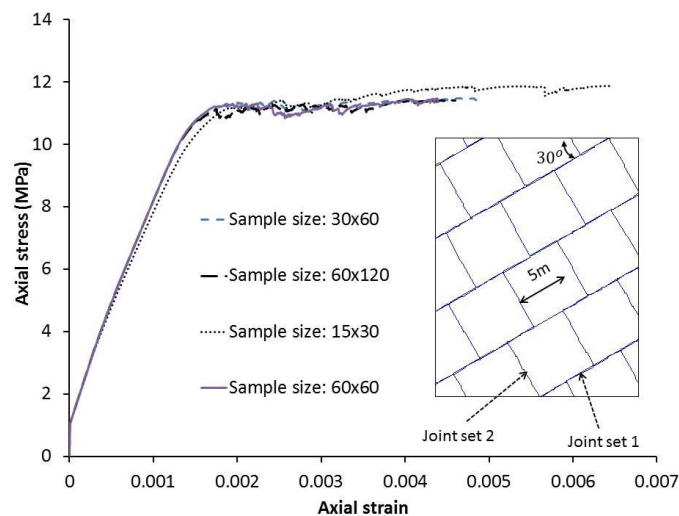
Figure 6.14 Axial stress-strain for block rock mass under confining stress of 1 MPa for dip angle of set 1=30 degree
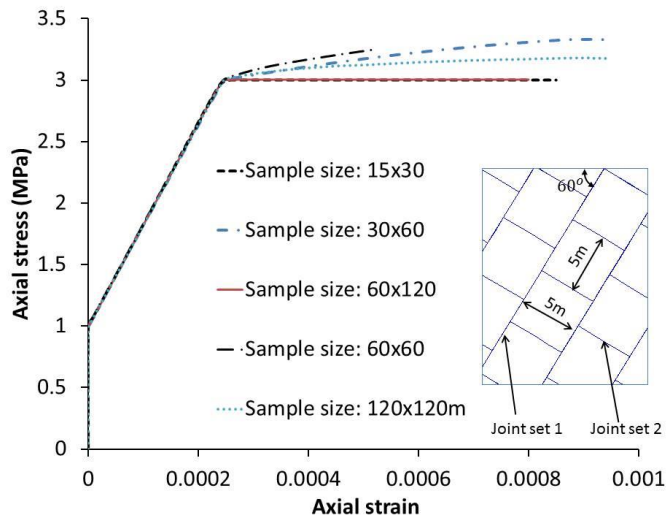
Figure 6.15 Axial stress-strain for block rock mass under confining stress of 1 MPa for dip angle of set 1=60 degree
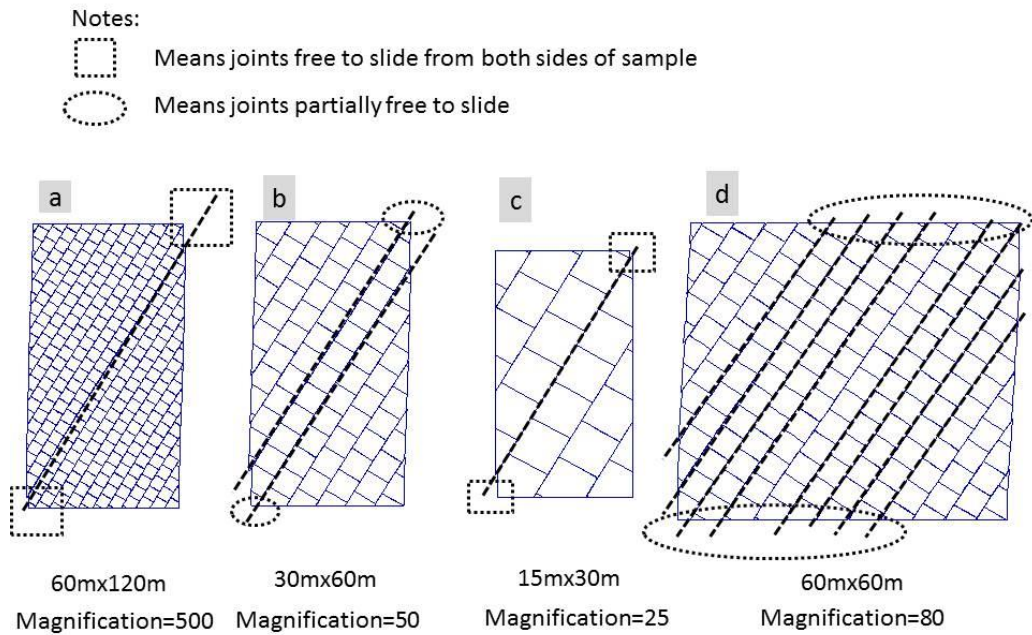
Figure 6.16 Magnification of block deformation for different sample sizes
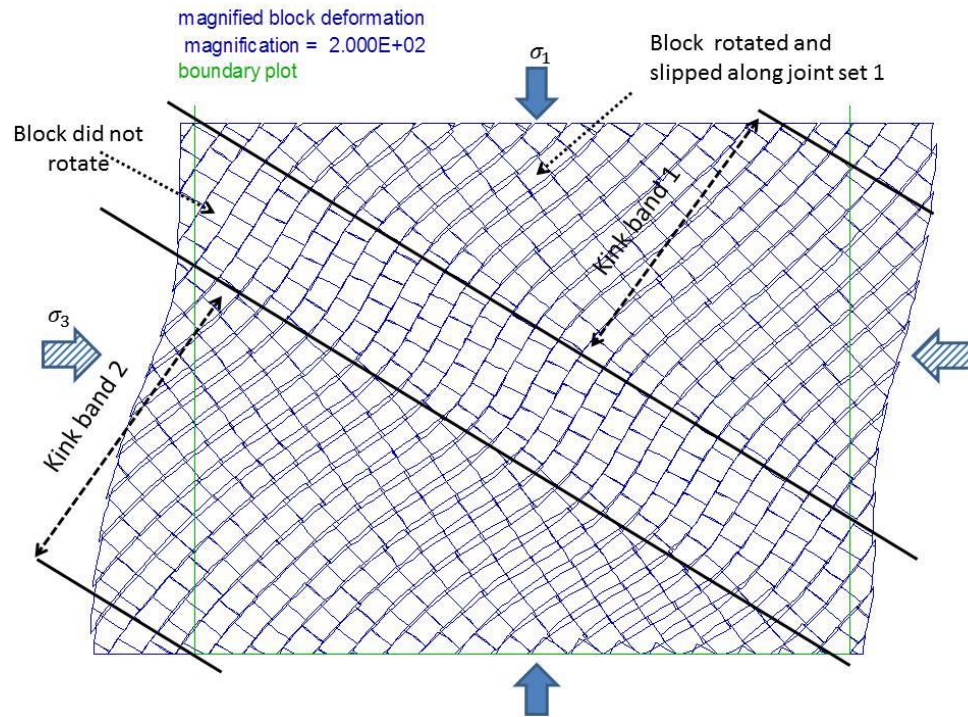
Figure 6.17 Double kink bands in square sample of size 120x120

6.3.4 Unconfined Tests

The unconfined compression tests were performed on samples sized 30 × 60 m of both intact rock and the blocky rock mass (5 × 5 m blocks). The smooth joints of a rock mass generally have zero dilation angle, cohesion and tensile strength (Barton et al., 1985; Kulatilake et al., 2001a) and therefore only the Mohr-Coulomb parameters of friction (Table 6.4) were applied to the joints in the rock mass tests. The modelled rock sample was placed between two smooth boundary platens. The upper platen was moved downward with a velocity of 10 mm/sec, while the lower platen was kept fixed. Reaction forces at both platens were recorded with development of axial strain.

Figure 6.18 shows the axial stress-axial strain relationship obtained from UDEC for the intact rock test. The failure plane and deformed shape are also shown in the Figure. The UDEC simulation results are typical of real rock behaviour under UCS test conditions. The following parameters for the intact rock were calculated from the data in Fig. 6.18: $\bar{E}$ = 10.4 GPa, $\bar{v}$ = 0.249, and UCS = 9.33 MPa. According to equations 6.2 and 6.3 the elastic parameters are E = 10. GPa and v = 0.2 which are the same parameters that were used as an input for the UDEC model. From this one can conclude that the deformation modulus and lateral strain produced by UDEC should be corrected according to equations 6.2 and 6.3.
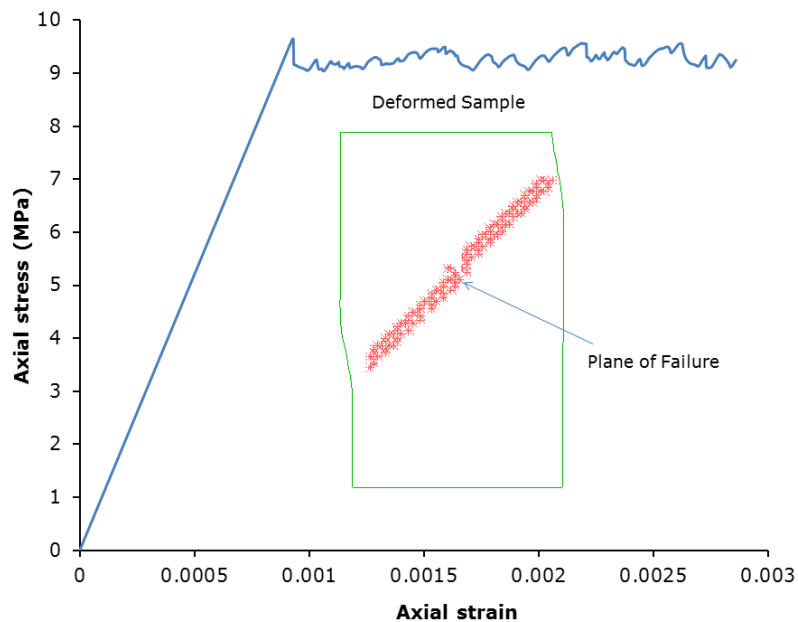
Figure 6.18 UDEC stress-strain result for UCS test on intact rock

The evaluation of strength parameters using unconfined tests on rock mass samples may not provide representative values, especially when cohesionless joints are encountered in the rock mass. In some cases, the unconfined rock mass will fail under its own self-weight, as mentioned by Kulatilake et al. (2001a). In this case the system behaves as a granular material since the friction angle of joints is smaller than the dip angle of the joints.

Figure 6.19 presents the unconfined compressive strength test results of rock mass samples of the foundation rock beneath the Pedrógão dam. The test produces zero unconfined compressive strength at specific joint set orientations. Also, three modes of failure are noted under low confining stress: shear mode, block rotation and slip, and sliding mode as illustrated in Figure 6.19. The unconfined compressive strength of the rock mass is effectively zero when the dip angle (θ_1) is between 30 and 80 degrees and because the joint is cohesion-less and friction angle is 30 degree, therefore, its behaviour like a granular material. In these cases, the weight of the blocks is sufficient to overcome the frictional resistance to sliding along the continuous joint set 1.

The failure mode of the sample J30 was changed when it was tested under a confining stress of 1 MPa. The failure mode was changed to slip with shear failure and tensile failure as shown in Figure 6.20. This shows the stages of failure in the model J30. It is very interesting to

see that all the staggered joints (joint set 2) slipped without sliding failure because of the rock bridge and the initial slope of the curve changed specifically at point (A) where the axial stress is 3.03 MPa. Then the curve changed its behaviour from a linear to a nonlinear behaviour at point B where the axial stress was 7.19 MPa. At this point the discrete slips occurred along set 1 but did not fully slip due to the fact that the friction angle of the joint is just equal to the dip angle of the joint and the confining stress of 1 MPa did not allow the sample to slide along the joints of set 1. The sample failed in shear at point c and this was followed by a block tensile failure as a result of block rotations. It should be noted that the effect of slips along the joints on the nonlinearity of axial stress-strain is similar to the effect of the micro-cracks on the intact rock behaviour although large blocks (5m*5m) were used inside the model.

Figure 6.21 shows the deformation modulus for different orientations of joint set 1. It was not possible to obtain results of unconfined deformation modulus for the J30 to J80 models because the samples failed under very small values of axial stress since the friction angle is 30 degrees. Brown and Trollope (1970) had similar problems in testing physically jointed rock samples and they used a small amount of adhesive tape and a weak glue to overcome this difficulty. Numerically, a marginal confining stress (in plane strain) of 0.05 MPa was applied in order to obtain an estimate of an unconfined deformation modulus for

these joint set configurations. The UDEC results were compared with the empirical Equation 6.5 (Goodman, 1989) for a single set of joints which were perpendicular to the direction of loading. The UDEC results are approximately similar to the empirical predictions except for model J30. The intact rock deformation modulus was also shown to be greater than the jointed rock mass modulus in Figure 6.21.

$$\frac{1}{E_{rm}} = \frac{1}{E_i} + \frac{1}{S*k_n}$$ 6.5

where E_{rm} is the deformation modulus, E_i is the modulus of elasticity of intact rock, S is joint spacing, and k_n is normal joint stiffness.

.
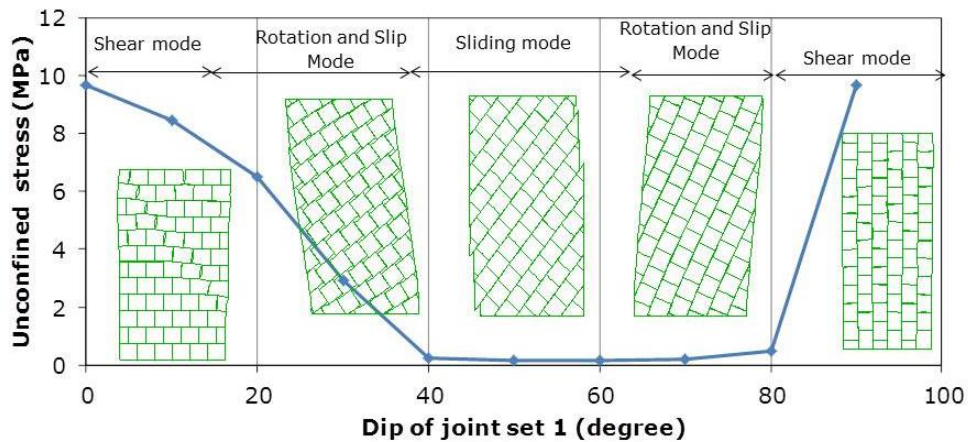
Figure 6.19 Unconfined compressive strength versus joint orientation
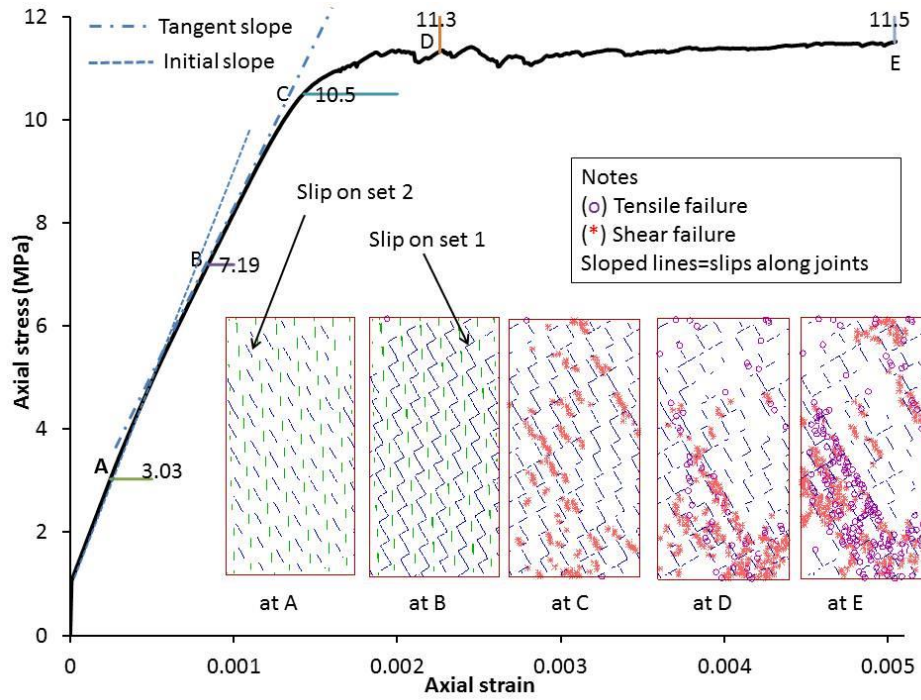
Figure 6.20 Failure processes for model J30 under confining stress of 1 MPa
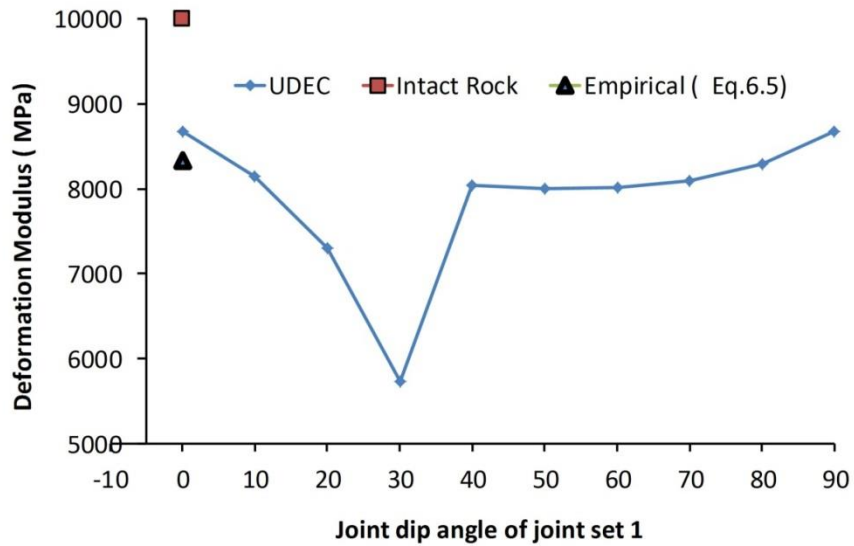
Figure 6.21 Deformation modulus versus the dip angle of joint set 1

6.3.5 Confined Tests

According to the unconfined test results, the models J0, J30, and J60 were selected to present the confined strength because these models represent the failure modes described in section 6.3.4. Figure 6.22(a) plots results of deviatoric stress versus axial strain for model J0 under different confining stresses. The rock mass behaviour is observed to be elastic-perfectly plastic, which indicates that the intact rock controls the behaviour of this type of rock mass. This conclusion is also sup- ported by the fact that the resulting strengths of the rock mass tests match the strengths obtained using intact samples, as shown in Figure 6.22(b).

Figure 6.23(a) shows the test results for Model J30. As can be seen, with increased confining stress, the relationship between the stress and strain becomes bilinear. For a confining stress of 4 MPa the de- formation modulus changes from 8.3 GPa to 7.4 GPa before the yield point. This is illustrated in Figure 6.23(a) by dashed lines. The first modulus value is due to the deformation in the intact rock blocks. When the joints dipped at 120 degrees begin to slip, the deformation modulus is reduced to 7.4 GPa up to the yield point. Ultimately, failure occurs in the intact rock blocks and, at the same time, slipping on the joints becomes continuous. Figure 6.23(b) shows strength envelopes for sample J30. The data shows a bi-linear increase in strength with confining stress. The reason for this non-linearity is due to the change

in failure mode that occurs as confining stress is increased; the mode was changed from rotation and slip mode at low confining stress to shear and tension mode at higher confining stresses. The shape of the failure envelope is similar to the Patton's bilinear failure envelops of saw cut teeth joint proposed by Patton in 1966 (Ladanyi and Archambault, 1969) in which when there is low normal stress on the joint the sliding will occur along the joint whereas under high normal stress the failure will be in intact rock blocks. Although, smooth joints were used in this study the overall behaviour is similar to Patton's model because partial slips along two joint sets created a saw-tooth like joint and under high confining stress the failure occurred in the intact rock blocks as a shear failure mode, see inset image of slips along the joint sets at point B in the Figure 6.20.

Figure 6.24 (a) presents the confined compression test results for the model J60 which represents the slide mode failure. It can be observed that the joint strength controls the behaviour of the whole rock mass. The strength parameters can be determined from Figure 6.24(b). As can be seen the shape of the failure envelope is linear.

The variation of the calculated values of deformation modulus with confining stresses is presented in Figure 6.25. The J30 model had the lowest stiffness under low confining stress. However, when confining pressure was more than 2 MPa, all the samples showed similar values

of deformation modulus and were also in general agreement with the

empirical relationship (Eq. 6.5)
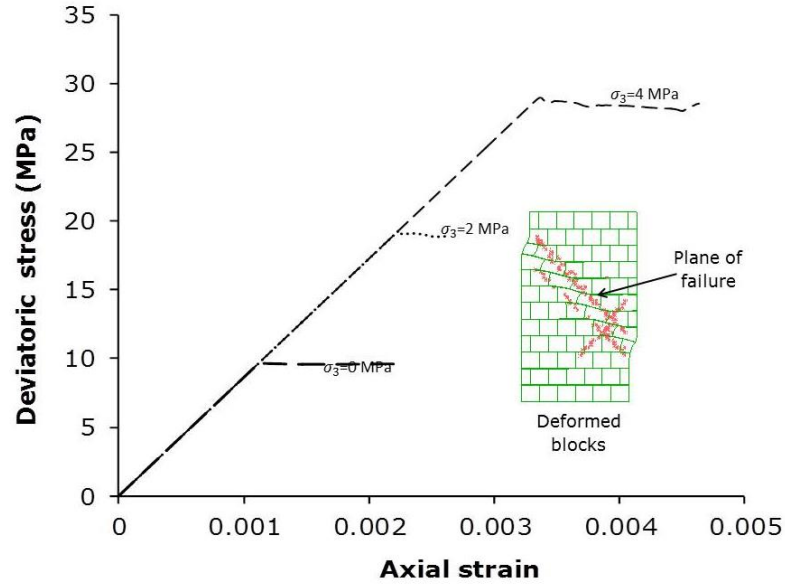
(a) Axial stress-axial strain
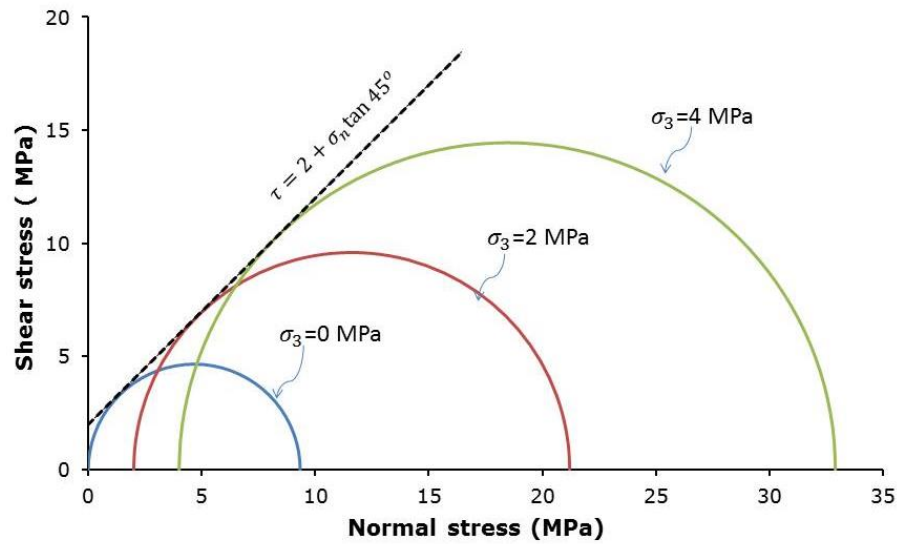
(b) Mohr-Coulomb strength envelope

Figure 6.22 Model J0 (a) axial stress-axial strain, (b) Mohr-Coulomb strength envelope
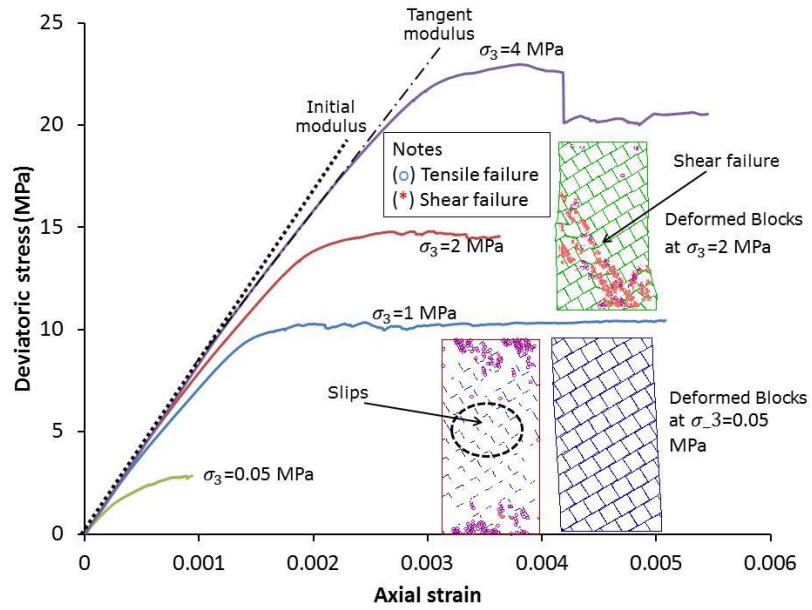
(a) Axial stress-axial strain
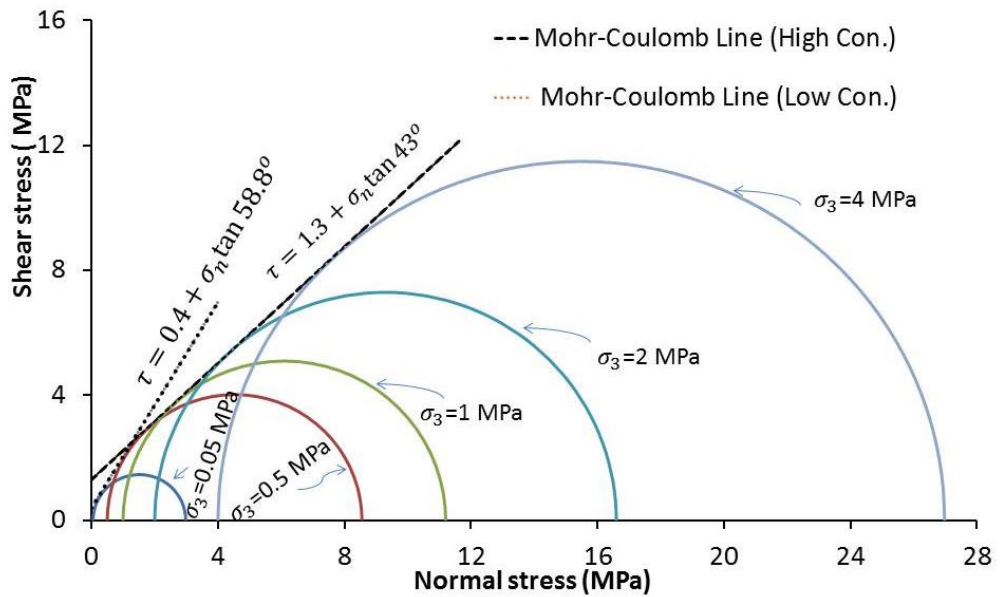
(b) Mohr-Coulomb strength envelope

Figure 6.23 Model J30 (a) axial stress-axial strain, (b) Mohr-Coulomb strength envelope
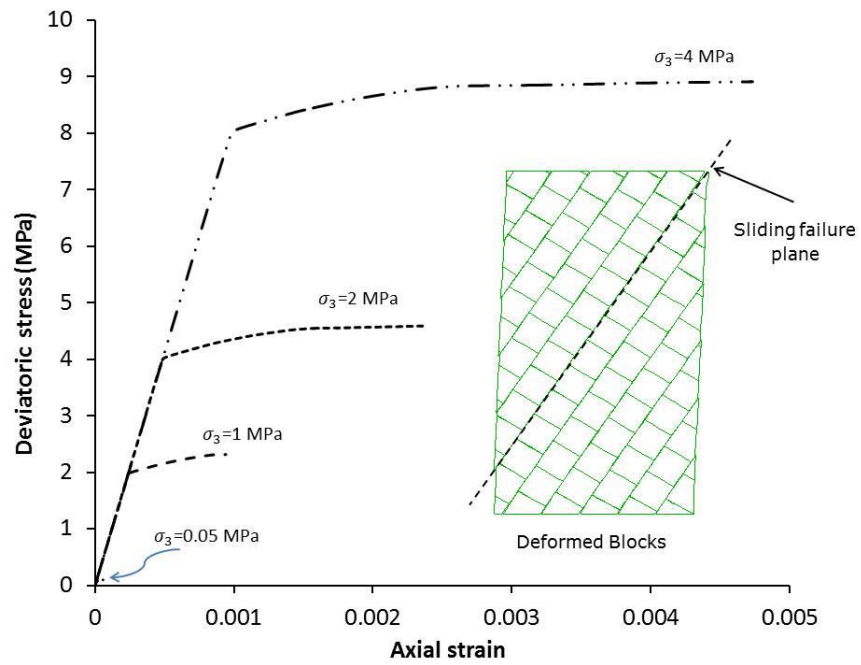
(a) Axial stress-axial strain
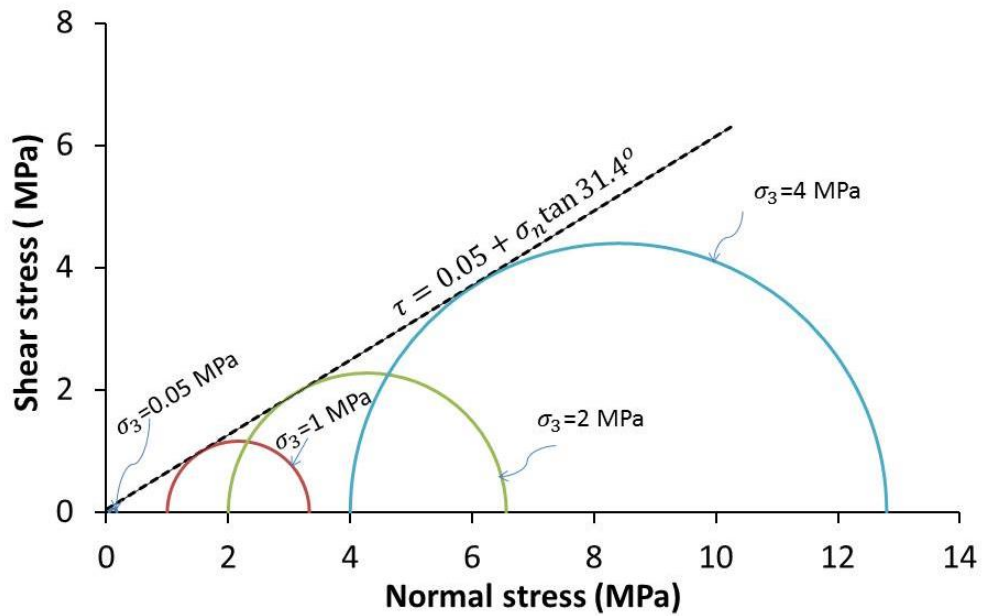
(b) Mohr-Coulomb strength envelope

Figure 6.24 Model J60 (a) axial stress-axial strain, (b) Mohr-Coulomb strength envelope
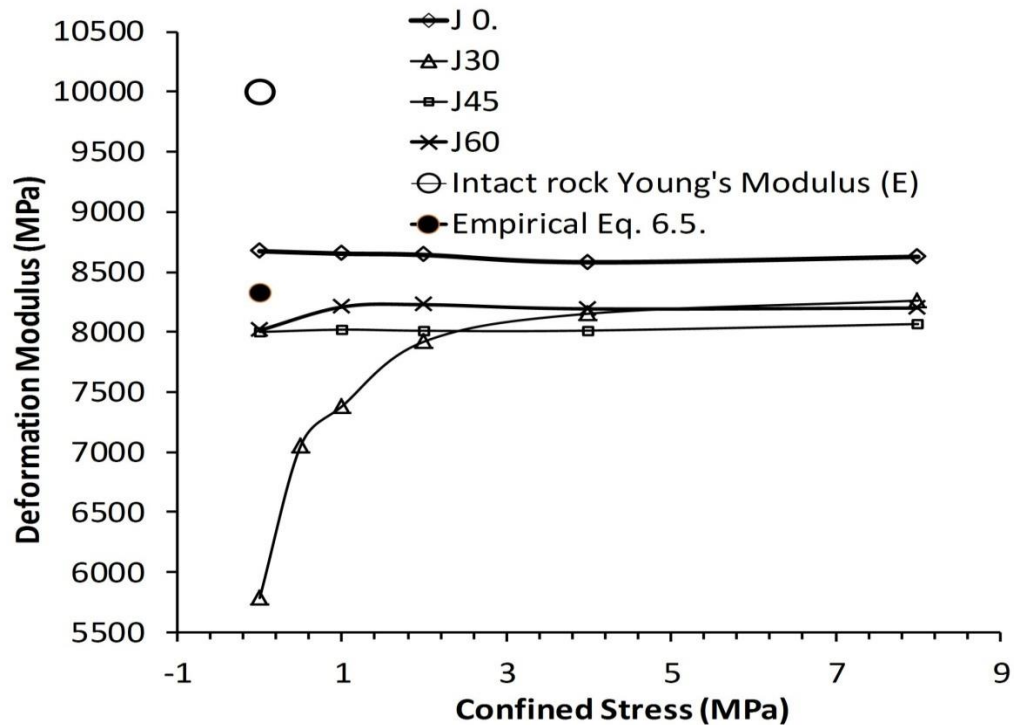
Figure 6.25 Deformation modulus of selected models versus confining stresses

6.3.6 The Effect of stiffness ratio on deformability parameters

Stiffness ratio can be defined as the ratio of the shear stiffness (ks) and the normal stiffness (kn) of the joints. The model J60 was selected to achieve a parametric study to demonstrate the effect of stiffness ratio on deformation modulus ($\bar{E}$) and lateral strain ratio ($\bar{v}$). The effect of stiffness ratio was studied in two cases with a confining stress of 1 MPa. In the first case the stiffness ratio was increased from 0.1 to 1 while holding the normal stiffness constant as 10 MPa/m whereas in

the second case the stiffness ratio was increased from 0.1 to 1 while keeping the shear stiffness constant (5 MPa/m).

Figure 6.26a shows the first case. As can be seen with increasing the stiffness ratio the deformation modulus increases and the lateral strain ratio decreases whereas in the second case, see Figure 6.26b, both deformability parameters decrease with an increase in stiffness ratio. From these we can conclude how the stiffness ratio can affect the deformability parameters. Therefore, these parameters should be selected very carefully for studying the rock mass behaviour using numerical modelling.
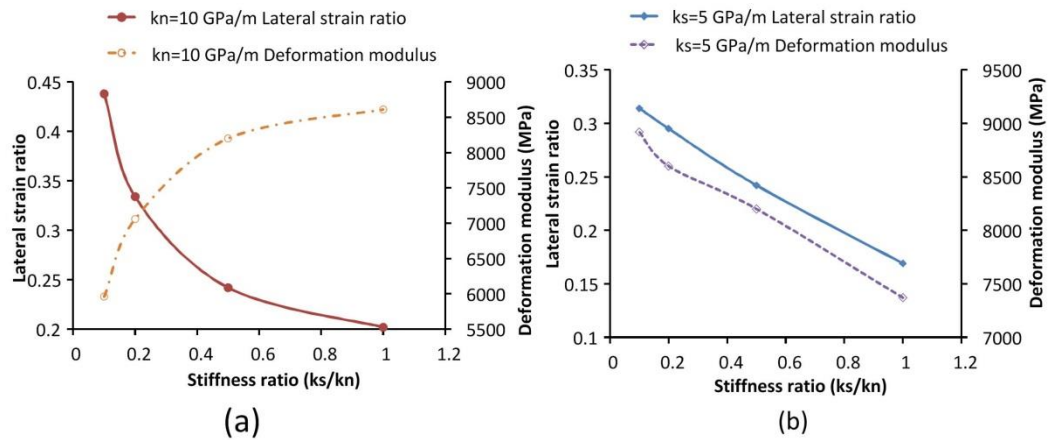
Figure 6.26 Effect of stiffness ratio on deformability parameters of Model J60: (a) normal stiffness constant (b) shear stiffness constant

6.3.7 Equivalent Strength and Deformability Parameters

The objectives of studying the rock mass is twofold. The first is to find out which geometry of joints gives the lowest strength so as to take this into account in the analysis of rock mass behaviour under dams; and the second is to predict the equivalent mechanical properties of the rock mass. To predict the equivalent material properties, Hoek Brown criterion (Hoek et al., 2002) can be used to find the equivalent strength property, however, the main problem with this criterion is that it cannot take into consideration the joint orientation and loading direction with regard to joint orientation. Also it cannot predict lateral strain ratio.

The determined equivalent Mohr-Coulomb strength parameters of friction angle and cohesion intercept are presented in Figure 6.27. The deformation modulus can be obtained from Figure 6.21. The lateral strain ratio was calculated for the models at 50% of the maximum compressive stress using secant modulus method for the unconfined tests (see Figure 6.28) and Poisson's ratio can be calculated using Eq. 6.2. As expected the model J30 has the maximum lateral strain ratio because it has the minimum deformation modulus under low confining stress and at initial loading the slip occurs along joints dipping at 30 degrees resulting in the lateral strain increasing significantly.
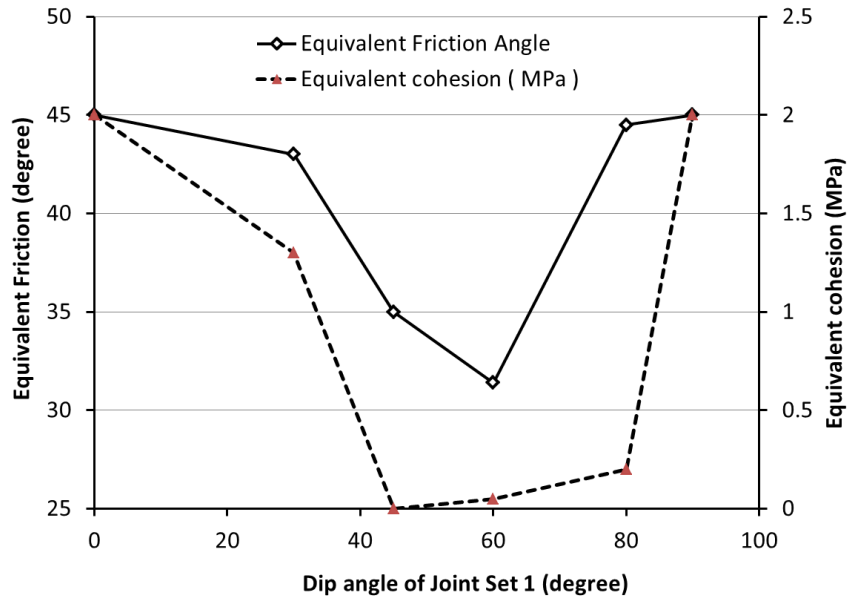
Figure 6.27 Equivalent strength properties
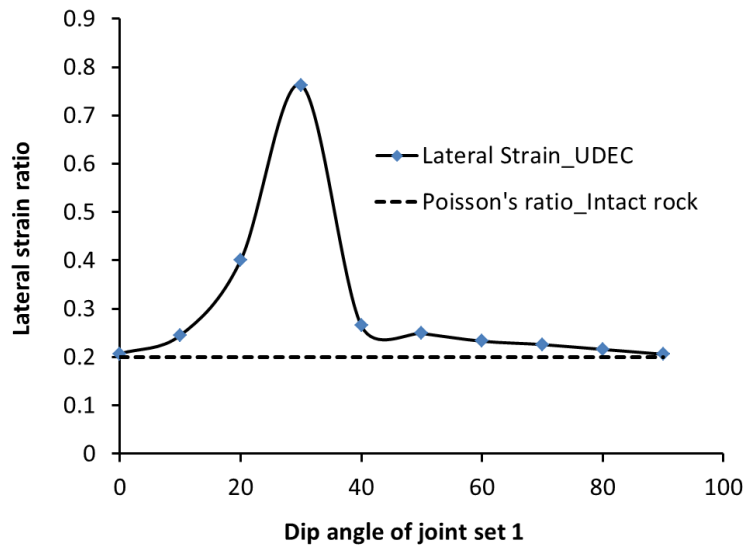
Figure 6.28 Lateral strain ratio with dip angle of joint set 1

Using to Hoek Brown criterion (Hoek et al., 2002), the strength parameters were predicted by using RocLab software as follow: mb=5.36, s=0.0039, and a=0.505. The equivalent Mohr-Coulomb parameters are: c=0.659 MPa and $\emptyset$=40.6 degree. The deformation modulus is 3071.9 MPa and uniaxial strength of the rock mass is 0.562 MPa. According to the RMR classification system (Bieniawski, 1989) the equivalent cohesion is 0.3-0.4 MPa and the equivalent internal friction angle of rock mass is 35-45 degrees. The equivalent deformation modulus is 4000 MPa.

In comparison with results obtained from UDEC, one can conclude that these parameters depend greatly on the loading direction on the rock masses. As can be seen from figures 6.21, the minimum deformation modulus is 5.73 GPa and the maximum deformation modulus is 8.7 GPa. From Figure 6.13, the range of lateral strain ratio is 0.2 to 0.85. As stated before, these parameters should be calibrated according to Equations 6.2 and 6.3 because the study was conducted under plane strain conditions. Based on this study the Hoek-Brown criterion may be developed by including the direction of loading on the rock mass.

6.4 Case Study: Pedrógão Dam

As stated earlier, the Pedrógão dam in Portugal with its rock mass foundation has been chosen as a case study for this part of the research, as described in Farinha et al. (2012). In their analysis of the dam, they compared UDEC and the limit equilibrium analysis to study

the effect of drainage conditions on the stability of the dam. In their UDEC analyses, they considered elastic block behaviour and elastic-perfectly plastic joints. In the analysis presented here, the aim was to study the effect of joint orientation on the stability of the dam. Therefore, the effect of drainage was not considered (the full uplift pressure was applied under the dam). The UDEC code was used and the blocks were assumed to be linearly elastic-perfectly plastic. The equivalent Mohr-Coulomb model parameters of the rock mass obtained in section 6.3.7 were used in a continuum analysis using FLAC so as to make a comparison between the continuum and discontinuum models.

6.4.1 The Discontinuum Model (UDEC)

Figure 6.4 shows the model that was used in this study. The mechanical parameters are given in Tables 6.3 and 6.4. The strength properties for intact rock of friction angle, cohesion and tension, were assumed as 45 degrees, 2 MPa and 1 MPa respectively. Following Farinha et al. (2012), the hydraulic aperture size parameters of a_0 and a_{res} were set to 0.17mm and 0.05mm, respectively, and the joint permeability factor was set to 83.3 $Pa^{-1}Sec^{-1}$.

The simulation of the construction of the gravity concrete dam was done in three stages. Stage 1: the foundation rock was constructed; in this stage the in-situ stresses were initialized and the displacements (after reaching equilibrium) were reset to zero. Stage 2: the dam body was applied and the necessary information about the displacements

and stresses were recorded at the "reservoir empty" stage. Stage 3: the reservoir was filled, loading the upstream face of the dam and the bed of reservoir, the stresses were coupled with flow, and the model was stepped to equilibrium and steady state flow. The same recordings as those in Stage 2 were made again. Figure 6.29 shows the block deformations for stages 2 and 3, respectively. In Stage 3, some of vertical joints were opened in the upstream area as a result of tensile stresses that developed due to the reservoir load.
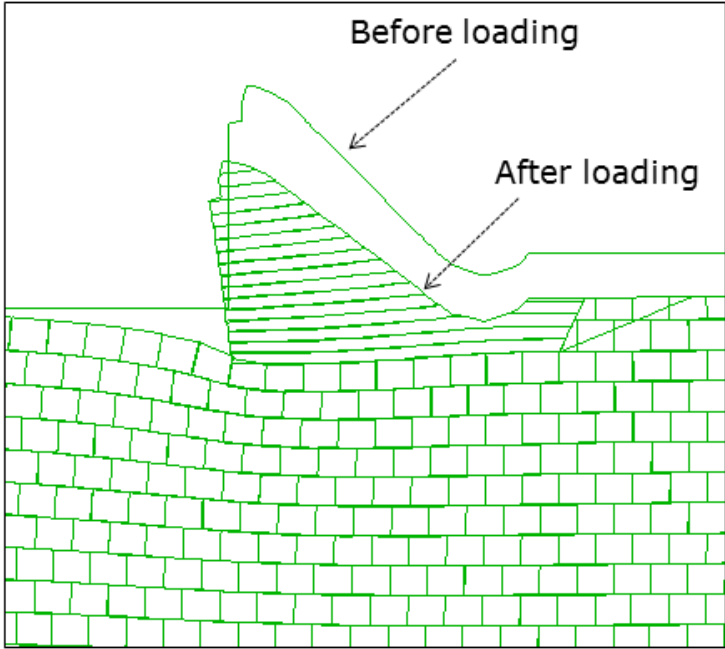
(a) Stage 2
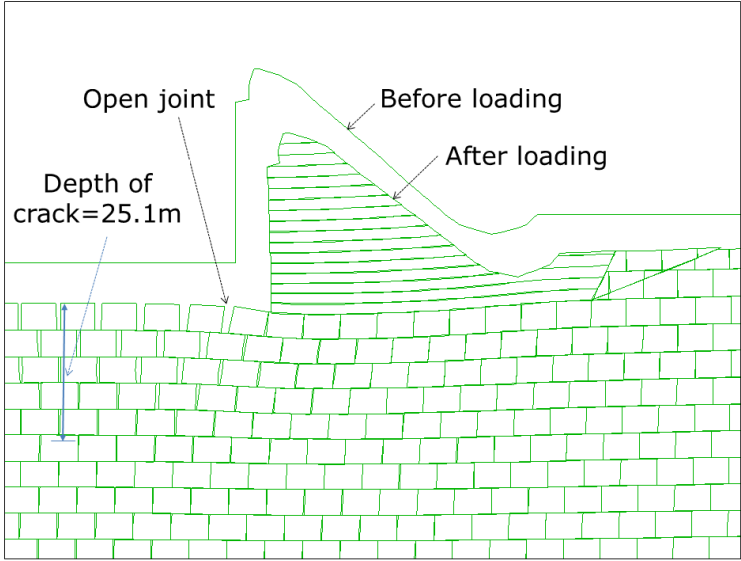
(b) Stage (3)

Figure 6.29 Close-up view of deformation at (a) Stage 2 and (b) Stage 3 from UDEC model

6.4.2 The Continuum Model (FLAC)

In order to obtain mechanical properties for a continuum model, the equivalent rock mass properties detailed in Section 6.3.7 were used. The mechanical parameters were selected according to the direction of the resultant force on the foundation under the dam, as estimated from the UDEC model illustrated in Figure 6.30. This region was selected for the estimation of the equivalent properties because it has the dominant effect on dam behaviour. The equivalent model parameters were selected based on a joint set rotation of 40 degrees. The strength parameters, which were estimated from the triaxial results of the same rock mass, are given in Table 6.5. It should be noted that the deformation modulus and lateral strain ratio were calculated from Figures 6.21 and 6.28 as 8037 MPa and 0.265 respectively and were corrected according to Equations 6.2 and 6.3 to give the realistic Young's modulus and Poisson's ratio. The same mechanical properties for concrete and the base of the dam used in the UDEC analysis were also used in the FLAC analysis (see Table 6.3). The equivalent permeability of the rock mass was set to 5.0×10^{-7}m/sec according to Farinha et al. (2012).
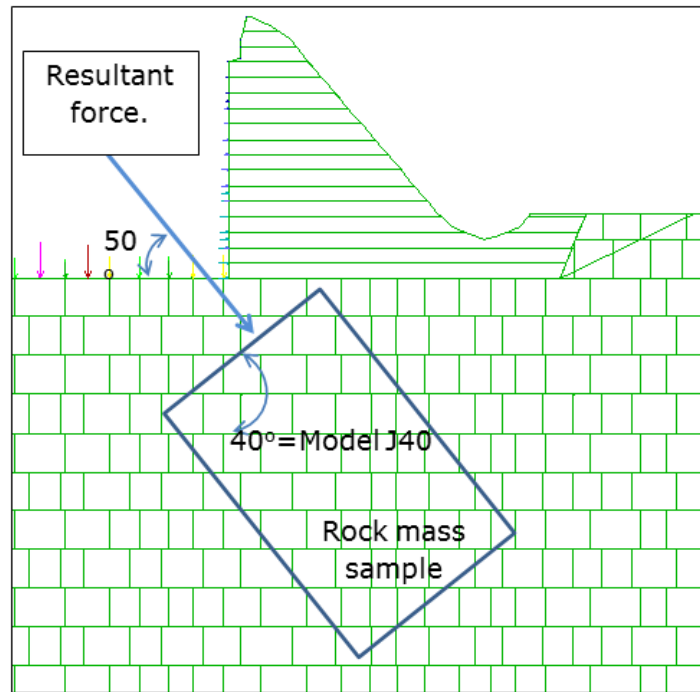
Figure 6.30 Direction of resultant force under the dam based on UDEC analysis

Table 6.5 Equivalent properties for FLAC model

Material	ρ kg/m^3	E_i GPa	v	c MPa	$\emptyset$ Degrees	σ^t MPa
Concrete	2400	30	0.2	-	-	-
Rock mass	2650	7.7	0.21	0.4	37.5	0.0

The FLAC simulation was performed in the same three stages as in the UDEC simulation. Figure 6.31(a) gives the deformation after applying the dam's body load (Stage 2) and Figure 6.31(b) shows the deformation due to the reservoir load (Stage 3). From these figures one can

conclude that the deformation trend is similar to the results from the discontinuum UDEC model.
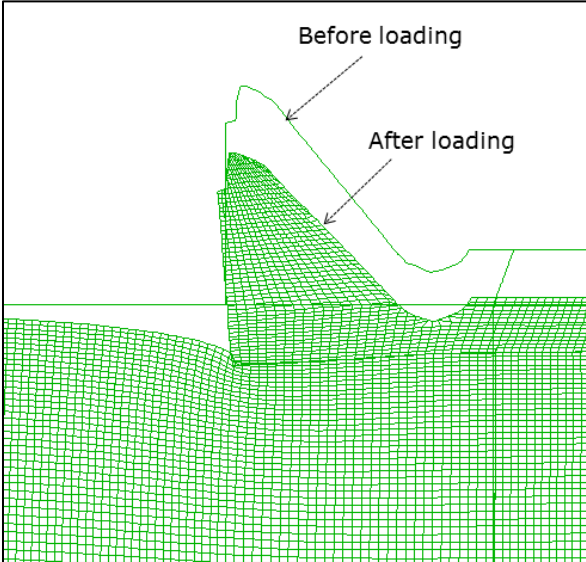
(a) Stage 2
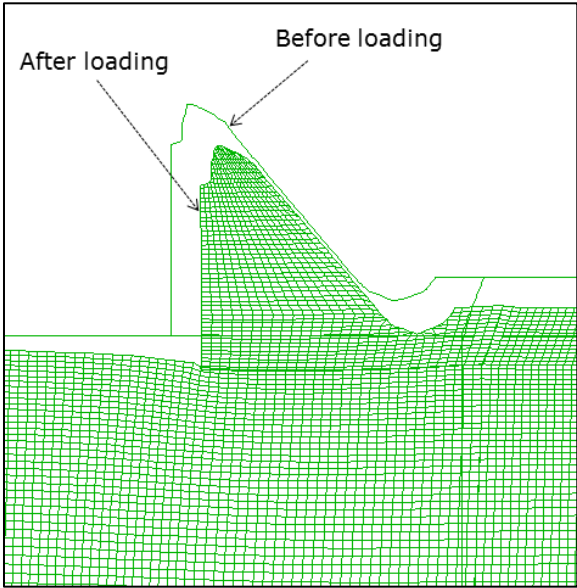
(b) Stage 3

Figure 6.31 Close-up view of deformation at (a) Stage 2 and (b) Stage 3 from FLAC model

6.4.3 Continuum versus Discontinuum

The results from UDEC and FLAC were used to evaluate the stability of the dam. Figure 6.32 shows the distribution of normal and shear stresses under the base of the dam and Figure 6.33 presents the uplift pressure under the dam. In Figure 6.33, the 'conventional method' refers a linear variation of hydrostatic water pressure between the heel and toe of the dam. It is clear that both numerical methods provide similar results for this type of model. The stability of the dam was evaluated by determining the sliding safety factor (F_s) using Eq. 6.5 (Barla et al., 2004) and the Shear Friction Factor (F_{SF}) using Eq. 6.6 (Jansen, 1988; Jian Liu, 2003b).

$$F_S = \frac{T}{N} = \frac{\sum_{i=1}^{n} T_i}{\sum_{i=1}^{n} N_i} = \frac{\sum_{i=1}^{n} \tau_{n,i} L_i}{\sum_{i=1}^{n} \sigma_{n,i} L_i} \qquad\qquad 6.5$$

$$F_{SF} = \frac{\sum A \sigma_n tan\emptyset + \sum CA}{\sum \tau_n A} \qquad\qquad 6.6$$

where i is the element number in the dam foundation interface, τ_n and σ_n are shear stress and normal stress in the interface elements, respectively, L_i is the element length, and A is contact area on which stresses are produced. In the calculation of F_{SF}, the value of c was taken as 0.

The values of F_s calculated by UDEC and FLAC were 0.45 and 0.42, respectively. For F_{SF}, values of 1.55 and 1.66 were evaluated for UDEC and FLAC, respectively. It can therefore be concluded that both methods can give a similar result. Barla et al. (2004) reported a considera-

bly lower value of F_{SF}=3.23 for UDEC compared to F_{SF}=4.28 using FLAC for similar loading conditions. This result is quite different to the results obtained in this analysis. For the FLAC results, the difference is attributed to the higher equivalent strength parameters used in Barla et al. (2004). For the UDEC analysis, the difference may be due to satisfaction of equilibrium conditions when the value of F_{SF} was calculated in the two analyses (chapter 4). In the current UDEC analysis, equilibrium was verified by checking that unbalanced forces and velocities within the model were below the specified required threshold in the software (this took more than the default solve limit steps of 100000 in UDEC v5).
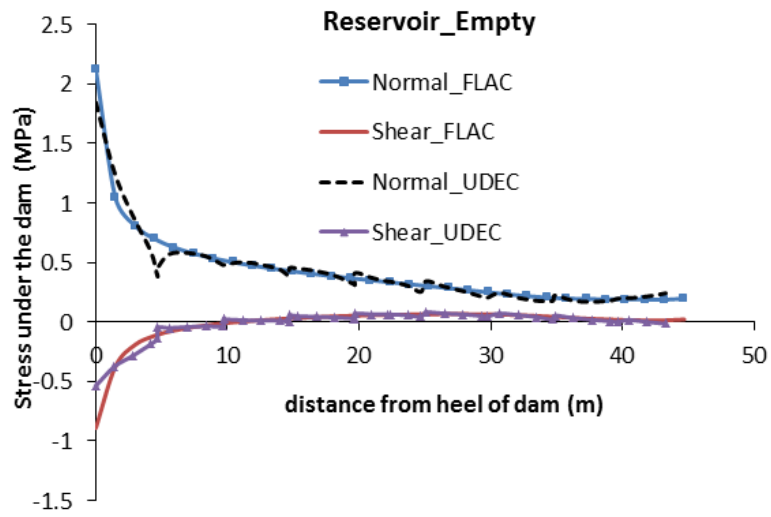
(a) Stage 2 - reservoir empty
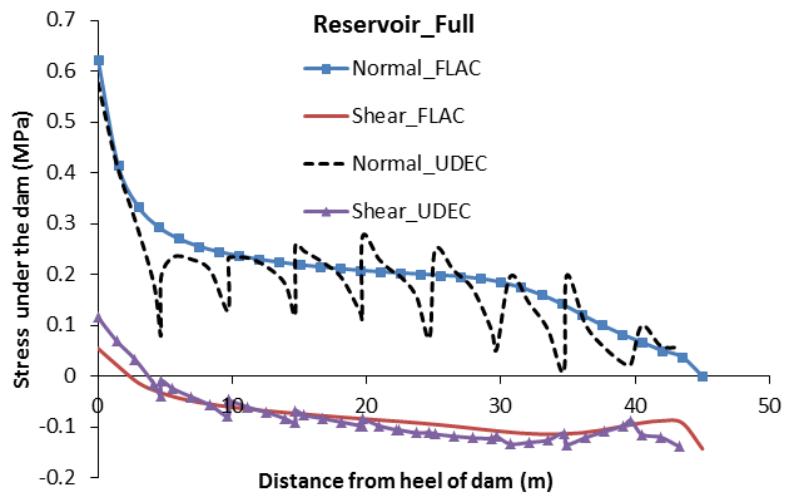
(b) Stage 3 - reservoir full

Figure 6.32 Shear and Normal Stresses at base of the dam: (a) reservoir empty; (b) reservoir full
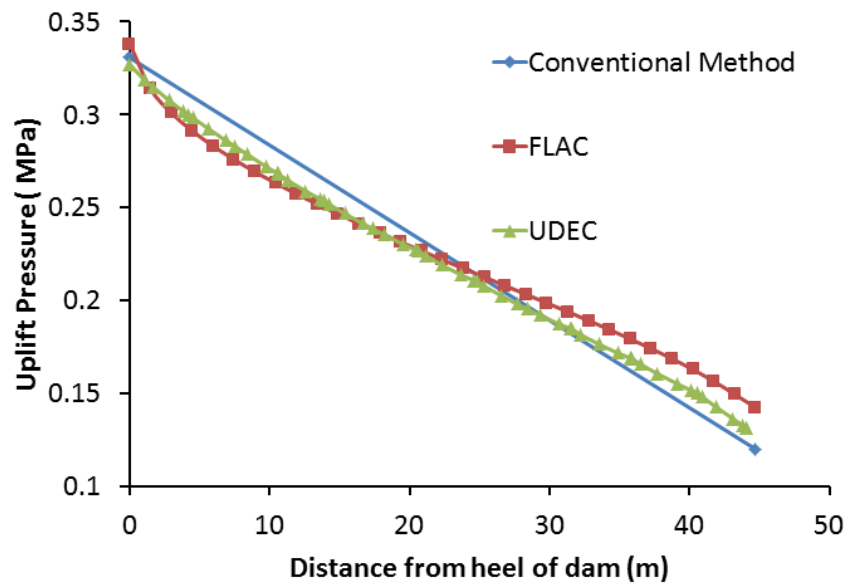
Figure 6.33 Uplift pressures under the base of dam (Stage 3)

Figure 6.34 shows the vertical displacement under the dam and illustrates that both continuum and discontinuum analyses gave similar predictions. Furthermore, tensile zone failure was studied by FLAC (Figure 6.35) and illustrates the potential development of a tension crack in the upstream region near the heel of the dam. In UDEC, a tension crack was noted, see Figure 6.29b, to extend to a depth of 25.1 m, whereas in the FLAC analysis, the tension zone extended to a depth of 30.2 m as illustrated in Figure 6.35.
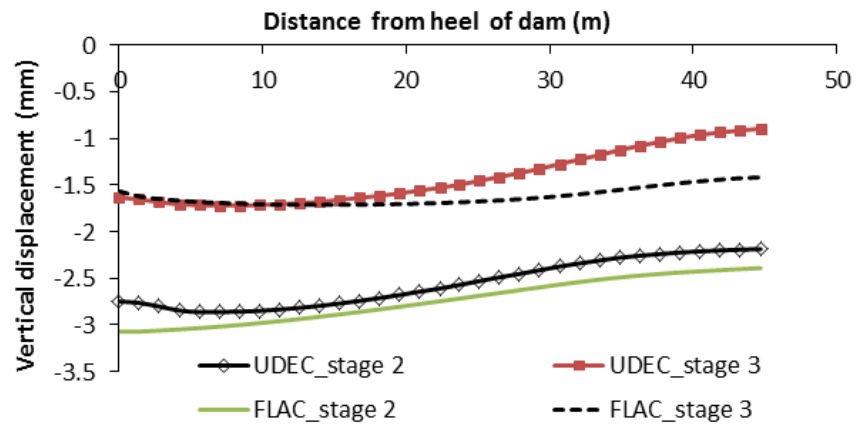
Figure 6.34 Vertical displacements under the dam at Stages 2 (reservoir empty) and 3 (reservoir full)
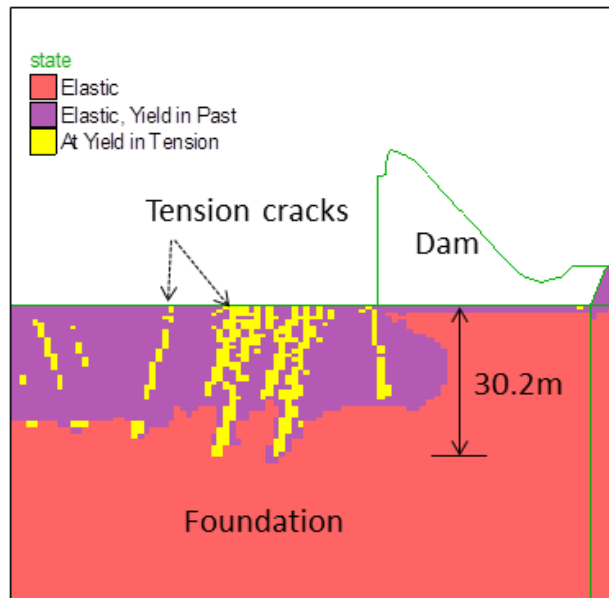
Figure 6.35 Tensile failure zones at Stage 3 (reservoir full)

6.5   Summary and Conclusions

In this chapter, two commercial numerical modelling codes, FLAC and UDEC, were used to simulate the behaviour of a concrete gravity dam on a jointed rock mass foundation, which is arguably the most common scenario encountered for this application. Triaxial tests were simulated using UDEC under plane strain conditions in order to find the equivalent strength and deformability parameters of a rock mass so that a representative continuum analysis using FLAC could be made. This study showed that UDEC can be positively used to determine the equivalent mechanical parameters of rock masses since it is really difficult to test the large rock mass samples in the laboratory. The validity of the output from UDEC prediction was checked by using the evaluated equivalent parameters in continuum modelling of a real dam foundation against the results from discontinuum modelling of the same dam foundation.

This line of research could contribute to the development of a specific rock mass classification system for dams, due to the fact that the available classification systems have been based predominately on slope stability and tunnelling applications. The only classification system that gives information for gravity dams is RMR by Bieniawski and Orr (1976) and Romana et al. (2003). However, there is scope for developing a more efficient rock classification system for dam design and

the work reported in this chapter might be used as a guideline to that end.

What was presented in this chapter was mostly about the application of the numerical modelling technique to study the equivalent rock strength and deformability parameters of a rock mass; but, is it reliable to use the numerical modelling technique to predict these parameters of a rock mass? The author will try to answer this important and challenging question in the next chapter by comparing the results of experimental work on a small scale jointed rock samples with the numerical modelling technique using UDEC.

Chapter 7 Laboratory tests and reliability of numerical modelling

7.1 Introduction

One of the most important and challenging tasks in rock mechanics is the accurate measurement of engineering properties of rock strength and deformability parameters, as well as the post failure behaviour. There have been many studies about the behaviour of jointed rock masses. Kulatilake et al. (2001a) and Kulatilake et al. (2001b), used physical and numerical methods in order to study the behaviour of jointed rock mass under uniaxial loading. They identified three modes of failure: (1) tensile splitting through the intact material, (2) failure by sliding along the joint plane, and (3) mixed mechanism of modes 1 and 2. They showed that the stress-strain diagram of mode 3 exhibited a ductile behaviour; however, the cause of this behaviour was not explained. Asef (2001) carried out triaxial tests on jointed sandstone rock samples using a Hoek cell (Figure 7.1b) in order to study the effect of confining pressure on deformation characteristics. He showed that jointed rock samples which have a dip angle of 60 degrees (measured from horizontal as shown in Figure 7.1a) exhibit strain hardening behaviour. Again, the cause of this behaviour was not fully explained. Similar behaviour was presented by Yoshinaka and Yamabe (1986) who studied jointed rock mass using experimental and numeri-

cal methods. Various other studies have also focused on the defor-mation and strength characteristics of rock mass (Asef and Reddish, 2002; Nasseri et al., 2003; Ramamurthy and Arora, 1994; Singh et al., 2002), but none give a detailed explanation of the cause of strain-hardening behaviour in a jointed rock mass. Recently, Tiwari and Rao (2006) presented results from triaxial $(\sigma_2 = \sigma_3)$ and true triaxial $(\sigma_2 \neq \sigma_3)$ tests on a physical model of an interlocked blocky rock mass to characterise post-failure behaviour. Their results indicated strain-hardening, strain-softening, and perfectly-plastic behaviour, depending upon the joint geometry and stress state. They concluded that strain hardening occurs when the dip of a joint (θ, measured from horizontal) is 40 and 60 degrees and is also dependant on the confining pressure. The literature clearly shows that strain hardening can occur within jointed rock mass; however a detailed explanation of the cause of the strain-hardening has not yet been provided.

For jointed brittle rock samples that have a low joint dip angle of around 30 degrees from horizontal, the failure mechanism is by shear along the intact rock blocks, and strain-softening behaviour is ob-served (Tiwari and Rao, 2006).

Since conventional soil triaxial tests (Figure 7.1a) do not generally have the capacity to fail a weak rock or jointed rock samples, a hard rock triaxial cell such as the Hoek cell (Figure 7.1b) is generally used for these purposes. The Hoek cell provides an effective method for

testing the strength and stiffness of strong rock material under high confining stresses that are not easily achievable using a conventional triaxial apparatus. However, the Hoek cell may not be ideally config- ured for testing weak samples and jointed rock (Bro, 1996a; Bro, 1996b) because the stiff jacket membrane and high friction of the con- tact between the loading platen and the cell membrane introduce un- quantified effects. Bro (1997) explained the cause of strain hardening in weak rock samples when tested using a multi stage triaxial appa- ratus. He argued that the cause of strain-hardening is due to the fact that weak rocks consist of a highly heterogeneous mixture of a strong skeleton of rock surrounded by a weaker matrix of clayey material. As loading initiates, the stiff skeleton takes the majority of the load, and the sample performs in an elastic manner. As the load increases fur- ther, bonds within the skeleton yield and begin to slide, resulting in plastic deformation. The weaker matrix provides confinement to the stronger rock components, and as loading is increased, the full strength of a greater proportion of the matrix is mobilised, thus pro- ducing a strain-hardening effect. The description by Bro (1997) may help to explain the strain-hardening behaviour in weak rock, however the reason for this behaviour in jointed rock samples is still not clear.

The aim of this chapter is to provide an explanation for why the strain- hardening behaviour occurs for samples of jointed rock tested using a typical soil mechanics triaxial cell (Figure 7.1a) and a conventional

Hoek cell (Figure 7.1b). A combination of experimental and numerical methods was used to achieve this aim. Experiments were conducted to quantify the shear and normal behaviour of the interfaces within the loading tests (i.e. rock-rock, rock-platen, and platen-platen). Numerical models were developed using the Distinct Element Method (DEM) code UDEC (Itasca, 2011) because it can, as mentioned in chapter 3, effectively model both rock/metal blocks, as well as the interfaces between the blocks. The effect of the interface properties on the stress-strain behaviour of a jointed rock mass tested within Hoek and triaxial cells is examined using the numerical methods. Comparison of numerical and experimental data will illustrate that the experimental conditions within the two tests has a significant effect on the observed post-yield behaviour. In addition, the results were compared with the analytical method.
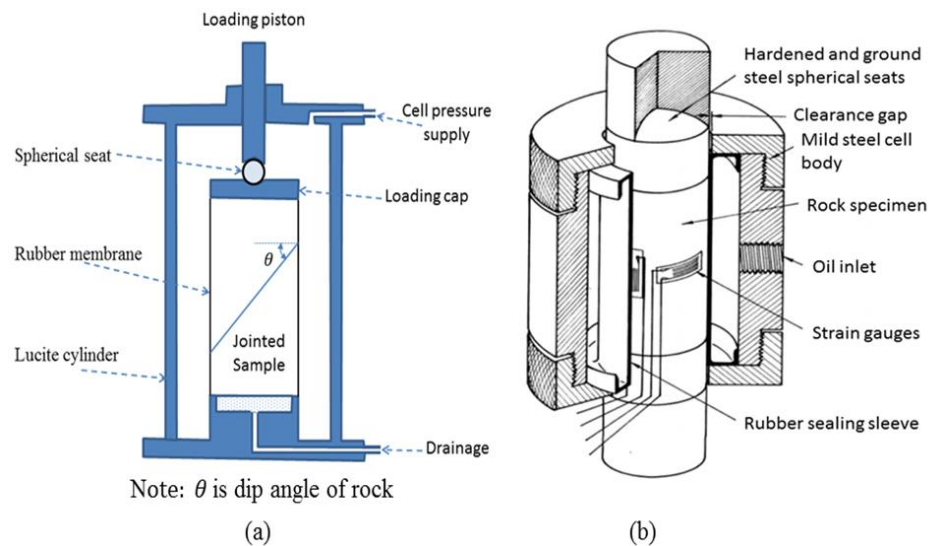
Figure 7.1(a) Typical soil triaxial and (b) Hoek cells (Hoek and Franklin, 1968)

7.2 Laboratory Tests

This section presents experimental data which are used for both input into the numerical models presented later (intact and interface properties) as well as for comparison against numerical results (loading tests using Hoek and soil triaxial cells). The intact rock properties are presented first, followed by interface test results and finally the loading test data.

7.2.1 Intact Rock Properties

Sandstone prepared from a uniform block sample of Birchover quarry in the UK was used for all rock samples. In order to evaluate the intact rock properties, uniaxial compressive strength (UCS), standard triaxial compression, and Brazilian tensile tests were conducted at the University of Nottingham rock mechanics laboratory as described in chapter 3. For UCS tests, three cylindrical samples of 84 mm length and 40 mm diameter were prepared. The stress-strain relationships for all tests are shown in Figure 7.2. The Young's modulus was computed using the tangent modulus at 50% of the failure stress from the axial-stress-strain curve (ISRM, 1981). The strength parameters, cohesion (c) and angle of friction (ϕ), were determined by using small scale triaxial test.
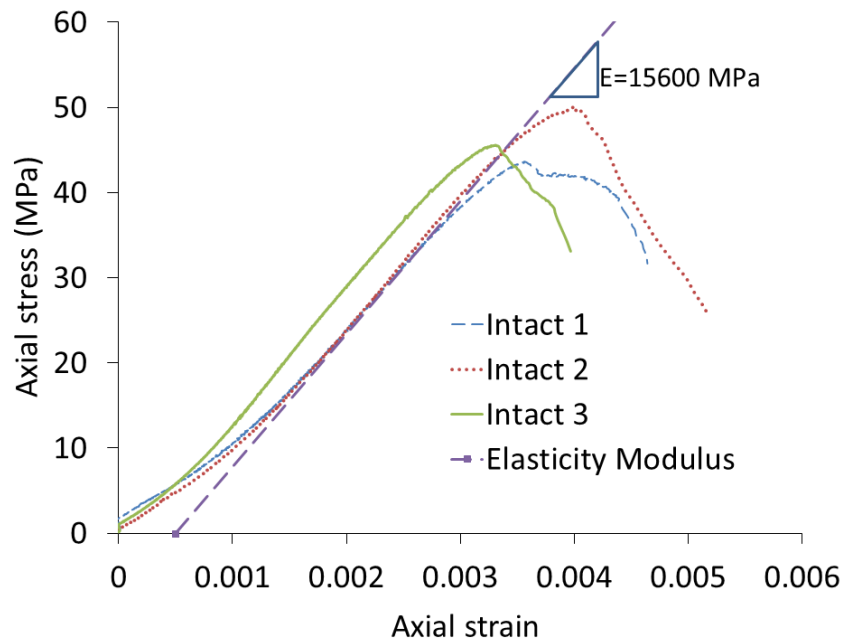
Figure 7.2 Experimental stress-strain data for UCS test on intact samples

For the triaxial compression tests, three cylindrical samples of 84 mm length and 40 mm diameter were prepared (results presented in Figure 7.3a); for Brazilian tests, five cylindrical specimens of 20 mm length and 40 mm diameter were used so as to determine the tensile strength of the intact rock as shown in Table 7.1. In this study, the intact rock was assumed to be a Coulomb material, hence its shear strength was characterised by a value of cohesion and an angle of internal friction, as shown in Figure 7.3b. Table 7.1 summarises the properties of the intact rock determined from the laboratory tests. In addition, the failure mode that was observed from the tests was shear for the intact rock samples (see inset image in Figure 7.3a). Steel platen properties obtained from the literature (Pine et al., 2006) are also provided in Table 7.1. Furthermore, the Poisson's ratio of the in-

tact sandstone was predicted using both video gauge and Digital Image Correlation (DIC) as 0.25 (Table 7.1).
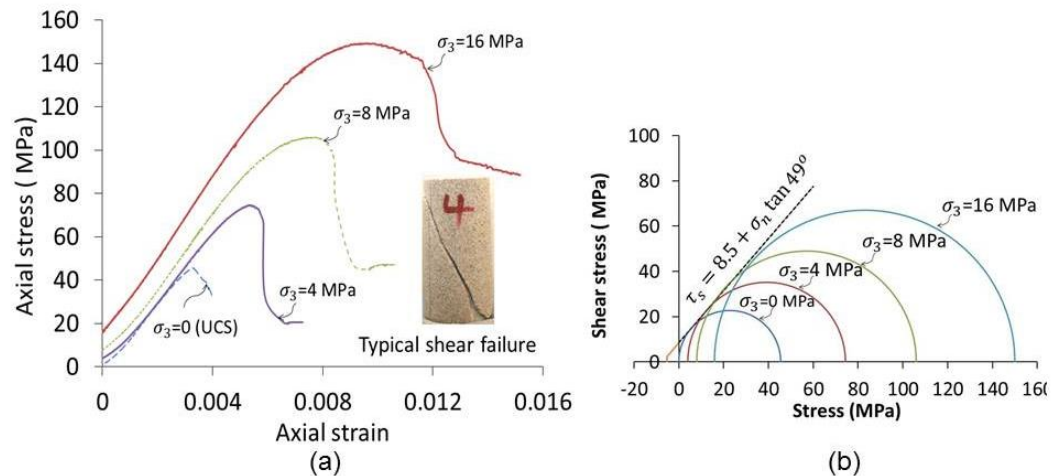
Figure 7.3 Intact sandstone results: (a) stress-strain and (b) Mohr-Coulomb envelopes

Table 7.1 Intact Rock Properties

Material	Density (ρ) kg/m^3	Poisson's ratio	Modulus (GPa) Bulk	Modulus (GPa) Shear	Cohesion (c) MPa	Friction angle (Ø) degrees	Tensile strength (σ^t) MPa
Intact rock (sandstone)	2220	0.25 see Appendix B	10.4	6.24	8.5	49	5.3
Steel Platen	7800	0.30 assumed	166.7	76.9	-	-	-

7.2.2 Joint (Interface) Properties

In order to simulate the jointed rock sample using UDEC, it is important that the mechanical properties of the joints (or interfaces) are known. The mechanical properties of the interface between the follow-

ing materials was tested using the direct shear apparatus described in chapter 3: rock-rock, rock-platen (the ground hardened steel end-platen used in the Hoek cell), and platen-platen. Special platens were manufactured and hardened to HRC 58 (ISRM, 1981). Joints were smooth planer type and ground according to the specification given in ISRM (1981). The following material properties were required for the contacts (joints) in the numerical study: shear stiffness (k_s), normal stiffness (k_n), cohesion (c_j), and friction angle ($\emptyset_j$).

Figure 7.4 presents the shear stress versus horizontal displacement data from the three interface tests. From the data, the values of k_s were determined as the slope of the initial linear portion of the curves. The data shows good consistency of k_s between tests with varying normal stress (NS). The resulting values of k_s for the rock-rock, rock-platen, and platen-platen were 3.3, 2.9, and 2.0 GPa/m respectively.

(a) Rock-Rock contact

(b) Rock-Platen contact

(c) Platen-Platen contact
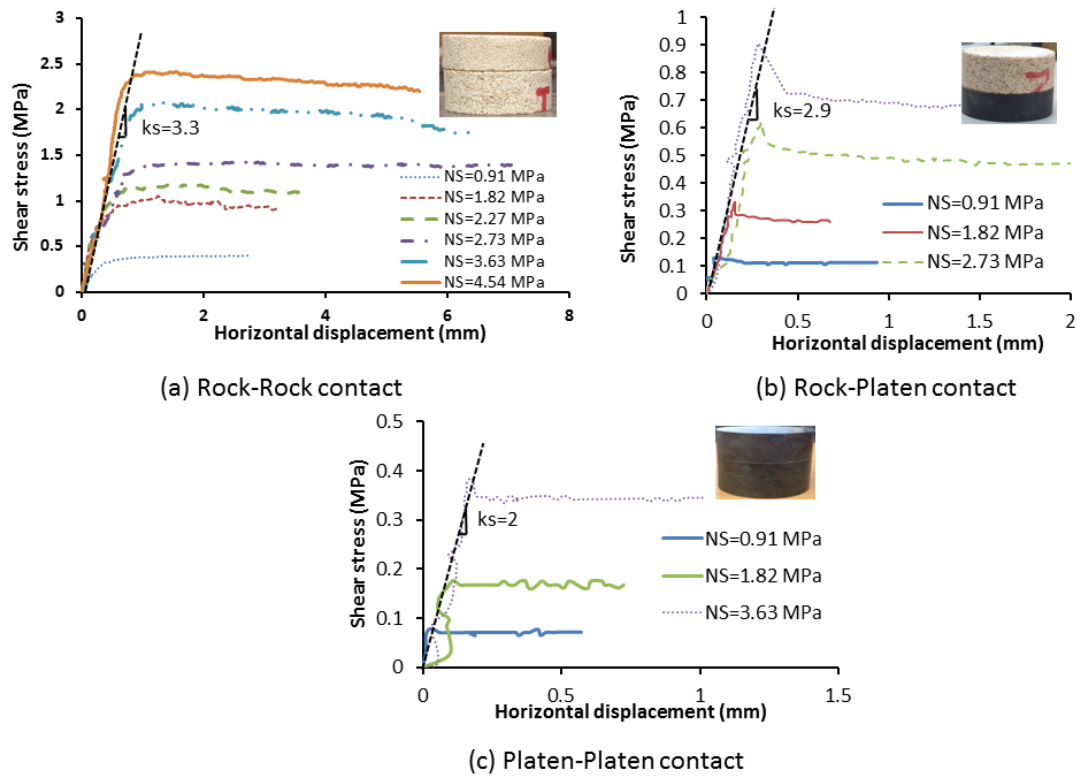
Figure 7.4 Shear stress – horizontal displacement for interface tests. Note: NS is normal stress

In order to evaluate the normal stiffness of the contact between rock blocks for the numerical simulations, uniaxial compression tests were conducted to measure the relationship between normal stress and vertical displacement for intact and jointed samples. Two samples (each 35mm long by 40mm diameter) were prepared: one intact and another split at its mid-section with a horizontal smooth planar joint, as shown in Figure 7.5. The rock-rock normal joint stiffness was calculated to be 455 GPa/m. This value was evaluated from the normal stress versus deformation curve which was obtained by subtracting the jointed sample data from the intact sample data. The normal stiffness of

the platen-rock contact was also assumed to be 455 GPa/m within the numerical models.
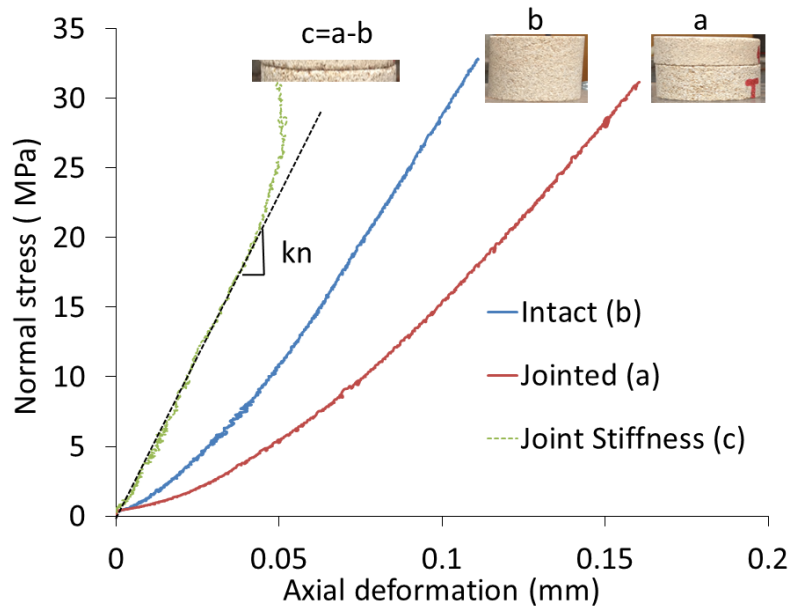
Figure 7.5 Normal stiffness of interfaces (rock–rock contact)

In addition, a Mohr-Coulomb failure envelope was utilized to find the strength properties of the interfaces, as presented in Figure 7.6. From the data, the friction angles for the rock-rock, rock-platen, and platen-platen interfaces were determined to be 29.2°, 10.7° and 5.6° respectively (a cohesion-intercept of zero was assumed). Table 7.2 summarize the mechanical parameters obtained from the laboratory testing of the joint contacts.
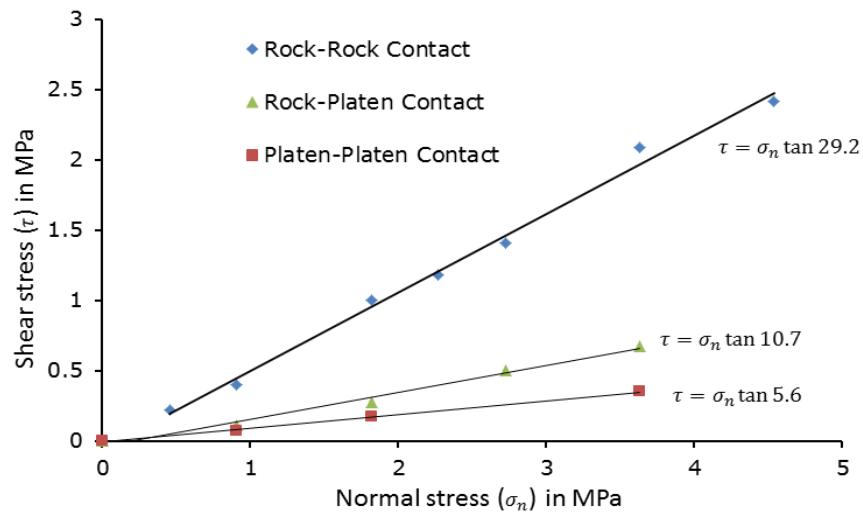
Figure 7.6 Shear strength envelopes for interfaces

Table 7.2 Mechanical properties of interfaces

Contact	Normal stiffness, (k_n) GPa/m	Shear stiffness, (k_s) GPa/m	Friction angle $(\varnothing)$ degrees	Cohesion MPa
Rock-rock	455	3.3	29.2	0
Rock-platen	455 assumed	2.9	10.7	0
Platen-platen	455 assumed	2	5.6	0

7.2.3 Jointed Rock – Hoek cell and triaxial tests

Jointed sandstone samples (120 mm long by 50 mm diameter) were prepared to study the effect of an induced smooth joint on the mechanical properties of the rock sample. Anisotropy was induced into cylindrical intact rock samples by creating a single smooth planar joint at a dip angle (θ) measured from horizontal that was polished smooth. Two joint angles were made; the first dipped at $\theta = 30^\circ$ (J30) and the other at $\theta = 60^\circ$ (J60), as shown in Figure 7.7. For the J30 samples, a series of Hoek cell tests were carried out at a range of confining pres-

sures. The axial load was applied using a displacement rate of 0.002 mm/sec. For the J60 samples, which require a lower axial load to induce failure than the intact and J30 samples, both conventional soil triaxial and Hoek cell tests were conducted.

Figure 7.7a shows the stress- strain curve for the J30 samples. The samples were failed by shear (see image in inset) through the intact rock. In addition, the post failure deformation is characterised by strain softening. Figure 7.7b shows that for the J60 sample, a sliding failure was induced along the joint, with associated post-failure strain hardening behaviour.

It is postulated here that the strain-hardening behaviour observed for the J60 sample is not a result of the material behaviour but that it is related to the rock-platen contact stiffness and the induced non uniform distribution of vertical stress within the sample caused by the experimental configuration. This argument is explored further using numerical analysis in Section 7.4.

(a) Jointed rock type J30

(b) Jointed rock type J60
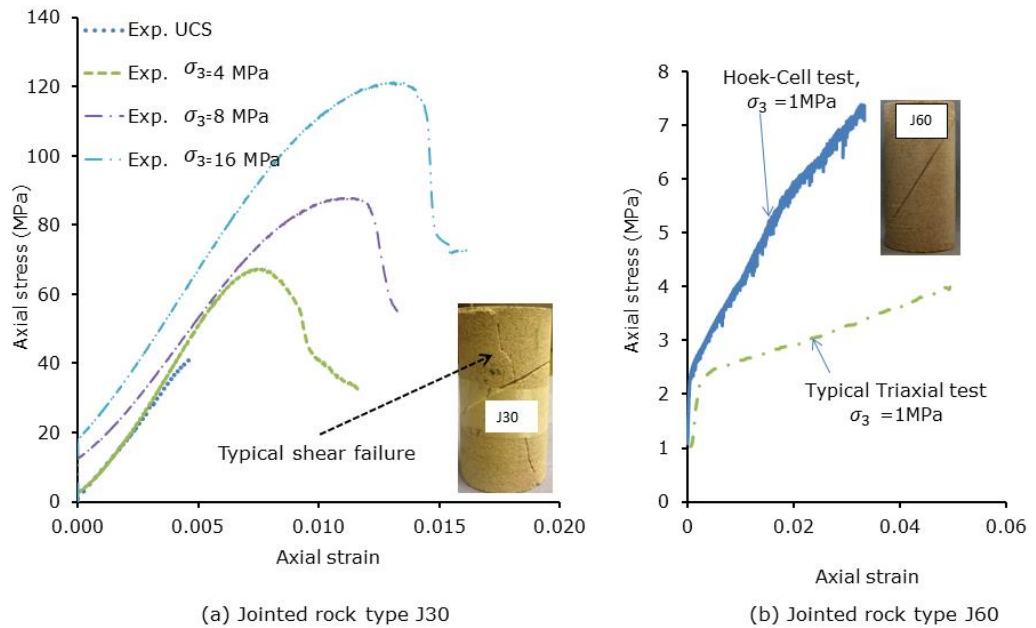
Figure 7.7 Stress-strain data from jointed rock tests

7.3   Analytical Solution

Analytical methods, if available, can be used as a guide to show the reliability of experimental and numerical results. Therefore, in this study the plane of weakness theory was selected so as to compare it with numerical and experimental results.

The analytical plane of weakness theory (Jaeger et al., 2009) can be used to predict the compressive strength of jointed rock samples in a triaxial test. The model is represented by Eq. 7.1 for slippage failure (which requires that the term $(1 - \tan\phi_j \tan\beta)$ must be greater than 0) and by the Mohr Coulomb failure criterion in Eq. 7.2.

$$\sigma_1 = \sigma_3 + \frac{2(c_j + |\sigma_3| \tan\phi_j)}{(1 - \tan\phi_j \tan\beta) \sin 2\beta} \tag{7.1}$$

$$\sigma_1 = \left(\frac{1+\sin\phi}{1-\sin\phi}\right)\sigma_3 + 2c\sqrt{\frac{1+\sin\phi}{1-\sin\phi}} \tag{7.2}$$

where σ_1 and σ_3 are the major and minor principal stresses, respective-ly, β is the angle formed by the direction of σ_1 and the plane of the joint, c_j is the cohesion of the joint, ϕ_j is the friction angle of the joint, c is the intact material cohesion and ϕ is the internal friction angle of the intact material. For given value of σ_3 and an increasing magnitude of σ_1, failure will be by slippage along the joint if Eq.7.1 is satisfied first or by shear through the intact rock if Eq.7.2 is satisfied.

Figure 7.8 shows the values of axial stress (σ_1) required to cause fail-ure (according to Equations 7.1 and 7.2) for the material parameters provided in Tables 7.1 and 7.2 for joint dip angles (θ) ranging from 0 to 90 degrees at two values of confining stress (σ_3). The plotted data illustrates the predicted transition from shear failure through the intact rock (highest and constant values of axial stress) for lower values of joint dip angles (or θ=90 degrees) to sliding failure along the joint for intermediate vales of joint dip angle. The data also illustrate that the minimum strength is obtained when the joint dip angle is 60 degrees.
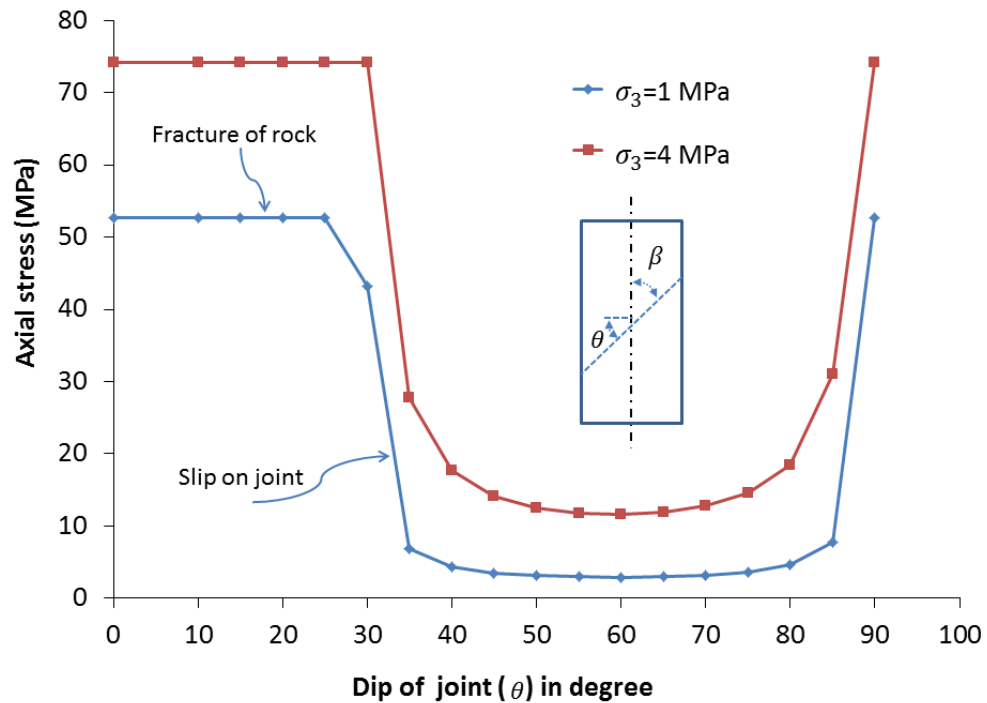
Figure 7.8 Axial stress at failure versus joint dip angle according to Equations 1 and 2

7.4 Numerical Modelling

Numerical models were developed using the DEM UDEC code in order to gain insight into the stress distributions that developed within the tested rock samples as well as the effect of the interfaces between rock blocks and various components of the experimental equipment. In the UDEC model, the domain of interest is represented as an assemblage of rigid or deformable blocks and the contacts between the blocks are identified and updated continuously during the entire loading/deformation process. The behaviour of the blocks and the inter-

block interactions are represented by appropriate constitutive models. In the analyses presented here, the behaviour of the intact material was treated as elastic perfectly-plastic (Mohr-Coulomb) and for joints the area contact Coulomb slip model (elastic perfectly plastic) was used.

7.4.1 Details of numerical model

Although the experiments were conducted under three-dimensional loading conditions, a two-dimensional (2D) plane-strain UDEC analysis was used for the numerical analysis. The 2D analysis does not give an exact replication of the experiments, but it can provide insights into the material behaviour during tests and the effect of particular components of the testing system. 2D measurements of the equivalent sample stiffness could be adjusted according to the method described by Potyondy and Cundall (2004) in order to obtain representative 3D values, however in the context of this work, this correction is not required since the analysis focuses on the post-yield behaviour of the rock. Plane-strain numerical analyses were conducted rather than axis-symmetric in order to ensure that a realistic failure mechanism and post-failure behaviour were replicated within the models.

During laboratory testing, axial load was applied in a displacement controlled mode. To replicate this in UDEC, loading was applied using the velocity command whereby the top loading platen was moved downwards with a velocity of 10 mm/sec in steps while the bottom

platen was kept fixed. A special FISH (a programming language used by Itasca software) routine was developed to perform the loading of the samples and to ensure data was obtained at a state of numerical equilibrium. After 20 time-steps within the numerical analysis, the top platen was stopped and the system was stepped to equilibrium. At this stage, the reactions on both platens, the average stress within the sample, and the axial and lateral strains were recorded. The developed FISH routine worked in a similar way to the servo-control that was used during the experimental tests.

The UDEC models are shown in Figure 7.9. Different models were created according to the configuration of the Hoek, UCS, and triaxial tests. A spherical seat in the upper and lower platen of the Hoek cell (Figure 7.9a) is included to compensate for any initial misalignment of the sample ends. For the UCS test, only one spherical seat is included in the upper platen (Figure 7.9b). For the triaxial test, a different spherical seat is used in the upper platen, as shown in Figure 7.9c. Once sufficient axial load is engaged in the Hoek and UCS tests, the spherical seats provide little benefit of compensating for misalignments that occur due to sample distortions (Hoek and Franklin, 1968).

In the numerical models, the joint stiffness ratio, $R = k_s/k_n$, was used to study the effect of interface properties on test results. The stiffness ratios of the three interfaces involved are denoted by R_{pp}, R_{pr}, and R_{rr}, where the subscripts 'pp', 'pr', and 'rr' denote platen-platen, platen-

rock, and rock-rock, respectively. The platen-rock and the rock-rock interfaces were found to have the most significant effect of the measured numerical stress-strain response. The value of R_{rr} was found to mainly affect the pre-yield stiffness modulus of the sample, whereas the value of R_{pr} affected the post-yield behaviour.
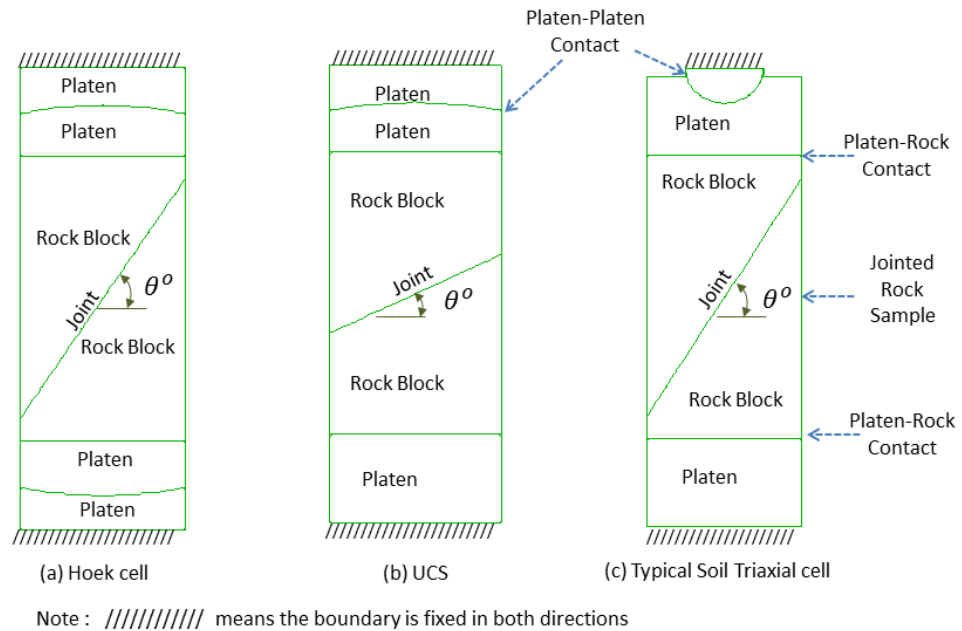
Figure 7.9 Simulating jointed rock samples by UDEC [σ_3 just along the rock sample]

7.4.2 Numerical results and analysis

7.4.2.1   Intact sample

In order to study jointed rock sample it is important to accurately replicate the intact rock sample behaviour. The intact rock sample 3 was chosen from Figure 7.2 because its peak stress acts as an average for the intact rock samples 1 and 2. In the numerical simulations, the ma-

terial property from Tables 7.1 and 7.2 were utilized. The results presented in Figure 7.10. As can be seen, the experimental curve can be well predicted by UDEC. From this one can conclude that the computer code that was prepared for this study is working correctly.

Since the numerical models were performed under plane strain conditions, the out-of-plane strain is required to be zero. Therefore, the equivalent modulus of deformation and Poisson's ratio obtained from the tests were modified according to Equations 6.2 and 6.3 (Potyondy and Cundall, 2004) in order to obtain conventional elastic parameter values.

The real values of v and E can by Equations 6.2 and 6.3 as 16554 MPa and 0.249 respectively which are the same input values in UDEC model. This confirms that the results from plane strain models should be corrected using Equations 6.2 and 6.3. There are many articles that used plane-strain models to study rock masses but did not correct the Young's modulus and Poisson's ratio such as Noorian Bidgoli and Jing (2014a).
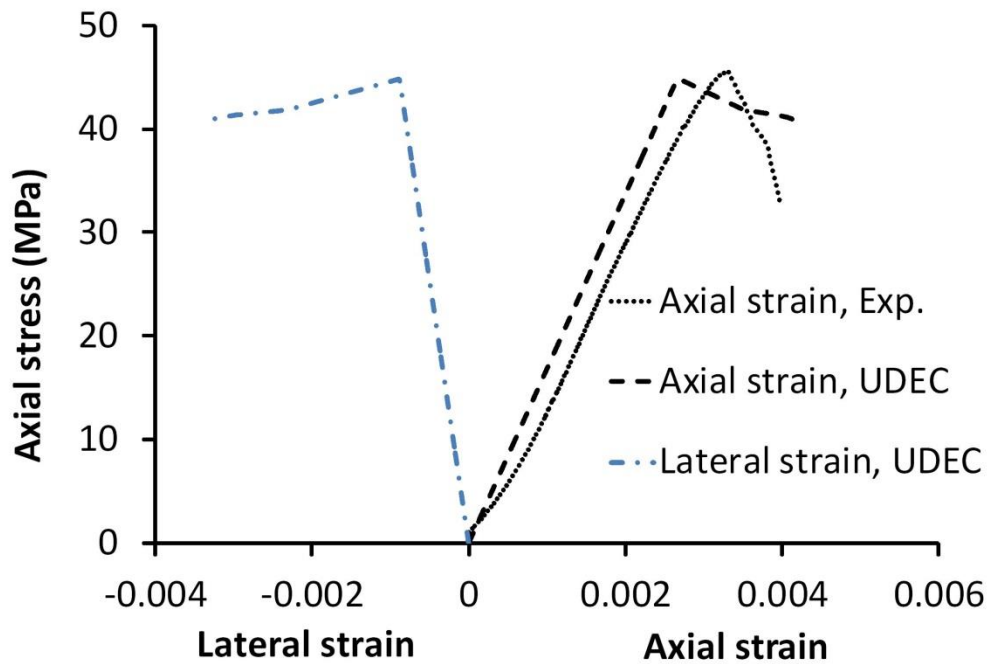
Figure 7.10 Axial stress-axial strain relations for intact rock sample

7.4.2.2 Sample type J30

The laboratory results of sample type J30 in Figure 7.7a showed that the post-yield stress-strain behaviour was strain softening for unconfined and confined compression tests and that the failure mode was shear through the intact rock blocks. Figure 7.11 compares results from the numerical and experimental tests. Two experimental axial stress-strains were selected so as to compare them with numerical results. The first sample was tested as UCS and the second sample was tested with confined pressure of 4 MPa so as to compare between numerical and experimental results. In the numerical simulations, the

material properties from Tables 7.1 and 7.2 were used. The numerical results show similar trends as the experimental data; strain softening behaviour and shear failure through intact rock blocks. However, the deformation modulus produced by numerical model is lower than that produced by experimental results because the shear deformation along the joint in the numerical models is more than that in experimental tests. As this deformation increases the vertical strain increases as a result deformation modulus decreases. This is due to fact that the configuration of Hoek cell is not suitable for testing jointed rock sample. Hoek cell configuration (Figure7.1b) prevents the sample ends from moving freely because the author thinks that this cell was developed for testing hard intact rock samples rather than for testing jointed rock samples and weak rock samples. To prove this by numerical method, the author fixed the samples ends and adjusted the value of R_{rr} to 100/455 in order to fit the experimental results and the results are shown in Figure 7.12. As can be seen, the Hoek cell overestimated the Young's modulus and should not be used for testing jointed rock and weak rock with old configuration. The author has proved this by comparing the results between Hoek cell and soil triaxial test in next section. In addition, since smooth joint with angle of friction of 29.2 is used in simulation and according to plane of weakness (Eq.7.1), shear deformation along the joint plays an important role in strength and deformability.
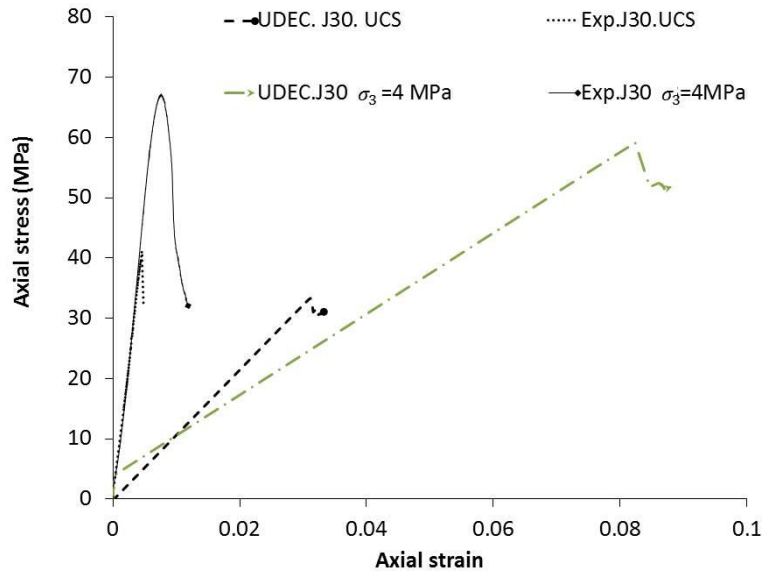
Figure 7.11 Axial stress-axial strain relationships for jointed rock type J30
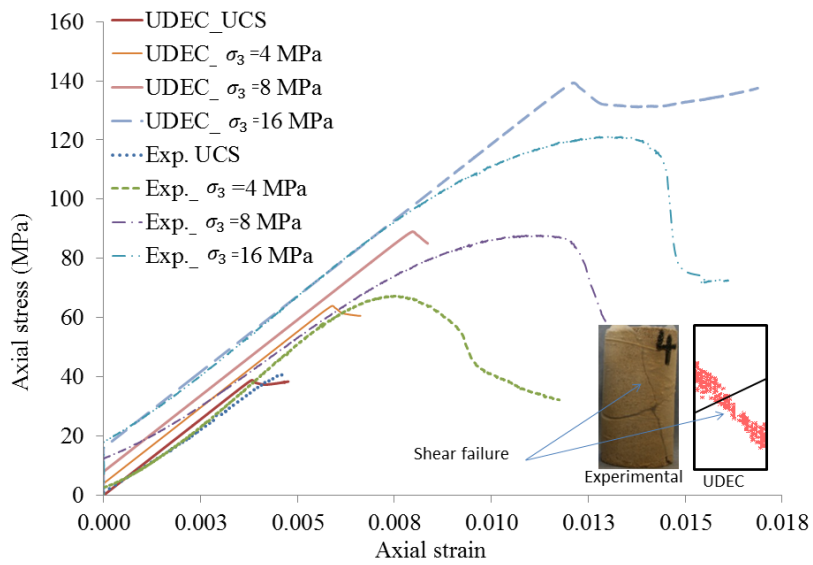
Figure 7.12 Axial stress-strain relationships for jointed rock type J30

7.4.2.3   Sample type J60

The laboratory results of sample type J60 (Figure 7.7b) show that the post-yield stress-strain behaviour was strain hardening for confined compression tests and the failure mode was continuous slip along the joint. Figure 7.13 shows the axial stress-axial strain results produced by UDEC and experimentally for sample J60 under a confining pressure of 1 MPa. The experimental data for both the soil triaxial cell and Hoek cell tests are shown. In the numerical simulations, the material properties from Tables 7.1 and 7.2 were used. As can be seen from the Figure 7.13, numerical results for both cells have similar trend as experimental results by soil triaxial test. However numerical predictions of the yield stress did not match well with the experimental data because firstly the stiff membrane resists the slip along the joint and secondly the loading configuration makes the non-uniform distribution of vertical stress and as a result strain hardening develops. Yield axial stresses produced in numerical models are very similar to the analytical method produced by Equation 7.1 but higher than that produced by experimental because the conventional direct shear test was used to predict the angle of friction of the joint. The convectional direct shear usually overestimates the angle of friction of the joint (Aghda et al., 2004; Asadzadeh and Soroush, 2009).

As can be seen from Figure 7.13, the strain hardening in Hoek cell is higher than that in soil triaxial cell. From this one can conclude that

this hardening behaviour is not related to the material behaviour but to the cell and loading configuration. This hardening is due to non-uniformity distribution of vertical stress as a result the sliding along the joint not follow the theory that was assumed for the jointed rock sample.
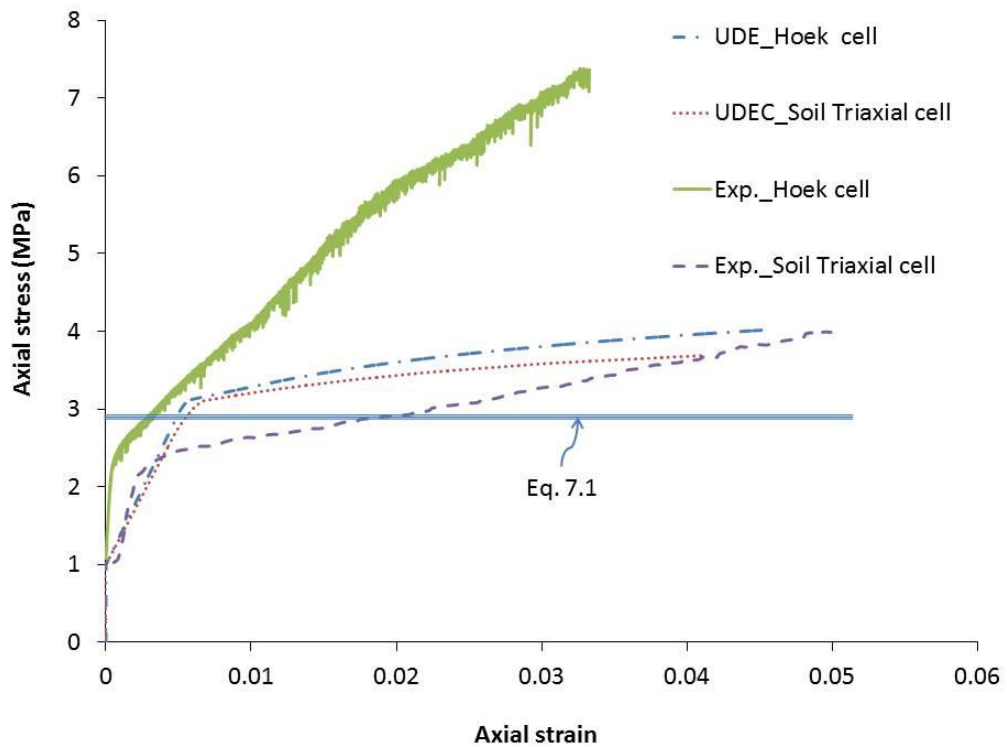
Figure 7.13 Axial stress-axial strain relationships for jointed rock type J60 with a confining pressure of 1MPa

To further investigate the cause of hardening behaviour, the properties of the joint will be adjusted so as to fit the numerical results with ex-perimental results. The rock-rock and rock-platen stiffness ratios were therefore adjusted within the numerical analyses (see values shown in

Figures 7.14 and 7.15) in order to get a better match with the experimental loading results.

The modified stiffness ratios required to obtain a good fit to the experimental data are indicative of the effect that the geometric configuration within the experiments have on test results for this joint orientation. To replicate the soil Triaxial cell test behaviour within UDEC, the value of R_{rr} was maintained according to interface test results (R_{rr}=3.3/455 from Table 7.2), however to match the post-yield response, a value of R_{pr}=1/455 was needed. Also in Figure 7.14 are data from a numerical simulation of the triaxial test with a value of R_{pr}=0/455. This data shows that, when the platen-rock interface effect is completely removed (zero shear stiffness), a perfectly-plastic behaviour is obtained. Therefore, it is likely that the reduced effect of the rock-platen interface in the triaxial test (given by the reduction in R_{pr} required to match the post-yield experimental data) is due to the beneficial effect that the test configuration has, whereby the spherical seat accommodates for sliding along the rock joint and helps to reduce the effect of the rock-platen interface friction.

In the Hoek cell, the pre-yield response was matched using a value of R_{rr}=18/455 and using joint angle friction of 25.2 degree instead of 29.2 degree. The spherical seats in numerical simulation for Hoek cell were removed since the cell configuration apply restriction of sample ends. As can be seen from Figure 7.14, the significant strain-hardening

experimental response was matched numerically using a value of R_{pr}=25/455 (data has again been shown for the case where $\mathrm{R_{pr}}$=0/455 to illustrate the effect that the platen-rock interface has on post-yield behaviour). The hardening slope after yield for the Hoek cell is higher than that in the soil triaxial test because the Hoek cell configuration (Figure7.1b) prevents the sample ends from moving freely as a result of the shear stress that develops in the contact between the platen and rock sample. This changes the direction of principal stresses within the sample and results in a separation between the rock sample and the bottom platen, a phenomenon which was observed experimentally and within the numerical analyses (see inset in Figure 7.14). It can therefore be concluded that the post-yield data obtained from the Hoek cell test of jointed rock sample J60 is significantly affected by the experimental configuration, and may not reflect the actual rock mass behaviour. The rock-platen interface roughness would appear to have the dominant effect on the post-yield behaviour of the J60 sample.

The cause of this strain hardening is examined further in Figure 7.15, which compares the distribution of axial stress within three samples. Figure 7.15(a) shows a Hoek cell test with a smooth platen-rock inter-face and illustrates a generally uniform distribution of stress within the sample, with high stress concentrations occurring near the shear fail-ure plane along the joint and all stresses being compressive. Figure 7.15(b) illustrates a typical soil triaxial test with a platen-rock stiffness

ratio of 1/455 based on the data in Figure 7.14. Here, one can see that the stresses within the sample are much less uniform than in Figure 7.15(a) and that some tensile stresses exist within the sample. In Figure 7.15(c), the platen-rock stiffness ratio from Figure 7.14 for the Hoek cell is used, and it is shown that a highly non-uniform distribution of stress is obtained, with higher tensile stresses than noted in Figure 7.15c.

The deformation modulus (E_{rm}) obtained from the initial linear stress-strain relationship in Figure 7.7b produced by the Hoek cell (E_{rm}=3120 MPa) is greater than that produced by the typical soil triaxial test (E_d=854 MPa). This is due to the fact that in the Hoek cell the sample ends cannot move freely, hence the need to increase the value of R_{rr} within the numerical analysis to get a good match to the pre-yield experimental data.

In order to overcome these issues within the Hoek cell, which is novelty of this study, an upper and lower platen with a spherical seat similar to that used in the soil triaxial cell could be used in order to avoid separation between the platen and rock sample. This will be shown in next section. This solution, however, might not be practical in real tests.
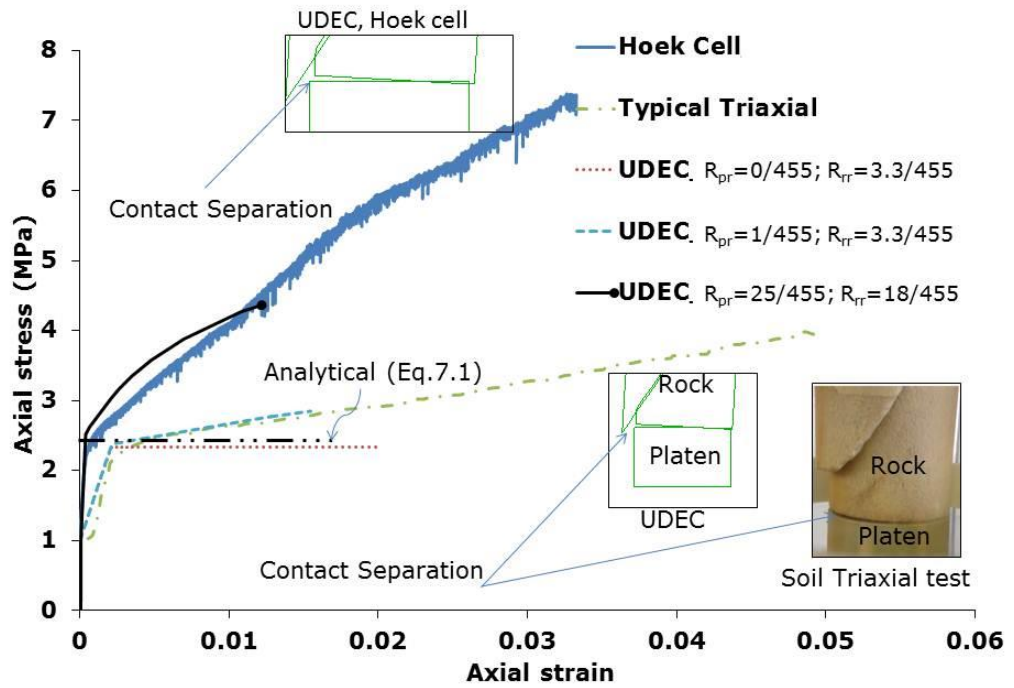
Figure 7.14 Axial stress-strain relationships for jointed rock type J60 with a confining pressure of 1MPa
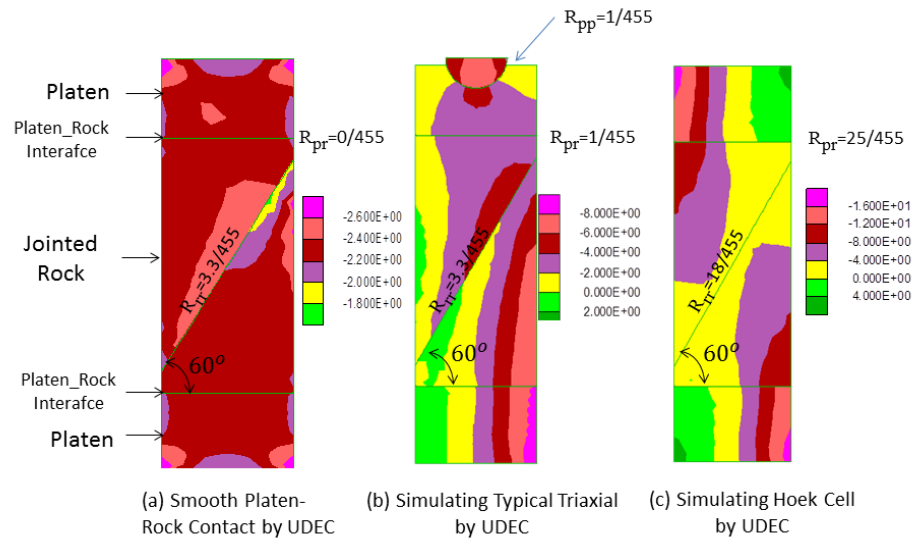
Note: negative stresses are compressive; values of stress in MPa

Figure 7.15 Axial stress distribution (σ_y) for sample type J60 for different contacts stiffness ratios

7.4.3 Proposed new loading configuration (NLC)

During the last five decades many empirical relationships have been developed to predict the deformation modus of jointed rock masses based on unconfined and confined compression test data. For unconfined compression tests, the loading configuration shown in Figure 7.9b was frequently used. For confined compression tests, the Hoek cell was mostly used despite the fact that the Hoek cell was designed by Hoek and Franklin (1968) for testing hard intact rock and not for testing jointed rock samples or weak rocks (Bro, 1996a; Bro, 1996b). In this study, based on the numerical and experimental results presented already, a new loading configuration has been developed. This loading configuration can be used for both unconfined and confined compression tests. The new loading configuration is shown in Figure 7.16.
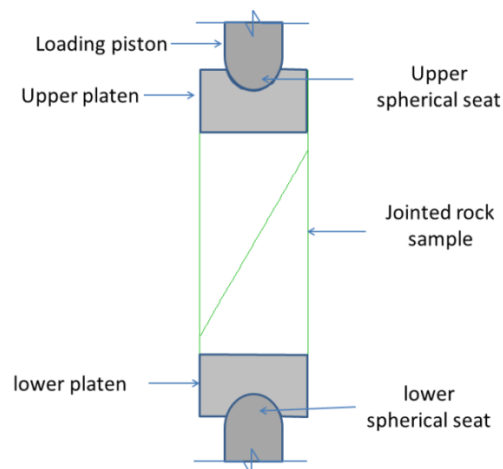
Figure 7.16 New loading configurations (NLC) for compression test

The new loading configuration (NLC) can be used so that the direction of the major principal stress is always in the direction of loading. It will be shown that a consequence of this is that strain hardening will not develop for single-jointed rock samples. To confirm this, a series of confined compression tests were conducted using the numerical simulation. In the new loading configuration, the material properties from Tables 7.1 and 7.2 were used without any adjustment. Figure 7.17 shows the axial stress axial strain relationship for sample type J60 with a confining pressure of 1 MPa produced using the new loading configuration system. As can be seen from the inset image in the Figure 7.17, the distribution of vertical stress inside the sample is uniform and the post-yield behaviour is perfectly-plastic (i.e. no strain-hardening).
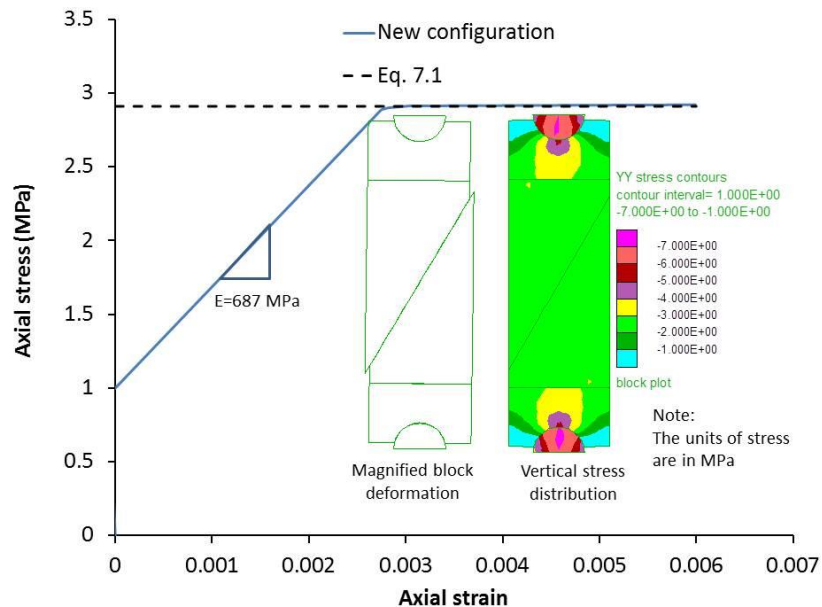
Figure 7.17 Axial stress-strain relationships for jointed rock type J60 by using new loading configuration

7.4.3.1   Laboratory tests using NLC

Based on the numerical modelling results, the triaxial experiments were modified to replicate the new loading configuration by introducing a lower spherical seat, as shown in Figure 7.18. Rock jointed samples with a single joint dipped at 60 degrees were prepared using the Birchover Sandstone. Figure 7.18c shows the new part that was manufactured in the University of Nottingham for testing the jointed rock samples. Meanwhile, Figure 7.19 shows the axial stress against axial strain curves for the jointed rock sample type J60 tested under confining pressures of 0.5 MPa, 1 MPa and 1.5 MPa using the new loading configuration (NLC) system developed in this study. As can be seen, there is no strain hardening and the model displays elastic-perfectly plastic behaviour. Since the failure was sliding along the smooth joint, the friction angle was calculated from the strength failure envelope shown in Figure 7.20. The resulting angle of friction of the joint was $\emptyset_j=26.0^o$. This value is lower than that produced by direct shear test and suggests that the direct shear test overestimates the friction angle when compared to the triaxial test. The lower friction angle of 26.0^o was used in Eq. 7.1 and in the UDEC model, so as to compare these results with the experimental data. The results are presented in Figure 7.19. Interestingly, there is excellent agreement between the experimental and UDEC results. As mentioned earlier in chapter 6 the deformation modulus produced by UDEC should be corrected according

to equations 6.2 and 6.3. Therefore, the deformation modulus was corrected and the results are presented in Figure 7.21.

In addition, a sensitivity analysis was performed to assess the effect of the stiffness ratio (ks/kn) on deformability parameters. Figure 7.22 shows the effect of the stiffness ratio on the lateral strain ratio and deformation modulus for models J30 and J60. In Figure 7.22 (a) and (c) show that as the stiffness ratio increases by fixing kn, the deformation modulus increases while the lateral strain ratio decreases. However, in Figure 7.22 (b) and (d) both parameters decrease by fixing ks while increasing the stiffness ratio. Meanwhile, Figure7.22 (e) and (f) show an increase in the deformability and lateral strain ratio parameters with increasing shear stiffness for a constant stiffness ratio.

Soil triaxial cell by GDS

The GDS 50kN load frame

Modified lower spherical seat
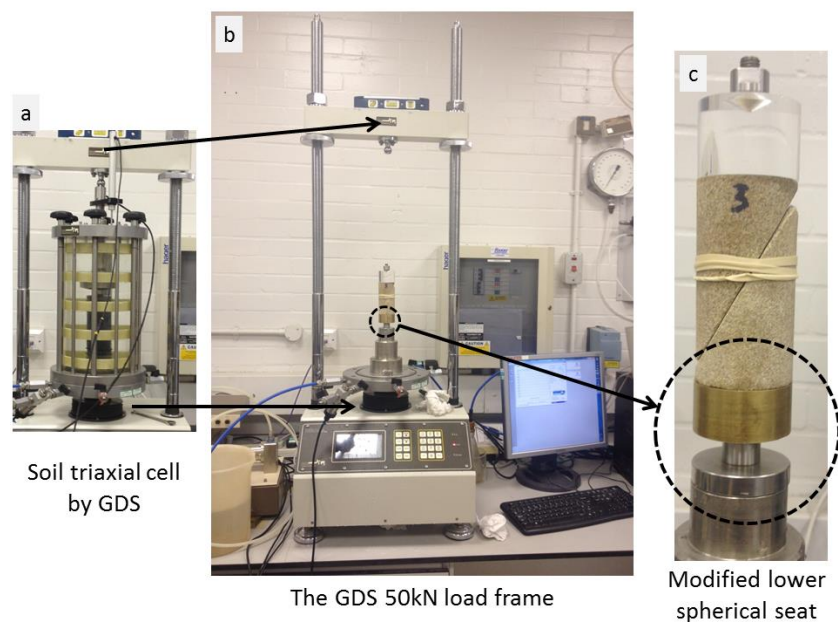
Figure 7.18 (a) Soil triaxial (b) the GDS 50kN load frame (c) the modified part of the new loading configuration.
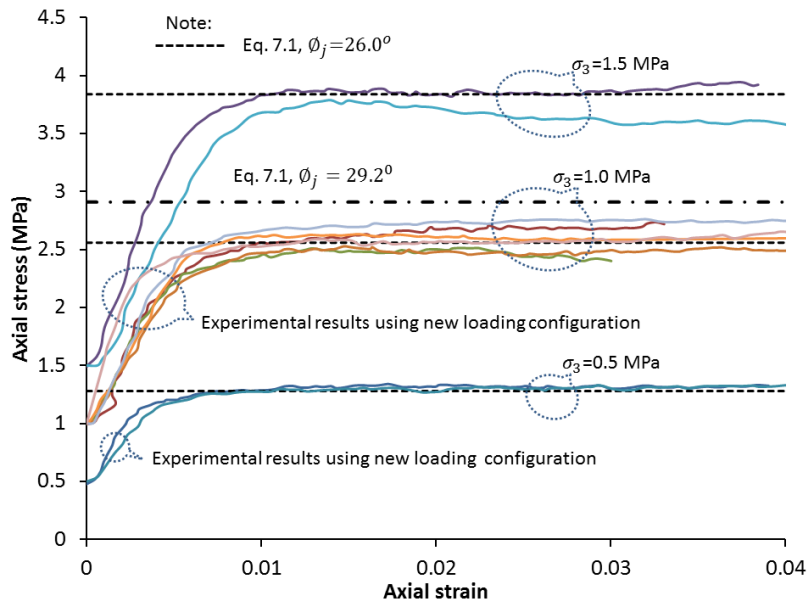
Figure 7.19 Axial stress-axial strain by new loading configuration.
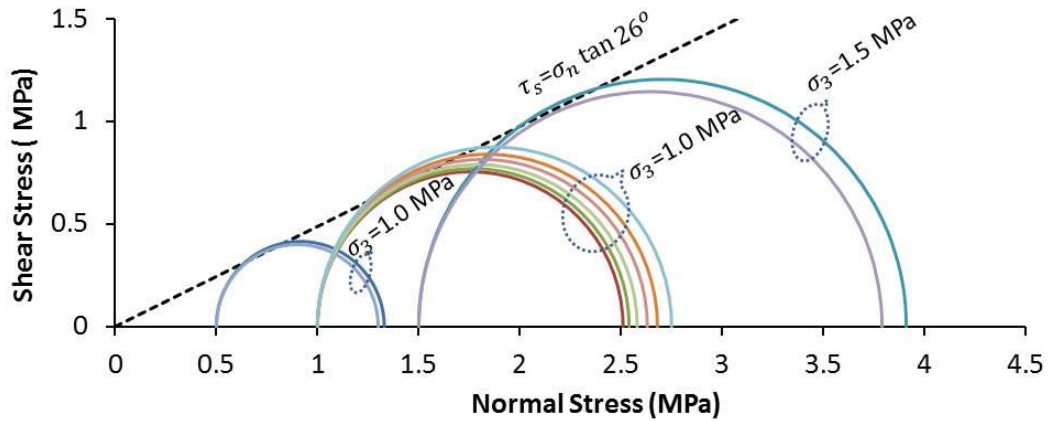
Figure 7.20 Strength failure envelope for model J60 by new loading configuration.
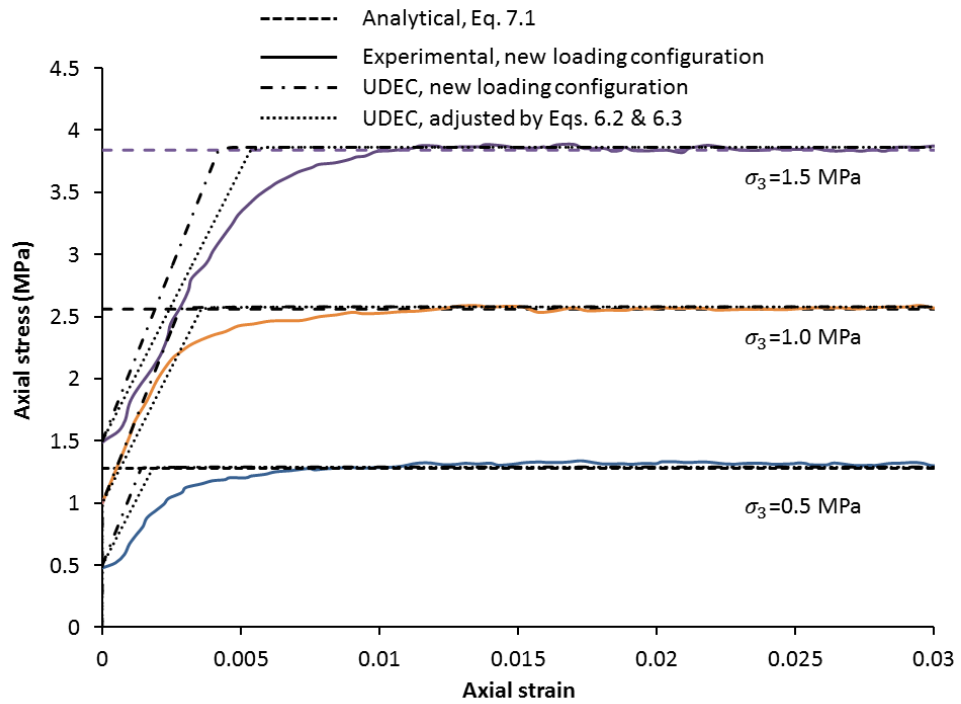
Figure 7.21 Adjusted deformation modulus of axial stress-strain of model J60
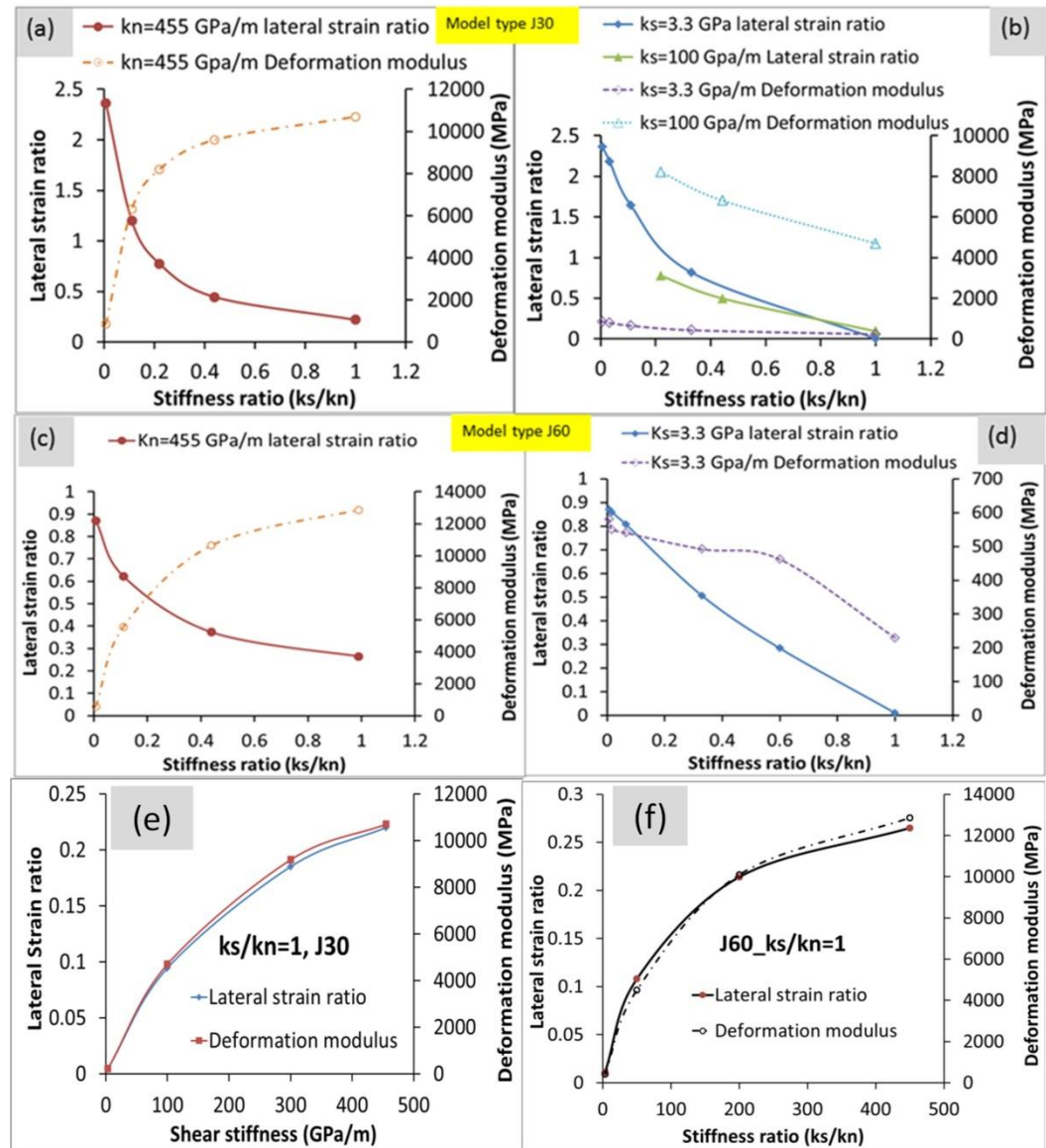
Figure 7.22 Effect of stiffness ratio on lateral strain ratio and deformation modulus

7.4.3.2   Jointed rock mass sample using NLC

Interlocking of rock blocks may cause strain hardening after yield stress and one should take this into account when testing blocky rock samples. It was concluded that the strain hardening produced in the

Hoek cell for a sample with a joint with a dip angle of 60 degree was due to the development of a non-uniform distribution of axial stress at the contact where platens transfer the axial stress into the jointed rock sample. However, there may be strain hardening in some loading conditions due to interlocking and block rotations. To illustrate this, a blocky jointed rock sample with two joint sets was analysed by UDEC using the proposed NLC and the traditional loading system in soil triaxial and Hoek cells. The results are presented in Figure 7.23. This figure shows that the strain hardening in a traditional loading system in the Hoek cell and soil triaxial cell are higher than that in the NLC. The minimal strain hardening in the NLC is due to block interlocking and rotations, whereas the strain hardening in the traditional loading configuration is due to the fact that the axial stress is not distributed uniformly on the jointed rock sample, as shown in Figure 7.24. As can be seen, the maximum vertical stress is 30 MPa in Hoek cell whereas the maximum verticals stress distribution is 12 MPa in soil triaxial cell using NLC. The high axial stress distribution inside the jointed rock sample using the traditional loading system can cause failure in individual rock blocks in tension or shear as shown in Figure 7.25a. The magnified block deformations for both loading configuration system are also revealed in Figure7.25 (b) and (d).
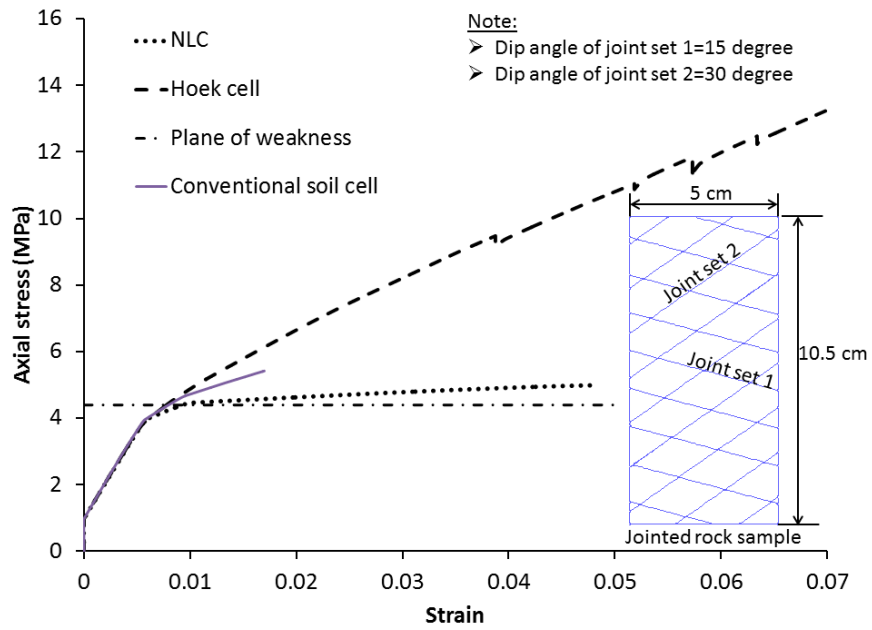
Figure 7.23 Axial stress-strain of blocky rock mass by NLC
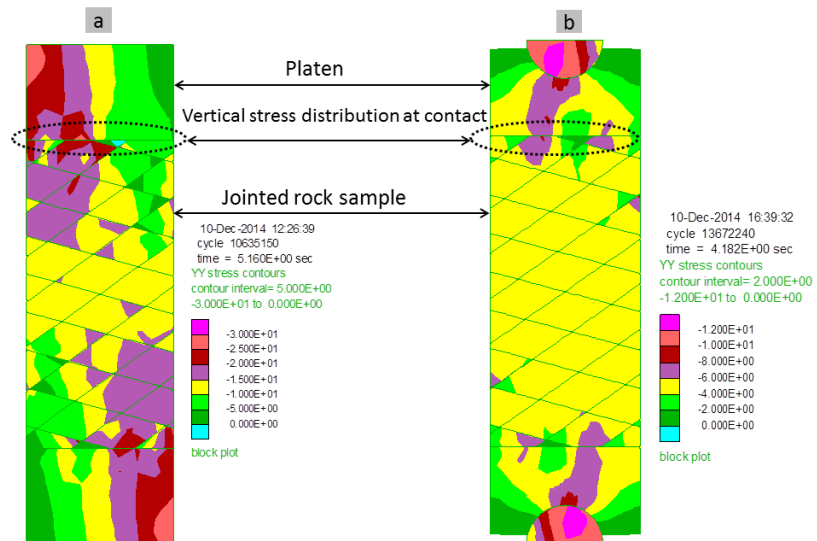
Figure 7.24 Vertical stress distribution (a) Hoek cell (b) Soil cell using NLC
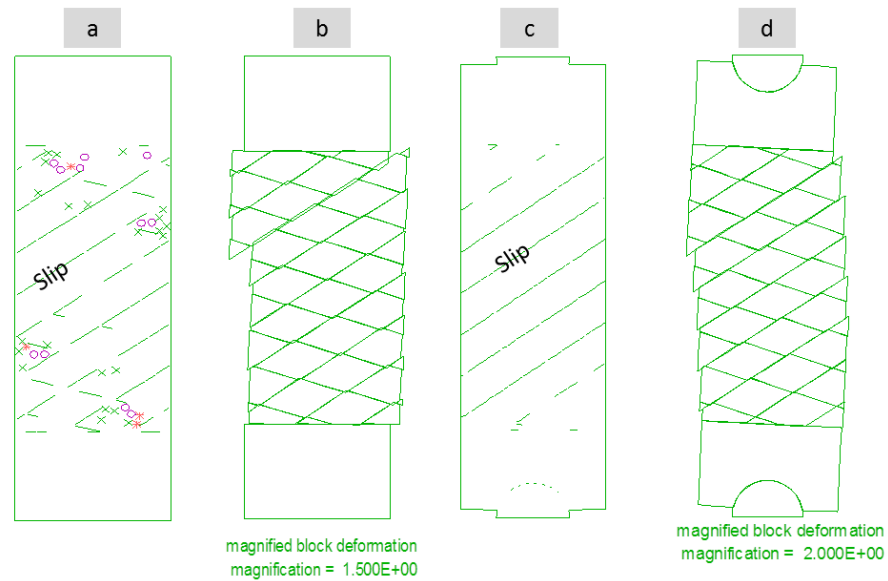
Note :
(o) Tensile failure, (*) shear failure, (x) yield in the past

Figure 7.25 (a) plastic state in Hoek cell, (b) block deformation for Hoek cell (c) plastic state for soil triaxial using NLC (d) block deformation in soil cell using NLC

7.5   Summary and conclusions

In this chapter an attempt has been made to illustrate the reliability of numerical modelling of small scale jointed rock samples by comparing numerical results against the laboratory results. It was shown that the numerical modelling technique can successfully be used to study the equivalent strength and deformability parameters of a rock mass.

UDEC was used to analyse the cause of the apparent strain hardening behaviour of a jointed rock sample, especially where the dip angle of a single joint or a set of joints is around 60 degrees. This study argues that the strain hardening behaviour measured in some tests may not

be entirely a material property of the jointed rock but may be a result of the platen-rock interaction. For the same sample, testing using the Hoek cell showed a higher strain hardening coefficient, whereas the typical soil triaxial cell showed a lower strain hardening coefficient. Since in the Hoek cell the sample ends are more fixed than in the typical soil cell, the shear and normal stiffness of the rock platen-contact is increased, causing the applied axial stress to distribute non-uniformly. This conclusion has been confirmed by numerical simulations using UDEC code and experimentally by modifying the lower spherical seat in the soil triaxial cell. In addition, the deformation modulus produced by the Hoek cell is greater than that produced by the typical soil triaxial test.

From this, one can conclude that the Hoek cell should not be used to evaluate the post-yield behaviour of jointed rock samples, as it may not give results which are representative of real jointed rock-mass. In addition, the numerical methodology that has been used in this study successfully mimicked the axial stress-axial strain behaviour for model J60 before and after yield.

The next chapter focuses on prediction of the mechanical properties of the rock mass of a real dam foundation in Iraq using rock classification systems and UDEC.

Chapter 8 Rock Mass Properties of a Real Dam foundation by UDEC

8.1 Introduction

To design dams on a jointed rock mass, a knowledge of the rock mass strength and deformability properties are essential. These properties are usually predicted using rock classification systems such as RMR and GSI. However, these systems may not predict the required properties, since their development was based on small-scale laboratory tests and experience in tunnelling and slope stability problems. Also, in these systems, the deformability is based on empirical equations developed by testing small-scale jointed rock samples which may not reflect reality, as shown in Chapter 7. Due to the fact that large-scale tests are difficult and time-consuming, UDEC can be used as a tool to evaluate representative rock mass properties. In this method the mechanical properties of intact rock and joints can be predicted by using small-scale laboratory tests and then using these properties as input data to the UDEC model of a large-scale sample.

In this study, the rock mass of the Surqawshan earth dam in the Kurdistan Region in North-Eastern Iraq was selected in order to estimate the equivalent strength and deformability properties using UDEC. A visit to the site of the Surqawshan Dam was made by the

author in May 2012 in order to collect rock samples from the dam's foundation site. About 76 kilograms of core (3-inch diameter) samples were brought to the rock mechanics laboratory in the University of Nottingham so as to find the mechanical properties of the dam's foundation (Figure 8.1). Also, the field study of the rock mass was conducted by the author. Figure 8.2 shows the study area and the location of boreholes on a topographic map of the site.

The Surqawshan Dam project is an earth dam that is still under construction. It is located on Chamirazan stream in Sulaymani Province, Kurdistan Region (coordinates 35.51 N, 44.56 E). The maximum height of the dam from the stream bed is 36 m, and from the bed rock it is 40 m. In addition, the dam elevation at bedrock is 440 m.

Table 8.1 presents the elevation of boreholes. The area was exposed to some tectonic deformations, whereby bedding planes have low dip angles. The apparent dip of strata is slightly greater than the slope of the valley. The shape of the valley is a deep U, bounded on the two sides by very steep rocky cliffs. The left side is relatively steeper, while the right side has a relatively gentle slope, which is covered by small trees and short plants (ZHINAB Consulting Co., 2011).

Figure 8.1 Core samples from Surqawshan Dam site
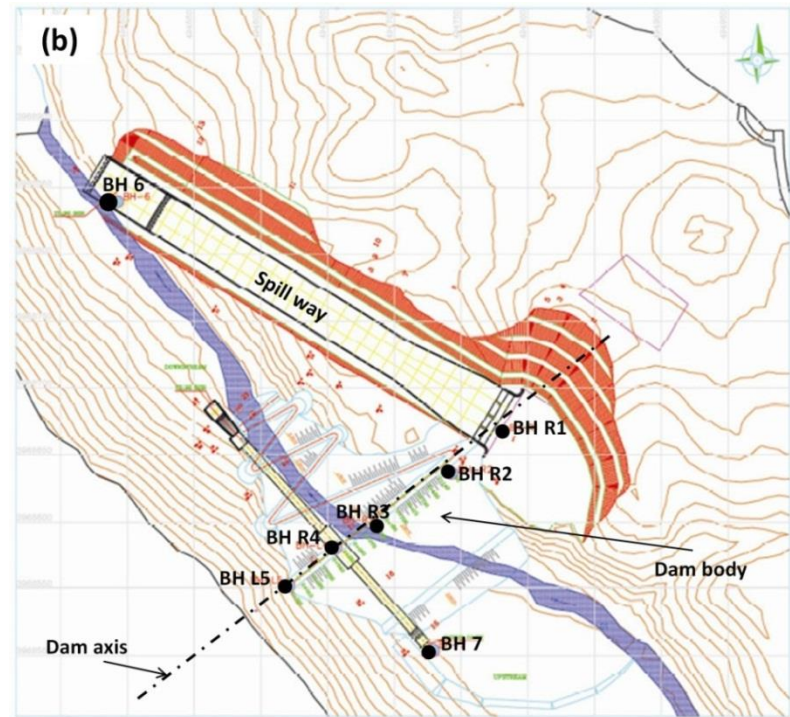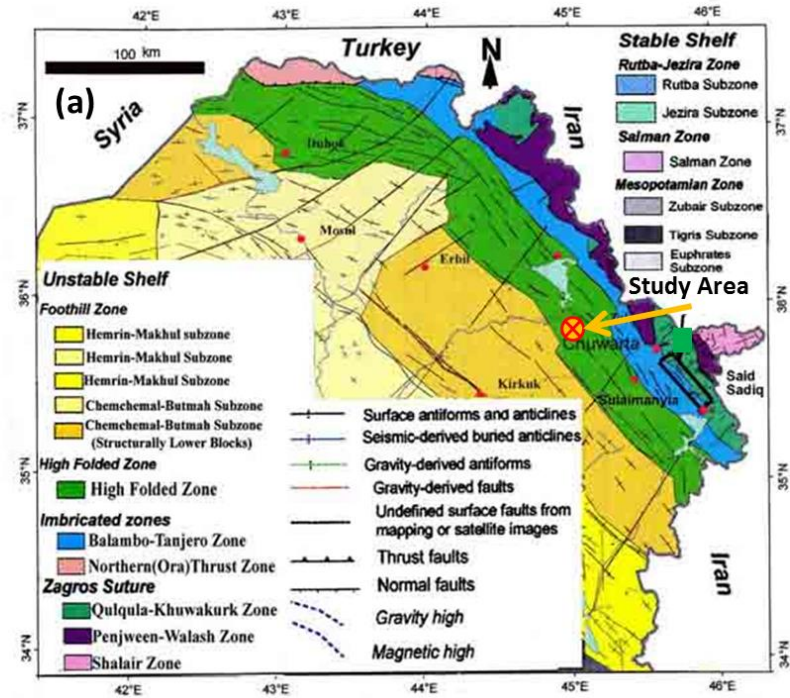
Figure 8.2 (a) map of study area(Jassim and Goff, 2006) (b) the location of Bore Holes on the map(ZHINAB Consulting Co., 2011)

Table 8.1 Borehole location and elevation

BH No.	Location	Boreholes Coordinate (UTM)			Depth(m)
		Elevation(m)	Y	X	
R1	Right abutment	476.8	3968661.601	494781.5624	40
R2	Right abutment	465.88	3968636.576	494728.5974	40
R3	River's bed	441.243	3968607.573	494669.054	40
R4	River's bed	441.57	3968586.096	494649.417	40
L5	Left abutment	478.73	3968546.837	494622.105	58
6	Stilling Basin	450.814	3968840.975	494513.8906	30
7	Intake	449.52	3968490.276	494740.688	21
8	Reservoir	455.489	3967938.29	495161.573	30
Note: The Elevation of Dam's Base=440m					

8.2 Geological Setting

The Gercus formation comprises molasse deposited following the Middle Eocene uplift (Al-Rawi, 1983). The formation was first described by Maxon in 1936 in the Gercus region of south-east Turkey, which extends into the Iraqi High Folded Zone (Jassim and Goff, 2006). The formation thickness is about 850m in the Dohuk area in northern Iraq and the thickness gradually decreases towards the south-east to less than 100m near the border between Iraq and Iran.

Al-Rawi (1983) stated that:

> "the Gercus Formation is basically a clastic sequence that consists of fining-upward cycles of carbonate-rich sandstones, siltstones and marls, together with some conglomerates and a few dolomite units"

Dhannoun et al. (1988) stated that "The Gercus rocks consist of various mixtures of terrigenous rock fragments composed mainly of dolomite". Jassim and Goff (2006) described the Gercus formation in the Dohuk area as red and purple shales, mudstones, sandy and gritty marls, pebbly conglomerates and sandstones. Halite and Gypsum lenses occur near the top of the formation. It seems that the composition of this formation is not constant but it changes according to location and environment.

As reported by the Zhinab Company, the dam will be constructed on this formation, which lithologically consists of red clastic sequence of pinkish red to purple siltstone and claystone alternating with green marl, grey to reddish brown coarse grained sandstone with conglomerate bed at the bottom of sandstone beds. The thickness of this formation at the site is about 100m and this formation is overlain by the Pila Spi (or Pilaspi) formation, which is a mostly limestone layer, and underlain by the Sinjar formation, which is mostly marly limestone (see Figure 8.3). The thickness of the Sinjar formation is about 350m at the site under the dam.

According to the fieldwork study, there are three main joint sets in the foundation of the Surqawshan Dam, one of which is the bedding plane. The dip and dip direction with spacing of each joint was measured and presented in Table 8.2.

Table 8.2 Details of discontinuities

Discontinuity name	Dip direction /Dip (degree)	Spacing (m)
D1=Bedding plane	295/10	0.1-0.7
D2	150/85	0.2-1
D3	050/75	0.1-0.5
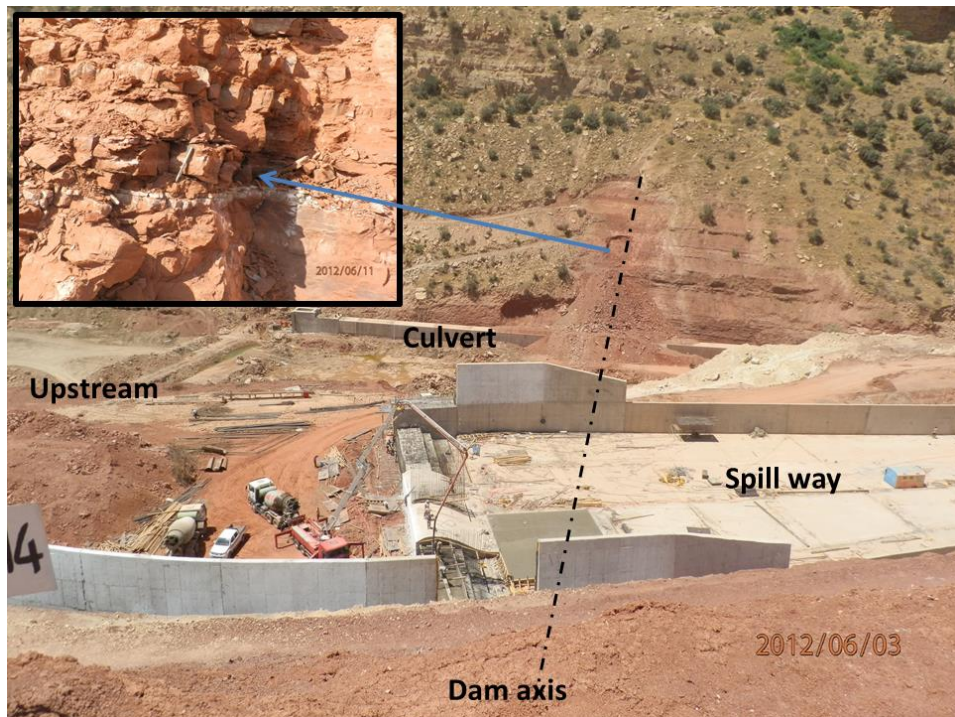
Figure 8.3 Outcrops of the Gercus formation at left abutment of the Surqawshan Dam

8.3   Gercus Formation's Materials at the Dam Site

8.3.1 X-ray diffraction (XRD)

During mechanical testing of rock samples (presented in section 8.4), it was recognized that the constituents of the rock samples were different from those mentioned in the geotechnical report of the Surgawshan Dam. As a result, XRD was performed on ten samples

selected from different boreholes and depths so as to determine their mineralogical composition.

The samples' details are given in Table 8.3. The representative prepared rock powders were analysed using a Siemens D500 diffractometer using CuK_α radiation at an accelerating voltage of 40 kV. The results are presented in Figure 8.4, from which it can be seen that the major mineral phase is dolomite. The results indicate that this formation may be described as an alternation of clastic reddish-brown dolomitic mudstone, olive grey dolomitic siltstone and blackish grey dolomitic shale with silt containing nodules of pyrite and clay minerals such as palygorskite, lizardite and clinochlore.

Table 8.3 Selected samples for XRD test

BH No.	R1	R3	R3	R3	R4	R4	L5	L5	7	8
Depth(m)	32-33	21.8-22	31.6-32	34-35	7-8	25-25.5	20-20.5	50-50.5	15.5-16	18.5-19
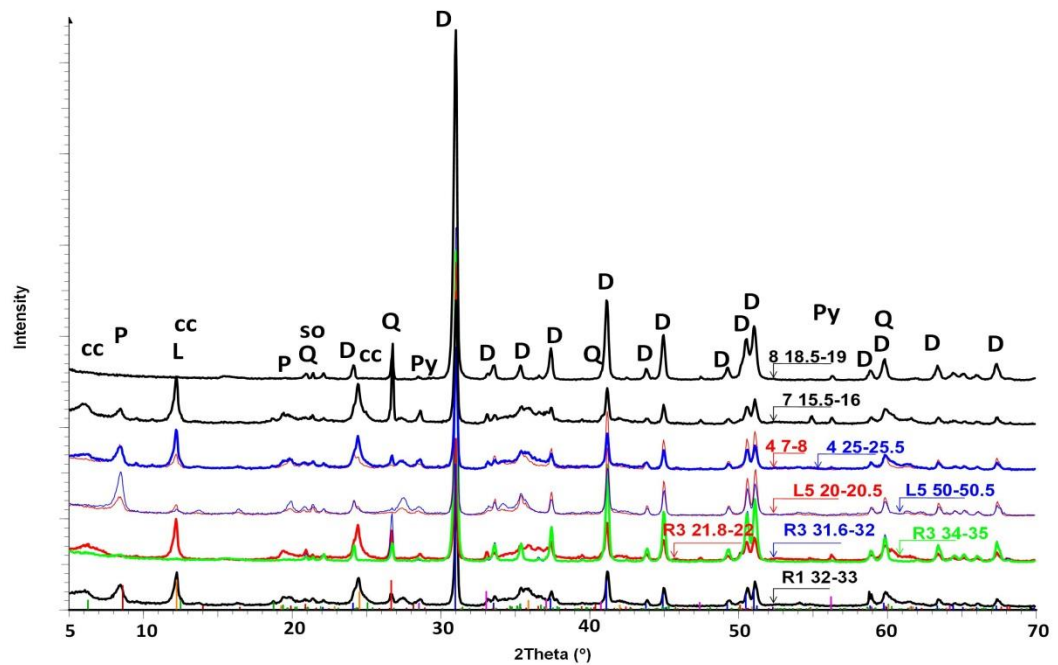
Figure 8.4 XRD pattern of selected rock samples

D=Dolomite,Q=quartz, L=Lizardite, P=Palygorskite,
SD=Sodium Aluminum Silicate, Py=Pyrite, and CC=Clinochlore

During saturation, two of the rock samples (BH 7: 15.5-16m and BH R3: 21.8-22m) were affected by water. The former sample was totally cracked and then collapsed in water while the latter sample was weakened. This encouraged the author to investigate the causes of this problem. Therefore, it was decided to utilize SEM-EDX to get more information about the elemental composition in the rock samples

8.3.2 SEM-EDX method

The Scanning Electron Microscope (SEM) combined with Energy Dispersive X-ray (EDX) was utilized using a Philips XL30 ESEM-FEG to investigate the elemental composition (mode BSE, spot size 3.0,

acceleration voltage=20 kv) as well as the microstructure of rock samples. The chemical composition was determined by EDX using point analysis on powdered samples and polished intact rock samples coated with carbon using an automatic sputter coater device. The data and image processing were achieved using the INCA-EDX software program.

Six samples were selected from different boreholes and depths as given in Table 8.4. Representative powder samples were prepared from rock material for the first four samples that are presented in Table 8.4, whereas intact polished surface samples were prepared for those samples that were affected by water (see samples 1, 5 and 6 in Table 8.4) in order to find the structure and composition of particles and minerals. All samples were coated with carbon of thickness 15nm. Therefore, the percentages of carbon (C), hydrogen (H), and Oxygen (O) cannot be estimated in this method. Figure 8.5 shows the electron images for selected powder samples and the estimated percent of elements predicted for the area of image. The estimated percentages of elements by weight in each sample are given in Table 8.4. The results in Table 8.4 revealed that dolomite, quartz and clay minerals form the main constituents. All samples have a high percentage of magnesium (Mg) and calcium (Ca). The high percentage of Ca was recorded in samples 2 and 4, which have a high percentage of Ca and almost double that amount of Mg. Also, the percentage of silicon (Si)

in samples 2 and 4 is much lower than in the other samples, which indicates that they are dolomitic limestone and the others are siltstone/mudstone and shale enriched in dolomite. There are traces of some elements such as chromium (Cr), Nickel (Ni), Sodium (Na), Chlorine (Cl), Manganese (Mn), Potassium (K), Aluminium (Al) and Titanium (Ti) that seem to be related with the clay minerals. Also, the existence of Sulfide (S) with Calcium (Ca) indicates that the samples contain anhydrite especially samples number 1, 5 and 6.

Table 8.4 Elements of selected samples estimated by SEM-EDX in % weight

Sample Label	1	2	3	4	5	6
Sample type	powder	powder	powder	powder	Intact	Intact
Analysis area $(\mu m)^2$	81914	81914	81914	81914	60434	60434
BH No.	7 15.5-16	8 18.5-19	L5 50-50.5	R3 34-35	BH7 15.5-16m	R3 21.8-22
Element	Weight %					
Mg K	28.44	27.09	21.41	28.79	26.06	21.72
Al K	2.46	0.8	4.33	0.93	2.12	2.09
Si K	37.45	6.81	41.95	10.57	36.24	45.37
S K	3.51	3.21	0.2	1.4	2.3	6.71
K K	0.15	0.02	0.45	0.08	0.13	0.19
Ca K	18.18	57.93	19.18	54.68	21.23	14.26
Ti K	0.11	-	0.3	-	0.11	0.21
Cr K	0.32	-	0.18	-	2.76	0.22
Mn K	0.12	-	0.21	0.16	-	0.1
Fe K	8.69	4.04	11.45	3.18	8.46	8.27
Ni K	0.45	-	0.33	-	0.43	0.7
Na K	0.07	0.1	-	0.11	-	0.16
Cl K	0.04	-	-	0.1	0.14	-
Totals	100	100	100	100	100	100
Samples 1,5 and 6 affected by water						

The XRD indicated that all of these samples contain nodules of pyrite with clay minerals and anhydrite. When pyrite is exposed to humidity and oxygen, they oxidize and sulphate crystal form, growing to many times their original size. The result of this is that the rock sample weakens or disintegrates. This is a very important finding which may endanger the stability of the Surqawshan earth dam during its service, because dissolving rock material will result in cavities in the dam's foundation. This problem may be solved by grouting the rock fractures, so as to protect the layer of this sample from water.
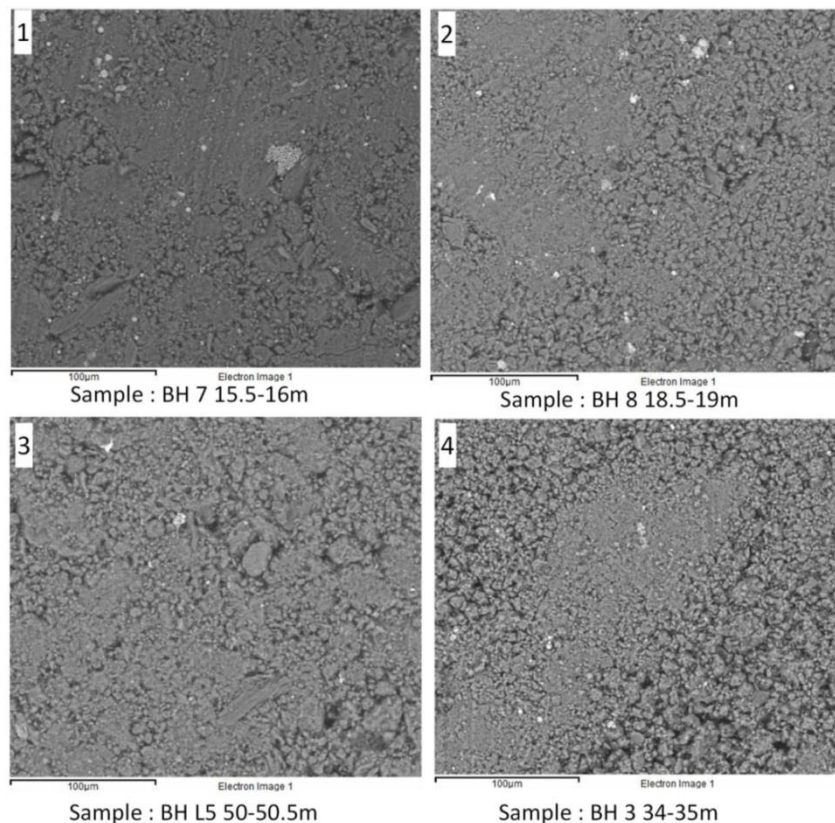
Figure 8.5 Electron image of powdered rock samples show the analysis area, the bar scale is 100 μm

Figure 8.6 and Figure 8.7 show the electron image of intact rock (polished surface) with maps of the main elements distribution in white determined by EDX for samples 5 and 6, respectively. The white colour in S and Fe map stands for pyrite nodules, and the white colour in Mg map and Ca map is for dolomite particle.

It is interesting to see that Pyrite is also present in sample 6 (R3 21.8-22m) as well and being randomly spread, as can be seen from the maps of S and Fe. From these one can conclude that the disintegration of rock in sample 5 and weakening of sample 6 may be because of sulfate and iron, which both result in Pyrite. Also, it should be noted that the availability of clay minerals such as clinochlore, chromite and palygorskite accelerated the swelling of rock samples (5 and 6) by absorbing water and creating a good environment for the chemical reaction of Pyrite with water.

Pyrite in sedimentary rock may cause damage to the structures, because, if it is exposed to water, it will produce sulphate, in which case, the oxidization of the formed sulphate crystals causes them to grow to several times their original size, depending on the amount of sulphate produced (Anderson, 2008). The chemical reaction of pyrite with water can be shown by the following:

$$2FeS_2 + 3H_2O + CaCO_3 + 6O_2 \rightarrow FeCa(SO_4) + 3H_2SO_4 + CO_2 + Fe \qquad 8.1$$
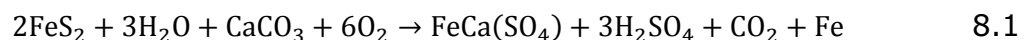
Also, the clay minerals with anhydrite can cause swelling of sedimentary rock as a result of absorption of water and/or chemical

transformation (Wittke, 1990). When water penetrates into the sedimentary rock due to clay minerals, the anhydrite ($CaSO_4$) may convert into gypsum ($CaSO_4$ $2H_2O$). This process can cause a volume increase of about 60% if swelling is unconfined (Butscher et al., 2011; Wittke, 2014). It should be noted that this transformation depends on the contents of the clay minerals. Madsen and Nuesch (1991) observed in the laboratory that rock samples containing only anhydrite in contact with water have only surface swelling, whereas rocks containing 70 to 75% anhydrite and 10 to 15% clay with some dolomite and quartz showed the maximum swell pressure (more than 4 MPa).

In this section an attempt was made to investigate the cause of swelling of samples 5 and 6. The detailed information about the chemical components and the grain sizes is not the aim of this study. Further research is needed to determine the problem of swelling in the foundation of the Surqawshan Dam under confining pressure in future.
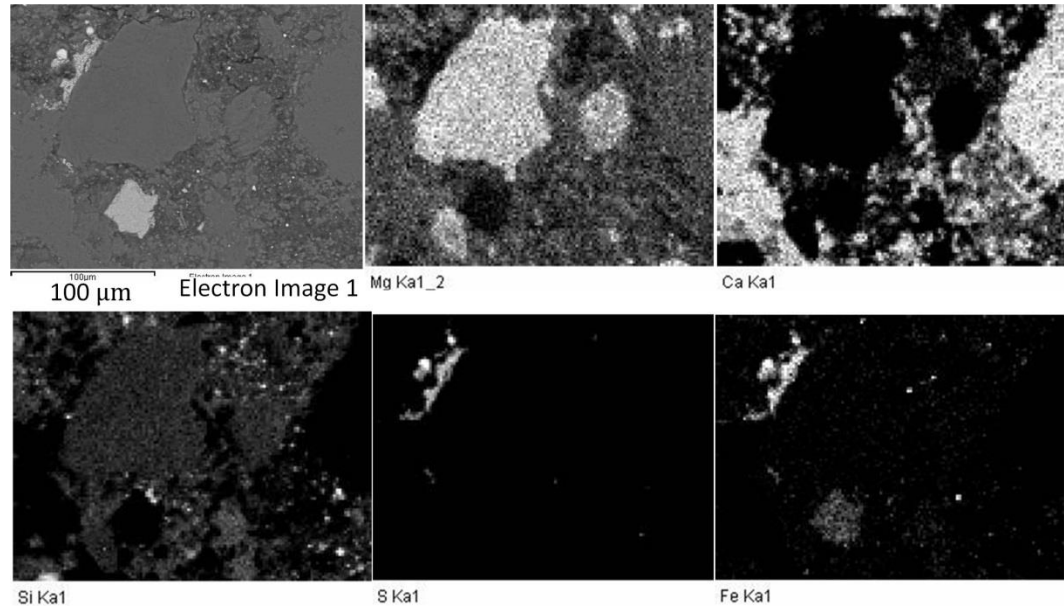
Figure 8.6 Electron image with maps of main minerals of sample 5 (B7 15.5-16m)
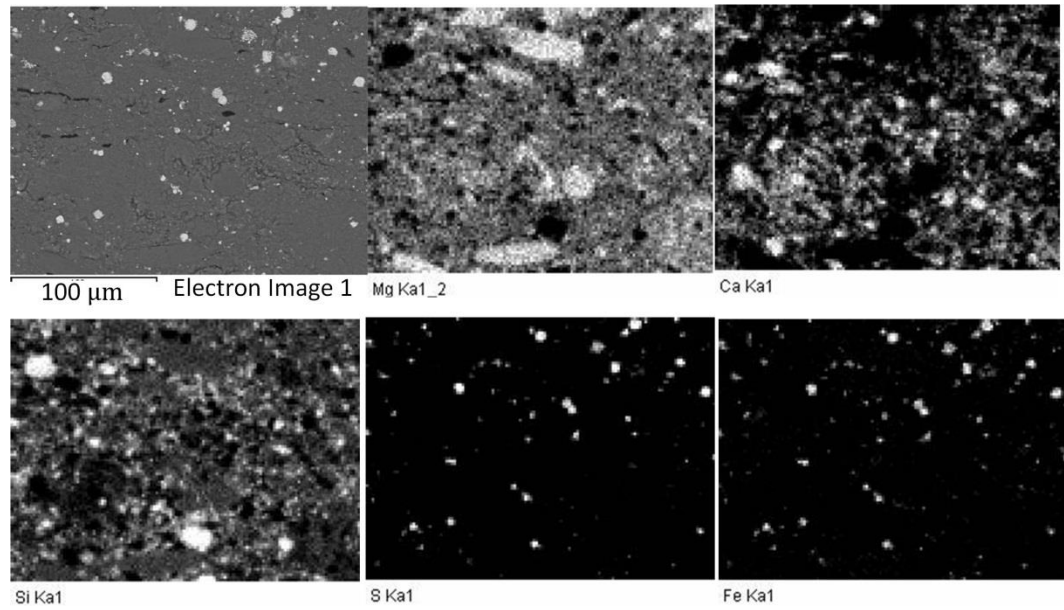
Figure 8.7 Electron image with maps of main minerals of sample 6 (R3 21.8-22m)

8.4 Intact Rock Strength

To study the strength of intact rock, the following tests were performed: Uniaxial Compressive Strength (UCS), triaxial test (normal and multistage), Brazilian Test and Point Load Test (PLT). Since the rock samples were taken from the foundation of the dam, and the research study is about the rock mass behaviour under dams, the samples were tested under dry and saturated conditions. The core samples were brittle material, so during the preparation samples for triaxial test some of the cores were broken. As a result, the numbers of samples were insufficient to conduct the normal triaxial test in both cases (saturated and oven dry). Therefore, the multistage triaxial test was chosen as an alternative for the normal triaxial test. The samples were tested according to borehole number and depth in order to give an accurate value for the intact rock in the foundation of the dams.

The procedures for testing and calculation of tests were achieved according to the suggested methods in International Society of Rock Mechanics (Bieniawski and Bernede, 1979) (ISRM, 1981). Table 8.5 presents the numbers of tests that were conducted on the prepared intact rock samples.

Table 8.5 Number of tests

Test Type	Oven Dry	Saturated
UCS	10	3
Normal Triaxial Test	4	1
Multistage Triaxial Test	3	8
Brazilian Test	15	12
Point Load Test	10	5

8.4.1 UCS test

Ten samples from different boreholes and depths that could be critical for the dam were tested in oven dry condition, whereas three samples were tested in saturated condition after immersion in water under vacuum for one week, or until all air bubbles came out of the samples. The UCS results are shown in Figures (8.8-8.10). It should be noted that, UCS results for saturated condition can be also predicted from the results of the multistage triaxial test (section 8.4.2) by using Equation 8.2, as shown in Table 8.6.

The range of compressive strengths obtained approximately between 40 to 200 MPa for oven dry case, and between 7.9-97MPa for saturated samples. These indicate that the water content has an important effect on the strength of intact rock and should be taken into account. The stress strain behaviour of Figure 8.9 is similar to the behaviour of Figure 6.23a because of micro fractures or joints (see inset image in Figure 8.9), although the latter is for large numerical triaxial testing of large block size in the rock mass. By this it can be

concluded that the numerical results capture the behaviour of a jointed

rock mass.

$$UCS(\sigma_1) = \frac{2*c*cos\emptyset}{1-sin\emptyset}$$ 8.2

**Table 8.6 Estimated UCS from multi-stage triaxial tests of satu-
rated samples**

BH no.	Depth(m)	Predicted UCS (MPa) (Eq. 8.2)
R3	34-35	97
R4	15-16	47.6
L5	6-7	32.1
L5	15.5-16	35.8
7	15.5-16	7.9
8	18.5-19	41.8
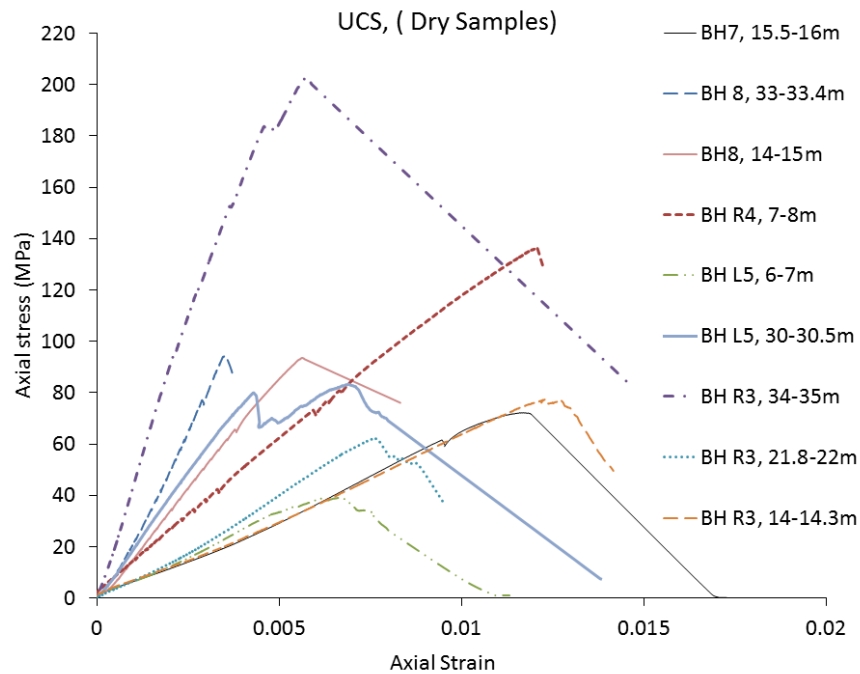
Figure 8.8 UCS tests for selected samples in oven dry case
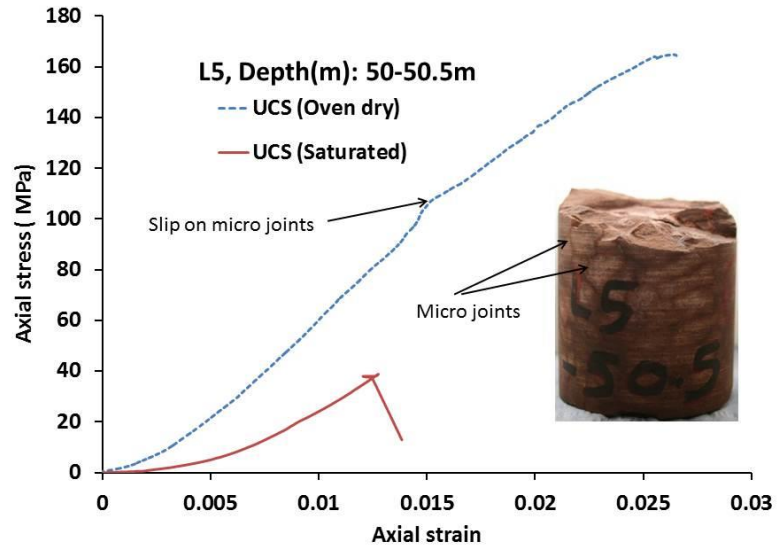
Figure 8.9 UCS test for a sample in both oven dry and saturated cases
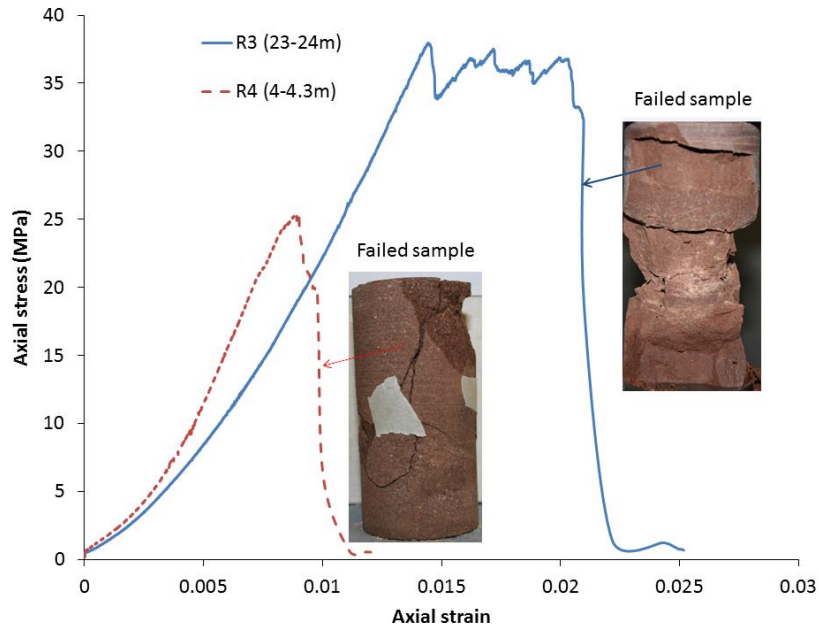
Figure 8.10 UCS tests for selected samples in the saturated case

8.4.2 Triaxial tests

The triaxial test is one of the most important laboratory tests that can be used to predict the strength parameters of intact rock. This test should include at least three homogeneous samples from the same core and same depth in order to determine the required strength parameters. This method is named normal triaxial test in this study. However, sometimes it is difficult to get three similar samples. In this case, the method of multi-stage triaxial test can be used (Kovari et al., 1983). In this section, both methods were used.

8.4.2.1   Normal triaxial test

Only five triaxial tests were achieved, because the numbers of samples were insufficient to do more. Four triaxial tests were done for oven dry samples, whereas one was conducted for a saturated sample. Figures 8.11-8.20 present the stress strain and Mohr-Coulomb strength envelopes for the samples. These results encourage conducting a multistage triaxial test because of non-homogeneity in some rock material, especially sedimentary rocks.

The axial stress–strain relationships showed generally linear elastic behaviour until yield stress, and then strain softening. This suggests that the linear elastic-plastic model will be valid for numerical study of the sedimentary rocks presented in this study. The failure mode was brittle for all samples. It is interesting to see that the saturated sample in Figure 8.20 gave high friction angle and high cohesion. This

suggests that the sample taken from borehole R3 from depth 34-35m was not affected by water, because this sample is mostly dolomitic limestone with little clay minerals such as palygorskite and sodium aluminum silicate (albite).

The failure strength envelopes were not relevant because it is difficult to get three homogeneous samples from the same block. Therefore it was decided to test the remaining samples by the multistage triaxial test method.
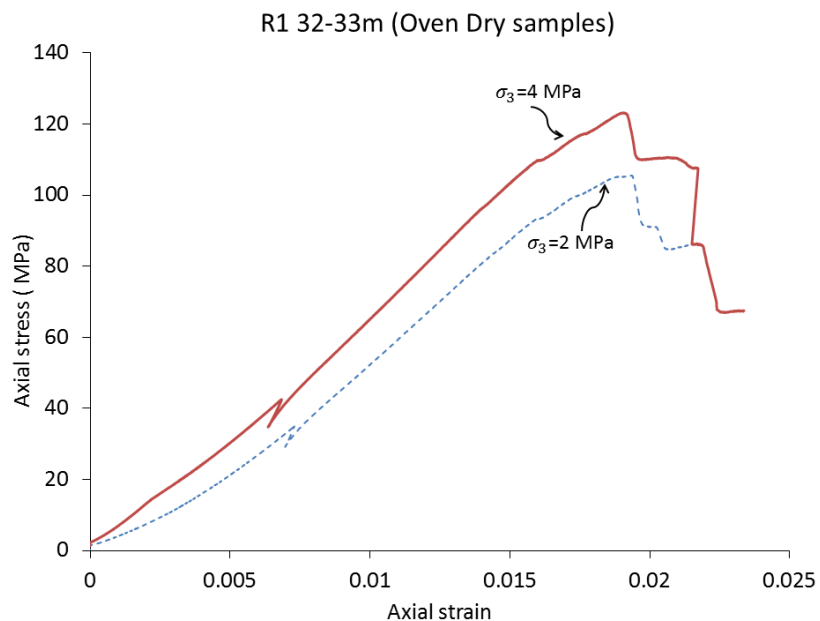
Figure 8.11 Axial stress-strain for samples from BH R1:32-33m
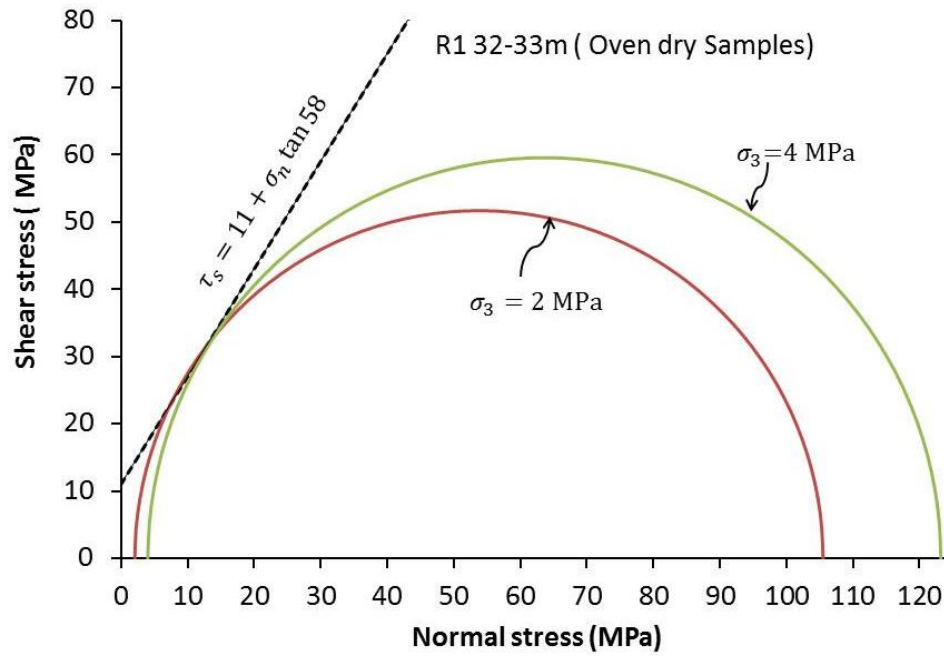
Figure 8.12 Mohr-Coulomb strength envelope for BH R1:32-33m
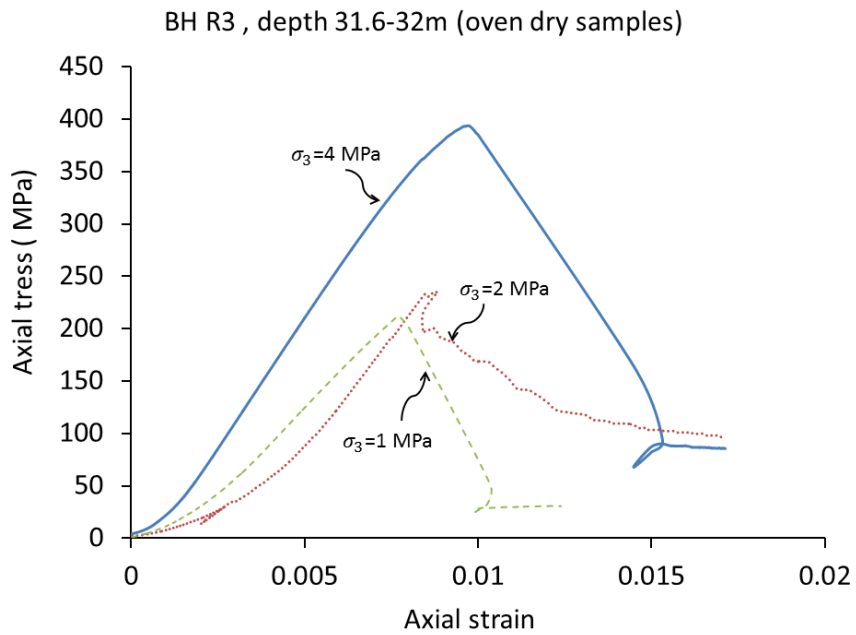
Figure 8.13 Axial stress-strain for samples from BH R3:31.6-32m
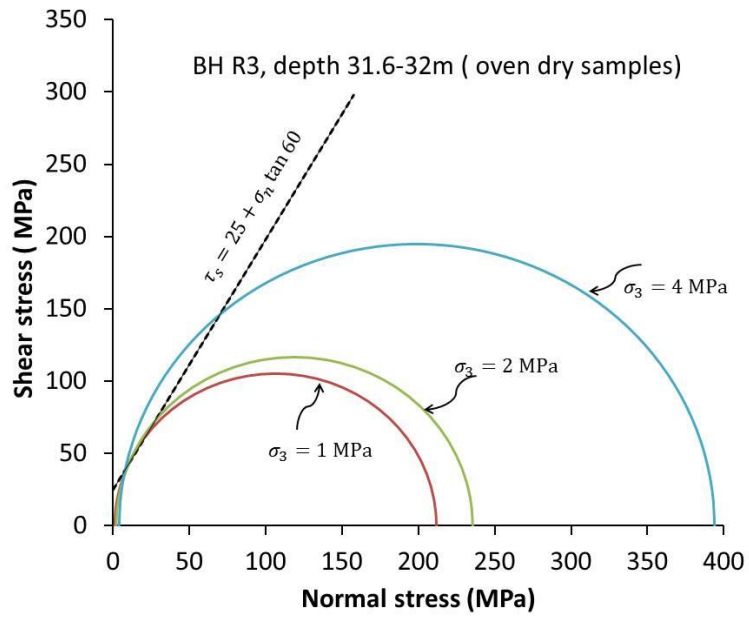
Figure 8.14 Mohr-Coulomb strength envelope for BH R3:31.6-32m
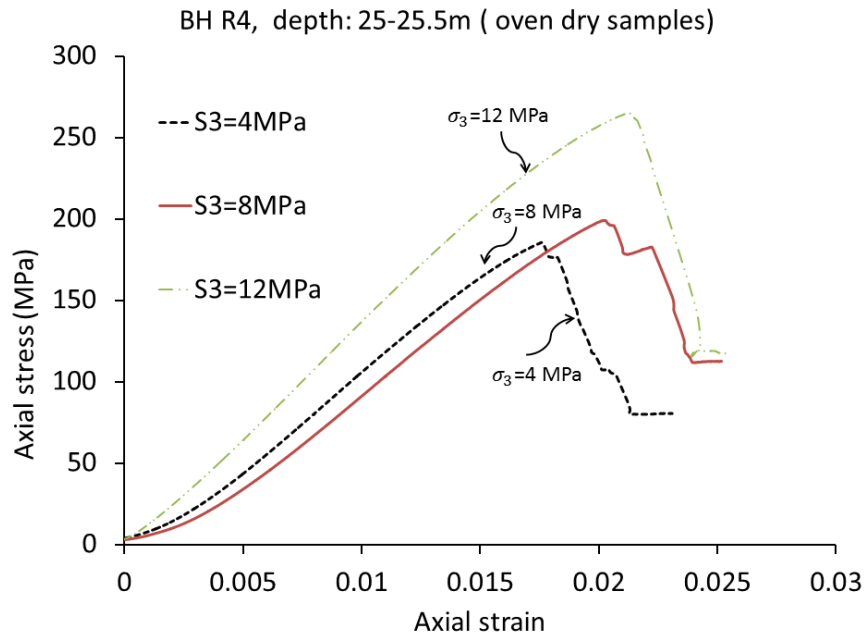
Figure 8.15 Axial stress-strain for samples from BH R4:25-25.5m
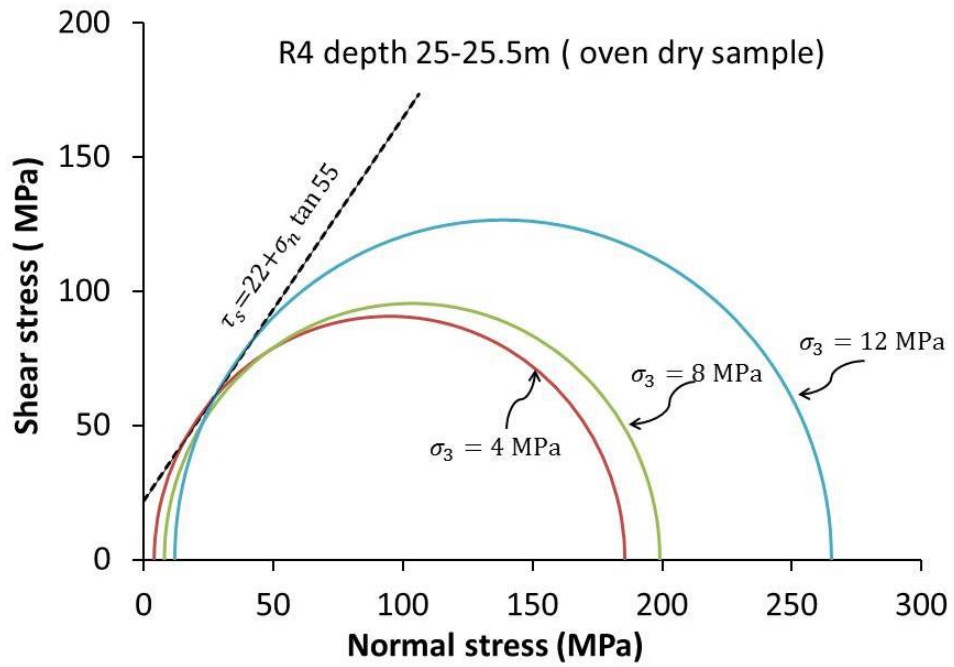
Figure 8.16 Mohr-Coulomb strength envelope for BH R3:25-25.5m
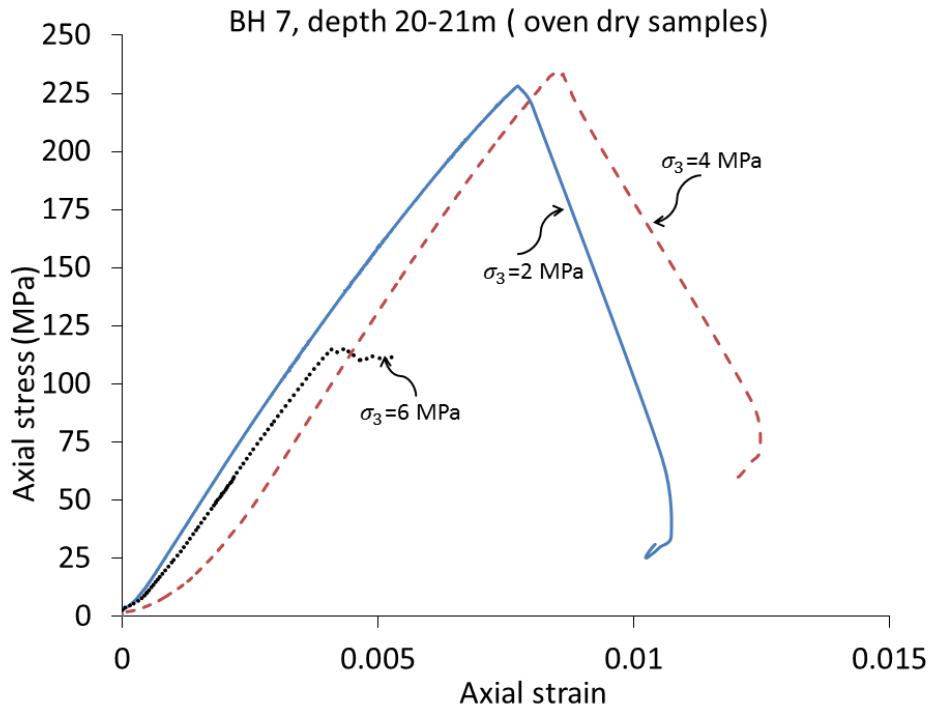
Figure 8.17 Axial stress-strain for samples from BH R4:20-21m
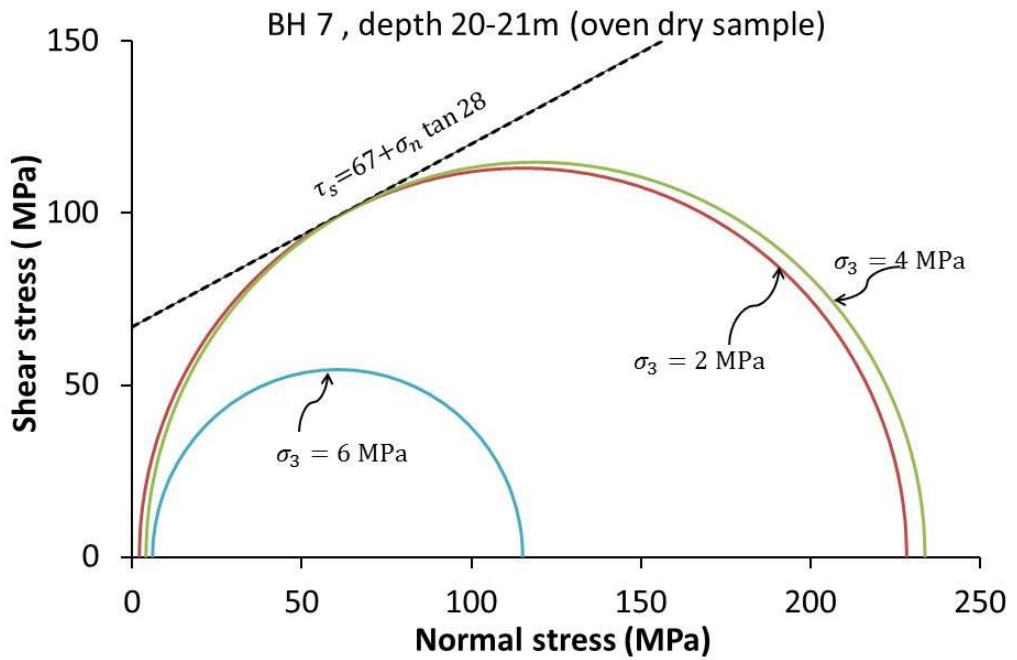
Figure 8.18 Mohr-Coulomb strength envelope for BH R3:20-21m
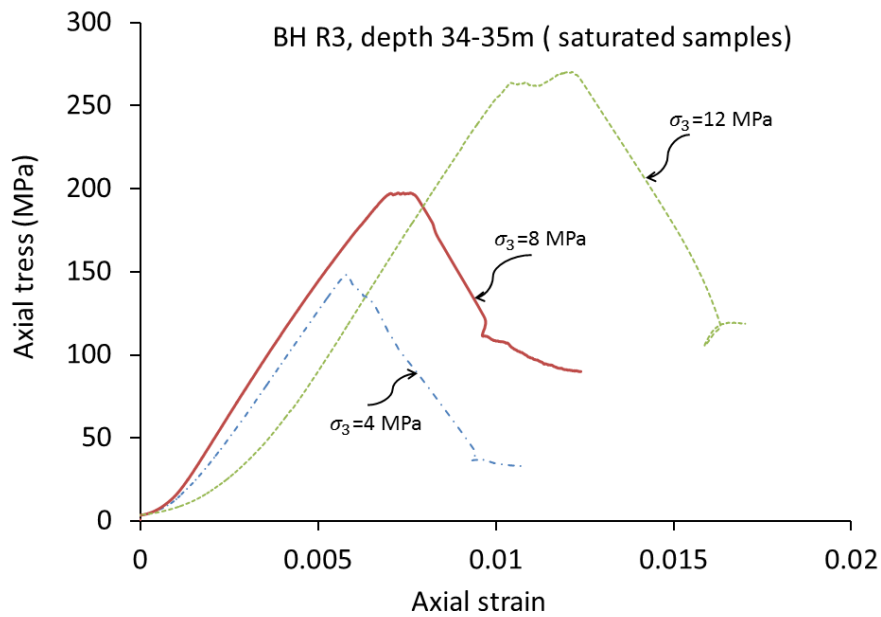
Figure 8.19 Axial stress-strain for samples from BH R4:34-35m

Plot titled "BH 7 , depth 20-21m (oven dry sample)" showing Mohr-Coulomb strength envelope with three circles and a tangent line $\tau_s = 67 + \sigma_n \tan 28$. Y-axis "Shear stress (MPa)" from 0 to 150, X-axis "Normal stress (MPa)" from 0 to 250. Labels: $\sigma_3 = 4$ MPa, $\sigma_3 = 2$ MPa, $\sigma_3 = 6$ MPa.
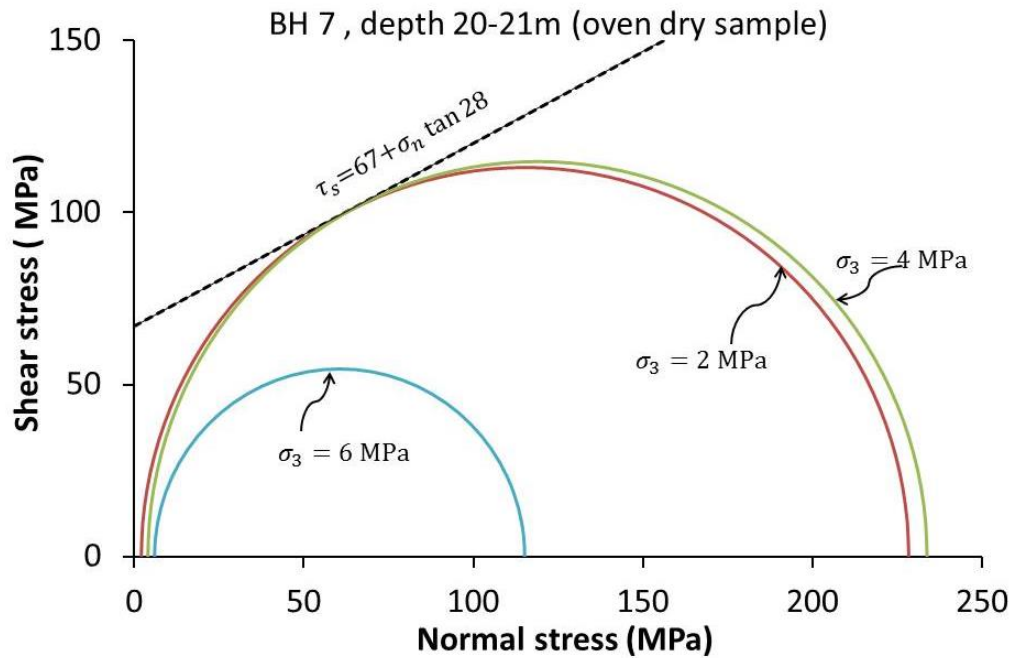
Figure 8.20 Mohr-Coulomb strength envelope for BH R3:34-35m

8.4.2.2   Multistage triaxial test

Since the processes of dealing with samples were according to boreholes and depths, there were insufficient numbers of samples to conduct the normal triaxial test on them, and it was concluded from the previous section that a reliable failure envelope cannot be obtained. Therefore, the idea of multistage triaxial testing is used in this study. It might be a good idea to do multistage, because of anisotropy in rock samples, even if the samples are taken from the same depth.

In this method, a single intact rock sample was used to obtain the failure strength envelope of intact rock samples by multistage axially

loading the sample with different confining stress in steps or stages. For each stage, the sample was compressed axially under confining stress up to yield stress, but without failing the sample. In the next stage, the confining stress was increased and then load on the sample was further increased until it approached peak stress without failing the sample. This was repeated until the required maximum confining stress was attained and finally the sample was axially loaded up to failure.

The residual strength can also be obtained by gradually reducing the confining stress, as illustrated by Li et al. (2005). However, the residual strength envelope will not be studied since the aim is to find the equivalent strength parameters as well as rock mass behaviour based on peak stresses.

Figures 8.21-8.36 show the results for multistage triaxial testing. From these figures one can conclude that the cementation of material was mainly affected if the samples were tested in saturated condition, except for the test illustrated in Figure 8.33, in which it can be seen that both parameters (friction and cementation) were affected by water, and its behaviour is similar to an un-drained unconsolidated (UU) test for clay material.

This is because this sample contains pyrite with clay minerals such as chromite, clinochlore and lizardite, which were detected by X-Ray and EDX tests. As can be seen using the multistage triaxial test, a

reasonable strength failure envelope can generally be produced. However, caution is needed to find the yield stress before failing the sample.
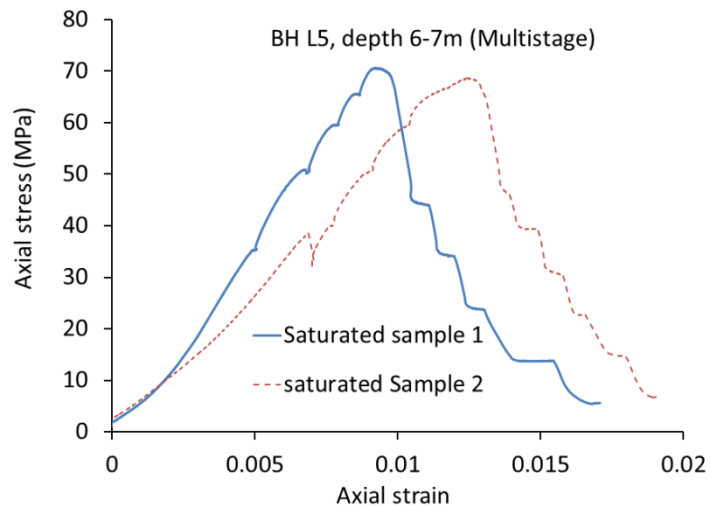
Figure 8.21 Axial stress-strain for samples from BH L5:6-7m
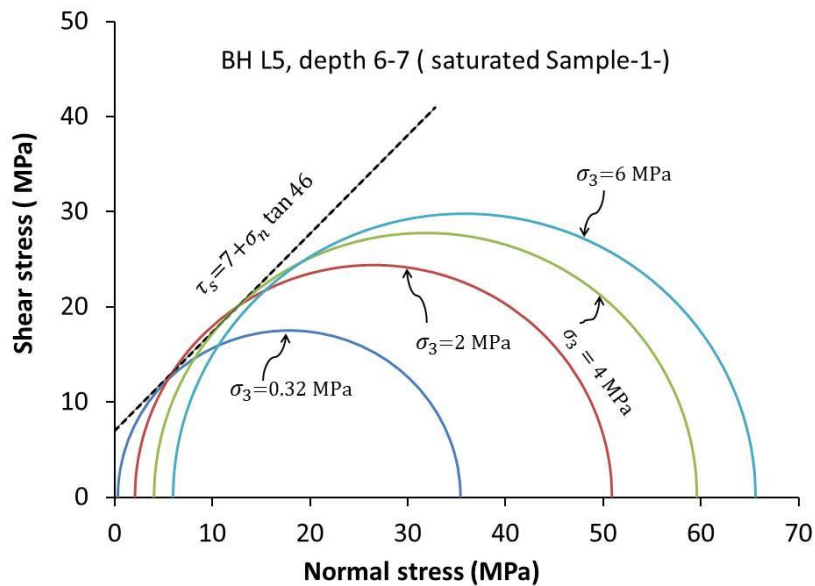
Figure 8.22 Mohr–Coulomb strength envelope for BH L5:6-7m/sample1 1
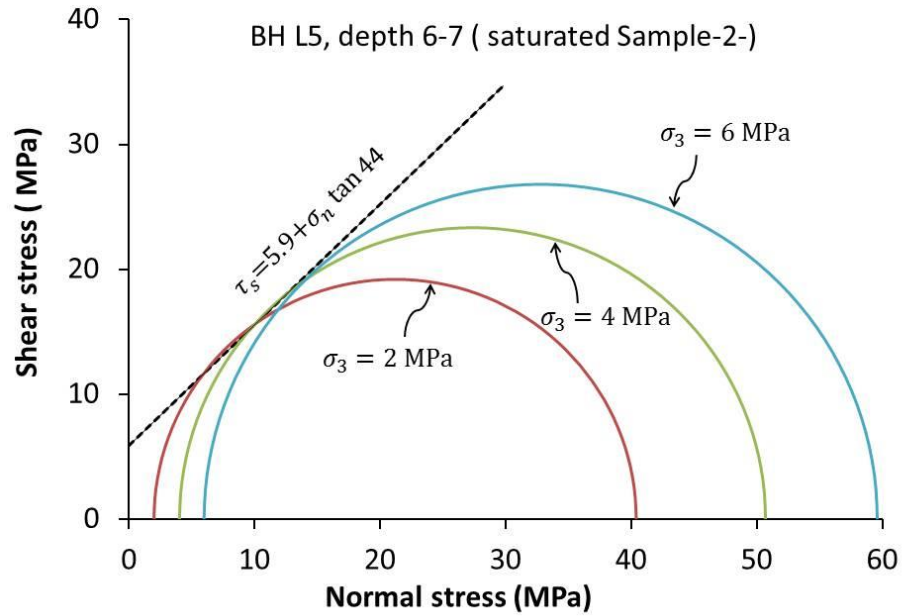
Figure 8.23 Mohr–Coulomb strength envelope for BH L5:6-7m/sample2 2
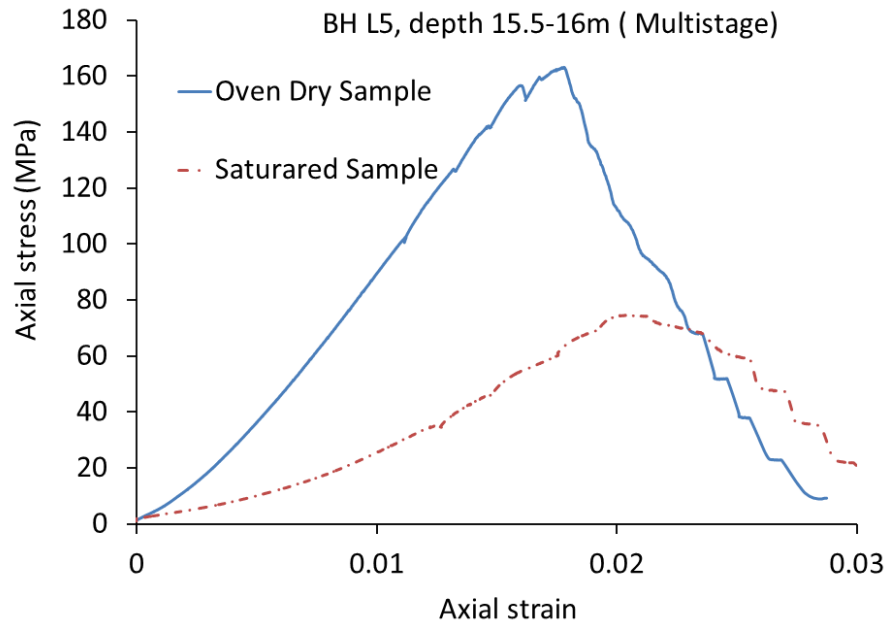
Figure 8.24 Axial stress-strain for samples from BH L5:15.5-16m
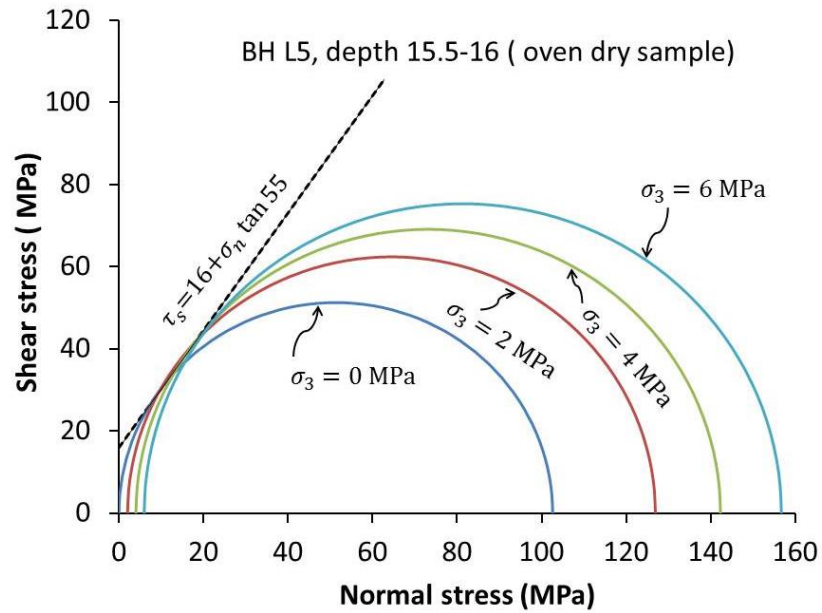
Figure 8.25 Mohr-Coulomb strength envelope for BH L5:15.5-16m/oven dry sample
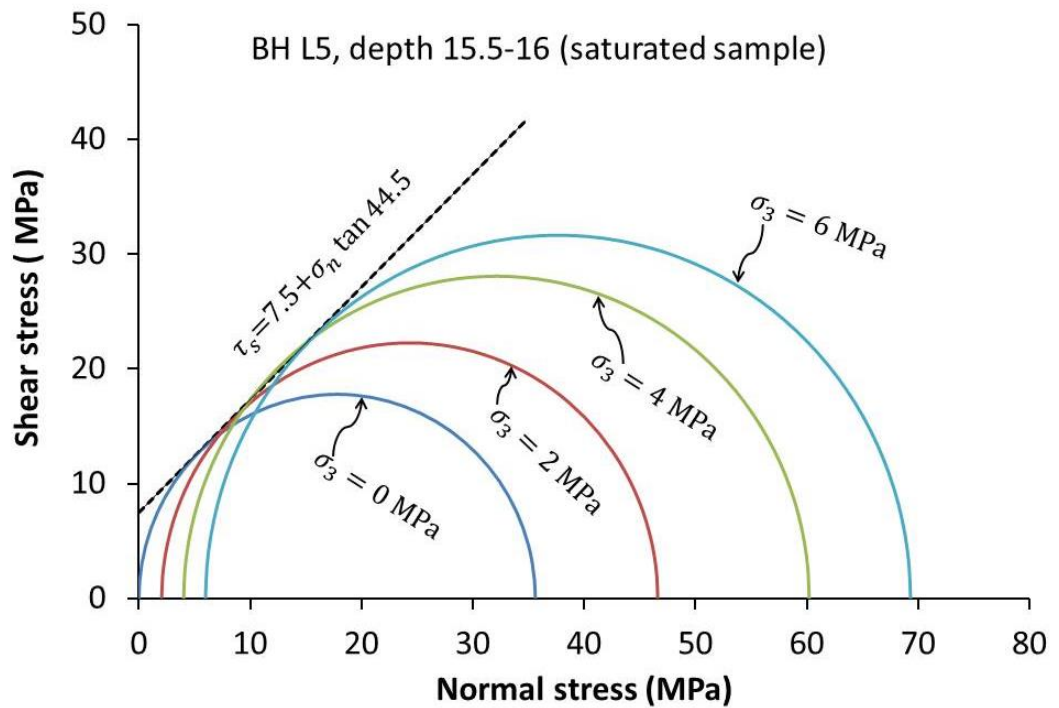
Figure 8.26 Mohr-Coulomb strength envelope for BH L5:15.5-16m/saturated sample
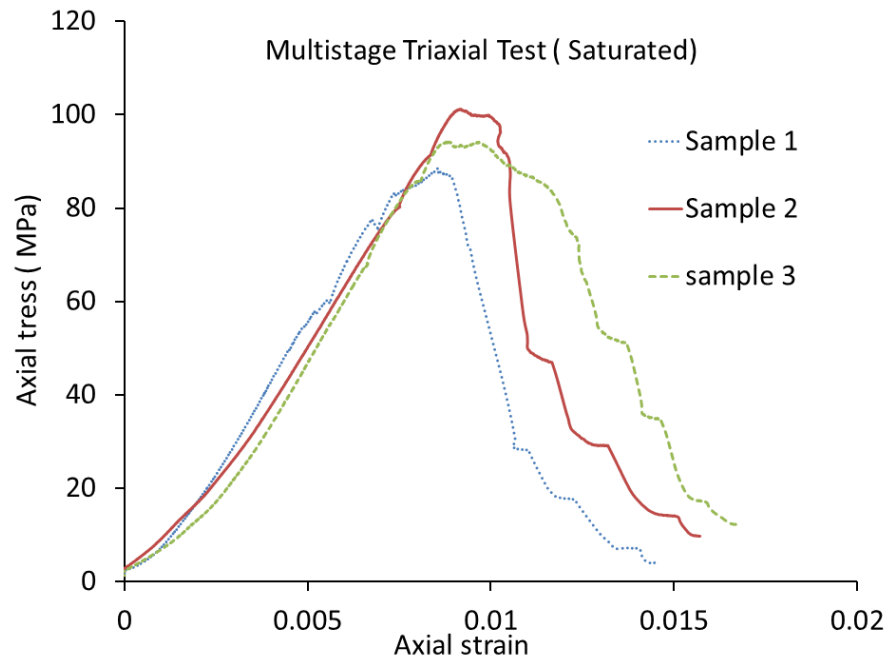
Figure 8.27 Axial stress-strain for samples from BH R4:15-16m
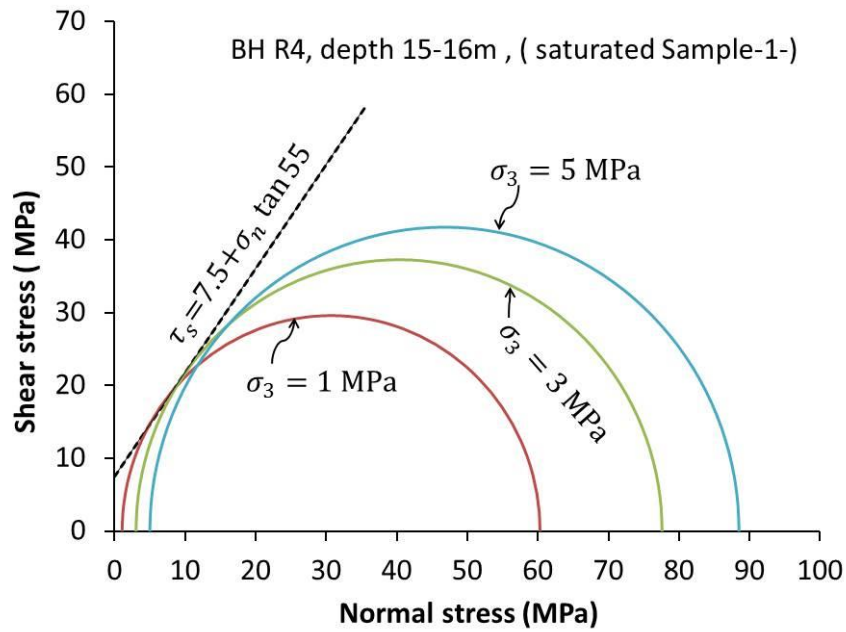
Figure 8.28 Mohr-Coulomb strength envelope for BH R4:15-16m/saturated sample 1
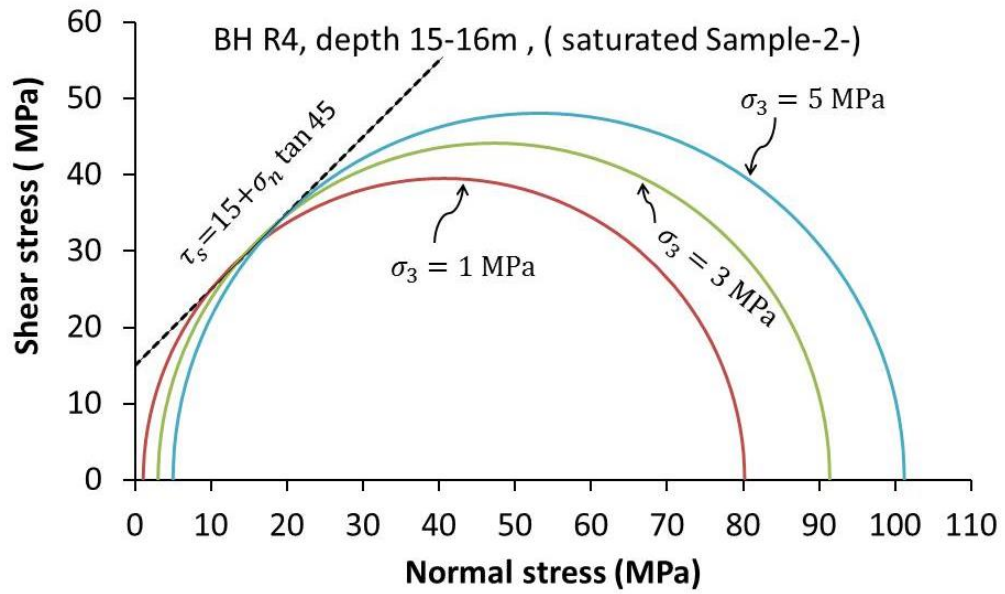
Figure 8.29 Mohr-Coulomb strength envelope for BH R4:15-16m/saturated sample 2
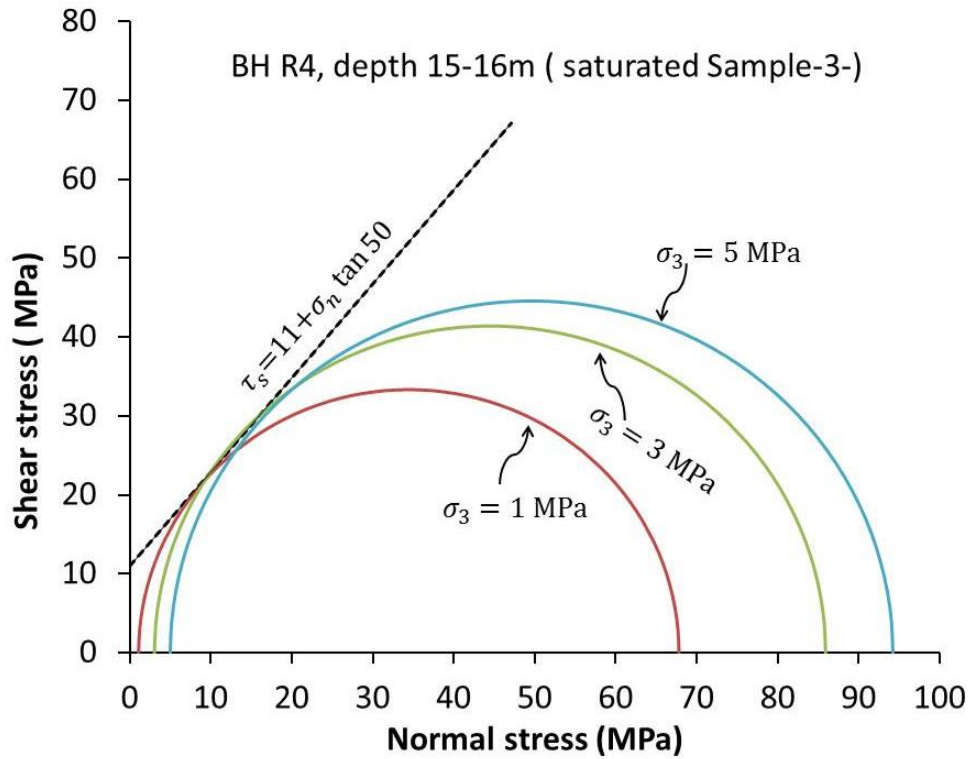
Figure 8.30 Mohr-Coulomb strength envelope for BH R4:15-16m/saturated sample 3
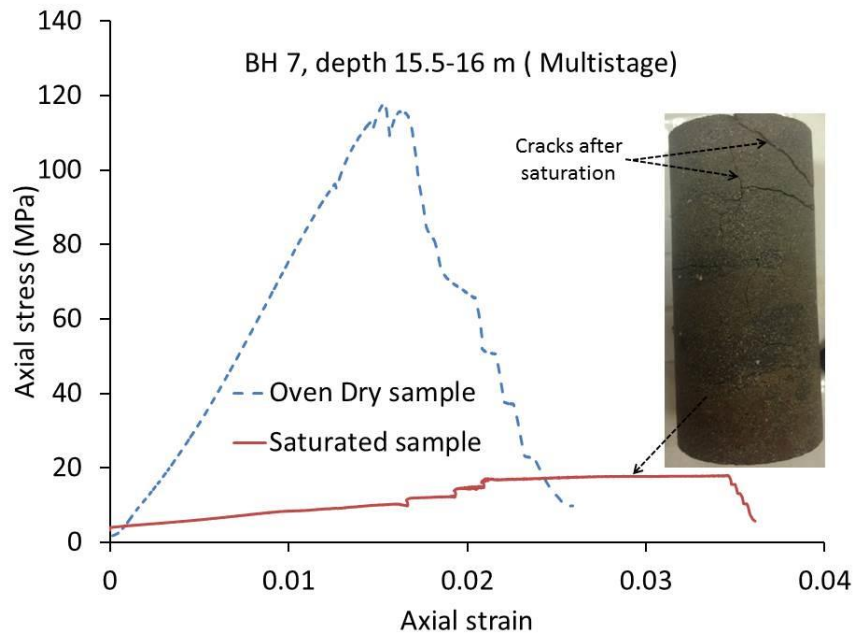
Figure 8.31 Axial stress-strain for samples from BH 7:15.5-16m
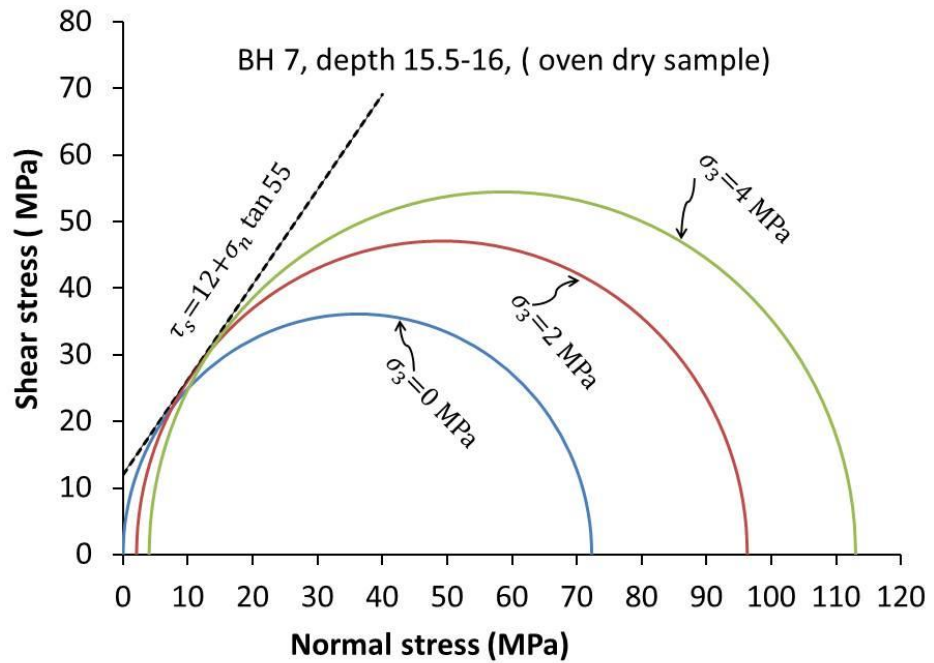
Figure 8.32 Mohr-Coulomb strength envelope for BH 7:15.5-16m/oven dry sample
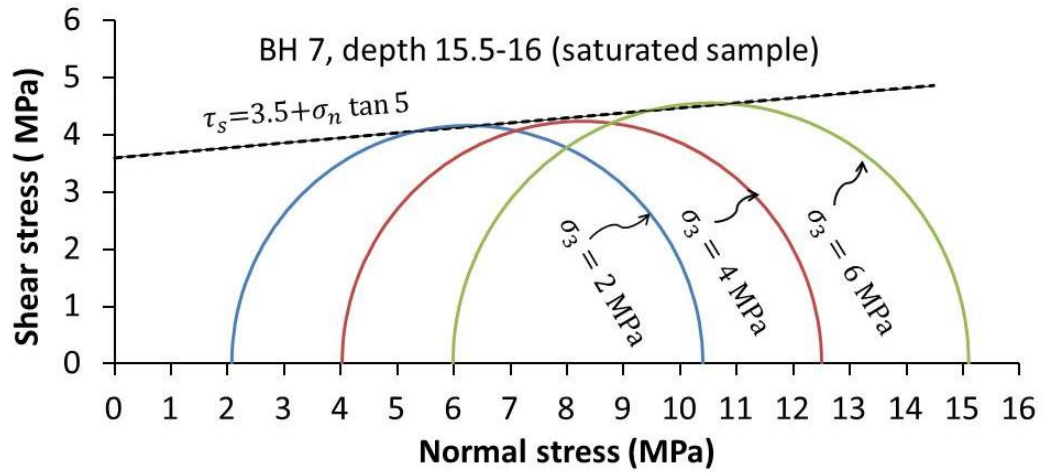
Figure 8.33 Mohr-Coulomb strength envelope for BH 7:15.5-16m/saturated sample
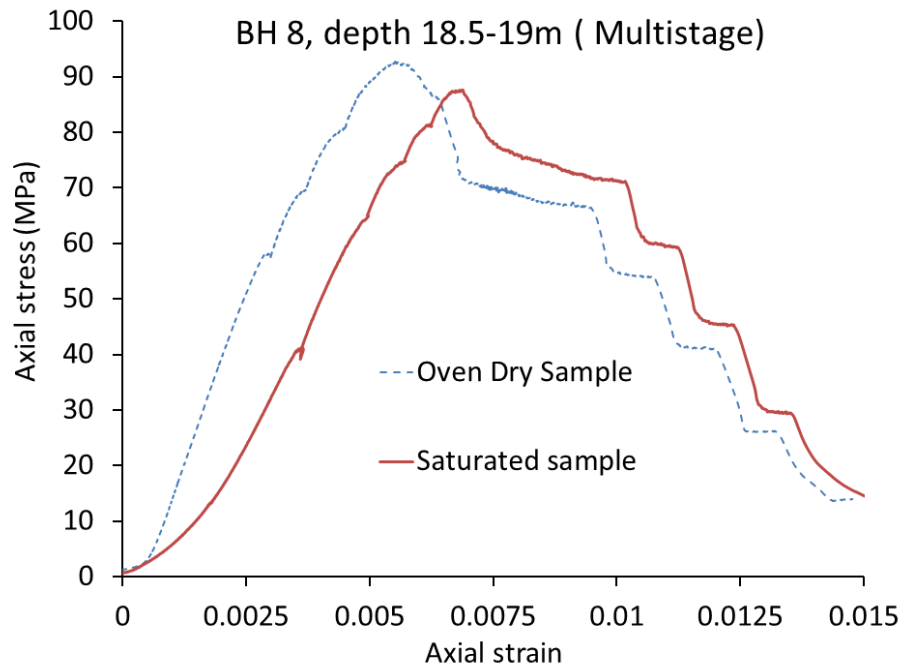
Figure 8.34 Axial stress-strain for samples from BH 8:18.5-19m
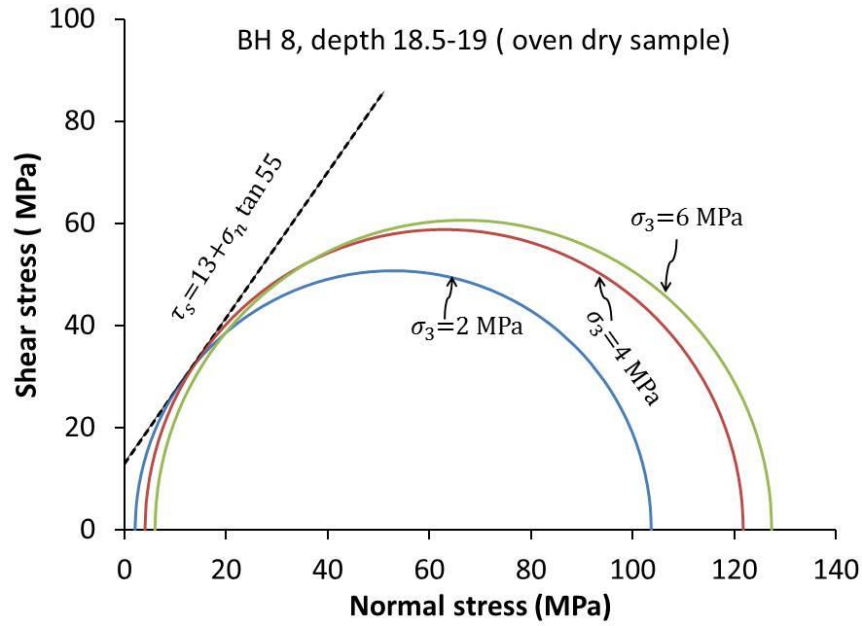
Figure 8.35 Mohr-Coulomb strength envelope for BH 8:18.5-19m/oven dry sample
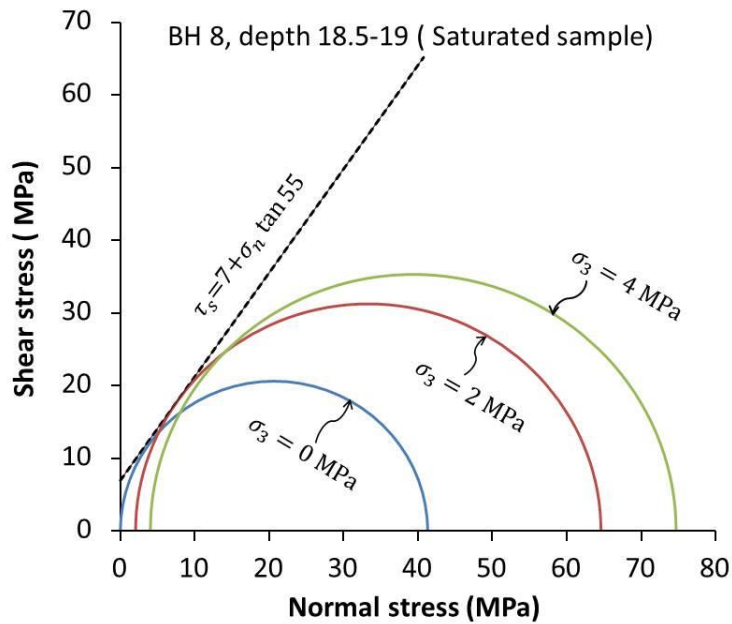
Figure 8.36 Mohr-Coulomb strength envelope for BH 8:18.5-19m/saturated sample

8.4.3 Tensile strength

The Brazilian indirect test using the procedure adopted in ISRM (1981) was conducted on selected samples according to their importance by location relative to the dam. Twelve samples were tested in dry condition and fifteen in saturated condition. Table 8.7 presents the results for both cases. It is clearly shown that the water content can dramatically change the tensile strength of the intact rocks, especially for the jointed rock mass in the foundation of the dams, if pyrite with clay minerals are involved in the rock's substance. This also indicates that the cementation of intact sedimentary rock will be reduced by saturation.

Table 8.7 shows the reduction of tensile strength in saturation conditions from 29.51-100%. Hoek and Brown (1997) reported that usually the strength of intact rocks containing clay mineral such as montmorillonite loses strength of 30-100% as a result of chemical deterioration of the clay or the cement binder.

Table 8.7 Tensile strength for saturated and oven dry of selected samples

Sample condition	Oven Dry Case			Saturated Case							Reduction %
BH No.	Depth (m)	Dry density (g/cm3)	Tensile Strength (Mpa)	BH No.	Depth (m)	Water content %	Porosity %	Dry density (g/cm3)	Sat density (g/cm3)	Tensile strength (Mpa)	
L5	50-50.5	2.261	4.45	L5	45-46	8.02	5.29	2.308	2.493	1.46	67
				8	14-15	4.19	5.02	2.513	2.619	5.63	
				8	14-15	4.79	5.65	2.480	2.599	1.79	
8	18.5-19	2.230	4.94	8	18.5-19	6.93	7.60	2.230	2.453	3.48	30
7	20-21	2.607	16.77	7	15.5-16	6.85	7.98	2.442	2.609	0.75	96
7	20-21	2.605	21.78								
				R3	14-14.3	6.29	8.18	2.404	2.555	0.77	
R3	21.8-22	2.333	7.29	R3	21.8-22	Collapsed	none	2.333	none	none	100
R3	31.6-32	2.710	18.41	R3	23-24	7.40	8.21	2.309	2.480	0.56	97
R3	23-24	2.305	11.28	R3	23-24	7.91	8.69	2.305	2.488	0.71	94
L5	20-20.5	2.596	7.03	L5	20-20.5	4.62	5.46	2.481	2.596	3.36	52
L5	15.5-16	2.460	6.44								
R1	32-33	2.386	5.66	R1	32-33	6.93	7.88	2.386	2.552	2.05	64
				R4	4-4.3	4.36	5.19	2.503	2.612	5.00	
R4	7-8m	2.381	5.56	R4	7-8m	6.71	7.61	2.381	2.541	3.09	44
				R4	15-16	2.08	2.63	2.655	2.711	9.49	
R4	25-25.5	2.430	8.23	R4	25-25.5	6.07	7.03	2.430	2.577	4.90	40

8.4.4 Point load test (PLT)

The uniaxial compression strength (UCS) was estimated from point load strength index (Is50) using Eq. 8.4 with a correlation factor of 24 (Bieniawski, 1974; Broch and Franklin, 1972; Brook, 1977; Greminger, 1982). However, this correlation factor might not be accurate for sedimentary rock, especially when it is saturated. Since this test is a cheap and quick method to predict UCS many researchers and geologists use it, especially in developing counties such as Iraq. Therefore, this test was conducted so as to suggest a correlation factor

for the Gercus formation in saturated condition as well as to give information about whether the water content has an effect on PLT or not. Table 8.8 presents the point load results for both cases (oven dry and saturated).

It can be seen that the water content has a crucial effect on point load value as well; the percent of point load reduction is about between 63 to 90% when immersed in water. Therefore, the correlation factor should be used with caution. According to UCS tests and results of point load, the suggested correlation factor for Gercus formation can be set to 10 for saturated condition.

$$PLT\ (MPa) = I_{s50} = \left(\frac{D}{50}\right)^{0.45} * \left(\frac{P}{D^2}\right) \qquad\qquad 8.3$$

where D is the diameter of the core sample in mm ad P is the failure load in Newton

$$UCS = Correlation\ factor * PLT \qquad\qquad 8.4$$

Table 8.8 Point load test results

Sample condition	Dry Samples				Saturated Samples	
BH No.	Depth (m)	D (mm)	P (N)	PLD (Dry)	PLD (Sat)	% Reduction
R4	7-8m	70.78	11.35	2.65	0.98	63.00
R1	32-33	70.74	7.40	1.73		
L5	45-46	70.68	6.40	1.50		
L5	30-30.5	37.36	8.10	5.09	0.50	90.12
R1	32-33	37.26	1.70	1.07		
R3	14-14.3	37.28	4.25	2.68	0.47	82.35
R4	25-25.5	40.53	4.60	2.55		
7	20-21	37.34	10.25	6.45	0.79	87.80
L5	50-50.5	70.29	7.20	1.70	0.57	66.67
R4	15-16	70.68	4.20	0.98		

8.5 Joint (Interface) Properties

8.5.1 Shear stiffness

Figure 8.37 presents the shear stress versus horizontal displacement data from the three interfaces tested in dry condition. From the data, the values of k_s were determined as the slope of the initial linear portion of the curves. The data shows good consistency of k_s between tests with varying normal stress (NS). The resulting values of k_s for the joints in siltstone, claystone, and mixed claystone-siltstone tested in dry condition were 3, 2.46, and 2.84 GPa/m respectively.

Figure 8.38 presents the shear stress versus horizontal displacement data from the three interface tests tested in saturated condition. Again the data shows good consistency of k_s between tests with varying normal stress (NS). One interface was chosen for siltstone whereas two interfaces were chosen for red claystone. The resulting value of k_s for the joint in Siltstone was 2.4 GPa/m, as shown in Figure 8.38a whereas the resulting values of k_s for the two interfaces in claystone were 1.9 and 2 GPa/m, as shown in Figure 8.38b and 8.38c respectively. From Figures 8.37 and 8.38, one can conclude that shear stiffness of the joints were affected by water and should be taken into account for study of rock masses using numerical technique.
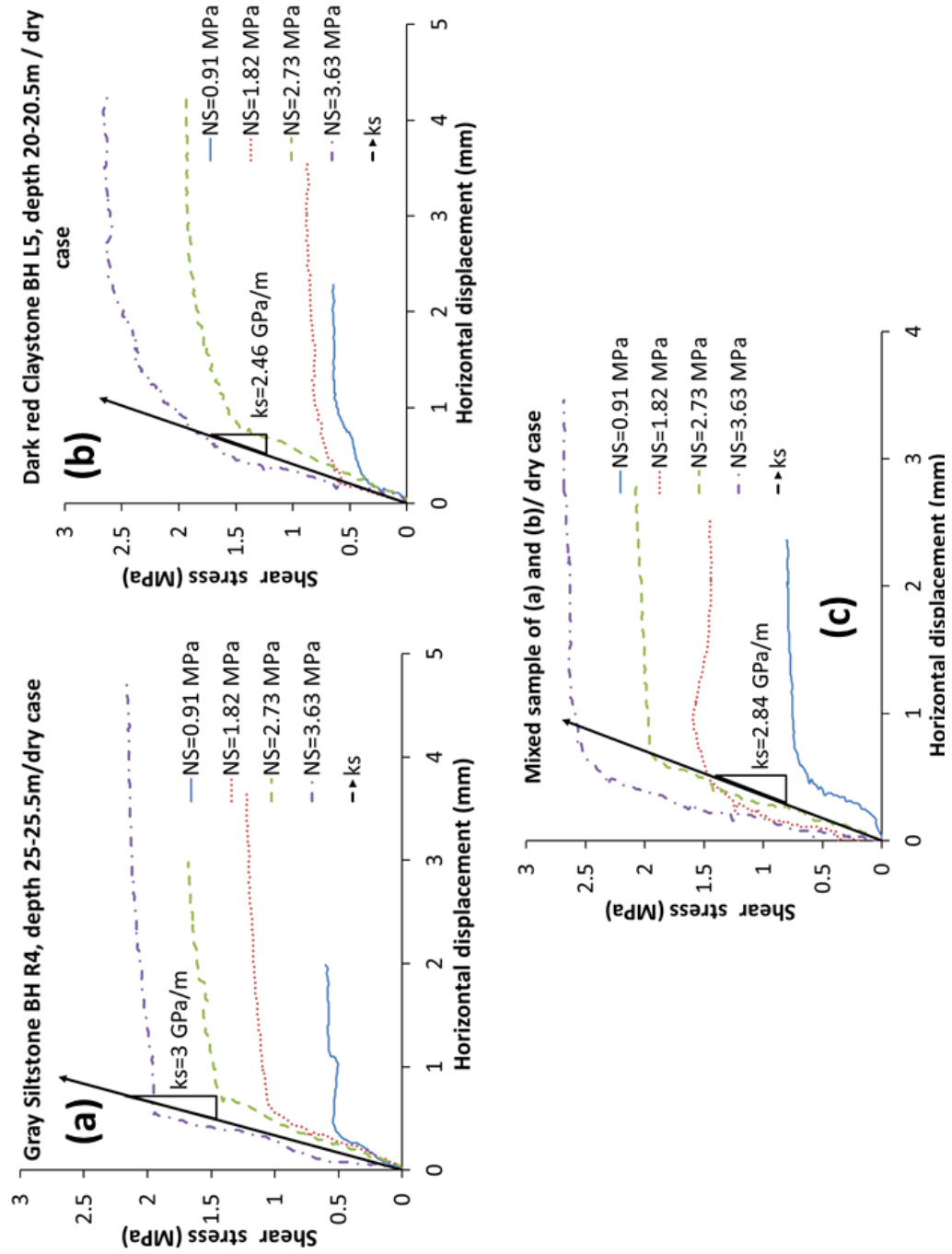
Figure 8.37 Shear stiffness for selected sample. Note: NS is normal stress / dry case
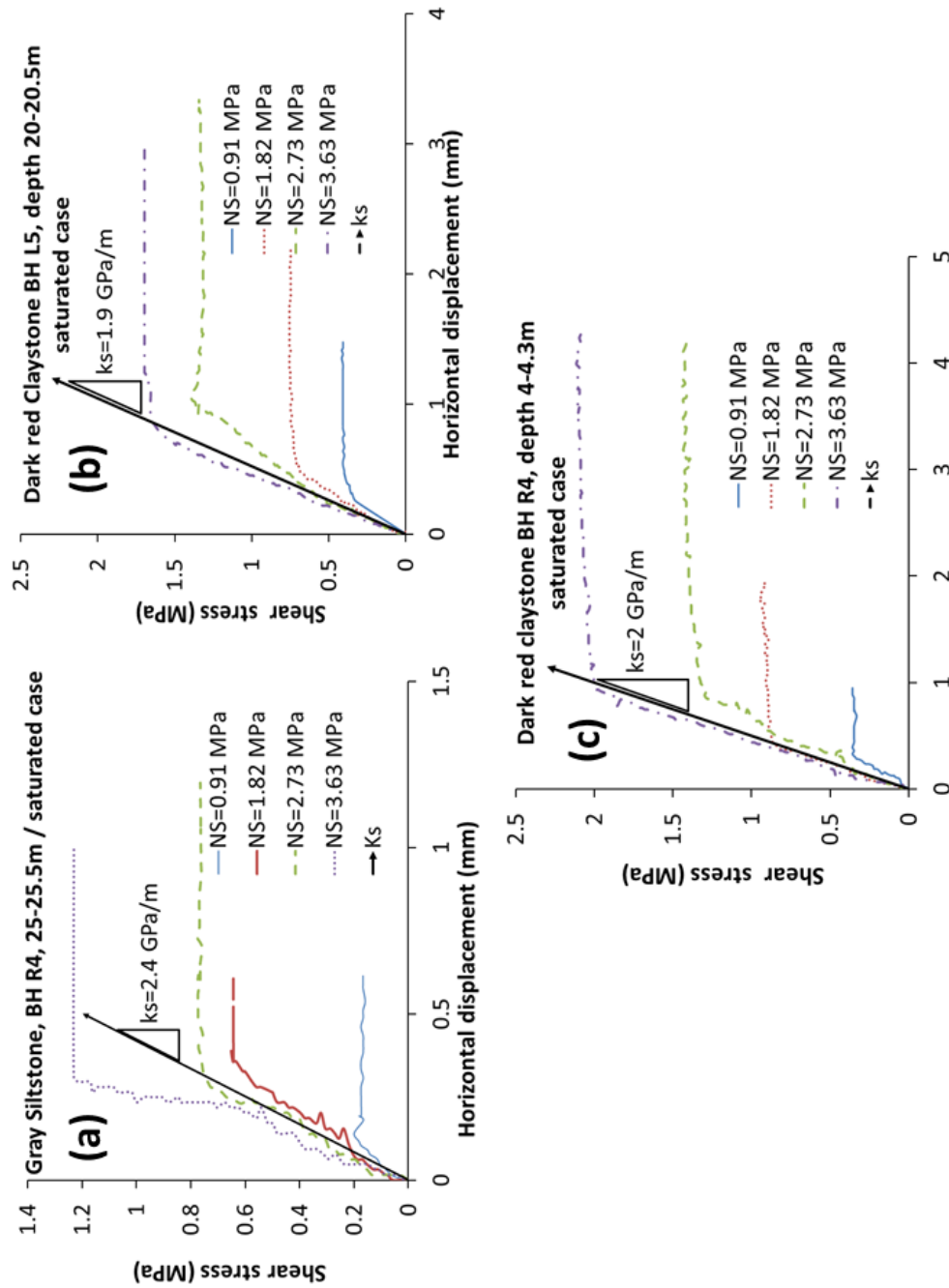
Figure 8.38 Shear stress-horizontal displacement for selected samples in saturated case. Note: NS is normal stress

8.5.2 Joints strength

To calculate the strength of joints, the ultimate shear stress produced in Figures 8.37 and 8.38 were used to calculate the strength of the smoothed rock joint. Figure 8.39 shows the strength envelopes for the joints tested in dry and saturated conditions. The range of angle of joint frictions was 31-36.5 degrees for dry condition, whereas this range was changed to 17-25 degrees when tested under saturated condition. It can be concluded that the wet surface affects the strength property of the joint and should be taken into consideration for studying rock mass behaviour. In addition, the correlation coefficient (R^2) was calculated for each case, showing good consistency in the data produced by the direct shear method.
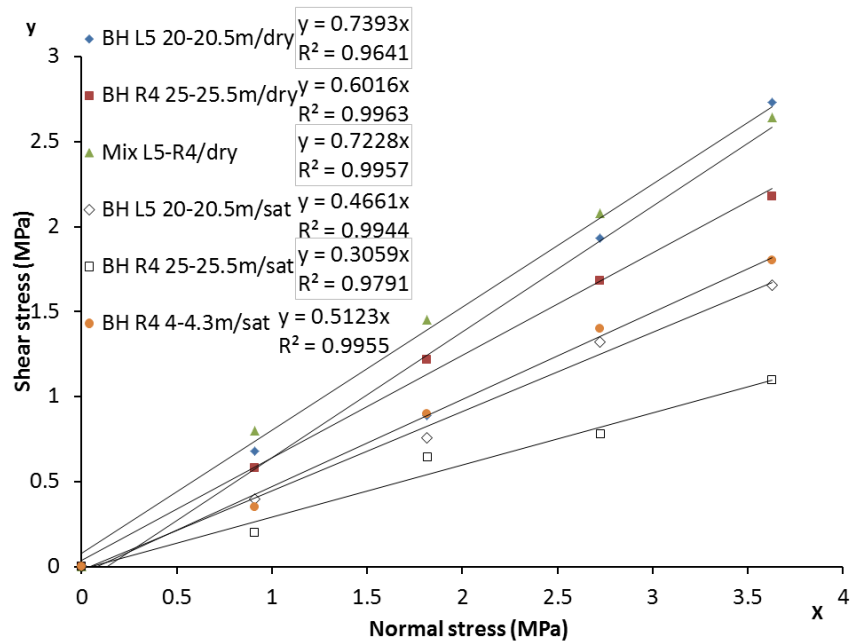
Figure 8.39 Shear strength envelopes for rock joints. Note: co-efficient of x represent $\tan \emptyset$

8.5.3 Normal stiffness

In order to evaluate the normal stiffness of the contact between rock blocks for the numerical simulations, a stress controlled method was conducted to measure the relationship between normal stress and vertical displacement for the jointed rock samples using the direct shear box apparatus (Wykeham Farrance model 27-WF2160). Two jointed rock samples (each 35mm long by 40mm diameter) were prepared in dry condition, as shown in Figure 8.40. The rock-rock normal joint stiffness was estimated to be 80 GPa/m. This value was evaluated from the normal stress versus deformation curve. It should be noted that the accurate method to find the normal stiffness was described in chapter 7. However, sensitivity analysis can be performed to show the effect of normal stiffness on the rock mass behaviour. According to Barton and Quadros (2014), the ratio of shear stiffness to normal stiffness can be up to 1:100 and usually normal stiffness is much greater than shear stiffness.
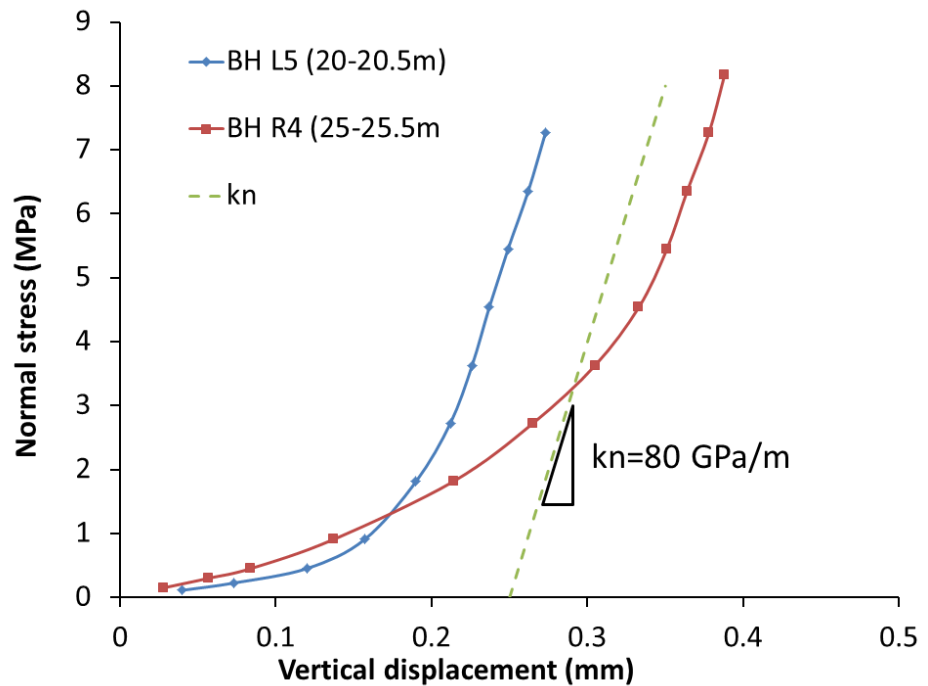
Figure 8.40 Normal stress-vertical displacement relationship

8.6   Rock Mass Description and Equivalent Properties

The rock mass of the left abutment of the Surqawshan Dam was selected in order to study the equivalent deformability parameters and strength parameters. The available rock mass classifications (RMR and GSI) as explained in the literature review were used and compared with UDEC. The discontinuities of the rock mass at the left abutment are shown in Figure 8.41. The nature of the discontinuities makes it possible to deal with rock mass as a plane strain condition. Because the dip angle of joint set D3 is nearly perpendicular to the dam axis and its dip direction is parallel with the dam axis (as shown in Figure

3.41c), it was not taken into account. Only two discontinuities (D1 and

D2) were taken into account.
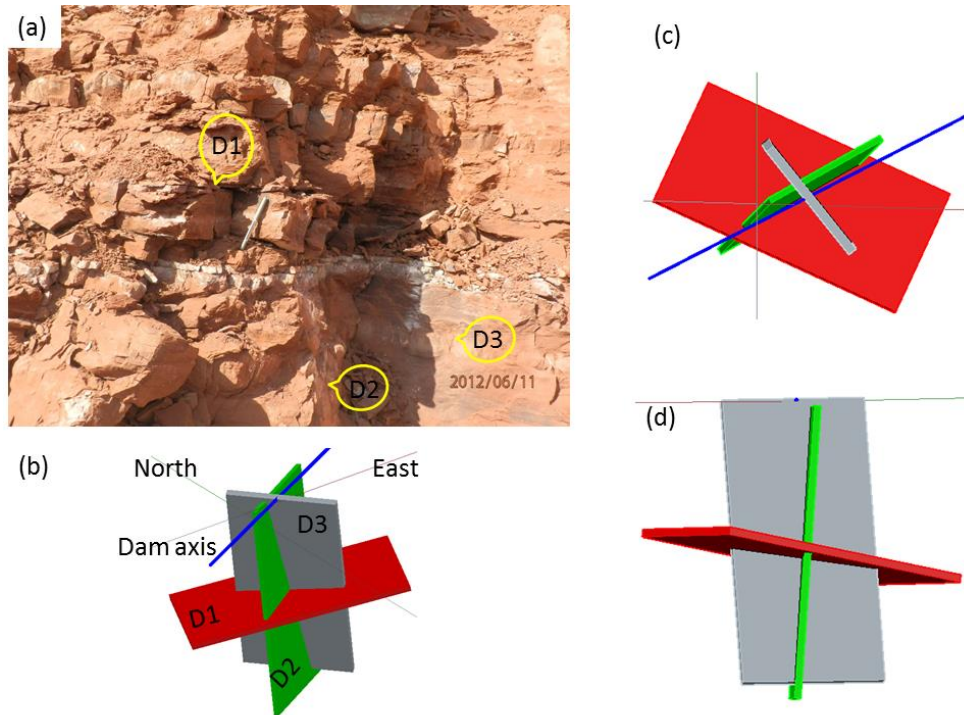
Figure 8.41 Discontinuities at the dams abutment of the Sur-qawshan dam

The strength and deformability parameters from the laboratory tests

on selected small-scale intact rock samples in a saturated condition

were used as an input into the rock classification systems and UDEC

model. The information about discontinuities was determined from

field study by the author. The intact rock properties were selected

from section 8.4 and the discontinuities properties were selected from

section 8.5 from borehole numbers L5 and R4 because these boreholes

represent the left abutment and their samples have similar behaviour and descriptions.

Table 8.9 shows the selected strength parameters from boreholes L5 and R4 for intact rock materials. The average tensile strength selected from these boreholes was found to be 3.6 MPa from Table 8.7 in the saturated case. The average Young's modulus was computed from Figures 8.9 and 8.10 in the saturated condition as 3997.2 MPa. The average value for UCS was calculated from Figure 8.10 as 31.95 MPa. The ratio of the average tensile strength to the average UCS is 0.11, which is reasonable for most brittle rocks.

Table 8.9 Selected strength parameters from boreholes L5 and R4

BH No.	Depth (m)	Friction angle (degrees)	Cohesion (MPa)
L5	6-7	46	7
L5	6-7	44	5.9
L5	15.5-16	44.5	7.5
R4	15-16	55	7.5
R4	15-16	45	15
R4	15-16	50	11
Average		47.4	8.98

According to the average values for c and ϕ from Table 8.9, the UCS should be equal to 46 MPa using Eq. 8.2. As can be seen, this value is higher than the average actual UCS test in saturated condition. This can result in an incompatibility of failure envelope using the Mohr-Coulomb criterion; therefore, a new cohesion was calculated as 6.22

MPa using Eq. 8.2. The final design failure envelope for intact rock

materials is shown in Figure 8.42.
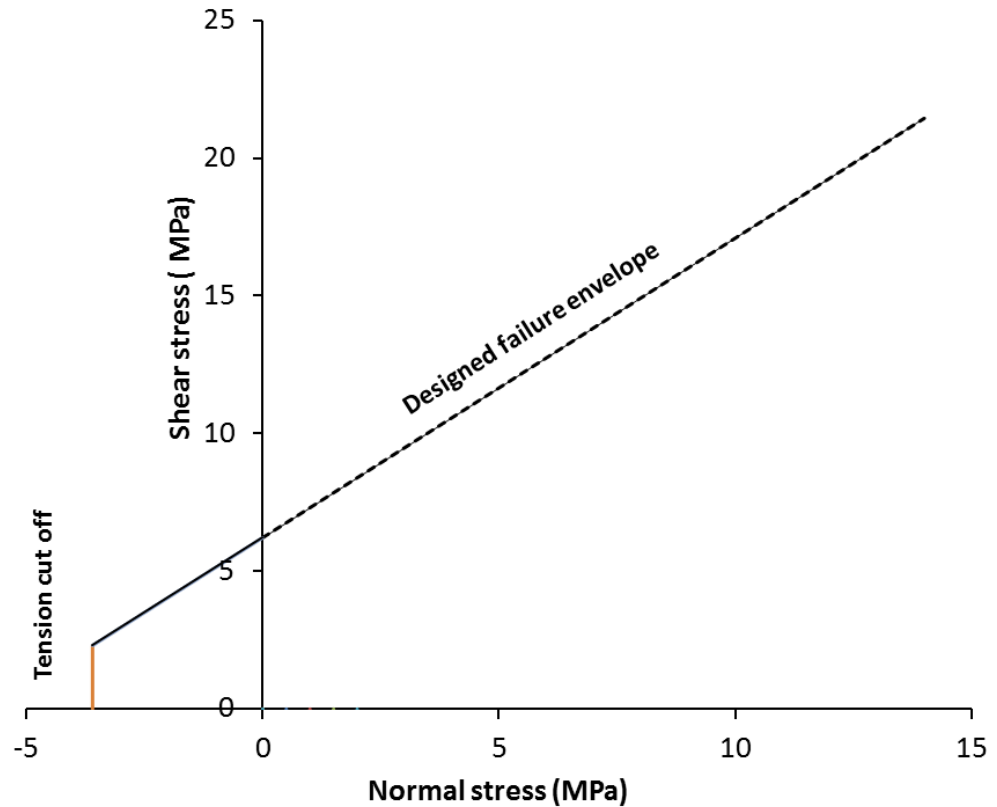
**Figure 8.42 Design Mohr-Coulomb failure envelope for intact
rock**

Tables 8.10 and 8.11 show the selected parameters that were used in

this study for intact rock and discontinuities respectively. These

properties were used in the following sub-sections in order to study

the rock mass behaviour in the left abutment of the Surqawshan Dam.

Table 8.10 Intact rock material properties

Material	Density(ρ)	UCS	E_i	v	c	$\emptyset$	σ^t
	kg/m^3	MPa	MPa		MPa	Degree	MPa
Intact Rock	2387	31.95	3997.2	0.24	6.22	47.4	3.6

Table 8.11 The joints properties for blocky rock mass

Joint	k_n	k_s	c_j	$\emptyset_j$	σ^t
	GPa/m	GPa/m	MPa	Degree	MPa
Planar joint	80	2.1	0.0	23.43	0

8.6.1 RMR classification system

To classify the rock mass at the dam site using the RMR system the whole rock foundation can be divided into a number of geotechnical units and each unit is classified separately. In this study the left abutment was considered as a unit and named RMLASQD (rock mass of left abutment of the Surqawshan dam).

Because there are three joint sets, as shown in Figure 8.41, the lowest rating should be taken into account. The lowest rating was for joint set 1 (D1). According to Table 2.4, six parameters are required to find the RMR of RMLASQD. From the first five parameters, the basic RMR can be calculated. Table 8.12 shows these parameters with their rating.

Table 8.12 Rating of RMLASQD

Parameters		Values or description	Rating
UCS (MPa)		31	4
RQD %		25-50	8
Spacing (mm)		>100	8
Discontinuities condition	Discontinuity length (m)	3-10	2
	Aperture (mm)	1-5	1
	Roughness	Smooth	1
	Infilling	Soft filling <5mm	2
	Weathering	Moderately weathered	3
Ground water		Dripping	4
Basic RMR			33

The final RMR is determined by adjusting the basic RMR using the joint orientations that are given in Table 2.3. As mentioned before, two joint sets were selected, D1 and D2, because the RMLASQD was assumed to be in plane strain. According to Table 2.3, the orientation of D1 (10 degrees) is very favourable (VF) and the final RMR is 33 whereas the orientation of D2 (85 degrees) is very unfavourable (VU) and the final RMR is 8. However, it was concluded in chapters 4 and 5 by using UDEC and FLAC that only the low dip of joint that dipped upstream may cause problems to stability of dams if the strength of the joint set that has a low dip angle is reduced. Therefore, the adjustment for joint orientation of joint set 2 will be neglected and the suggested value for final RMR value is set to 33.

The purpose of using the classification systems is to find the deformability and strength of rock masses. From section C of Table 2.4 the rock class number of RMLASQD is IV, which indicates poor rock. By matching this number in section D of Table 2.4, the range of cohesion is 100 to 200 and the range of friction angle is 15-25 degrees. By using the interpolation for these ranges, the designed values for friction angle and cohesion were 18.3 degree, 163.2 kPa, respectively.

The value of deformation modulus (E_{rm}) was estimated from Equation 2.18. As a result, the value of E_{rm} was calculated as 3.758 GPa.

8.6.2 GSI system

The GSI is one of the few attempts that have been made to develop a system to characterise the jointed rock mass to predict the strength and deformability indirectly (Cai et al., 2004). This system provides a complete set of mechanical properties such as the strength constant (m_b and s) in the Hoek-Brown criterion and constants (c and $\emptyset$) of the equivalent Mohr-Coulomb criterion as well as elastic deformation (E_{rm}). However, the Hoek-Brown criterion should not be used for problems in which failure is likely to occur by slip on one or two discontinuities as, for instance, in wedge failures of slope (Fortsakis et al., 2012; Hoek and Brown, 1980).

To apply the Hoek-Brown criterion for predicting the strength of a jointed rock mass, three properties are required of the rock structure. These properties are uniaxial compression strength of intact

substance, the value of the Hoek-Brown constant m_i for intact substance and the value of GSI.

The fabric of the rock mass can be seen from the outcrop of the rock mass of RMLASQD, which was revealed during the process of excavation at the site, as shown in Figure 8.41a. As can be seen, it is a well-interlocked blocky rock mass. This information can be used as input data to the software RocLab v 1.033 in order to get the deformability and strength properties of RMLASQD. Figure 8.43 shows the proposed model for the studied area driven from the RocLab code; the suggested value for GSI is approximately 40.
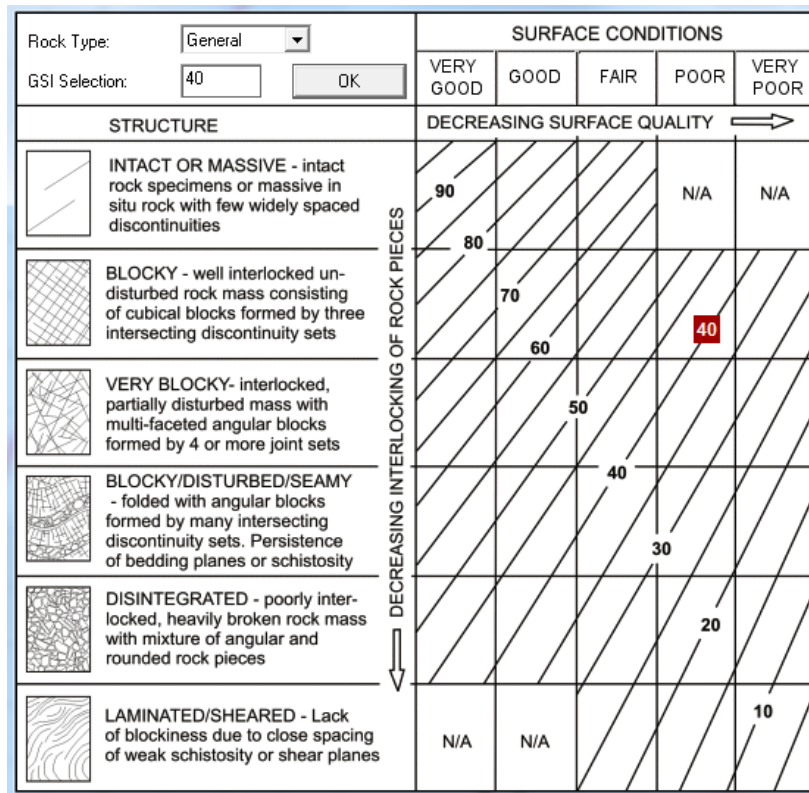
Figure 8.43 The GSI value for RMLASQD produced by RocLab code

The value of GSI with intact properties from Table 8.10 was used as input data so as to estimate the strength and deformability properties according to the modified Hoek Brown criterion. The results are shown in Figure 8.44.
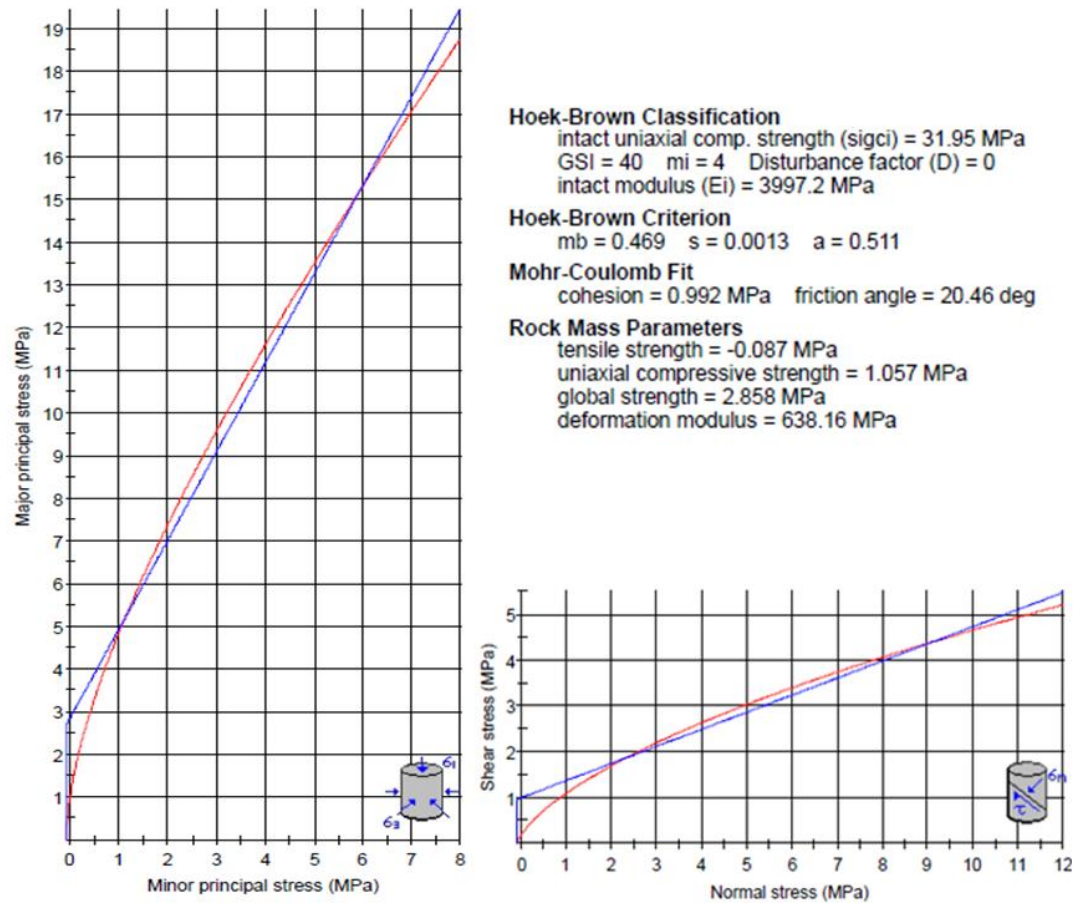
Figure 8.44 Analysis of rock mass strength using RocLab code

8.6.3 UDEC technique

In this section the equivalent strength and deformability parameters of RMLASQD unit were determined using UDEC. The strength of discontinuities and intact rock material were determined using small-

scale laboratory samples, whereas the overall strength and deformability of the rock mass were predicted using UDEC. To do a fair comparison with the classification systems similar assumptions that were used in the classifications systems were used in the UDEC model.

The rock mass was analysed numerically by conducting large-scale tests (2.5m × 5.0m) in a plane strain condition but under a range of different directions of loading on the rock mass. The rotation of loading was achieved by rotating the direction of loading 90 degree in steps ($\theta=15^o$/ step) counter-clockwise from the vertical axis, and one model was measured from the vertical axis in counter-clockwise direction, as illustrated in Figure 8.45a. Seven models were developed and the models were named according to loading direction. These models are R0, R15, R30, R45, R60, R75 and R90, as shown in Figure 8.45b.

Three other loading directions were chosen because of their significant condition. One of them loaded in 80 degrees counter-clockwise from the vertical axis was named as R80, whereas the other two directions loaded in -5 and -15 degrees were measured clockwise from vertical axis and were named as R-5 and R-15 respectively. For each model the deformation modulus and strength properties were calculated from the relation between axial stress-axial strain curves under a range of confining stress (0.05, 1, 2, and 4 MPa). The numerical model has two joint sets D1 and D2 with joint spacing of 0.1m and 0.2m respectively.

(a)

Note: $R\alpha^o$ is Resultant load with angle direction measured from the vertical axis

(b)
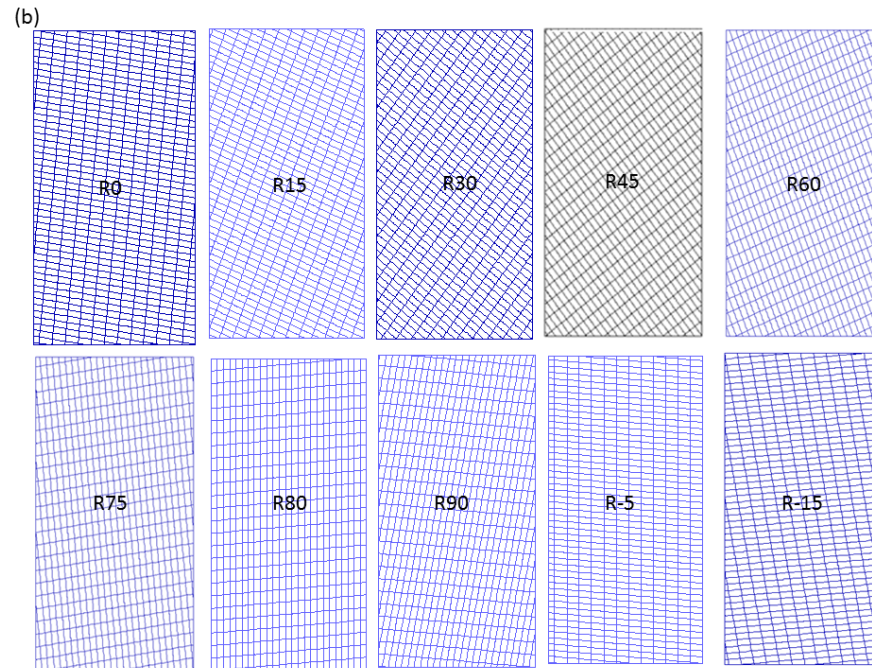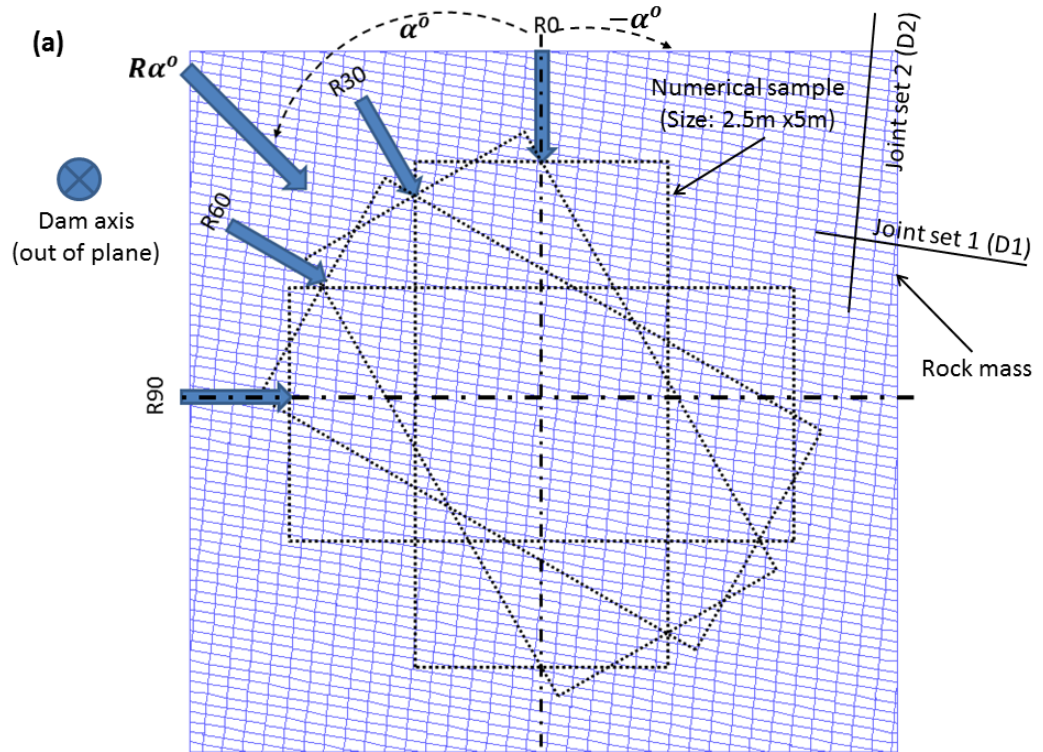
Figure 8.45 Numerical samples and loading direction on the RMLASQD: (a) loading direction, (b) generated numerical samples

The numerical samples were placed between two smooth boundary platens so as to eliminate the effect of the platen-rock contact interaction, as shown in Figure 8.46. The upper smooth boundary was moved downward with a velocity of 10 mm/sec, while the lower smooth boundary was kept fixed. Reaction forces at both boundaries were recorded with the development of axial strain. The special FISH function used in chapter 6 was utilised to obtain recordings of reaction forces during the displacement control tests (i.e. at a state of numerical equilibrium at each displacement increment). The axial stress was computed by dividing the average values of reaction forces on the platens by sample cross section width and the axial strain was computed using the displacement of the top platen. Also, the lateral strain was recorded with loading at mid-point of the sample's height using horizontal displacements at both sides of the numerical sample.
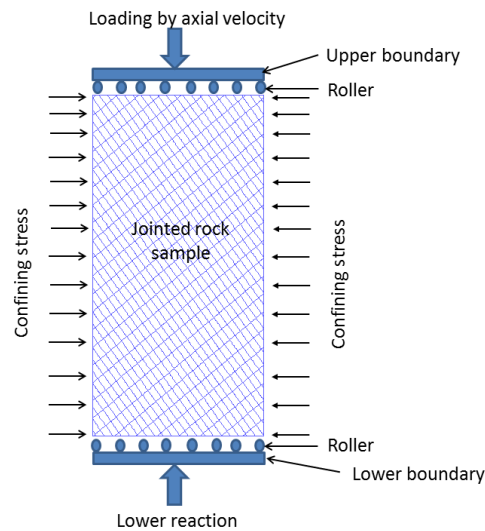
Figure 8.46 Numerical sample with boundary condition for compression test

8.6.3.1   Axial stress-strain

Axial stress-axial strain and lateral strain relationships were obtained from the numerical compression test and were used to study the deformability and strength properties of RMLASQD unit. The numerical study revealed three modes of failures. These failures were: slipping along discontinuities followed by block rotations at sample ends named as mode 1, sliding along discontinuities (mode 2), and shear failure (mode 3) through intact rock blocks. Figure 8.47 shows a typical axial stress-strain curve for model R0 to represent mode 1. The produced curve has two parts. The axial stress-strain was linear until a yield point (yield stress). At this stage slipping occurred along joint set 2 (D2) and then the sample deformed nonlinearly with strain hardening observed until reaching failure stress (ultimate stress). This nonlinearity was due to block rotations at sample ends; see the inset image in Figure 8.47. Because the bottom of the sample was fixed in the vertical direction, as a result blocks were rotated and tensile failure occurred in the blocks at the samples' ends.

Figure 8.48 shows a typical axial stress versus both lateral strain and axial strain for model R45 to symbolize failure mode 2, which is sliding along discontinuities. As can be seen, the ultimate stress is nearly equal to yield stress. At yield stress the sample failed along joint set 1. It should be noted that this failure occurred because the dip angle of joint set 1 is larger than the internal friction of the joint set 1.

Figure 8.49 shows a typical axial stress-strain relationship for model R80 to represent failure mode 3, which is shear failure through intact rock. Only this mode of failure exhibited peak stress and strain softening behaviour. Generally, this type of failure occurred when the direction of loading was parallel with one of the joint sets, and it made an angle less than the friction angle of the discontinuities with the normal to the other joint set. Table 8.13 shows the numerical samples with their mode of failure.

Table 8.13 Mode failures of numerical samples

Numerical sample No.	Mode of failure
R0, R15, R60, R75, R90, R-15	Mode 1
R30, R45	Mode 2
R80, R-5	Mode 3
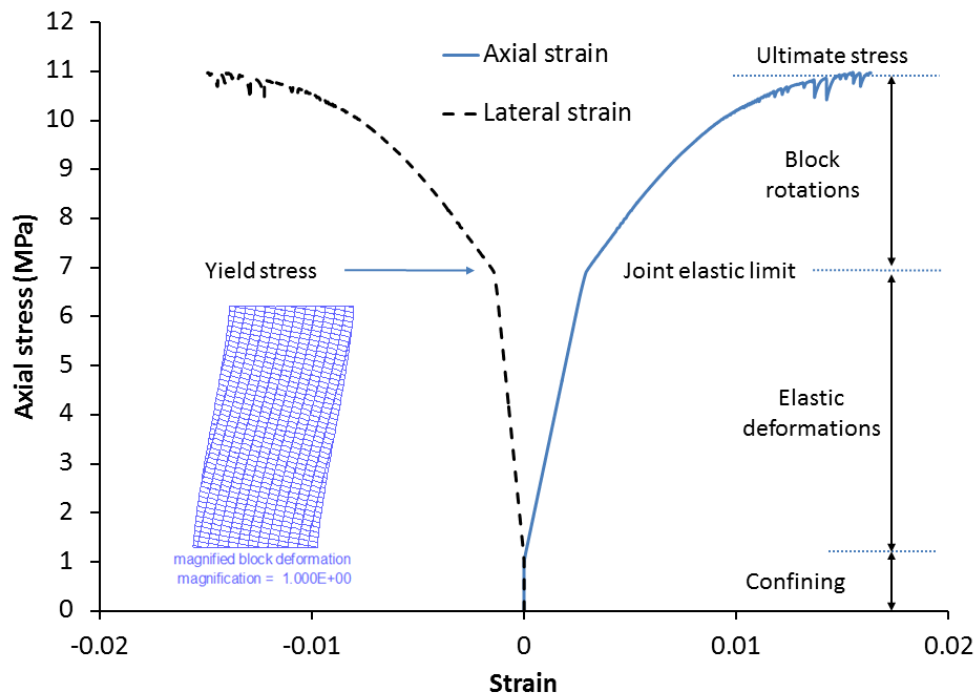
Figure 8.47 Typical axial stress-strain for model R0 under con-fining stress of 1 MPa
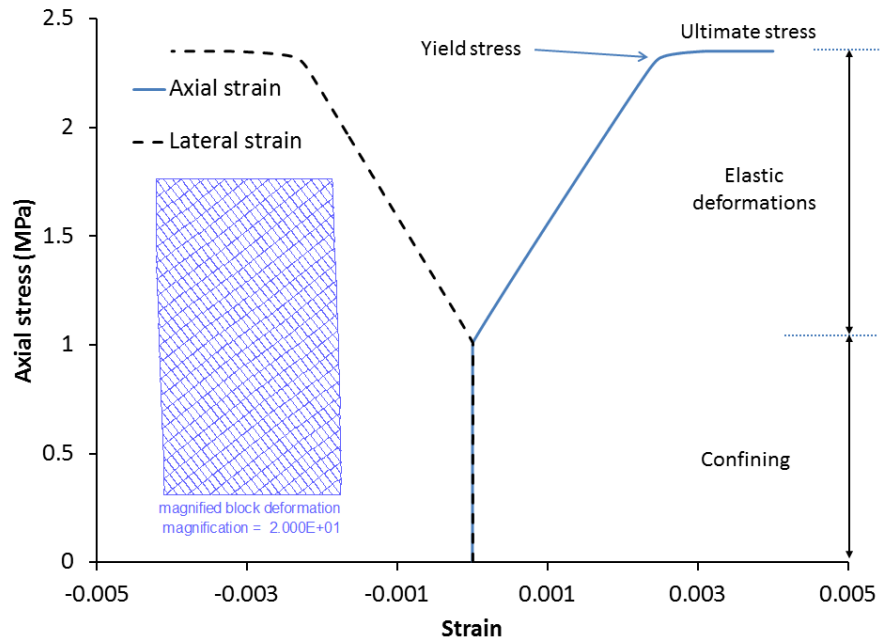
Figure 8.48 Typical axial stress-strain for model R45 under confining stress of 1 MPa
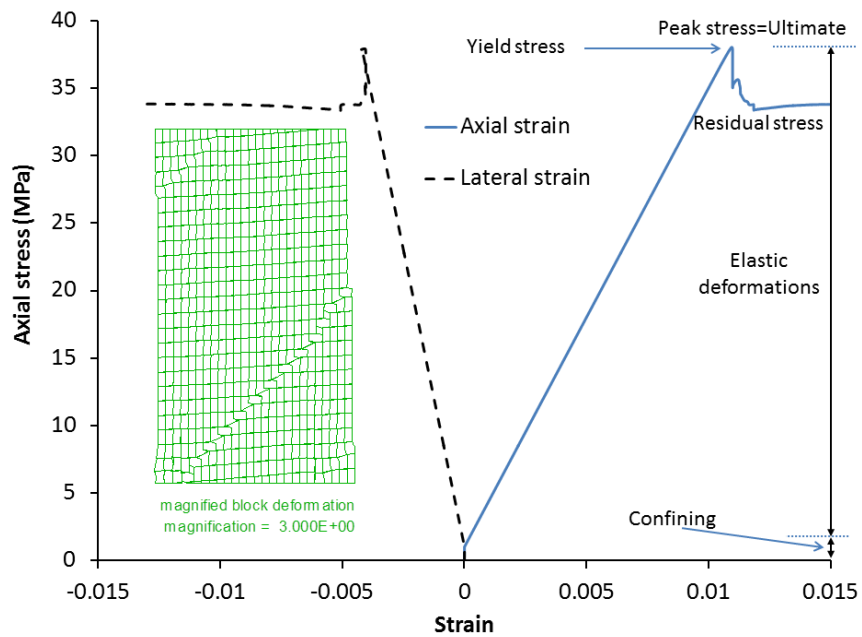
Figure 8.49 Typical axial stress-strain for model R80 under confining stress of 1 MPa

8.6.3.2   Effect of confining stress on failure mode

In this study it was noticed that the failure mode 1 may change under high confining stress. The Model R0 was selected to achieve numerical compression test under different confining stress within the range 0.05-30 MPa. The axial stress-axial strain relationships results are presented in Figures 8.50 and 8.51. The graphs show linear elastic behaviour until yield stress, then strain hardening occurring in all samples until they reached an ultimate stress, except for confining stress of 20 and 30 MPa, at which strain softening occurred.

It is very interesting to see that the numerical results for sample R0 under low confining stress (Figure 8.50) show the phenomena of stick-slip oscillations similar to physical tests results achieved by Brown and Trollope (1970) on the smooth jointed rock samples of sizes (8 x 4 x 4 inches) using triaxial and direct shear tests. Their typical results are shown in Figure 8.52.

Figure 8.52a shows the jointed rock sample's geometry and Figure 8.52b shows the axial load in LB-axial deformation for intact rock and jointed rock samples. Figure 8.52c shows the axial stress-axial strain relationships for a sample that has dip angles of two joint sets of 30 and 60 degrees. This figure shows that there is an effect of platen-sample's ends interaction on the results because under a confining stress of 1000 Psi (6.9 MPa) and 500 Psi (3.45 MPa) the samples gave similar deformation modulus whereas under confining stress of 2000

Psi (13.8 MPa) the deformation modulus was very high by far than confining stress of 1000 Psi (6.9 MPa).

In addition, according to the plane of weakness (Eq.7.1) and the numerical results of a jointed rock sample having a single joint that dipped 60 degree, presented in chapter 7, see Figure 8.52c , should display elastic-plastic behaviour and not strain hardening. As was concluded in chapter 7, the strain hardening of a joint that dipped around 60 degrees may result from the platen-sample's ends interaction.

Brown and Trollope (1970) showed the occurrence of stick-slip oscillation for smooth sample tested by direct shear, as shown in Figure 8.52d, which is similar to the results of the numerical compression test using UDEC in Figure 8.50. This is because the strength of joint sets controlled the rock mass behaviour in Figure 8.50. From these one can infer that UDEC can be positively used to test large rock samples as an alternative method of testing large rock samples in the laboratory. However, both UDEC and physical modelling should be performed under similar boundary conditions.

The strength failure envelope of model R0 is show in Figure 8.53. The shape of failure envelope is similar to Patton's bilinear model (Ladanyi and Archambault, 1969). This bilinear model occurs because the failure mode changed at a confining stress of 20 MPa from mode 1, which is block rotations with slips along the joints, to mode 3, which is

failure in shear through intact rock blocks. The processes of plastic

state in samples with confining stress are presented in Figure 8.54.
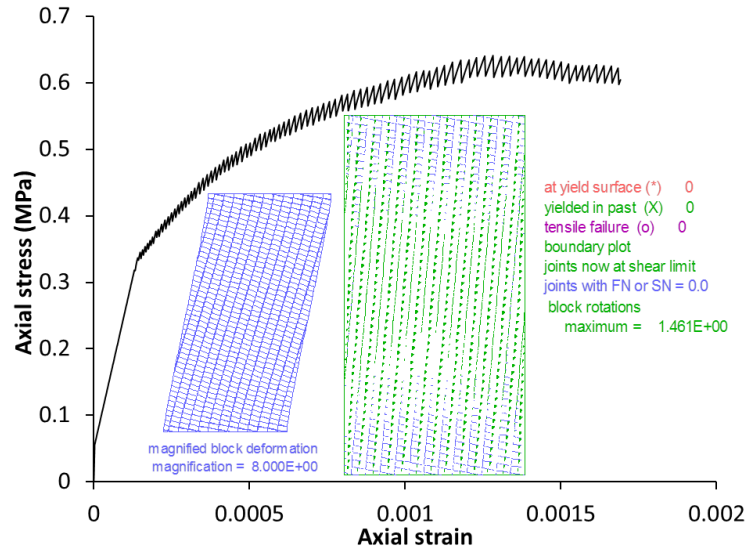
Figure 8.50 Axial stress-axial strain for model Ro under 0.05 MPa
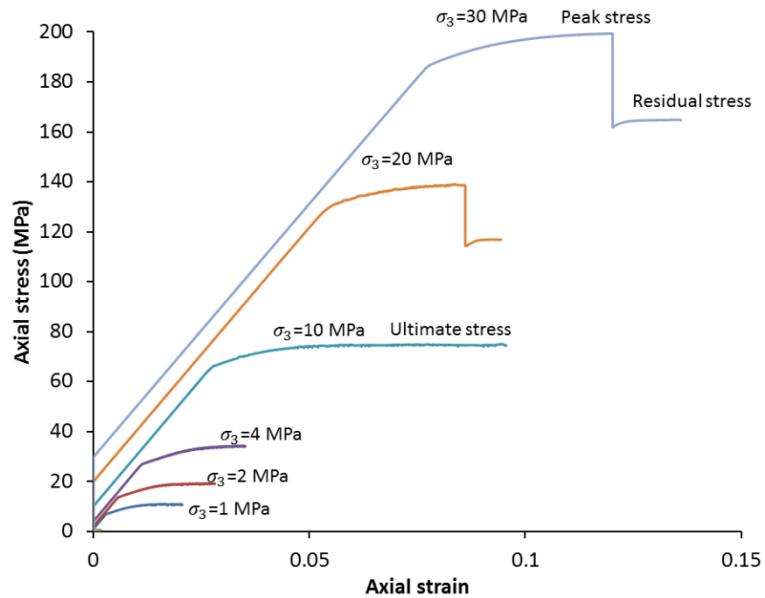
Figure 8.51 Axial stress-axial strain for model Ro under different confining stress.
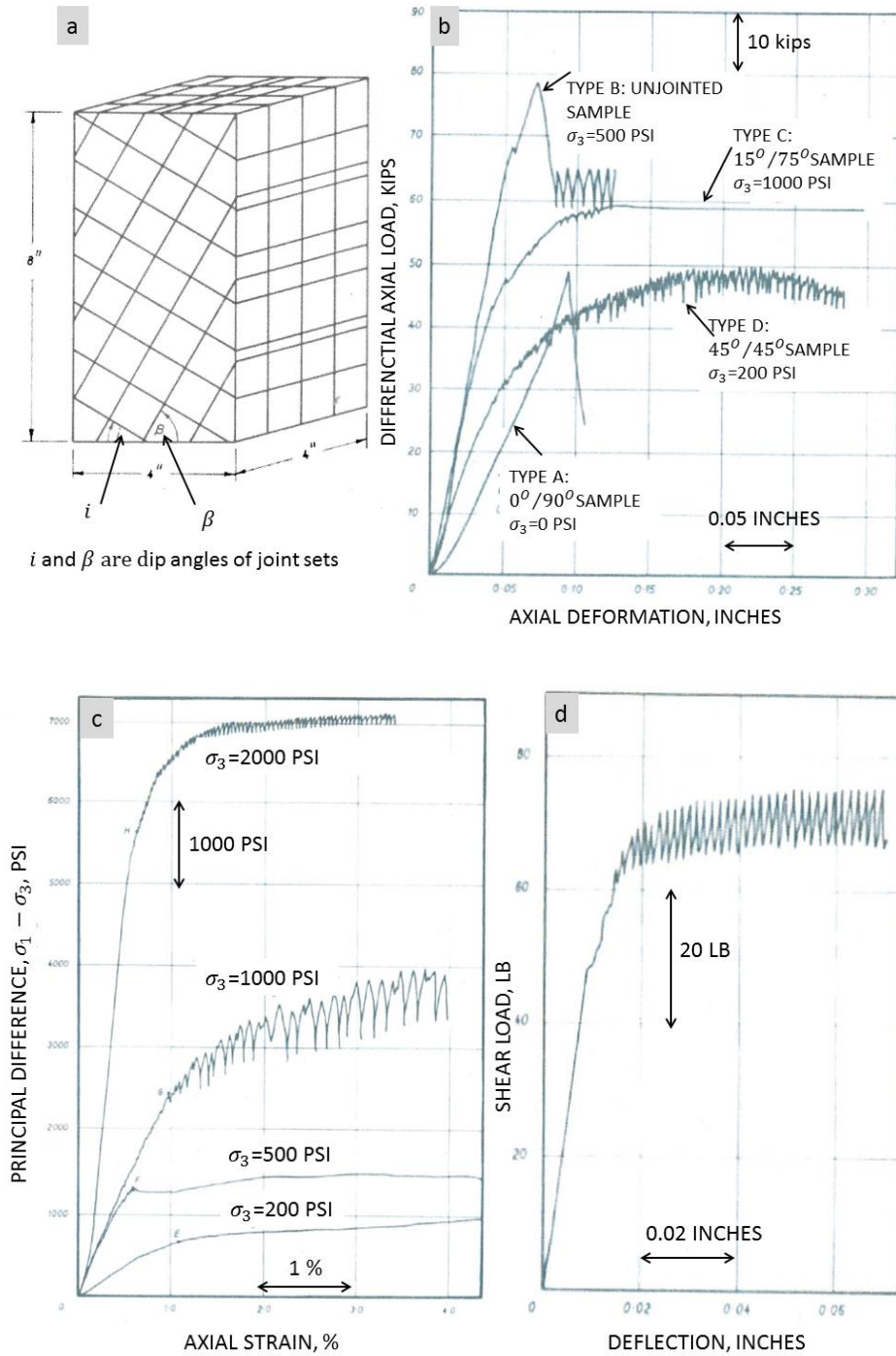
Figure 8.52 Physical triaxial tests (a) jointed rock sample (b) triaxial results for cases: Intact; 0°/90°; 15°/75° and 45°/45° (c) triaxial results for case 30°/60° (d) direct shear test. After Brown and Trollope (1970)
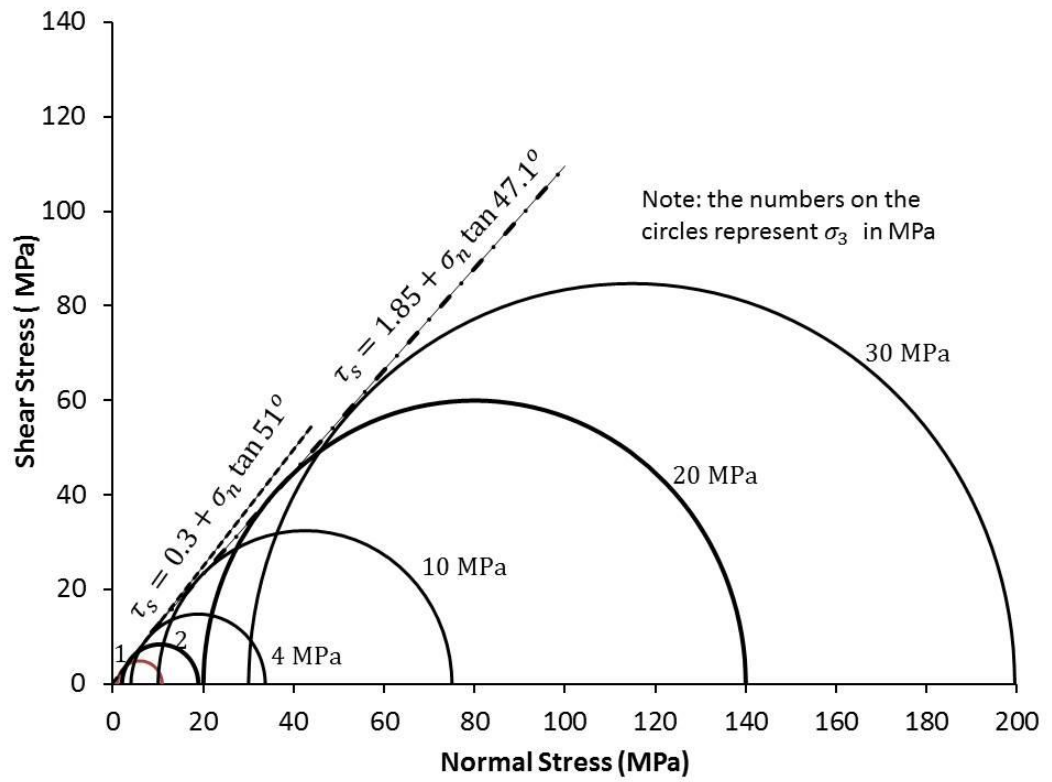
Figure 8.53 strength failure envelopes for the model R0
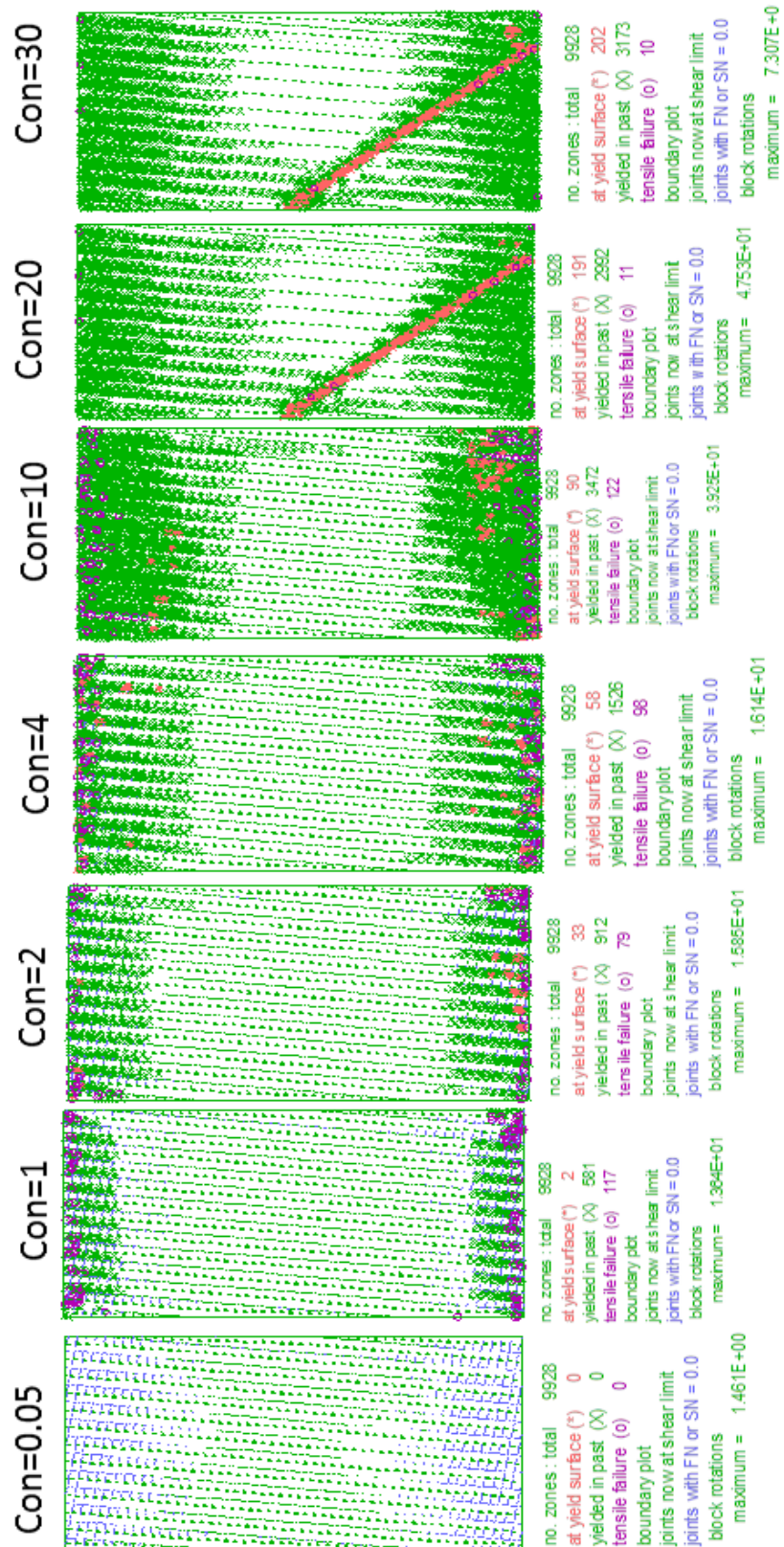
Figure 8.54 Plastic state with confining stress of Model R0

8.6.3.3   Equivalent strength properties

The equivalent strength properties, which are cohesion (c) and internal friction angle, were predicted using Mohr-Coulomb criterion. These parameters were predicted using two levels of stress: yield stress, when slips started along discontinuities; and ultimate stress, when maximum stress was reached. According to Table 8.13 there were three modes of failure. For mode 1 the ultimate stress was higher than yield stress whereas for other modes the yield stress was the same as the ultimate or peak stress. The results are shown in Figure 8.55. As can be seen, for mode 1 there was an increase in friction angle due to block rotations. A result of block rotation was that dilation occurred, although smooth joints were used in the study. This depended on joint sets' dip angles. The figure shows that the strength properties are highly dependent on the load direction on the jointed rock mass.
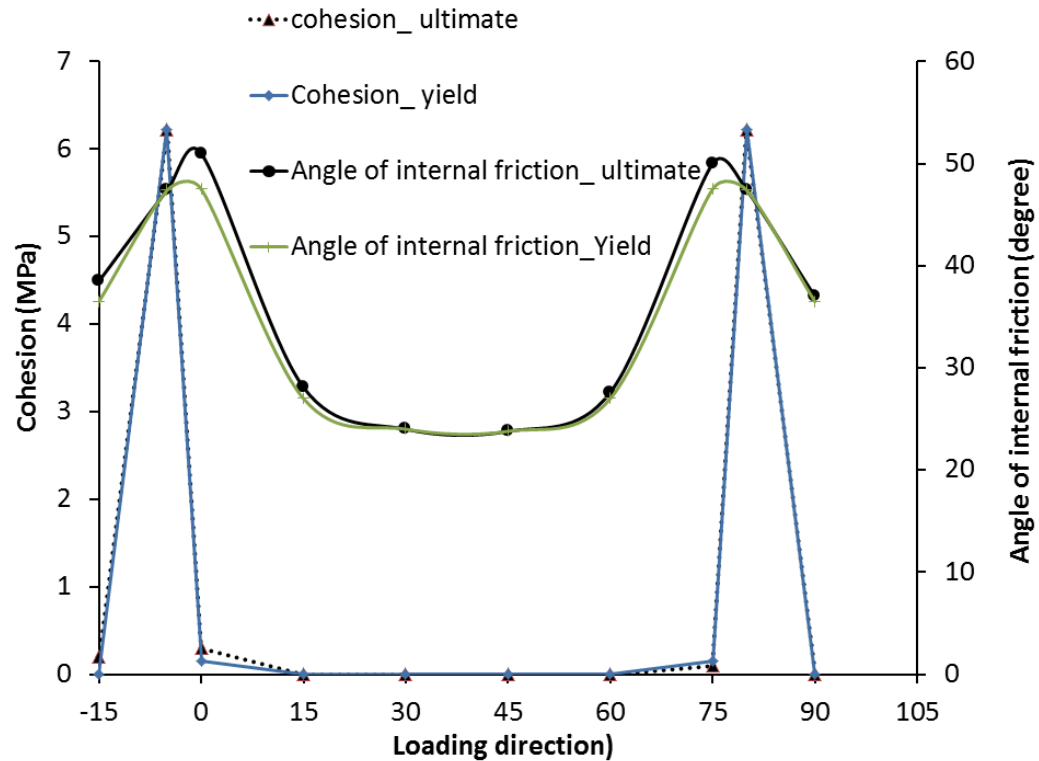
Figure 8.55 Equivalent strength properties according to loading direction

8.6.3.4   Equivalent deformability properties

As presented earlier in chapter 6, the equivalent Young's modulus and Poisson's ratio cannot be obtained directly from the axial stress-strain curves produced by UDEC, but they should be predicted indirectly from axial stress and axial strain curves using Equations 6.2 and 6.3. The equivalent deformation modulus and lateral strain ratio were calculated at 50% of the maximum axial stress according to the procedure mentioned in ISRM (1981) for intact rock. Also, analytical methods were utilized to predict the deformation modulus. Figure 8.56 shows the results according to the loading direction. As can be seen,

there is a good match between the numerical results against analytical method (Eq. 6.1 and Eq. 6.5). It should be noted that Eq. 6.5 was used only for two loading directions (R80 and R-5) because this equation can only be used when the loading direction is perpendicular to a single joint set and the author concluded that this equation may be used for two joint sets on condition the dip of the second joint set is smaller than the friction angle of the joint set to ensure that the sample would not be failed by sliding along the second joint set.

Again it is obvious that the loading direction has a significant influence on the deformation modulus and lateral strain ratio. It can be concluded that the maximum deformation modulus was for mode 3 whereas the minimum deformation modulus was for mode 2.

The maximum lateral strain was for mode 2 and as expected the minimum lateral strain was for mode 3 because the intact rock controlling its behaviour over the discontinuities behaviour.
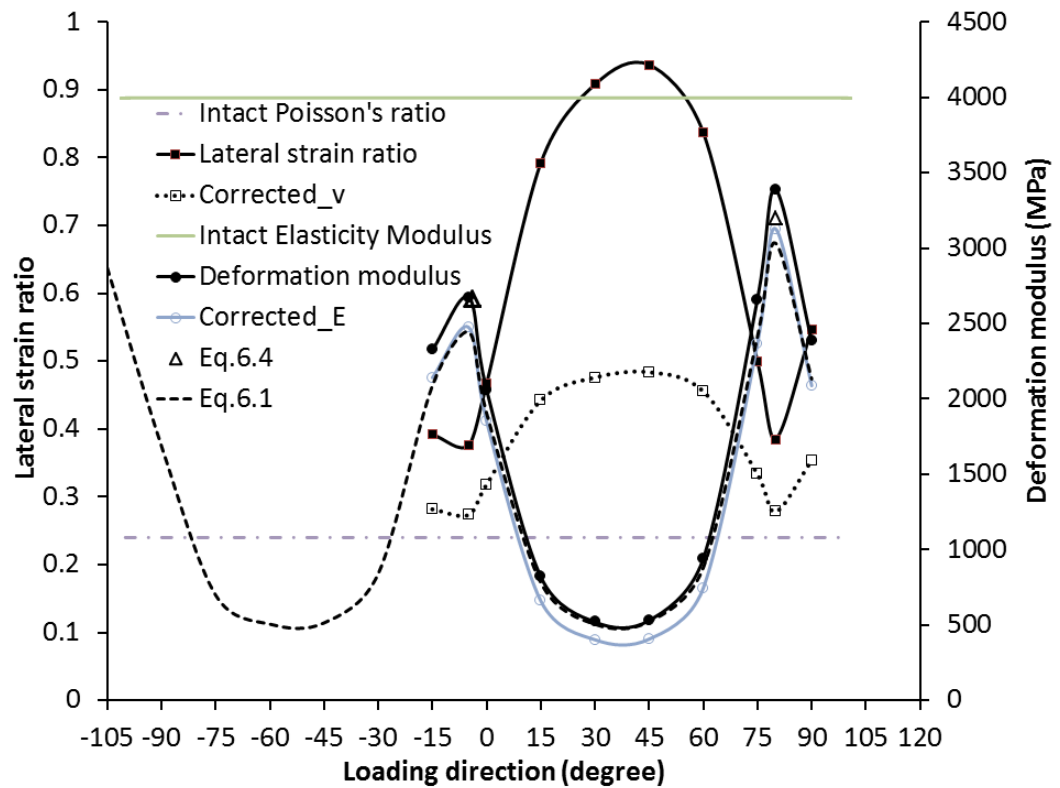
Figure 8.56 Equivalent deformability properties according to loading direction

Figure 8.57 shows the effect of stiffness ratio (k_n/k_n) on the deformability parameters for selected model R45. Figure 8.57a was produced by changing the stiffness ratio while fixing shear stiffness. It is shown that both deformability parameters decrease with increasing stiffness ratio. Figure 8.57b was produced by fixing normal stiffness while increasing the stiffness ratio. It can be seen that the lateral strain ratio decreases with increasing stiffness ratio whereas the deformation modulus increases with increasing stiffness ratio. Figure 8.57c shows the relationship between the shear stiffness and deformability parameters by fixing the stiffness ratio. It was concluded

that there is an increase in deformability parameters with increasing

shear stiffness or normal stiffness parameter and there is a non-linear

relationship between them similar to a parabolic curve. From these

one can conclude that the stiffness ratio is very important and both

normal stiffness and shear stiffness should be selected with caution.

Also, this sensitivity study may encourage using nonlinear behaviour

for normal stiffness as well as for shear stiffness in the future study.
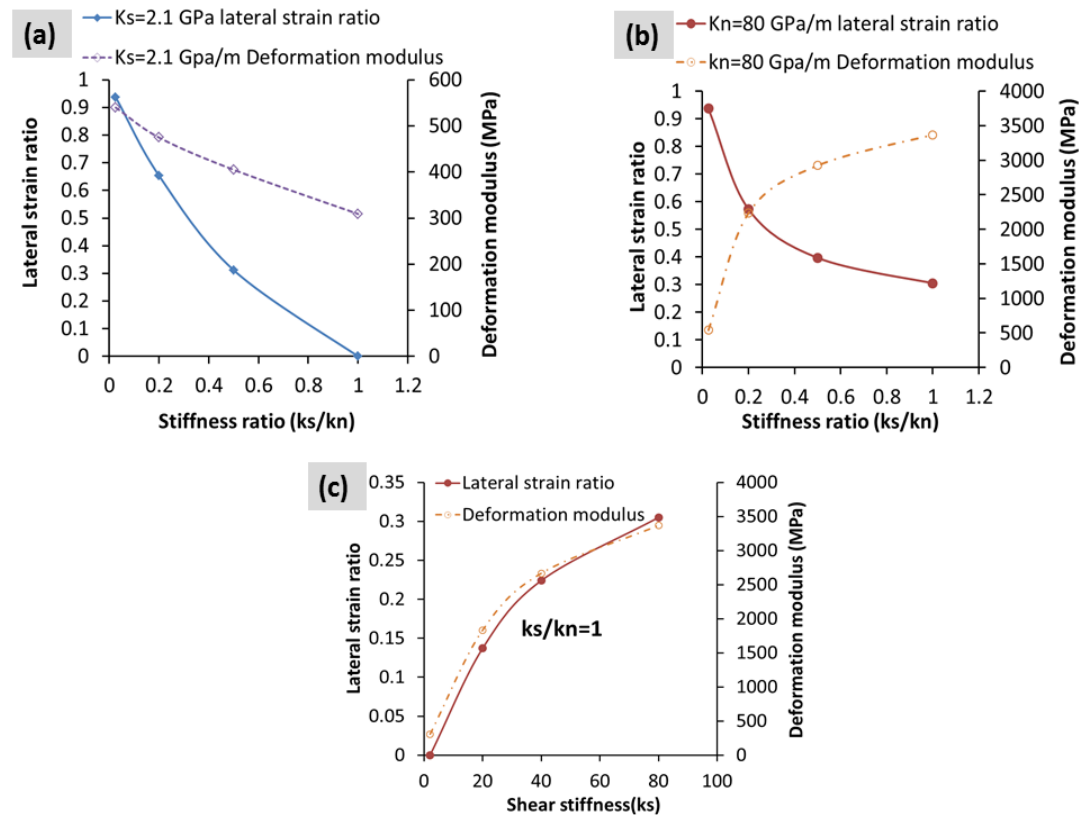
Figure 8.57 Effect of stiffness ratio on lateral strain ratio and deformation modulus for model R45 under confining stress of 1 MPa

8.6.4 Assessment and discussion

Table 8.14 shows the strength and deformability parameters produce by different methods that were used in this study. The friction angle predicted by RMR and GSI are almost the same, whereas the cohesion by GSI is higher than that produced by RMR. It seems that GSI overestimates the cohesion parameters. This can be confirmed by comparing the GSI results with results of UDEC; one can conclude that the friction parameter matches with mode 2, whereas the cohesion property is much higher than mode 1 and 2 and much lower than mode 3. The strength parameter by RMR matches the mode 2 by UDEC.

Concerning the deformability properties, the classification systems only provide the empirical equation to calculate the deformation modulus, and from Table 8.14 it can be concluded that the RMR overestimated the value of deformation modulus, whereas the GSI system prediction matches with failure mode 1 by UDEC. It is obvious that the UDEC can give mostly reasonable results for all parameters, as it was validated by analytical results in chapter 6 and experimental results in chapter 7. Overall, for rapid estimation of deformability and strength parameters, especially for weak sedimentary rock, the deformation modulus can be predicted using GSI system whereas the strength parameters can be estimated using RMR for sedimentary rocks.

Table 8.14 Strength and deformability parameters produced by different methods

Method		Index	Friction angle	Cohesion (MPa)	Elastic modulus (MPa)	Poisson's ratio
RMR		33	18.3	0.163	3758	
GSI		40	20.5	0.992	638.16	
UDEC	Mode 1	Yield	27-47.5	0-0.15	659.8-2364.4	0.282- 0.456-
		Ultimate	27.6-51	0-0.3		
	Mode 2	Ultimate	23.8-24	0	402.2-406	0.476- 0.484
	Mode 3	Ultimate	47.4	6.22	2475.3-3128.	0.273- 0.278

8.7   Summary and Conclusions

In this chapter the laboratory test results of a real dam foundation containing a jointed rock mass were obtained. The rock samples were tested under oven dry and saturated conditions. There were significant reductions in rock strength and deformability parameters in saturated condition, which was considered in the study. These results were used in UDEC to characterize the strength and deformability parameters of a rock mass in the left abutment of the Surqawshan Dam.

The results from UDEC were compared with the RMR and GSI systems. It was concluded that numerical models can be positively used to determine the equivalent strength and deformability parameters of a rock mass, since there is a difficulty in testing large jointed rock samples in the laboratory at this time. Also, UDEC appears to be most promising tool to study rock mass behaviour.

According to the UDEC results, all methods give similar predictions of friction angle, however GSI overestimates the cohesion. The UDEC and

GSI gave reasonable estimation of deformation modulus, whereas RMR overestimated it.

Generally, for rapid estimation of deformability and strength parameters, especially for weak sedimentary rocks, the deformation modulus can be predicted from the GSI system, whereas the strength parameters can be estimated using RMR.

Chapter 9 Conclusions and Recommendations

9.1 Conclusions

This research studied rock mass behaviour using numerical modelling technique utilising two software packages to analyse the stability of gravity dams on jointed rock masses. These packages, which are extensively used in rock mechanics, are UDEC and FLAC. Conceptual models and real gravity dams quoted from the literature were analysed. The strength and deformability parameters were also predicted by using UDEC and supported by testing small-scale, jointed rock samples. The results are valuable for engineers involved in future dam design. The study has resulted in the following conclusions:

1) Both codes can give similar results to the conventional theoretical approach, as long as the rock foundation blocks are not rotated by the stress regime created by the dam and reservoir. However, this similarity was found to depend on the joint strength. As the joint strength is reduced, UDEC was found to provide a better representation of the behaviour of a jointed system and arguably a more realistic prediction of the stress distribution under the dam

2)   Different locations of a weak joint with varying dip angles were studied using FLAC in order to investigate the critical configuration that has the most significant effect on the dam's stability.

The research shows that both the location and orientation of the weak joint have an important effect on the predicted deformation of the dam, especially where a weak joint is located downstream and dipped at a low angle toward the upstream direction

3) UDEC can efficiently be used to predict the strength and deformability parameters of a rock mass and, at certain specific joint configurations, the rock mass behaviour was similar to the behaviour of granular material.

4) For loading conditions on a jointed rock sample using UDEC, both the strain-controlled and stress-controlled method can give similar results under similar boundary condition; however, the strain-controlled method may give higher axial stress than the stress-controlled one if the platen is not simulated with a jointed rock sample. In this case the boundary condition will be different and this is why strain-controlled method gives higher axial stress than the stress-controlled one.

5) In blocky rock masses, there were three main types of failure modes. These modes were shear through intact blocks, slip and block rotations, and slide failure. The slip and block rotation mode may change to shear mode under high confining stress. As a result the failure envelope of strength follows Patton's bilinear model.

6) The strain hardening of a jointed rock sample is a result of non-uniform axial stress distribution because of rock-platen interac-

tion in triaxial testing using either Hoek cell or soil triaxial cell. To reduce this effect, a novel loading configuration was developed and was verified by experimental results.

7) The study of rock mass strength and deformability parameters of a real dam's foundation in Iraq were determined using UDEC and available rock classification systems: RMR and GSI. According to the UDEC results all methods give a similar prediction of friction angle; however, GSI overestimates the cohesion. The UDEC and GSI gave reasonable estimations of deformation modulus, whereas RMR overestimated it. Generally, for rapid estimation of deformability and strength parameters, especially for weak sedimentary rock, the deformation modulus can be predicted from the GSI system, whereas the strength parameters can be estimated using RMR.

8) It was shown that for sedimentary rock, the saturation condition has an effect on cementation between rock particles. For dam construction the saturation condition must be taken in account, especially where expansive clay minerals with pyrite and anhydrite are involved in the rock fabric.

9) Under similar boundary conditions both numerical modelling technique and experimental model may give similar results by selecting an appropriate constitutive model.

10) In UDEC, the Young's modulus and Poisson's ratio can be determined indirectly for rock samples tested under a plane strain

condition from the axial stress-axial strain relationships using Equations 6.2 and 6.3.

11) The stiffness ratio (k_s/k_n) of the joints has an important effect on the lateral strain ratio and deformation modulus. By fixing k_n and increasing the stiffness ratio, the deformation modulus increases while the lateral strain ratio decreases, whereas by fixing k_s both parameters decrease while increasing the stiffness ratio.

12) Based on the results presented in this research a more efficient rock classification system for dam construction can be developed using UDEC and 3DEC.

9.2 Recommendations for Further Work

Based on the results of this project, the following recommendations for future study are proposed:

1) The effect of joint configuration of a rock mass on arch dams should be studied using 3DEC.

2) Rock mass behaviour under dams using BB (Barton-Bandis) model in UDEC need to be investigated to deal with discontinuities as rough joints.

3) The effect of a weak joint on arch dam stability under 3D using FLAC3D code should also be investigated.

4) Since it is difficult to build a large scale physical model of a gravity dam with a jointed rock mass in the laboratory, this can be simulated by using a small scale model in a centrifuge test.

5) We need to investigate the effect of a weak layer on the stability of a dam that has sloping ground in the downstream direction, using FLAC2D.

6) The equivalent strength and deformability parameters of the Discrete Fracture Network (DFN) model should be estimated using UDEC.

7) Kink band failure in an anisotropic rock mass could be studied using UDEC.

8) The new loading configuration in high cell pressure could be used to find out whether the deformation changes with confining stress.

9) The Surqawshan dam in Kurdistan in Iraq could be modelled with its foundation jointed rock mass, using FLAC and benefitting from the equivalent mechanical properties predicted by UDEC in this study.

10) Studying the crushing or cracking of rock blocks under dams should be studied using the idea of cohesive contact particle or Bonded-Particle Model (BPM).

11) A new rock mass classification for dams could be developed using UDEC and 3DEC.

12) The empirical equations derived during the last four decades for jointed rock samples based on tests in a Hoek cell should be checked using the new loading configuration proposed in this study.

13) Since the current version of UDEC cannot model the flow through continuum media, it cannot be used to model an earth dam on jointed rock mass. However, this problem could be overcome by coupling UDEC with FLAC.

REFERENCES

Aghda, S. M. F., Rayhani, M. H. T. & S.Sh.Yasrebi 2004. Evaluation of Mechanical Behaviour of Sandstone and Andesibasalt Rockfill Materials Using Triaxial & Direct Shear Tests. *Journal of Science Kharazmi University,* 2(No.3&4): 13-22.

Al-Rawi, Y. 1983. Origin of red color in the Gercus Formation (Eocene), northeastern Iraq. *Sedimentary Geology,* 35(3): 177-192.

Anderson, W. H. 2008. *Foundation problems and pyrite oxidation in the Chattanooga Shale, Estill County, Kentucky.* Kentucky Geological Survey, University of Kentucky.

Asadzadeh, M. & Soroush, A. 2009. Direct shear testing on a rockfill material. *Arabian Journal for Science and Engineering,* 34(2B): 379-396.

Asef, M. R. 2001. *Rock-support Interaction Analysis for Tunnel Design: A Numerical Modelling Based Approach.* Ph.D. thesis, department of Civil Engineering, University of Nottingham, Nottingham, U.K.

Asef, M. R. & Reddish, D. J. 2002. The impact of confining stress on the rock mass deformation modulus. *Geotechnique,* 52(4): 235-241.

Baghbanan, A. 2008. *Scale and stress effects on hydro-mechanical properties of fractured rock masses.* PhD thesis, Royal Institute of Technology (KTH)

Barla, G., Bonini, M. & Cammarata, G. 2004. Stress and seepage analyses for a gravity dam on a jointed granitic rock mass. *Proceedings of the 1st international UDEC/3DEC symposium: numerical modeling of discrete materials in geotechnical engineering, civil engineering, and earth sciences, Bochum, Germany.* Rotterdam: Balkema.

Barton, N., Bandis, S. & Bakhtar, K. 1985. Strength, deformation and conductivity coupling of rock joints. *International Journal of Rock Mechanics and Mining Sciences & Geomechanics Abstracts,* 22(3): 121-140.

Barton, N., Lien, R. & Lunde, J. 1974. Engineering classification of rock masses for the design of tunnel support. *Rock mechanics,* 6(4): 189-236.

Barton, N. & Quadros, E. 2014. Anisotropy is Everywhere, to See, to Measure, and to Model. *Rock Mechanics and Rock Engineering,* 1-17.

Bhasin, R. & Høeg, K. 1998. Numerical modelling of block size effects and influence of joint properties in multiply jointed rock. *Tunnelling and Underground Space Technology,* 13(2): 181-188.

Bieniawski, Z. 1973. Engineering classification of jointed rock masses. *Trans. S. Afr. inst. civ. eng.,* 15(12): 335-344.

Bieniawski, Z. 1974. Engineering classification of jointed rock masses. *journal of the south african institute of mining and metallurgy,* 74(8): 312-320.

Bieniawski, Z. 1978. Determining rock mass deformability: experience from case histories. *International Journal of Rock Mechanics and Mining Sciences & Geomechanics Abstracts,* 15(5): 237-247.

Bieniawski, Z. T. 1989. *Engineering rock mass classifications.* NewYork, John Wiley & Sons.

Bieniawski, Z. T. & Bernede, M. J. 1979. Suggested methods for determining the uniaxial compressive strength and deformability of rock materials: Part 1. Suggested method for determination of the uniaxial compressive strength of rock materials. *International Journal of Rock Mechanics and Mining Sciences & Geomechanics Abstracts,* 16(2): 137.

Bieniawski, Z. T. & Orr, C. M. 1976. Rapid site appraisal for dam foundations by the geomechanics classification. Proc. 12th Congr. Large Dams, ICOLD, Mexico City. ICOLD, 483-501.

Boyer, D. D. 2006. Geological factors influencing dam foundation failure modes. *The Role of Dams in the 21st Century, 26th Annual USSD Conference.* San Antonio, Texas, USA: U.S. Society on Dams.

Bro, A. 1996a. A low friction spherical seat for shear testing in a triaxial cell. *International Journal of Rock Mechanics and Mining Sciences & Geomechanics Abstracts,* 33(2): 205-214.

Bro, A. 1996b. A weak rock triaxial cell. *International Journal of Rock Mechanics and Mining Sciences & Geomechanics Abstracts,* 33(1): 71-74.

Bro, A. 1997. Analysis of multistage triaxial test results for a strain-hardening rock. *International Journal of Rock Mechanics and Mining Sciences,* 34(1): 143-145.

Broch, E. & Franklin, J. A. 1972. The point-load strength test. *International Journal of Rock Mechanics and Mining Sciences & Geomechanics Abstracts,* 9(6): 669-676.

Brook, N. 1977. The use of irregular specimens for rock strength tests. *International Journal of Rock Mechanics and Mining Sciences & Geomechanics Abstracts,* 14(4): 193-202.

Brown, E. T. & Trollope, D. H. 1970. Strength of a model of jointed rock. *Journal of Soil Mechanics & Foundations Div,* 96(SM2): 685-704.

Butscher, C., Huggenberger, P., Zechner, E. & Einstein, H. H. 2011. Relation between hydrogeological setting and swelling potential of clay-sulfate rocks in tunneling. *Engineering Geology,* 122(3): 204-214.

Cai, M., Kaiser, P. K., Uno, H., Tasaka, Y. & Minami, M. 2004. Estimation of rock mass deformation modulus and strength of jointed hard rock masses using the GSI system. *International Journal of Rock Mechanics and Mining Sciences,* 41(1): 3-19.

Cundall, P. A. 1980. UDEC-A Generalized Distinct Element Program for Modelling Jointed Rock. *U.S. Army, European Research Office and Defense Nuclear Agency, Contract DATA 37-79-C-0548.*

Cundall, P. A., Marti, J., Beresford, P., Last, N. & & Asgian, M. 1978. Computer Modelling of Jointed Rock Masses. *U.S. Army Engineer Waterways Experiment Station, Vicksburg, Mississippi.* Report N-78-4.

de Vallejo, L. I. G. & Ferrer, M. 2011. *Geological engineering.* London, UK, CRC Press.

Deere, D. U. & Deere, D. W. 1989. Rock Quality Designation (RQD) after Twenty Years. DTIC Document.

Dhannoun, H. Y., Al-Dabbagh, S. M. A. & Hasso, A. A. 1988. The geochemistry of the Gercus red bed formation of northeast Iraq. *Chemical Geology,* 69(1–2): 87-93.

Dolezalova, M. 2004. Numerical analysis of an old masonry dam using UDEC. *Proceedings of the 1st international UDEC/3DEC symposium: numerical modeling of discrete materials in geotechnical engineering, civil engineering, and earth sciences, Bochum, Germany.* Rotterdam: Balkema.

Douglas, K. J. 2002. *The shear strength of rock masses.* PhD Thesis.The University of New South Wales, Sydney, Australia.

Edelbro, C., Sjöberg, J. & Nordlund, E. 2007. A quantitative comparison of strength criteria for hard rock masses. *Tunnelling and Underground Space Technology,* 22(1): 57-68.

Farinha, M. L. B., Bretas, E. M. & Lemos, J. V. 2012. Hydromechanical Analysis for the Safety Assessment of a Gravity Dam. *Innovative Dam and Levee Design and Construction for Sustainable Water Managementportuguese National Laboratory for Civil Engineering, 32nd Annual USSD Conference.* New Orleans, Louisiana: U.S.Society on Dams.

Fishman, Y. A. 2009. Stability of concrete retaining structures and their interface with rock foundations. *International Journal of Rock Mechanics and Mining Sciences,* 46(6): 957-966.

Fortsakis, P., Nikas, K., Marinos, V. & Marinos, P. 2012. Anisotropic behaviour of stratified rock masses in tunnelling. *Engineering Geology,* 141–142(74-83.

Franklin, J. A. 1985. Suggested method for determining point load strength. *International Journal of Rock Mechanics and Mining Sciences & Geomechanics Abstracts,* 22(2): 51-60.

Gaziev, E. G. & Erlikham, S. A. 1971. Stresses and strains in anisotropic rock foundation (model studies). *proceeding Symposium of Rock Fracture.* Report II-I, Nancy, France International Society for Rock Mechanics (ISRM).

Gimenes, E. & Fernández, G. 2006. Hydromechanical analysis of flow behavior in concrete gravity dam foundations. *Canadian Geotechnical Journal,* 43(3): 244-259.

Goodman, R. E. 1989. Introduction to rock mechanics.: John Wiley & Sons.

Greene, B. H. & Christ, C. 1998. Mistakes of man: The Austin Dam disaster of 1911. *Pennsylvania Geology,* 29(2/3): 7-14.

Greminger, M. 1982. Experimental studies of the influence of rock anisotropy on size and shape effects in point-load testing. *International Journal of Rock Mechanics and Mining Sciences & Geomechanics Abstracts,* 19(5): 241-246.

Hoek, E. 1983. Strength of jointed rock masses. *Géotechnique,* 33(3): 187-223.

Hoek, E. 1994. Strength of rock and rock masses. *ISRM News Journal,* 2(2): 4-16.

Hoek, E. & Brown, E. T. 1980. Empirical strength criterion for rock masses. *J. Geotech. Engng Div., ASCE,* 106(GT9): 1013-1035.

Hoek, E. & Brown, E. T. 1997. Practical estimates of rock mass strength. *International Journal of Rock Mechanics and Mining Sciences,* 34(8): 1165-1186.

Hoek, E., Carranza-Torres, C. & Corkum, B. 2002. Hoek-Brown failure criterion-2002 edition. In: Proceedings of NARMS-TAC Conference, Toronto, Canada. 267-273.

Hoek, E. & Diederichs, M. S. 2006. Empirical estimation of rock mass modulus. *International Journal of Rock Mechanics and Mining Sciences,* 43(2): 203-215.

Hoek, E. & Franklin, J. A. 1968. *A simple triaxial cell for field or laboratory testing of rock.* Trans. Inst. Mining & Metallugy. Vol.77, pp A22-A26.

Hoek, E., Kaiser, P. & Bawden, W. 1995. Support of underground excavations in hard rock. *Balkema, Rotterdam*.

Hoek, E. & Marinos, P. 2007. A brief history of the development of the Hoek-Brown failure criterion. *Soils and Rocks,* 2(1-8).

Hoek, E., Wood, D. & Shah, S. 1992. A modified Hoek-Brown criterion for jointed rock masses. In: Proceedings of the International ISRM Symposium on Rock Characterization, Chester, UK. 209-214.

Hudson, J. A. & Harrison, J. P. 1997. Excavation principles. *In:* Hudson, J. A. & Harrison, J. P. (eds.) *Engineering Rock Mechanics: An Introduction to the Principles.* Oxford: Pergamon.

ICOLD 1974. Lessons From Dam Incidents. *International Commission on Large Dams (ICOLD)* Paris.

ICOLD 1983. Deterioration of Dams and Reservoirs. International Commission on Large Dams (ICOLD). Paris.

ICOLD 1995. Bulletin 99-Dam failures statistical analysis. *International Commission on Large Dams.* Paris.

ISRM 1978. International society for rock mechanics commission on standardization of laboratory and field tests: Suggested methods for the quantitative description of discontinuities in rock masses. *International Journal of Rock Mechanics and Mining Sciences & Geomechanics Abstracts,* 15(6): 319-368.

ISRM 1981. *Rock Characterization, Testing and monitoring. ISRM Suggested Methods.* Pergamon Press.

Itasca 2008. FLAC Code (Fast Lagrangian Analysis of Continuum). Minneapolis, USA.

Itasca 2011. UDEC (Universal Distinct Element Code). Version 5.0 Minneapolis.

Jaeger, J. C., Cook, N. G. & Zimmerman, R. 2009. *Fundamentals of rock mechanics.* John Wiley & Sons.

Jansen, R. B. 1988. *Advanced Dam Engineering For Design, Construction, And Rehabilitation.* USA, Van Nostrand Reinhold.

Jassim, S. Z. & Goff, J. C. 2006. *Geology of Iraq.* First edition. Czech Republic, Dolin.

Jian Liu, X.-T. F., Xiu-Li Ding 2003a. Stability assessment of the three-Gorges dam foundation, China, using physical and numerical

modeling-Part II: numerical modeling. *International Journal of Rock Mechanics and Mining Sciences,* 633-652.

Jian Liu, X.-T. F., Xiu-Li Ding, Jie Zhang, Deng-Ming Yue 2003b. Stability assessment of the three-Gorges dam foundation, China, using physical and numerical modeling-Part I: Physical model tests. *International Journal of Rock Mechanics and Mining Sciences,* 609-631.

Kaiser, P. K., MacKay, C. & Gale, A. D. 1986. Evalution of rock classifications at B.C. Rail Tumbler Ridge Tunnels. *Rock mechanics and rock engineering,* 19(4): 205-234.

Kovari, K., Tisa, A., Einstein, H. & Franklin, J. 1983. Suggested methods for determining the strength of rock materials in triaxial compression: revised version. *International Journal of Rock Mechanics and Mining Sciences,* 20(6): 283-290.

Kulatilake, P. H. S. W., Liang, J. & Gao, H. 2001a. Experimental and Numerical Simulations of Jointed Rock Block Strength under Uniaxial Loading. *Journal of Engineering Mechanics,* 127(12): 1240-1247.

Kulatilake, P. H. S. W., Malama, B. & Wang, J. 2001b. Physical and particle flow modeling of jointed rock block behavior under uniaxial loading. *International Journal of Rock Mechanics and Mining Sciences,* 38(5): 641-657.

Ladanyi, B. & Archambault, G. 1969. Simulation of shear behavior of a jointed rock mass. *The 11th US Symposium on Rock Mechanics (USRMS), American Rock Mechanics Association.*

Li, Z., Sheng, Y. & Reddish, D. 2005. Rock strength reduction and its potential environmental consequences as a result of groundwater rebound. Proceedings of the 9th International Mine Water Association Congress: Mine Water 2005—Mine Closure.

Londe, P. 1987. The Malpasset Dam failure. *Engineering Geology,* 24(1–4): 295-329.

Madsen, F. & Nuesch, R. 1991. The swelling behaviour of clay-sulfate rocks. *7th ISRM Congress.* International Society for Rock Mechanics.

Marinos, P. & Hoek, E. 2001. Estimating the geotechnical properties of heterogeneous rock masses such as flysch. *Bulletin of Engineering Geology and the Environment,* 60(2): 85-92.

Martt, D. F., Shakoor, A. & Greene, B. H. 2005. Austin Dam, Pennsylvania: the sliding failure of a concrete gravity dam. *Environmental & Engineering Geoscience,* 11(1): 61-72.

Mas Ivars, D., Pierce, M. E., Darcel, C., Reyes-Montes, J., Potyondy, D. O., Paul Young, R. & Cundall, P. A. 2011. The synthetic rock mass approach for jointed rock mass modelling. *International Journal of Rock Mechanics and Mining Sciences,* 48(2): 219-244.

Nasseri, M. H. B., Rao, K. S. & Ramamurthy, T. 2003. Anisotropic strength and deformational behavior of Himalayan schists. *International Journal of Rock Mechanics and Mining Sciences,* 40(1): 3-23.

Nicholson, G. A. 1983. Design of gravity dams on rock foundations: Sliding stability assessment by limit equilibrium analysis and selection of shear strength parameters. Geotechnical Laboratory, U.S. Army Corps of Engineers, Waterways Experiment station.

Noorian Bidgoli, M. & Jing, L. 2014a. Anisotropy of strength and deformability of fractured rocks. *Journal of Rock Mechanics and Geotechnical Engineering,* 6(2): 156-164.

Noorian Bidgoli, M. & Jing, L. 2014b. Effects of loading conditions on strength and deformability of fractured rocks-a numerical study. Rock Engineering and Rock Mechanics: Structures in and on Rock Masses-Proceedings of EUROCK 2014, ISRM European Regional Symposium, Vigo, Spain. CRC Press., 365-368.

Noorian Bidgoli, M., Zhao, Z. & Jing, L. 2013. Numerical evaluation of strength and deformability of fractured rocks. *Journal of Rock Mechanics and Geotechnical Engineering,* 5(6): 419-430.

Novák, P., Moffat, A., Nalluri, C. & Narayanan, R. 2007. *Hydraulic structures.* 4th ed. CRC Press.

Palmström, A. 2009. Combining the RMR, Q, and RMi classification systems. *Tunnelling and Underground Space Technology,* 24(4): 491-492.

Pine, R. J., Coggan, J. S., Flynn, Z. N. & Elmo, D. 2006. The Development of a new Numerical Modelling Approach for Naturally Fractured Rock Masses. *Rock Mechanics and Rock Engineering,* 39(5): 395-419.

Potyondy, D. O. & Cundall, P. A. 2004. A bonded-particle model for rock. *International Journal of Rock Mechanics and Mining Sciences,* 41(8): 1329-1364.

Ramamurthy, T. & Arora, V. K. 1992. Simple stress-strain model for jointed rocks : Proc 7th ISRM International Congress on Rock Mechanics, Aachen, 16–20 September 1991 V1, P323–326. Publ Rotterdam: A A Balkema, 1991. *International Journal of Rock Mechanics and Mining Sciences & Geomechanics Abstracts,* 29(4): 240.

Ramamurthy, T. & Arora, V. K. 1994. Strength predictions for jointed rocks in confined and unconfined states. *International Journal of Rock Mechanics and Mining Sciences & Geomechanics Abstracts,* 31(1): 9-22.

Ramamurthy, T., Rao, G. V. & Singh, J. 1993. Engineering behaviour of phyllites. *Engineering Geology,* 33(3): 209-225.

Reik, G. & Zacas, M. 1978. Strength and deformation characteristics of jointed media in true triaxial compression. *International Journal of Rock Mechanics and Mining Sciences & Geomechanics Abstracts,* 15(6): 295-303.

Romana 2003. DMR (Dam Mass Rating). An Adaptation of RMR Geomechanics Classification for use in Dams Foundation, Int. Cong. on Rock Mechanics, (Technology Roadmap for rock Mechanics). *South African Institute of Mining and Metallurgy.*

Romana, M., Serón, J. B. & Montalar, E. 2003. SMR geomechanics classification: application, experience and validation. *Proceedings of the ISRM,* 981-984.

Serafim, J. L. & Pereira, J. P. 1983. Considerations on the geomechanical classification of Bieniawski. Lisbon, Portugal: Proc. Int. Symp on Eng. Geol. and Underground Construction.

Singh, B. & Varshney, R. S. 1974. Effect of faults in the foundations on dam behaviour. *Irrigation and power.* New Delhi: Central Board of Irrigation and power.

Singh, M., Rao, K. S. & Ramamurthy, T. 2002. Strength and deformational behaviour of a jointed rock mass. *Rock Mechanics and Rock Engineering,* 35(1): 45-64.

Singh, M. & Singh, B. 2008a. High lateral strain ratio in jointed rock masses. *Engineering Geology,* 98(3–4): 75-85.

Singh, M. & Singh, B. 2008b. Laboratory and numerical Modelling of a Jointed Rock mass. *12th international Conference of International Association for computer methods and advances in Geomechanics (IACMAG).* Goa, India.

Snell, E. & Knight, K. 1991. Susceptibility of dams to failure by sliding on sub-foundation strata that dip upstream. *17th International Congress on Large dams (ICOLD).* Vienna, Austria.

Starfield, A. M. & Cundall, P. A. 1988. Towards a methodology for rock mechanics modelling. *International Journal of Rock Mechanics and Mining Sciences & Geomechanics Abstracts,* 25(3): 99-106.

Thomas, H. H. 1976. *The Engineering of Large Dams.* UK, John Wiley & Sons, Ltd.

Tiwari, R. P. & Rao, K. S. 2006. Post failure behaviour of a rock mass under the influence of triaxial and true triaxial confinement. *Engineering Geology,* 84(3–4): 112-129.

U.S. Army Corps of Engineers 1981. Engineering and design, Sliding stability for concrete structures. Technical letter No. 1110-2-256.

Underwood, L. B. & Dixon, N. A. 1977. Dams on Rock Foundations. *Rock Engineering for Foundations & Slopes.* ASCE.

USACE 1995. (US Army Corps of Engineers), Engineering and design: Gravity dam design. *Report EM1110-2-2000.* Washington, D.C.

USBR 1988. *Training Aids for Dam Safety module: Evaluation of concrete dam stability.* United States Bureau of Reclamation.

Varshney, R. S. 1972. Rock foundation characteristics and dam design. *International Journal of Rock Mechanics and Mining Sciences & Geomechanics Abstracts,* 9(5): 645-659.

Varshney, R. S. 1982. *Concrete Dams.* New Delhi, Mohan Primlani.

Vermeer, P. A. 1984. Non-Associated Plasticity for Soils, Concrete and Rock. *In:* Borst, R. d. (ed.). Heron.

Wei, Z., Xiaolin, C., Chuangbing, Z. & Xinghong, L. 2008. Failure analysis of high-concrete gravity dam based on strength reserve factor method. *Computers and Geotechnics,* 35(4): 627-636.

Witherspoon, P. A. 1980. Validity of Cubic Law for Fluid Flow in a Deformable Rock Fracture. *Water Resources Research.*

Wittke, W. 1990. *Rock mechanics: theory and applications, with case histories.* Springer-Verlag.

Wittke, W. 2014. *Rock Mechanics Based on an Anisotropic Jointed Rock Model (AJRM).* John Wiley & Sons.

Wittke, W. & Leonards, G. 1987. Modified hypothesis for failure of the Malpasset Dam. *Engineering Geology,* 24(1): 407-421.

Wyllie, D. C. 1999. *Foundations on Rock.* London and New York, The Bath Press, Bath.

Wyllie, D. C. 2003. *Foundations on Rock: Engineering Practice.* 2nd. CRC Press.

Yoshinaka, R. & Yamabe, T. 1986. Joint stiffness and the deformation behaviour of discontinuous rock. *International Journal of Rock Mechanics and Mining Sciences & Geomechanics Abstracts,* 23(4): 19-28.

Zhang, H., Zhang, L., Wang, W. & Wang, D. 2008. Stability Analysis of Gravity Dams on Sloping Layered Rock Foundation against Deep Slide. In Earth & Space 2008, Engineering, Science,

Construction, and Operations in Challenging Environments. ASCE, 1-6.

Zhang, L. 2005. *Engineering properties of rocks.* Amsterdam, Netherlands, Elsevier Ltd.

Zhang, L. 2010. Estimating the Strength of Jointed Rock Masses. *Rock Mechanics and Rock Engineering,* 43(4): 391-402.

Zhang, L. & Einstein, H. H. 2004. Using RQD to estimate the deformation modulus of rock masses. *International Journal of Rock Mechanics and Mining Sciences,* 41(2): 337-341.

ZHINAB Consulting Co. 2011. Geotechnical & Rock Mechanical Report for Surqawshan Earth Dam. *Unpublished Report.* Kurdistan of Iraq, Iraq: ZHINAB Consulting Eng.

Zhu, H.-H., Yin, J.-H., Dong, J.-H. & Zhang, L. 2010. Physical modelling of sliding failure of concrete gravity dam under overloading condition. *Geomechanics and Engineering,* 2(2): 89-106.

Appendix A   RMSPUDEC CODE and FISH FUNCTION

This appendix presents the code with the developed FISH function (a programming language embedded within Itasca codes to enable users to write their own tasks) which was written based on Itasca manual. This code used in UDEC simulation of UCS and trixial tests.

```
;Code:RMSPUDEC.dat (Rock Mass Strength Problem Using UDEC)
;Title: Simulation of compression test using UDEC
New
config
round 0.08
edge 0.16
;Sample size
block 0,-60. 0,0 60,0 60,-60
jregion id 1 -1,-60. -1,0 60,0 60,-60
;Joint sets
jset angle 60 spacing 5 origin 60.0,-60. range jregion 1
jset angle 150 trace 5 gap 5  spacing 5 origin 57.5,-64.33 range jregion 1
jset angle 150 trace 5 gap 5 spacing 5 origin 56.9,-55.2 range jregion 1
; Generate edge zoning for block model (Blocks are made deformable)
gen edge 2.5 range jregion 1
group zone 'Foundation:Blocks' range jregion 1
; material properties (Mohr-Coulomb model)
;zone model elastic density 2.65E-3 bulk 5.5555E3 shear 4.167E3 range
group 'Foundation:Blocks'
zone model mohr density 2.65E-3 bulk 5.5555E3 shear 4.167E3 friction 45
cohesion 2 ten 1 range group 'Foundation:Blocks'
group joint 'Foundation:Joints' range jregion 1
; Contact properties, area-contact Coulomb slip model
joint model area jks 5E3 jkn 10E3 jfriction 30 range group 'Foundation:Joints'
; new contact default
set jcondf joint model area jks 5E3 jkn 10E3 jfriction 30
set small
```

;Boundaries stresses

boundary stress -01,0.0,-0.0 range -1,.5 -60,0.

boundary stress -01,0.0,-0.0 range 59.5,60.5 -60,0.

; set in-situ stresses

insitu stress -01.,-0.,-01. szz -01.

;fix the bottom and top boundaries

boundary yvelocity 0 range -1,61 -61,-59.8

boundary stress -0,0.,-1.0 range -1,60.5 -.1,1

reset jndisp hist time disp

set ftime=0

; Select points for measurement of displacements

def p_cons

  p_s1 = gp_near(0.0,-30.0)

   p_s2 = gp_near(60,-30.0)

    p_n1 = gp_near(30.0,0.0)

   p_n2 = gp_near(30.0,-60.0)

  ntab = 1

 end

p_cons

def set_lim

 i_gt = gp_near(0,-0)

 i_gb = gp_near(0,-60)

end

set_lim

;The developed FISH function for loading the sample using either strain-controlled or stress-controlled methods.

def loads_sn

 loop n_step1(1,n_steps2)

; For strain-controlled use the following :	;For stress-controlled use the following
command boundary yvelocity -1E-2 range -1,60.5 -0.1,1 cyc 50 boundary yvelocity 0 range -1,60.5 -.1,1 solve ratio 1.0E-5 endcommand	command boundary stress 0,0,-0.10 range -1,60.5 -0.1,1 solve ratio 1.0E-5 endcommand

```
        sum =0.0
          sum1=0.
            ib = block_head
              loop while ib # 0
                ig = b_gp(ib)
                  loop while ig # 0
                    if gp_y(ig) = -0.
                      ibou=gp_bou(ig) ; index of boundary corner
                      if(ibou) > 0 then ; exterior boundary
                      forcey = bou_yreaction(ibou) ; total y-force
                    sum = sum - forcey
                  endif
                else
                if gp_y(ig) = -60.
                  ibou=gp_bou(ig) ; index of boundary corner
                if(ibou) > 0 then ; exterior boundary
                forcey = bou_yreaction(ibou) ; total y-force
              sum1 = sum1 - forcey
            endif
          endif
        endif
      ig = gp_next(ig)
    endloop
  ib = b_next(ib)
 endloop
; Calculate the axial stress on upper boundary
P_load1 = sum /60.
; Calculate the axial stress on lower boundary
P_load2=sum1/60.
;Calculate the lateral strain (s_strn) and normal strain (n_strn)
s_strn = ((gp_xdis(p_s1))-(gp_xdis(p_s2)))/60
n_strn = (gp_ydis(p_n1)-gp_ydis(p_n2))/60.
if n_strn # 0 then
; Calculate the lateral strain ratio
P_R=s_strn/(n_strn)
```

```
endif
sum3=0.0
  z_count = 0
    i_b = block_head
     loop while i_b # 0
       i_z = b_zone(i_b)
        loop while i_z # 0
          sum3 = sum3 - z_syy(i_z)
        i_z = z_next(i_z)
      z_count = z_count + 1
    end_loop
  i_b = b_next(i_b)
end_loop
; Calculate the average axial stress in the zones of blocks
sigmav = sum3/z_count
xtable(2,n_step1) = n_strn
ytable(2,n_step1) = sigmav
ev = (abs(gp_ydis(i_gb))-abs(gp_ydis(i_gt)))/(gp_y(i_gt)-gp_y(i_gb))
endloop
end
;History files for recording interested data
hist P_R
  hist n_step1
    hist P_R
      hist s_strn
       hist  n_strn
      hist sigmav
    history P_load1
  history P_load2
hist ev
;Select the number of steps and start loading the sample
set n_steps2=200
loads_sn
```

Appendix B   POISSON'S RATIO BY NEW TECHNOLOGY

Introduction

In most numerical simulations of rock masses or intact rock, the Poisson's ratio is usually assumed; however, it can be measured accurately by using new technology methods. In this study both video gauge and Digital Image Correlation (DIC) were used to predict Poisson's ratio of intact sandstone rock of Birchover Quarry in the UK. Also, the results validated using linear variable differential transformers (LVDT).

Video Gauge Technique

Video gauge can be used to measure the deformation using only one camera based on a measurement apparatus. It can measure 2D positions on selected targets of rock sample in real-time video camera frames. The video gauge method requires the following components:

1 High resolution digital camera;

2 Computer with software for video gauge;

3 Voltage input/output;

4 Lighting;

5 Adjustable camera holder; and

6 Lenses.

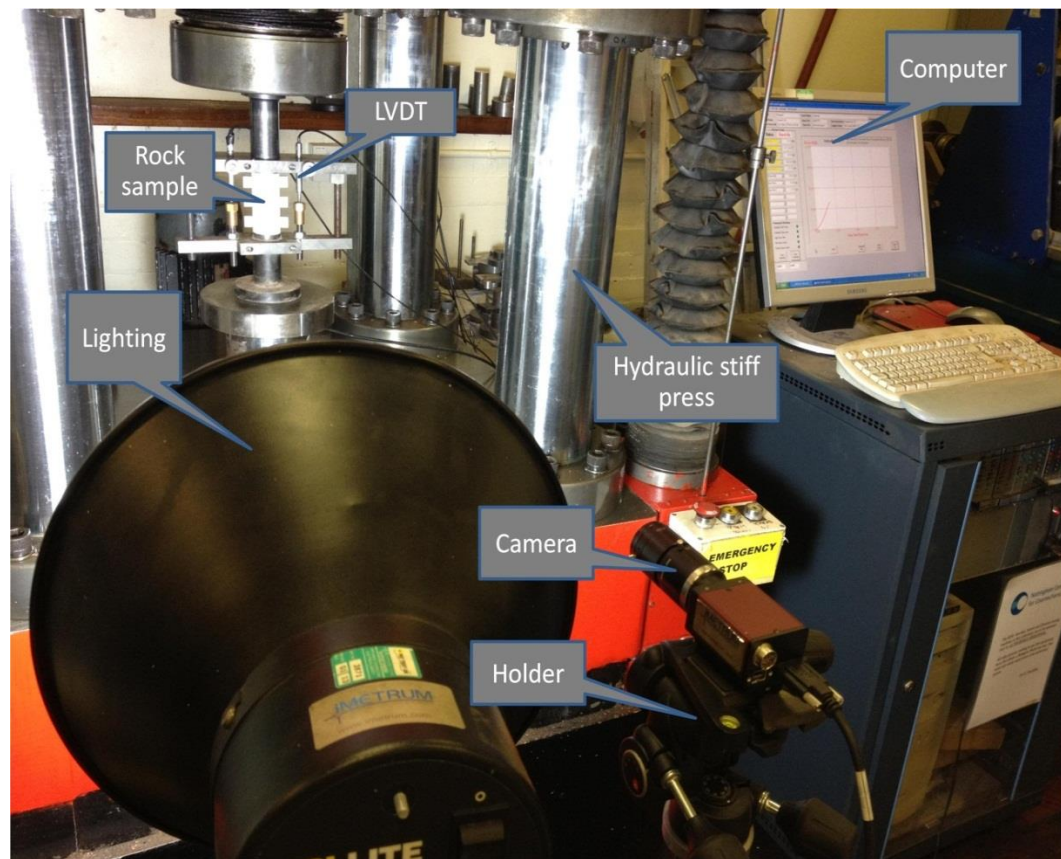The setup of video gauge with the RDP Howden 1000 kN servo-controlled hydraulic stiff press is shown in Figure B1.

Figure B1 Video Gauge setup with loading Machine

The video Gauge can measure the 2D position of any target on the sample. In this study eight targets were used to measure the lateral and axial strain as shown in Figure B2. Targets 1 and 2 on sample's ends were utilized to measure axial strain whereas six targets (Tag. 1 to 6) on lateral sides of the rock sample were utilized to measure the lateral strain.

A speckle pattern must be applied using white and black paints on the sample's surface as well as the lateral targets those attached to both sides of the sample so as to identify these targets by the camera. It should be noted that the camera can only read these targets in pixels. To convert these pixels to mm, a special calibration has to be done by finding how many pixels are in 1 mm for each target using a steel ruler. The accuracy of video gauge method was measured by comparing the axial deformation with LVDTs.
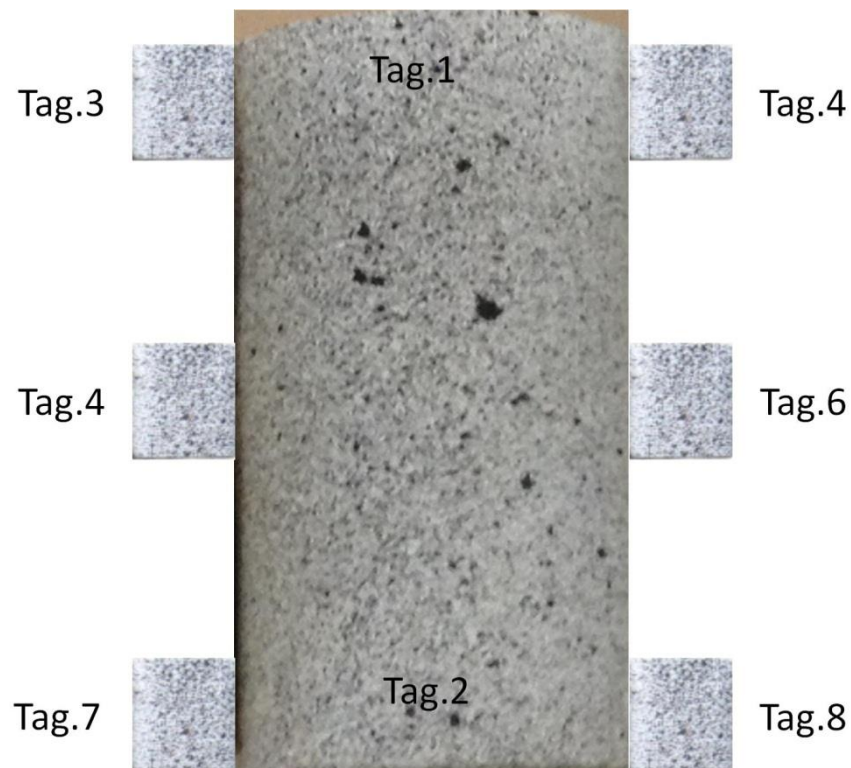

Figure B2 The rock sample with targets

Figure B3 presents the axial stress against lateral and axial strains for intact rock sample taken from Birchover Quarry. The axial stress was

determined by dividing the axial load that measured simultaneously with deformation to the cross section area of the sample. The lateral strain was calculated as an average of lateral displacement difference to sample's width. Axial strain was computed by dividing the axial displacement difference between targets (1 and 2) on the distance between these targets.

Also, LVDTs were used to measure the axial strain for checking the accuracy of Video Gauge. As can be seen from Figure B3, there is a good trend between LVDS and Video Gauge. The resulted Poisson's ratio was calculated using tangent modulus at 50% of maximum axial stress as 0.25 according to the procedure mentioned in ISRM (1981). This is reasonable for intact sandstone rocks.
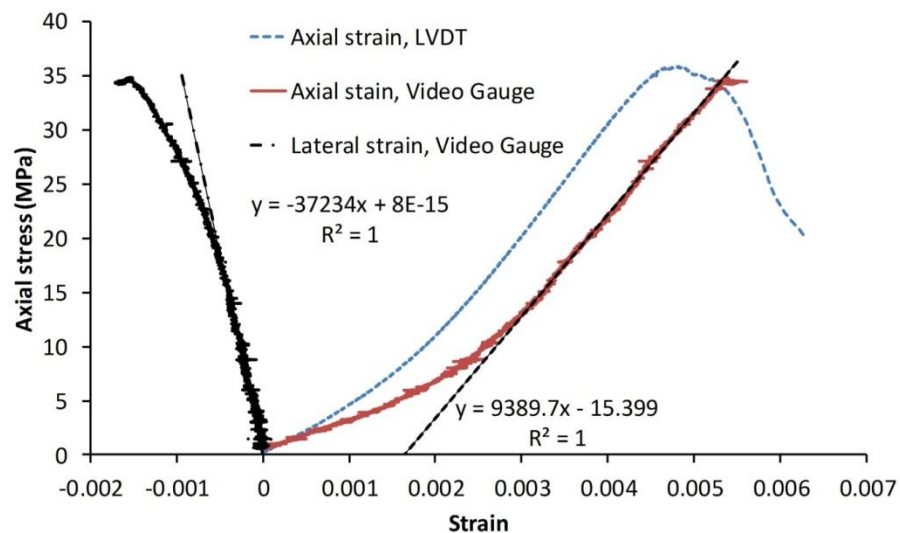

Figure B3 Axial stress-strain using video gauge

The Digital Image Correlation method (DIC)

DIC can be employed to measure the surface deformation in 3D using two cameras. Dantec Dynamics Q-400 Digital Correlation system was used in this study. As in video gauge method, the speckle pattern must be applied on the sample's surface using white and black paints. The system captures images of the sample surface at desired rate during the test. The process of data was performed using a software Astra 4D to determine the average axial and lateral strains. Also, two LVDTs were used to measure axial strain for checking the accuracy of DIC. The calibration of the system can be done manually using the calibration plate provide with the system. Details can be found in the manual of ISTRA 4D software.

Two intact rock samples were tested and the results are shown in Figures B4 and B5. It can be seen that there is an excellent match between LVDTs and DIC, which encouraged the researcher to use this new technique. The Poisson's ratio was computed for both samples as 0.27 and 0.271, respectively.
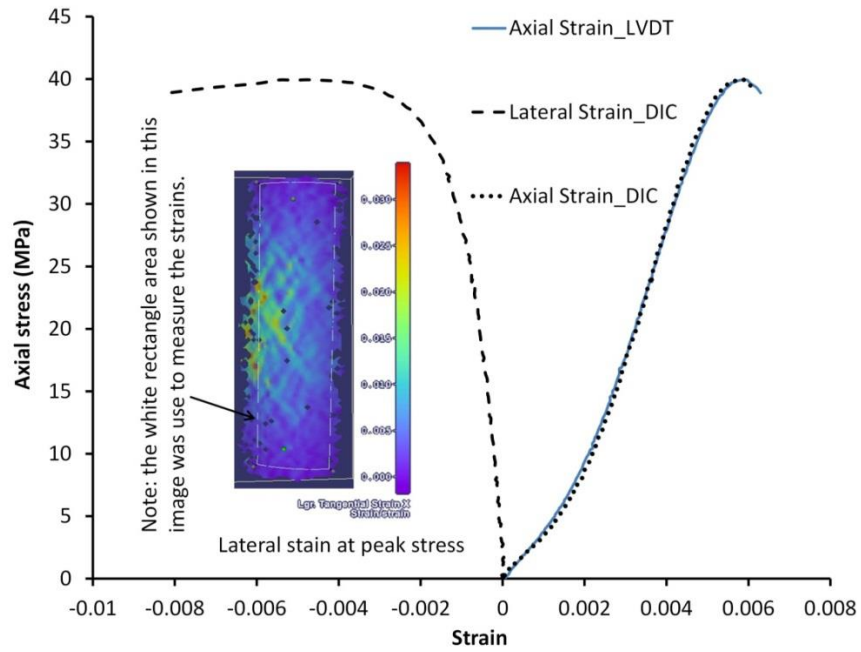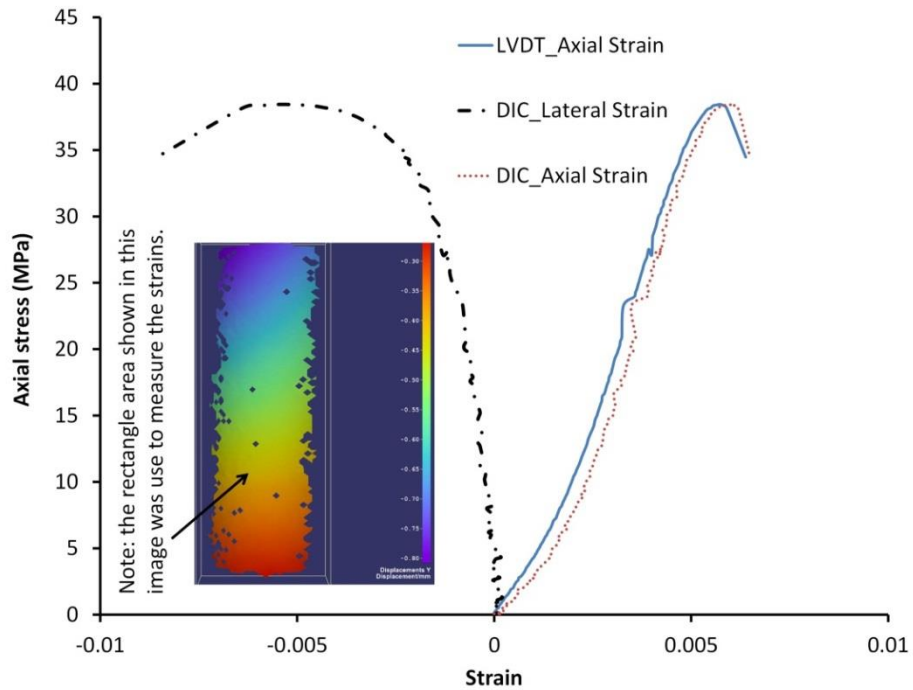
Figure B4 Axial stress-strain for sample 1 DIC

Figure B5 Axial stress-strain for sample 2 DIC